Calibration of the ALICE Transition Radiation Detector and a study of Z^0 and heavy quark production in pp collisions at the LHC

Dem Fachbereich Physik
der Technischen Universität Darmstadt

Zur Erlangung des Grades
eines Doktors des Naturwissenschaften
(Dr. rer. nat.)

vorgelegte Dissertation von
Dipl.-Phys. Raphaëlle Bailhache
aus Nantes

Darmstadt 2008
D 17

Zusammenfassung

Das ALICE Experiment ist eines der vier großen Experimente am Large Hadron Collider (LHC). Einer seiner Detektoren, der Transition Radiation Detector (TRD), ist ein Gasdetektor, welcher zur Elektronenidentifikation und zum Auffinden von Teilchenspuren geladener Teilchen verwendet wird. Geladene Teilchen ionisieren dabei entlang ihres Weges durch den Detektor das Driftgas und die Elektronen driften in einem Feld der Stärke 700 V/m über eine Strecke von 3 cm, bevor ihr Signal verstärkt wird. Wir entwickelten eine Prozedur zur Kalibrierung der Driftgeschwindigkeit, der Nullzeit , des Verstärkungfaktors und der Breite der Pad Response Funktion (PRF), welche die Verteilung der deponierten Ladung über benachbarte Pads beschreibt. Anhand simulierten *pp*-Kollisionen bei einer Schwerpunktsenergie ($\sqrt{s}$) von 14TeV sowie an den ersten realen Daten, der Aufnahme kosmischer Strahlung, wurde die Performance des Algorithmus getestet. Die Kalibrierungssoftware wurde auf dem Data Aquisition System (DAQ) am CERN installiert und wird nun parallel zu den Messungen ausgeführt, um eine erste Bestimmung der oben genannten Größen zu erhalten.

Des Weiteren enthält diese Arbeit eine Studie über die Möglichkeit der zentralen ALICE Detektoren zum Nachweis von Z^0-Bosonen über den Zerfall $Z^0 \rightarrow e^+e^-$ in *pp*-Kollisionen bei $\sqrt{s}$=14TeV. Der Produktionswirkungsquerschnitt ist mit einem kleinen theoretischen Fehler aus der QCD versehen, und ein Vergleich zwischen experimentellen Ergebnissen und theoretischen Erwartungen ermöglicht eine Überprüfung des Verständnisses des Detektorsignales bei hohen Transversalimpulsen. Wir zeigen, dass ein sehr klares Signal im rekonstruierten Spektrum der invarianten Masse charakteristisch für den Zerfall $Z^0 \rightarrow e^+e^-$ ist. Bei so hohen Transversalimpulsen (etwa 45 GeV/c=cM_{Z^0}/2) werden die Elektronen mit Hilfe des Transition Radiation Detektors identifiziert. Der Untergrund bestehend aus fehlerhaft identifizierten Pionen und Elektronen aus den Zerfällen schwerer Hadronen kann unterdrückt werden, indem man zwei isolierte Teilchenspuren fordert. Die größte Herausforderung stellt jedoch die kleine Produktionsrate dar. Wir schätzen die Effizienz des Triggers , welcher auf einer niedrigen Schwelle bei niedrigen p_T und Teilchenidentifikation mit Hilfe der TRD basiert, und zeigen, dass unter Verwendung eines solchen Triggers 100 Z^0s pro Jahr rekonstruiert werden können.

Ein weiteres physikalisch Thema, welches in dieser Arbeit untersucht wurde, ist die Messung von charm- und bottom Produktion über deren semi-leptonischen Kanäle. Die Messung erlaubt bei hohen Transversalimpulsen einen Test der pQCD-Berechnungen für *pp*-Kollisionen und ist notwendig zum Verständnis des Quark-Gluon-Plasmas, wovon man erwartet, dass es in *PbPb*-Kollisionen gebildet wird. Wir untersuchen die Elektronen aus den *c*- und *b*-Zerfällen, die in den zentralen Detektoren nachgewiesen werden. In 10^8 minimum-bias Ereignissen (ursprünglich für das Jahr 2008 erwartet) ist eine Untersuchung bis zu $p_T = 6$ GeV/c möglich. Die Elektronen werden mit der Time Projection Chamber (TPC), dem Transition Radiation Detetector (TRD) und der Time-Of-Flight identifiziert. Erste Schätzungen der Effizienz der Teilchenidentifikation basierend auf dem Verfahren von Bayes wurden durchgeführt. Bei hohen p_T sind Elektronen aus den zerfällen schwerer Hadronen dominant, bei niedrigen p_T sind jedoch die

Elektronen aus Gamma-Konversionen und Dalitz-Zerfällen die größte Quelle. Wir zeigen, dass das Signal/Untergrund-Verhältnis, welches dem des PHENIX Experimentes bei $\sqrt{s}$=200 GeV sehr ähnelt, eine Messung des charm- und bottom-Wirkungsquerschnittes ermöglicht.

Summary

The ALICE Experiment is one of the four experiments installed at the Large Hadron Collider (LHC). One of its detector-systems, the Transition Radiation Detector (TRD), is a gas detector designed for electron identification and charged particle tracking. The charged particle ionizes the gas along its path and electrons drift in an uniform field of 700 V/cm over 3 cm before being amplified. We implemented procedures to calibrate the drift velocity of the electrons, the time-offset of the signal, the amplification factor and the width of the Pad Response Function (PDF) characterizing the sharing of the deposited charge over adjacent pads. Physics events (*pp* and *PbPb* collisions) will be used. The performances of the algorithms were tested on simulated *pp* collisions at $\sqrt{s}$=14 TeV and on first real data taken with cosmic-rays in the ALICE setup. The calibration software was installed on the Data Acquisition System at CERN and executed continuously during the cosmic-ray data taking in 2008, providing a first determination of the calibration constants.

This thesis presents also a study on the capability of the ALICE central barrel to detect the Z^0 boson through the decay $Z^0 \rightarrow e^+e^-$ in *pp* collisions at 14 TeV. The production cross-section has small theoretical errors in QCD and a comparison between the experimental results and the theoretical calculations allows to check the understanding of the detector response at high transverse momentum. We demonstrated that the $Z^0 \rightarrow e^+e^-$ is characterized by a very clean signal in the dielectron reconstructed invariant mass spectrum. At such high transverse momentum (about 45 GeV/c=$m_{Z^0}/2$), the electrons from Z^0 are identified with the Transition Radiation Detector. The remaining background from misidentified pions and electrons from heavy-flavored decays are rejected by the requirement of two isolated reconstructed tracks. The main challenge comes from the very small production rate. Therefore we estimated the efficiency of a trigger based on a low p_T cut and electron identification with the TRD and showed that about 100 $Z^0 \rightarrow e^+e^-$ can be reconstructed per year employing such a trigger.

Another physics topics investigated in this thesis is the measurement of the charm and bottom production via their semileptonic decays. These measurements allow at high p_T to test pQCD calculations in *pp* collisions and are essential prerequisites for the understanding of the Quark Gluon Plasma expected to be produced in *PbPb* collisions. In this work, we studied the electrons from *c* and *b* decays reconstructed in the central barrel. For 10^8 minimum-bias events at $\sqrt{s}$=10 TeV (as was initially expected for the year 2008), a p_T of about 6 GeV/c can be reached. The electrons are identified with the Time Projection Chamber, TRD and Time-Of-Flight. First estimations of the contamination and Particle Identification efficiency based on a Bayesian approach were performed. At high p_T, electrons from heavy-flavored hadrons become dominant but at low p_T the main source of electrons is gamma conversion in the detector material and the π^0 Dalitz decay. We showed that the expected signal-to-background ratio, which was found to be similar as in the PHENIX experiment for *pp* collisions at $\sqrt{s}$=200 GeV, will allow a measurement of the charm and bottom cross-sections.

Contents

1 Generalities **1**

1.1 Physics Background . . . 1

1.1.1 Properties of the strong interaction . . . 1

1.1.2 QCD phase diagram and Quark Gluon Plasma . . . 2

1.1.3 Ultra-relativistic Heavy-Ion Collisions . . . 4

1.1.4 Experimental observables . . . 5

1.2 The ALICE experiment . . . 6

1.2.1 General Overview of the LHC and its experiments . . . 6

1.2.2 The ALICE detector layout . . . 7

1.2.3 The ALICE Transition Radiation Detector . . . 10

1.3 The ALICE TRD readout chambers . . . 11

1.3.1 Deposited energy in the gas . . . 12

1.3.2 Amplification of the signal . . . 13

1.3.3 Drift of the electrons . . . 14

1.3.4 Tracking capabilities . . . 17

I Calibration of the Transition Radiation Detector **21**

2 Calibration **22**

2.1 What has to be calibrated? . . . 22

2.2 Expected variations . . . 22

2.3 The global strategy with physics events . . . 23

2.3.1 Reconstruction of the events . . . 23

2.3.2 Determination of the calibration constants . . . 25

2.4 Expected accuracy of the calibration constants . . . 25

3 Gain calibration **26**

3.1 Use of the energy loss . . . 26

3.1.1 Fluctuations of the energy loss . . . 26

3.1.2 The calibration procedure . . . 27

3.2 Simulated data . . . 31

3.3 Test-beam data . . . 34

3.3.1 Particle Identification . . . 35
3.3.2 Events quality . . . 36
3.3.3 Relative gas gain calibration . . . 37
3.4 Cosmic-ray data . . . 39
3.4.1 Gas gain as a function of the anode voltage . . . 39
3.4.2 Systematic effect of the drift velocity . . . 40
3.4.3 Gain factor dispersion and systematic effect of the trigger . . . 41
3.5 First gain calibration of the four supermodules installed at CERN . . . 43

4 The calibration of the drift velocity 45
4.1 Algorithm with or without tracking . . . 45
4.1.1 Use of the average pulse height . . . 45
4.1.2 Calibration using simulated events . . . 49
4.1.3 Calibration using the Test-beam 2007 data . . . 51
4.1.4 Calibration using the Test-beam 2004 data . . . 56
4.1.5 Calibration using cosmic-ray data . . . 57
4.2 The algorithm with global tracking . . . 58
4.2.1 Principle . . . 59
4.2.2 Algorithm . . . 61
4.2.3 Results on simulated data . . . 62

5 The calibration of the Pad Response Function 65
5.1 Algorithm . . . 65
5.1.1 Independent determination of the y cluster coordinate . . . 65
5.1.2 Systematic effect of the Time Response Function . . . 66
5.1.3 Measurement of the Pad Response Function . . . 67
5.2 Results on simulated data . . . 69
5.2.1 The straight line fit of the tracklet . . . 69
5.2.2 The width of the PRF . . . 71

6 Online Calibration 74
6.1 Introduction to the online architecture . . . 74
6.2 Calibration on DAQ . . . 76
6.2.1 DAQ architecture . . . 76
6.2.2 Algorithms on DAQ for the TRD . . . 76
6.3 Pedestal algorithm . . . 77
6.3.1 Algorithm . . . 77
6.3.2 Pad capacitance and noise . . . 80
6.3.3 Pad status . . . 81
6.3.4 Dependences of the noise on the running conditions . . . 83
6.3.5 Noise and pad status in the reconstruction . . . 84
6.4 The Drift velocity algorithm . . . 85

6.4.1 Algorithm . . . 85
6.4.2 Results . . . 86
6.5 Calibration using the HLT . . . 88
6.6 The TRD preprocessor at the Shuttle . . . 89

II Feasibility study of $Z^0 \rightarrow e^+e^-$ measurement with the ALICE central barrel in pp collisions at $\sqrt{s}$=14 TeV 92

7 Z^0 production in hadron collisions 96
7.1 Physics Processes . . . 96
7.2 PYTHIA Generation . . . 97
7.2.1 Comparison with total $W^{\pm}$ and Z^0 cross-sections at CERN Collider and Tevatron . . . 98
7.2.2 Comparison with p_T- and y-spectra at Tevatron . . . 100
7.2.3 Predictions for pp collisions at the LHC energy . . . 101

8 Z^0 production in heavy-ion collisions 104
8.1 Number of nucleon-nucleon collisions . . . 104
8.2 Application of Glauber Model to hard processes . . . 106
8.3 Z^0 production in $PbPb$ collisions at 5.5 TeV . . . 107
8.3.1 Geometrical scaling . . . 107
8.3.2 Break of the binary collision scaling . . . 108

9 Response of the ALICE central barrel 109
9.1 Fast Simulation . . . 109
9.1.1 Why Fast Simulation? . . . 109
9.1.2 The concept of Fast Simulation . . . 110
9.2 Response Functions . . . 111
9.2.1 What has to be parametrized? . . . 111
9.2.2 What does it depend on? . . . 112
9.2.3 How can the dependencies be optimized? . . . 113
9.3 Build of response functions . . . 114
9.3.1 Simulated events . . . 114
9.3.2 Analysis . . . 114
9.4 Results at Low-multiplicity . . . 117
9.4.1 Efficiency . . . 117
9.4.2 Transverse momentum resolution . . . 119
9.4.3 Polar angle resolution . . . 123
9.4.4 Azimuthal angle resolution . . . 125
9.4.5 Results at lower transverse momentum . . . 125
9.5 Results at High-multiplicity . . . 127

9.6 Parametrization of the Particle Identification . . . 128
9.7 User package . . . 129

10 Z^0 acceptance in the ALICE central barrel 130
10.1 Selection criteria . . . 130
10.2 Signal acceptance . . . 131

11 Background studies 135
11.1 Background at lower energies . . . 135
11.2 Background sources studied in pp collisions at 14 TeV . . . 136
11.3 Jets . . . 137
11.4 $D\bar{D}$ and $B\bar{B}$ simultaneous semi-electronic decay . . . 139
11.4.1 $c\bar{c}$ and $b\bar{b}$ production . . . 140
11.4.2 Fragmentation of c and b quarks and decay electrons . . . 141
11.5 Weak processes . . . 143
11.5.1 $Z^0 \rightarrow \tau^+\tau^- \rightarrow (e^\pm/\pi^\pm)(e^\pm/\pi^\pm)+X$ . . . 143
11.5.2 $W^\pm \rightarrow e\nu_e$ . . . 144
11.5.3 $t\bar{t}$ . . . 144
11.6 Final estimated background . . . 144
11.6.1 Single electron spectra . . . 145
11.6.2 Invariant mass yields . . . 146
11.7 Efficiency of the isolation cut . . . 147

12 Trigger strategy and performances in other LHC experiments 149
12.1 Nominal conditions . . . 149
12.2 L1 trigger with the TRD . . . 150
12.3 First expectations for a simple L1 trigger . . . 151
12.4 Other decay channel and LHC experiments . . . 152
12.5 $Z^0 \rightarrow \mu^+\mu^-$ in the ALICE muon spectrometer . . . 152
12.6 Other LHC experiments . . . 153

III Measurement of $c\bar{c}$ and $b\bar{b}$ cross-sections through semi-electronic decays of heavy-flavored hadrons in pp collisions 155

13 Measurement of $c\bar{c}$ and $b\bar{b}$ cross-sections in ALICE 156
13.1 Physics Motivations . . . 156
13.2 Previous measurements . . . 157
13.3 Computed cross-sections at the LHC . . . 157
13.4 How to measure $c\bar{c}$ and $b\bar{b}$ cross-sections in ALICE? . . . 158

14 Acceptance and Particle Identification **161**
14.1 Acceptance 161
14.2 Particle Identification 164

15 Background study **170**
15.1 Sources of background 170
15.2 Monte Carlo simulation of the background 171

A Role of the Shuttle **175**

B Kinematic Variables **177**

C Nuclear shadowing **180**
C.1 Definition of the x Bjorken variable 180
C.2 Parton distribution function (PDF) 181
C.3 x probed by the Z^0 boson 183
C.4 Shadowing effects 184

Acknowledgements **195**

Chapter 1

Generalities

In this chapter, we will first briefly motivate the study of the Quark Gluon Plasma (QGP) in Heavy-Ion Collisions (HIC). The Large Hadron Collider (LHC) will be then presented together with its four main experiments dispersed along the ring. Since A Large Ion Collider Experiment (ALICE) is the subject of this thesis, we will focus on this experiment.

1.1 Physics Background

1.1.1 Properties of the strong interaction

In analogy to Quantum Electro-Dynamics (QED), the theory which describes electromagnetically interacting systems, the Quantum Chromo-Dynamics (QCD) was developed for strongly interacting systems. In QED, the interaction between electrically charged particles is mediated through virtual photons. In QCD, the fundamental particles are quarks and gluons, which carry color charge. The color quantum number was initially introduced to avoid the violation of the Pauli exclusion principle. Quarks are fermions (s=1/2), classified in three generations. Their properties are summarised in Table 1.1. One of the main differences between QCD and QED is that the intermediate gauge bosons in QCD, the 8 gluons, carry themselves color charge and can therefore interact with each other. As a consequence the intensity of the strong force varies in a different way as a function of the distance between the interacting partons, leading to the confinement and asymptotic freedom. Another particularity of QCD is the chiral symmetry restoration/breaking.

confinement/asymptotic freedom The intensity of the electromagnetic force is given by the QED coupling constant. At low energies, the coupling is in the order of the fine structure constant $\alpha=\frac{e^2}{4\pi\epsilon_0\hbar c}=1/137$. Due to vacuum polarisation, it increases with the momentum transferred in the interaction Q^2. Nevertheless the weakness of the electromagnetic coupling ($\alpha\ll1$) facilitates the application of perturbation theory. The cross-sections are computed as an expansion in powers of α. Since α is small, the higher orders (next-to-leading order(s)) can be neglected.

Gen.	Weak Isospin	I_z	S	C	B	T	Name	Symbol	Charge e	Mass [MeV/c^2]
1	+1/2	+1/2	0	0	0	0	Up	u	+2/3	1.5 - 3
	-1/2	-1/2	0	0	0	0	Down	d	-1/3	3 - 7
2	+1/2	0	0	1	0	0	Charm	c	+2/3	1250±90
	-1/2	0	-1	0	0	0	Strange	s	-1/3	70 - 120
3	+1/2	0	0	0	0	1	Top	t	+2/3	174200±3300
	-1/2	0	0	0	-1	0	Bottom	b	-1/3	4200 - 4700

Table 1.1: The properties of quarks in QCD. The mass reported are current mass, i.e., the mass of the quark in absence of confinement [1].

Similarly, the intensity of the strong interaction is given by the strong coupling constant α_s:

$$\alpha_s(Q^2) = \frac{\alpha_s(\Lambda^2_{QCD})}{1 + \frac{33-2N_f}{12\pi}\alpha_s(\Lambda^2_{QCD})\ln(Q^2/\Lambda^2_{QCD})} \approx \frac{4\pi}{(11 - 2/3N_f)\ln(Q^2/\Lambda^2_{QCD})} \qquad (1.1)$$

where N_f is the number of flavors (N_f<16) and Λ_{QCD} the QCD scale (Λ_{QCD}=217^{+25}_{-23} MeV). The QCD vacuum polarisation differs from the QED because besides the screening of quark-anti-quarks pairs there exists anti-screening of gluon pairs. As a consequence, α_s decreases at short distances or high Q^2 and the quarks behave as quasi-free particles. This is the asymptotic freedom [2, 3, 4]. At large distances, the strong coupling has large values ($\alpha_{QCD}\geq$1). The quarks are confined in neutral color states, the baryons and mesons. This is known as color confinement. The QCD cross-sections can be computed within the perturbative QCD (pQCD) only at high Q^2 (hard processes), where $\alpha_s \ll 1$. At small Q^2 (soft processes), non-perturbative theory like lattice QCD, has to be used.

chiral symmetry In the absence of masses, the QCD Lagrangian shows no interaction between left and right-handed quarks. For mass-less up and down quarks, this constitutes an SU(2)$_L$×SU(2)$_R$ symmetry. Nevertheless quarks can interact, leading to an increase of their masses up to their constituent masses of 300MeV/c^2 (u and d). The chiral symmetry is spontaneously broken since it is always possible to find a reference system in which a right-handed massive quark has a spin anti-parallel to the momentum. When Q^2 becomes much higher than Λ_{QCD}, the quark interaction is reduced and one expects a partial restoration of the chiral symmetry.

1.1.2 QCD phase diagram and Quark Gluon Plasma

The QCD phase diagram gives the expected state of the QCD matter (the quarks) as a function of the temperature T and the baryochemical potential μ. The baryochemical potential measures the system net baryonic number (number of baryons minus anti-baryons). Fig. 1.1 presents a schematic view of the QCD phase diagram. The ground state of the nuclear matter is at μ_0=931 MeV and T=0 MeV. The hadronic matter at low temperature and/or baryon density

can be seen as bags of mass-less quarks (MIT bag model). The confinement is then the result of an inwards acting bag pressure B. At high T and low μ, the pressure B is balanced by the thermal pressure (kinetic energy) of the quarks and gluons. At low T and high μ, the Pauli exclusion principle produces a degeneracy pressure acting against the pressure B. In both cases, at a critical temperature T_c or a critical baryon number density μ_c, the thermal or degeneracy pressure exceeds the bag pressure and a deconfined state becomes possible. Deconfinement doesn't imply the absence of interaction, but only means to get rid of the requirement to form color neutral bound states.

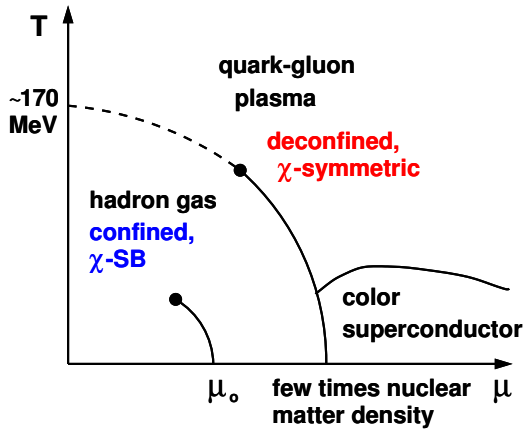

Figure 1.1: Schema of the QCD phase diagram [5] (see also [6]).

In the case of ideal relativistic gases at vanishing baryonic number, the energy density and pressure can be analytically computed. A mass-less Hadronic Gas (HG of pions for instance) has a different number of degrees of freedom than a gas of quarks and gluons. The degeneracy factor g is given by:

$$g = n_b + \frac{7}{8} n_f \tag{1.2}$$

with n_b and n_f the number of boson and fermion degrees of freedom respectively. The energy density ϵ is:

$$\epsilon = \frac{g}{30} \pi^2 T^4 \tag{1.3}$$

For the HG, n_b=3 and n_f=0, whereas for the QGP state:

$$n_b = 8(\text{color}) \times 2(\text{spin}) = 16 \tag{1.4}$$

$$n_f = 3(\text{color}) \times 2(\text{spin}) \times 2(\text{flavour}) \times 2(\text{quark + antiquark}) = 24 \tag{1.5}$$

Thus the transition from hadronic matter to a deconfined state occurs with a sudden increase of the energy density as a function of the temperature. Precise lattice calculations have been carried out with different number of included quark flavors and quark masses. The estimated critical temperature is of the order of 170 MeV at μ=0. For the systems created in HIC, a global fit of the measured particle ratios using statistical models allow to extract the temperature T and baryonic potential μ at freeze-out. To increase the c.m.s energy of the collisions per

nucleon pair up to LHC energies, enables closer approach to vanishing net baryon density, getting closer to the stage which is believed to have dominated in the early universe in its first few microseconds.
The phase transition into the QGP state is expected to be a first order phase transition at low temperatures and high baryon densities, which would change to a continuous crossover transition at a certain critical point.

1.1.3 Ultra-relativistic Heavy-Ion Collisions

The extreme conditions required to form a deconfined state can be attained in the laboratory by colliding nuclei at ultra-relativistic energies. At very high energies, the stopping power of the two nuclei is small and the two colliding nuclei are transparent for each other. They pass through in a crossing time $\tau_{cross} \approx 2R/\gamma$ much smaller than the characteristic time of the strong interaction $\tau_{strong} \approx 1/\Lambda_{QCD} \approx 1\,\mathrm{fm/c}$. In the central-rapidity region, the net baryon density is quasi null. The evolution of a HIC is sketched in Fig. 1.2.

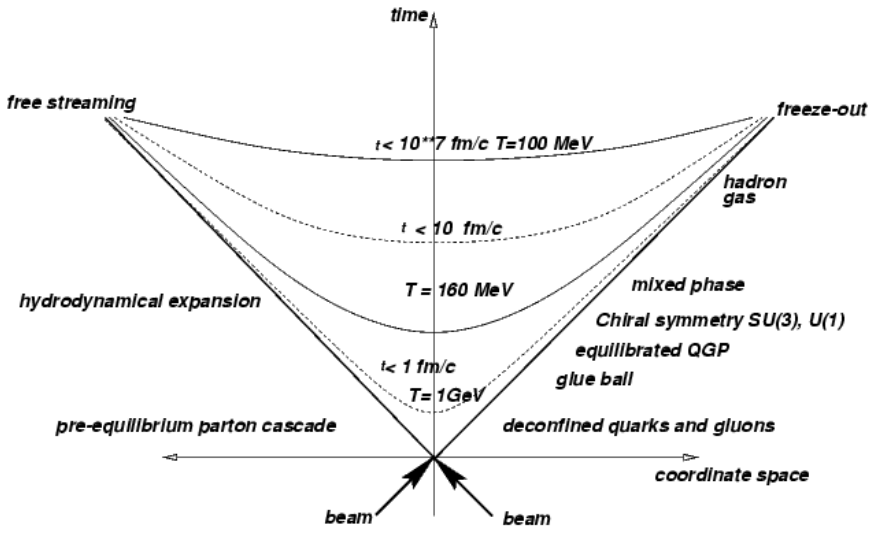

Figure 1.2: Space-time picture of a nucleus-nucleus collision.

Assuming that thermal equilibrium is attained within the time τ_{eq} in the early stage of the collision, the space-time evolution of the system can be described within hydrodynamical models knowing the initial conditions at $t{=}\tau_{eq}$. For an initial temperature above the critical temperature T_c, the deconfined parton state (QGP) expands isentropically and adiabatically due to its internal pressure and cools down until $T{=}T_c$. A phase transition from QGP to hadronic matter occurs at quasi constant temperature. The heat is consumed in the conversion of the parton degrees of freedom into those of hadrons. The hadron gas continues then to expand to reach a point in time where no inelastic collisions happen anymore. At chemical freeze-out, the particle

yields (relative abundance) among the hadronic states are frozen. Finally the kinematic or thermal freeze-out is achieved. The momentum spectra of the hadrons are fixed.
The initial energy density can be evaluated with the Bjorken scenario [7]. This assumes that $\tau_{cross} \ll \tau_{strong}$ and the system expands in a homogeneous and longitudinal manner. Table 1.2 gives the estimated times and attained energy densities for the RHIC and LHC energies. At LHC, temperature above $3T_c$ should be reached.

	Nuclei	$\sqrt{s}$ [GeV]	ϵ [GeV/fm^3]	dN_{ch}/dy	τ_{eq} [fm/c]	τ_{QGP} [fm/c]
RHIC	^{197}Au	200	4.1	$\approx$700	$\leq$0.2	2-4
LHC	^{208}Pb	5500	11.6 (?)	2-3$\times 10^3$	$\leq$0.1	10

Table 1.2: Estimations of the attained energy density, charge density at mid-rapidity, thermal equilibrium time τ_{eq} and lifetime of the QGP τ_{QGP} at RHIC and LHC.

1.1.4 Experimental observables

Experimentally the characteristics of the produced high energy density QCD matter can be analysed from the kinematic and chemical properties of the particles emitted in the reaction. Practically only pions, kaons, (anti-)protons, electrons (positrons), muons, (anti-)neutrons and photons reach the detector. Through decay topology, they can also give information about earlier existing particles. It is common to subdivide the adopted QGP signatures into three classes:

- **Global observables** like the particle collective flow, the distribution of charged particle density per rapidity unit (dN_{ch}/dy), the energy density per rapidity unit ($d\epsilon/dy$) and Hanbury-Brown-Twiss (HBT) interferometry. With these observables one tries to answer to the questions, when the thermal equilibrium occurred and what the initial conditions are.

- **Hadronic probes with large cross-section** like strangeness enhancement, particle abundances and spectra. They are easy to detect since the processes have large cross-sections. However they come from the late stage of the system evolution and don't give so much information about the early state.

- **Electromagnetic probes and probes of small cross-section** like J/Ψ production (through di-leptonic decays), $c\bar{c}$ and $b\bar{b}$ production (through hadronic or semi-electronic decays), QGP thermal radiation (thermal photons) and jet quenching. They are hard to detect due to their low cross-section, small di-leptonic branching ratio and large abundant background. The photons and leptons don't interact strongly with the medium and provide therefore information about the nuclear matter state at their production time. They are produced nevertheless at all stages of the collisions.

1.2 The ALICE experiment

1.2.1 General Overview of the LHC and its experiments

The Large Hadron Collider (LHC) is an accelerator ring installed in a tunnel of 27 km in circumference, buried 50-175 m below ground. It is located between the Jura mountain range in France and the Lake of Geneva in Switzerland at the European Organisation for Nuclear Research (CERN). Collisions will take place between two beams of particles, either protons or heavy ions (Pb). The maximal nucleon pair centre-of-mass energy $\sqrt{s_{NN}}$=14 TeV in proton-proton collisions is a factor 7 higher than the TEVATRON energies, whereas $\sqrt{s_{NN}}$=5.5 TeV in lead-lead collisions is a factor 30 with respect to the RHIC collider. The effective time per year is estimated to be 10^7 s in *pp* and 10^6 s in *PbPb* operation. This leads to a total number of *pp* recorded events of about 10^9 for a data acquisition rate of 100 Hz and 2×10^7 central (0-5 % centrality) *PbPb* events per year for 20 Hz data acquisition rate. The characteristics of the accelerator are summarised in Table 1.3. In *pp* collisions the highest luminosity will be decreased for ALICE located at P2 by defocusing the beams and eventually displacing them. Thus the pile-up will be reduced in the detectors, particularly in the TPC. This will facilitate the study of probes with large cross-section.

	$\sqrt{s}$ [TeV]	L [cm^{-2}s^{-1}]	Time between Bunches [ns]	Particles per Bunch	interaction rates	pile-up in TPC
pp	14.0	10^{34}	25	3-4$\times10^{10}$	1 GHz	10^5
		10^{29} at P2			10 kHz	1
PbPb	5.5 [TeV/A]	0.5×10^{27}	100	7×10^7	4 kHz	0.4

Table 1.3: Some LHC parameters in *pp* and *PbPb* operation and running conditions at interaction point 2 in the ALICE experiment. The pile-up in the TPC gives the number of events, which overlap within the 88 μs drift time in the detector.

From the 10th to the 19th September 2008, the LHC was commissioned with single beams of protons. The initial commissioning was performed with one single bunch at 450 GeV moving later towards 43 bunches on 43 bunches with moderate intensities. An incident occurred at mid-day on Friday 19 September during the commissioning without beam of the final LHC sector 34 at high current for operation at 5 TeV. It resulted in a large helium leak into the tunnel. The sector has to be warmed up for repairs to take place. As a consequence the comissioning will continue in May-June 2009.

The two beams will meet at four interaction points (see Fig. 1.3). The experiments ATLAS (A Toroidal LHC Apparatus) and CMS (Compact Muon Solenoid) are mainly devoted to *pp* collisions. They are intended to analyse the nature of mass, especially to find the Higgs Boson(s). The LHCb (LHC Beauty Experiment) should measure CP violation in b-meson systems to better understand the imbalance of matter and antimatter in the Universe. ALICE

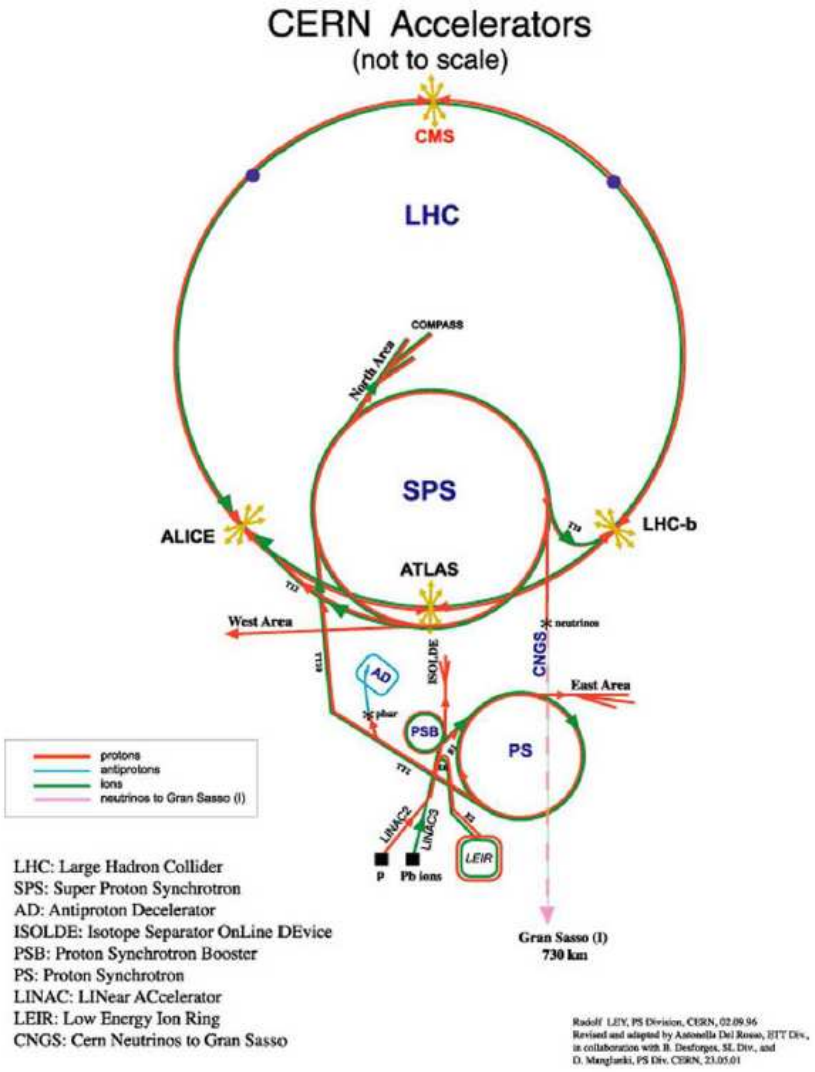

Figure 1.3: The CERN accelerator system [8].

is dedicated to the study of the QGP created in $PbPb$ collisions, but will also study pp collisions.

1.2.2 The ALICE detector layout

The ALICE experiment will investigate a wide range of observables from very low ($\approx$ 100 MeV/c) up to fairly high ($\approx$100 GeV/c) transverse momenta. The detector was designed to track and identify particles (pions, kaons, (anti-)protons, electrons (positrons), muons, and photons) in this p_T interval in a low (pp collisions) and very large ($PbPb$ collisions) particle multiplicity environment (up to 8000 particles per unit of rapidity at mid-rapidity). Fig. 1.4 shows the detector layout.

In the central rapidity region (η<0.9), the particle momenta are obtained by tracking procedures within the L3 magnet with solenoidal field up to 0.5 T. The main detector components are:

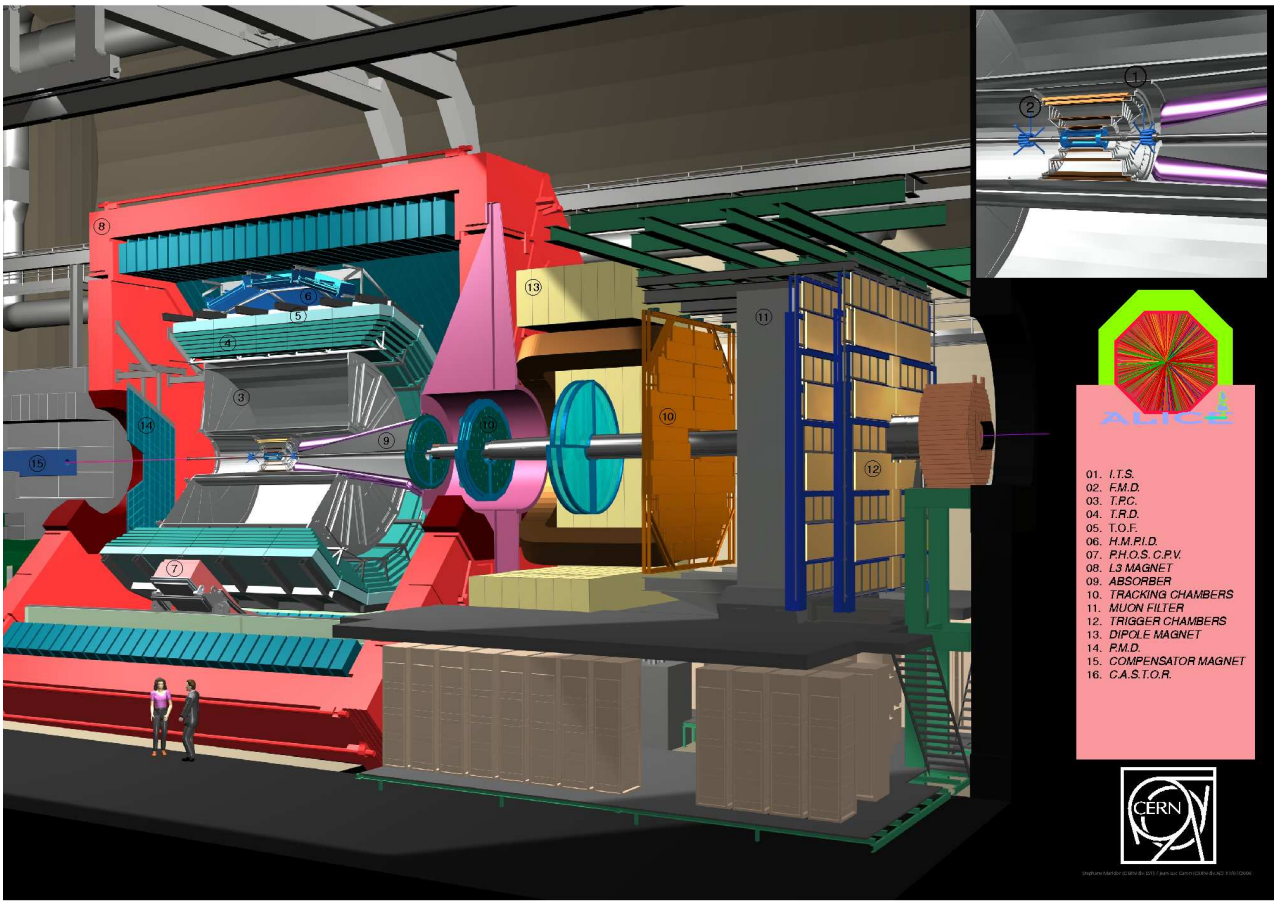

Figure 1.4: The ALICE detector layout.

- a complete Inner Tracking System (ITS), consisting of six layers of high resolution tracking Si detectors for the reconstruction of the primary and secondary vertices.
- a Time Projection Chamber (TPC), the main tracking system of ALICE, which provide also particle identification through dE/dx.
- a Transition Radiation Detector (TRD) for electron/pion separation at momenta above 1 GeV/c.
- a Time-Of-Flight Detector (TOF) to extend the particle identification of ALICE at low ($e^{\pm}$ below 0.5 GeV/c) and intermediate momenta p ($\pi^{\pm}$,$K^{\pm}$ below 2.5 GeV/c and (p,$\bar{p}$) below 4.5 GeV/c).
- a High Momentum Particle Identification Detector (HMPID) based on Ring Imaging Cherenkov Counter (RICH) for $\pi^{\pm}/K^{\pm}$ and $K^{\pm}/(p,\bar{p})$ discrimination respectively up to 3 GeV/c and 5 GeV/c.
- a Photon Spectrometer (PHOS) covering an azimuthal angle of 20° for photon identification from prompt and direct photons as well as those from high-p_T neutral meson decays.

In the rapidity range of $2.5 < \eta < 4$, a muon spectrometer (FMS) is designed to measure Quarkonia at forward rapidity and allow their study via their di-muon decays.

Element	η	$\Delta\phi$	z/r	Main Functions-Characteristics
			z [cm]	Trigger and Centrality
VZERO	(-3.7,-1.7)	360°	-90	Fast trigger (σ<1 ns),centrality
	(2.8,5.1)		340	indicator and control beam luminosity
TZERO	(-3.3,-2.9)	360°	-70	Provide a collision initial time
	(4.5,5.0)		350	L0 trigger (σ<50 ps), multiplicity, centrality
			r [cm]	Centrality region
ITS	±0.9	360°	3.9-49	Primary vertex (σ<100 μm)
				secondary vertices
				PID with p<100 MeV
TPC	±1.2	360°	84-246	Determine charged particle momenta
				PID at low momenta
				(100 MeV/c < p_T < 100 GeV/c)
TRD	±0.9	360°	290-370	$e^{\pm}/\pi^{\pm}$ rejection for $p > 1$ GeV/c
		80° in 2008		L1 trigger for $p_T > 3$ GeV/c single e or e-pairs
TOF	±0.9	360°	370-399	$\pi^{\pm}$,$K^{\pm}$ identification for 0.2 - 2.5 GeV/c
				proton identification for 0.4 - 4.5 GeV/c
				$e^{\pm}$ identification for 0.1 - 0.5 GeV/c
PHOS	±0.12	100°	460	Identify photons and neutral mesons
		20° in 2008		
HMPID	±0.6	57.61°	500	$\pi^{\pm}/K^{\pm}$ separation up to 3 GeV/c
				$K^{\pm}/(p,\bar{p})$ separation up to 5 GeV/c
			z [m]	Forward rapidity region
FMS	(-4.0,-2.5)	360°	(-5,17)	Track and identify $\mu^{\pm}$ with p_T>4 GeV/c
				Single, dimuon low and high p_T trigger

Table 1.4: The main detectors of ALICE and their coverage for the first *pp* collisions [9].

The first *pp* collisions will be triggered in the central rapidity region by a VZERO detector, made of two arrays of scintillator counters located at z=340 cm and z=-90 cm and the two first layers of the ITS, the silicon pixel detectors (SPD) at a radius of 3.9 cm ($|\eta|$<1.95) and 7.6 cm ($|\eta|$<1.5). The VZERO detector allows to reject the background from interaction of the beam with the residual gas in the beam pipe. The combination of the VZERO and SPD trigger signals is useful due to the complementarity of the two detectors in the geometrical acceptance. It will provide a minimum bias trigger. Other global (fast) detectors have specific tasks, like the TZERO detector, made of two arrays of Cherenkov counters at z=-70 cm and z=350 cm, for the measurement of the collision time needed by the TOF, the measurement of the z position

of the primary vertex with a resolution of 1.3 cm and the early wake-up signal required by the TRD. Table 1.4 summarises the main detectors of ALICE with their function.

1.2.3 The ALICE Transition Radiation Detector

The TRD covers $|\eta| \leq 0.9$ and is situated between the TPC and the TOF at a radius of (2.9,3.7 m) with $|z| < 3.5$ m. It is composed of 18 supermodules, each covering 20° in the azimuthal angle ϕ, like the TPC sectors (see Fig. 1.5). Each supermodule contains five stacks in the beam axis direction (z). One stack is made of 6 detector modules corresponding to 6 layers in the radial direction. The module consists of a radiator of 4.8 cm thickness and a multi-wire proportional chamber (MWPC) with cathode pad readout. The front-end electronics is mounted on the back of the cathode pad plane.

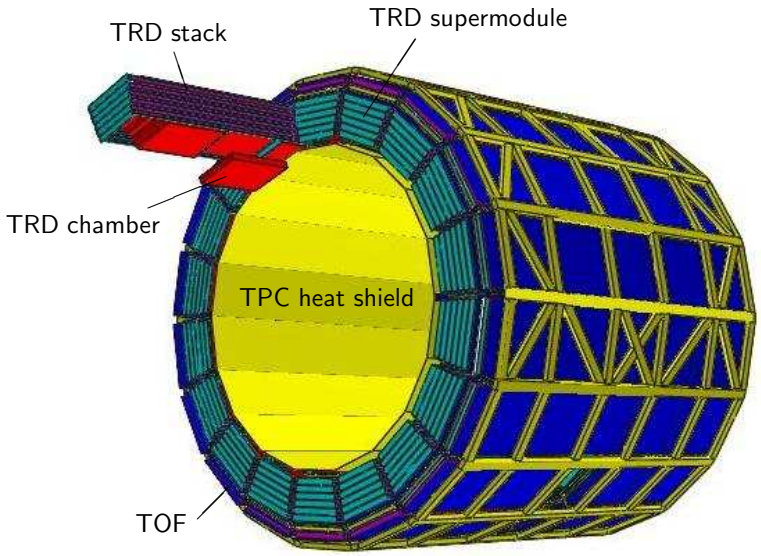

Figure 1.5: The structure of the ALICE TRD [10].

The principle of a transition radiation detector is based on the fact that when a relativistic charged particle traverses the boundary of two media of different electric constant, it produces transition radiation (TR). The radiator was built such that it is a very inhomogeneous material. The total energy loss by TR depends on the Lorentz-factor γ of the charged particle, which makes it suitable for particle discrimination. Since the TR-photons are in the keV range, they can be detected by a gaseous detector. They are mostly emitted at very small angles within a cone of $1/\gamma$ angle with respect to the charged particle direction. Thus the TRD detects the sum of the ionization loss (dE/dx) of the charged particle in the gas and the energy deposition of the X rays. To optimise the absorption of the X rays, a xenon-rich gas mixture (Xe/CO_2

85 %/15 %) was chosen as the nominal gas. Fig. 1.6 presents a sketch of a TRD chamber and the measured averaged signal versus time for electrons and pions. The electron signal with and without the presence of TR is plotted. Because pions are heavier, their dE/dx energy loss is smaller than the one of electrons for the same momentum. In addition they do not produce TR below about 100 GeV/c. The TR photons are preferably absorbed at the entrance of the gas volume. They are responsible for a peak of the electron average signal at latter time. The first peak of the signal is due to the transition of the particles through the amplification region. The deposited charge is added on both sides.

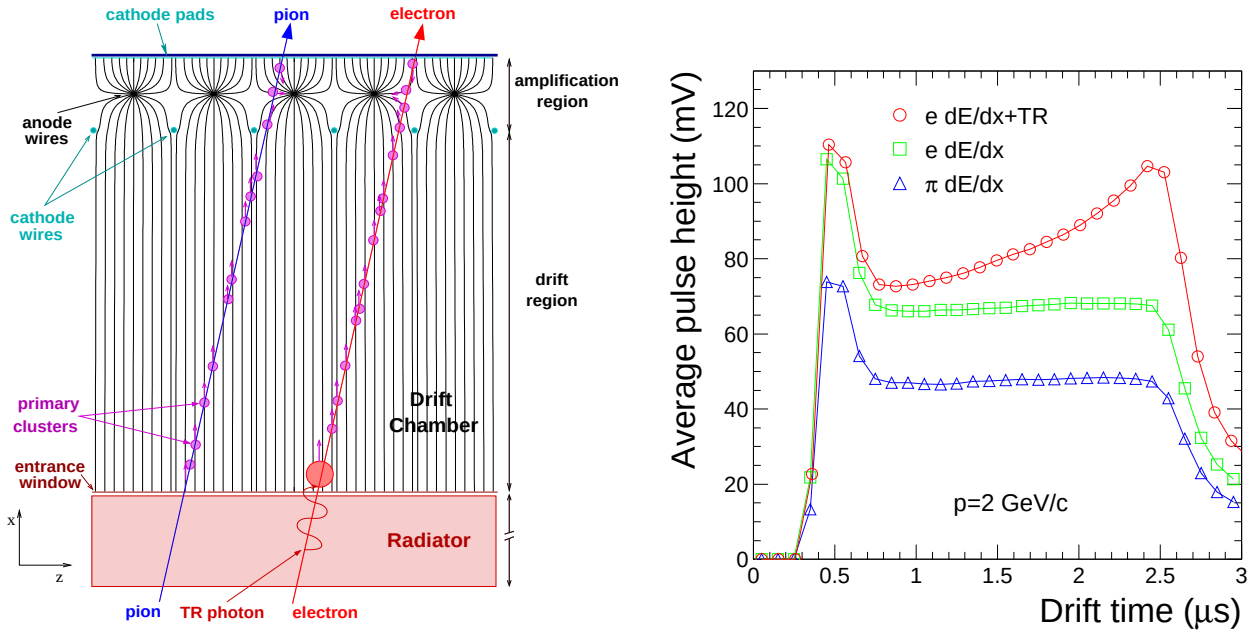

Figure 1.6: Left panel: principle of the ALICE TRD. Right panel: average pulse height as a function of time for pions and electrons of 2 GeV/c in the nominal conditions [11].

The main functionality of TRD is to provide electron identification for momenta above 1 GeV/c by using the amplitude and shape of the pulse height as a function of time to separate e from π. Since it is a fast tracker, it will be also used as trigger for high p_T electrons and charged particles (L1 trigger for single tracks of $p_T > 3$ GeV/c), and for electron pairs.

1.3 The ALICE TRD readout chambers

The gas volume of the readout chambers consists of a drift region of 3.0 cm separated by cathode wires from an amplification region of 0.7 cm. The cathode wires, as well as the cathode pad plane, are at the ground potential. By tuning of the anode voltage and the drift voltage, the gas gain and the drift velocity can be independently adjusted. The nominal running conditions are given in Table 1.5. Some of the parameters will be explained in the next paragraphs.

Detector gas	Xe,CO_2 (15 %)
Gas volume	27.2 m^3
Anode voltage	1550 V
Gas gain	≈7000
Drift voltage	-2100 V
Drift field	0.7 kV/cm
Drift velocity	1.5 cm/μs
Diffusion, longitudinal	$D_L = 250\,\mu m/\sqrt{cm}$
Diffusion, transversal	$D_T = 180\,\mu m/\sqrt{cm}$
Nominal magnetic field	0.5 T
Lorentz angle	9.8 °

Table 1.5: The nominal running conditions of the ALICE TRD readout chambers [12].

1.3.1 Deposited energy in the gas

A charged particle crossing the TRD deposits energy in the gas volume due to ionization of the gas molecules along its path and, in case of electrons, absorption of the TR photons produced in the radiator.

Ionization energy loss The average ionization energy loss per unit path length is given by the Bethe-Bloch formula in relativistic quantum mechanics [13]:

$$\langle\frac{dE}{dX}\rangle = -\frac{4\pi N_e e^4}{m_e c^2}\frac{z^2}{\beta^2}\{\frac{1}{2}\ln(\frac{2m_e c^2\beta^2\gamma^2 E_M}{I^2} - \beta^2 - \frac{\delta(\beta)}{2})\} \tag{1.6}$$

where the rest energy of the electron is $m_e c^2$. The properties of the gas are contained in the number density of electrons in the medium N_e and the effective ionization potential I. The parameters depending on the charged particle are its charge z, its velocity β and its γ factor. The energy E_M is the maximum energy transfer allowed in each interaction. The mean ionization energy loss depends mainly on the $\beta\gamma$ factor of the charged particle. At low $\beta\gamma$, $\langle\frac{dE}{dX}\rangle$ falls proportionally to $1/\beta^2$ due to a decreasing time of interaction. Charged particles at the minimum ionization are called Minimum Ionizing particle (MIP). As $\beta\gamma$ increases, the electromagnetic field of the charged particle becomes relativistic and expands as $1/\gamma$ in the transverse direction. One observes a so-called relativistic rise in $\langle\frac{dE}{dX}\rangle$. Finally polarizations of the medium screen the Coulomb field of the charged particle. The mean energy loss saturates. As TR, the dE/dx energy loss is appropriate to identify charged particle, onces their momentum is known from a tracking detector. Nevertheless for momenta above 2.5 GeV/c, $\pi^{\pm}$, $K^{\pm}$, $\mu^{\pm}$ and $e^{\pm}$ are already in the saturated part and it becomes impossible to separate them.

Transition radiation To discriminate $\pi^{\pm}$ from $e^{\pm}$ at momenta above 1 GeV/c, TR produced in the radiator are used. The resulting deposited energy is the convolution of the emitted TR

photons spectrum, depending on the γ factor of the charged particle and photoabsorption cross-section in the gas roughly proportional to Z^5. The shell structure of the Xenon influences the absorbed spectrum with a peak at 34,58 keV corresponding to its atomic K-shell.

1.3.2 Amplification of the signal

For a MIP, about 850 electron-ion pairs (i.p.) are produced in the 3 cm of the drift region due to ionization. Given the cathode pad capacitance (≈20 pF), this would lead to a signal of the order of 2.36 μV without any amplification. Therefore, it is absolutely necessary to amplify the signal.

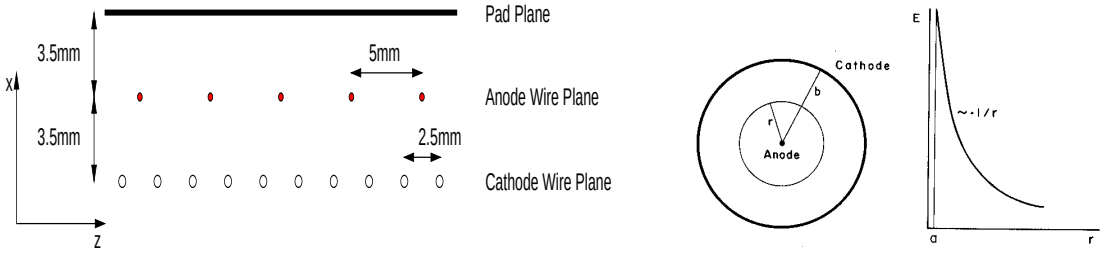

Figure 1.7: left panel: wire geometry of the ALICE TRD readout chambers. right panel: a coaxial cylindrical proportional counter and the shape of the electric field around the anode wire.

The amplification region can be considered as an array of small independent proportional counters (see Fig. 1.7). In the vicinity of the anode wire, the electric field grows proportional to $\frac{1}{r}$. When the ionization electrons arrive in the amplification region, they are accelerated and gain enough energy to ionize themselves the gas. They develop avalanches and secondary electrons are collected on the anode wires. The final detected charge is proportional, through the amplification factor or gas gain M, to the original deposited energy.
In the proportional mode the amplification factor is described by the first Townsend coefficient α. The quantity α is the number of i.p. produced per unit length per electron, it corresponds to the inverse of the mean free path for ionization. After a path dr, the number of electrons at a given position N_e fulfills the equation:

$$dN_e = N_e \alpha dr \tag{1.7}$$

In a first approximation, the number of electrons depends only on the radial distance r. The gas gain is then defined as the ratio of the total number of collected electrons at the anode wire radius a and the number of electrons, which induce the start of the avalanche at r_0:

$$M = \frac{N_e(a)}{N_e(r_0)} = \exp(\int_{r_0}^{a} \alpha(r) dr) \tag{1.8}$$

In a region of moderate gas gain, α can be considered linearly dependent on the energy of the electrons ϵ=E/α. It can be shown that this implies an exponential dependence of the

amplification factor on the anode voltage [13]. An increase of 3 % of the anode voltage from 1550 V to 1600 V results in a rise of 60 % for M. Since the high voltage power supply is controlled with a precision better than 1 V, time variations of the gain due to the anode voltages can be neglected. Nevertheless variations of the gas density ρ, determined by the pressure and temperature ($\rho \propto P/T$), affect also the gas gain. An 1 % increase in ρ leads to a decrease of the order of 6-7 % for the gas gain.
At high gas gain, the space charge created by the positive ions produced in the avalanche becomes not negligible compared to the electric field of the anode wire. The local variation of the anode charge density leads to a decrease of the gas gain as a function of time. This space-charge effect is more pronounced for tracks at normal incidence to the anode wires, for which all charge is collected in a very confined region. To reduce its influence, it is convenient to have a relative high anode voltage together with a moderate amplification factor. Given the gas mixture of the TRD, the gas gain has to be kept below 10^4. Otherwise one could observe deteriorations of the electron-pion separation.

1.3.3 Drift of the electrons

The electrons produced by ionization of the gas molecules drift towards the amplification region with a mean average drift velocity v_d of about 1.5 cm/μs in the uniform drift electric field of 700 V/cm.

Diffusion Due to diffusion, a point-like cloud of electrons will spread over a certain distance before arriving at the amplification region. After a drift time t in the z direction, the charge density follows a three-dimensional Gaussian distribution:

$$n(\mathbf{x},t) = \left(\frac{1}{\sqrt{4\pi D_L t}}\right)\left(\frac{1}{\sqrt{4\pi D_T t}}\right)^2 \exp\left(-\frac{x^2+y^2}{4D_T t} - \frac{(z-v_d t)^2}{4D_L t}\right) \tag{1.9}$$

with $\sigma_x = \sigma_y$.

$$\sigma_x = \sigma_y = \sqrt{2D_T t} \quad \sigma_z = \sqrt{2D_L t} \tag{1.10}$$

The longitudinal and transverse diffusion coefficients, D_L and D_T, are usually given in $\mu\text{m}/\sqrt{cm}$. They are then defined as $\sigma/\sqrt{L}$, where $L = v_d \cdot t$ is the distance in cm travelled by the electron cloud in the drift field direction. Over the drift distance of 3 cm, the spread of a point-like electron cloud is about 300 μm in the transversal directions and 500 μm in the drift field direction (see Table 1.5). The effects on the position resolutions can be neglected.

Electron drift velocity During their drift, the electrons scatter on the gas molecules. Besides the drift field E and the density of the gas ρ, the nature of the gas determines also the macroscopic drift velocity. One distinguishes the *cold* gas, like CO_2, from the *hot* gas, like Xe and Ar. Contrary to the rare gas, the CO_2 molecules has internal degrees of freedom responsible for a large fraction of energy lost by the electron in one collision, and a short mean time between collisions. The drift velocity v_d depends indirectly on the electron energy ϵ through

the effective scattering cross-section, the Ramsauer cross-section σ_R, and the average fractional energy loss per collision λ. If the electron thermal energy can be neglected, a simple classical model allows to show [14]:

$$v_d^2 \sim \frac{eE}{m_e \rho \sigma_R} \sqrt{\frac{\lambda}{2}} \tag{1.11}$$

The Ramsauer cross-section presents a characteristic minimum, called the *Ramsauer minimum*, at an electron energy ϵ of about 0.4 eV for all gas (0.3 eV for Ar and CO_2 and 0.5 eV for Xe). In *cold gas* the electron energy is small, close to that of the Ramsauer minimum. Fig 1.8 shows the electron drift velocity as a function of the drift field for different gas compositions relevant for the TRD calculated with GARFIELD/MAGBOLTZ [15, 16]. The drift velocity v_d is maximal when the electron energy is at the Ramsauer minimum. In pure xenon, v_d is very low but increases by adding some amount of CO_2. At some point a saturation mode is achieved. It is convenient to work in the saturation region since then the drift velocity doesn't depend so much on the fluctuations of the drift field. For the case of the TRD the nominal drift velocity is chosen to be 1,5 cm/μs to have a signal spread over about 2 μs. Therefore it is impossible to work in the saturation mode for any reasonable CO_2 concentration. Too high drift velocity will increase the correlation between the time bins and reduce the position resolutions. At 0.7 kV/cm and a CO_2 content of 15 %, the nominal drift velocity is reached.

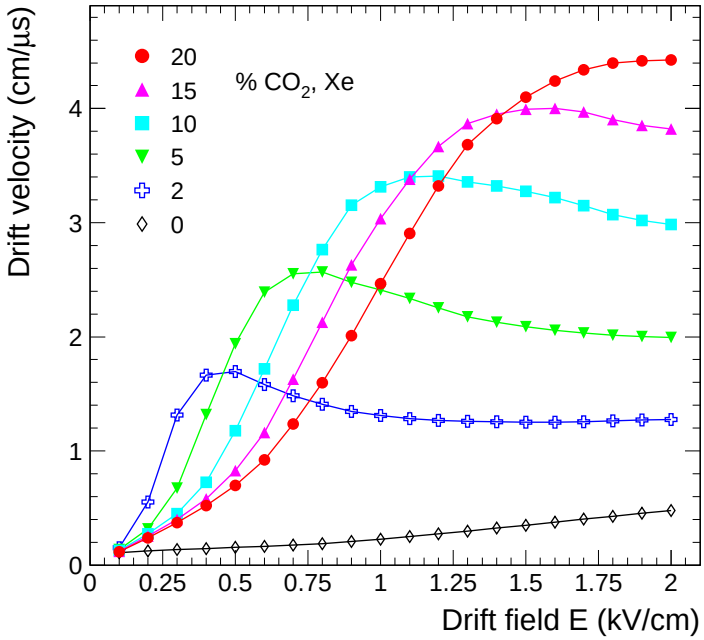

Figure 1.8: Drift velocity as a function of the drift electric field for different contents of CO_2.

The drift velocity depends on the pressure, P, and the temperature, T, through the gas density ρ.

$$v_d = f(1/\rho) = f(T/P) \tag{1.12}$$

Therefore the time variation of T and P is usually monitored.

Drift of ions Due to their higher mass, the ion drift much slower in the gas. Their drift velocity is quasi proportional to the drift field E at low field. That is why, one often uses the mobility μ defined as μ=v_d/E instead of the drift velocity v_d. At high drift field, E, the situation is similar to the one of the electrons. The ions drift velocity is proportional to $\sqrt{E}$. Various ionic species are produced during the ionization of the gas but they all disappear quickly except that which has the lowest ionization potential. Thus the drift velocity is determined by the ions with the lowest ionization potential. The relevant mobility for the TRD is that of the Xe ions. Its value is very small ($0.57\,\mathrm{cm^2V^{-1}s^{-1}}$) compared to the mobility of the electrons ($2143\,\mathrm{cm^2V^{-1}s^{-1}}$).

Effect of the magnetic field To measure the transverse momentum of the charged particle, the tracking detectors of ALICE are placed inside a magnetic field of 0.5 T along the beam axis. The drift velocity is changed in the following way:

$$\mathbf{v_d} = \frac{e\tau E}{m_e}\frac{1}{1+\omega^2\tau^2}\left(\frac{\mathbf{E}}{E} + \omega\tau[\frac{\mathbf{E}}{E}\times\frac{\mathbf{B}}{B}] + \omega^2\tau^2\left(\frac{\mathbf{E}}{E}\cdot\frac{\mathbf{B}}{B}\right)\frac{\mathbf{B}}{B}\right) \tag{1.13}$$

where ω is the electron cyclotron frequency:

$$\omega^2 = \omega_x^2 + \omega_y^2 + \omega_z^2 = (e/m_e)^2\mathbf{B}^2 \tag{1.14}$$

Given the geometry of the TRD, the magnetic field is perpendicular to the electric field in the drift region of the chambers. The vector $\mathbf{v_d}$ is not parallel to $\mathbf{E}$ anymore but has a velocity component in the direction of $\mathbf{E}\times\mathbf{B}$. The so-called *Lorentz angle*, α_L, is the angle formed by $\mathbf{v_d}$ with the drift field.

$$\tan\alpha_L = \omega\tau = (e/m_e)|\mathbf{B}|\tau \tag{1.15}$$

The electron drift velocities in the electron drift direction, $\mathbf{v_d}$, and in the drift field direction, $\mathbf{v_{dE}}$, are then given by:

$$\frac{\mathbf{v_d}^2(\omega)}{\mathbf{v_d}^2(0)} = \frac{|\mathbf{v_{dE}}(\omega)|}{|\mathbf{v_{dE}}(0)|} = \frac{1}{1+\omega^2\tau^2} \tag{1.16}$$

The energy loss fluctuations (Landau fluctuations) and the Time Response Function of the detector and electronics are responsible for correlations between adjacent time bins. As a consequence, the position resolution is deteriorated for tracks with incident angle perpendicular to the chamber far from -α_L. Therefore α_L has to stay small. One way to reduce α_L is to decrease the magnetic field. This is not possible since this will affect the p_T resolution. An other way is to reduce the average time between collisions by increasing the content of CO_2 in the gas mixture. A compromise has to be found between increasing the content of CO_2, which decreases α_L and thus improves the position resolution in the $r\phi$ direction, and keeping the content of CO_2 relatively low, so that the TR absorption efficiency is still high.

The dependence of α_L on the drift field is shown in Fig 1.9 for different values of the magnetic field and CO_2 contents. The Lorentz angle presents a maximum as a function of E, which corresponds to the *Ramsauer minimum*. For E=700 V/cm and B=0.5 T, α_L= 9.8° with the

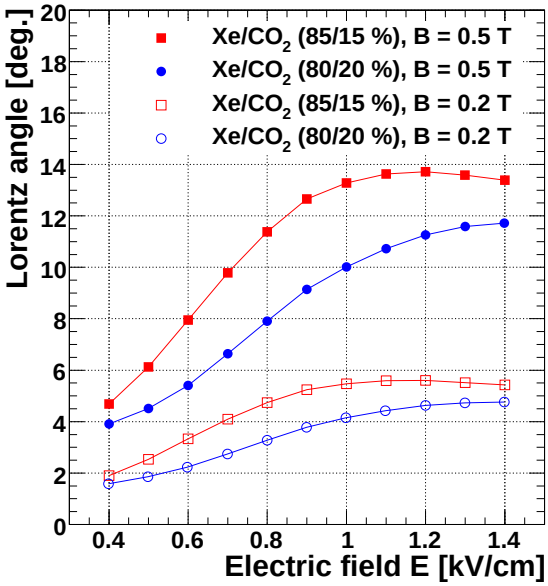

Figure 1.9: GARFIELD/MAGBOLTZ calculations of the Lorentz angle as a function of the electric drift field for different values of the magnetic field and different gas compositions [12]

nominal gas composition (15 % CO_2). A reduction of about 2.9 % is expected for $|\mathbf{v_{dE}}|$.
The presence of the magnetic field has a positive influence on the transverse diffusion of electrons cloud:

$$\frac{D_T(\omega)}{D_T(0)} = \frac{1}{1+\omega^2\tau^2} \tag{1.17}$$

The effect is nevertheless negligible for the nominal conditions (2.9 % for α_L=9.8°). The longitudinal diffusion is not affected.

1.3.4 Tracking capabilities

The trajectory of the charged particles crossing the TRD chambers is reconstructed in three dimensions.

In the radial direction The radial position of the particle is given by the arrival time of the electrons. One needs basically the start time t_0 corresponding to the time, when the particle reached the cathode pad plane, and the drift velocity of the electrons v_d. The radial particle path is then determined as:

$$r(t) = r_c - v_{dE}(t - t_0) \tag{1.18}$$

where r_c is the known position of the cathode pad plane. Nevertheless, in the amplification region the electric field is not uniform. As a consequence v_{dE} depends strongly on the distance to the next anode wire. This effect is called unisochronity.

Fig. 1.10 shows the drift time of electrons starting close to the drift electrode as a function of their position relative to the anode wire y. The time variations correspond to variations of the

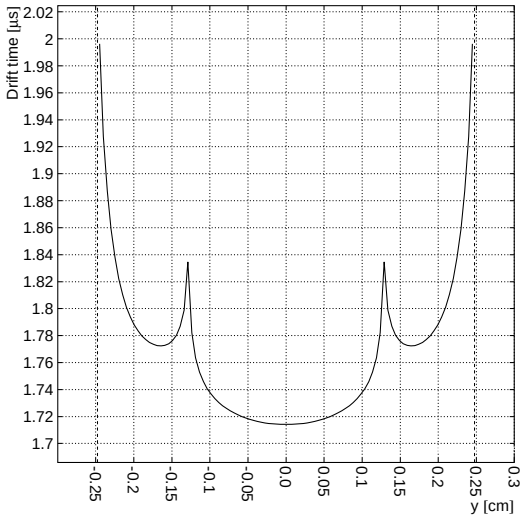

Figure 1.10: Drift time variation for electrons starting at the drift electrode within a drift cell. The anode wire is at y=0 cm, the cathode wires are at y=±0.125 cm (U_a=1400 V, U_d=-2100 V) [12]

drift velocity in the order of 15 %. In the detector simulation, this effect is taken into account by using a two dimensional map in r and y of the drift velocity.

$$r(t) = \int_{t_0}^{t} v_{dE}(t) \cdot dt \approx v_{dE}^{sim}(r, y) \cdot (t - t_0) \tag{1.19}$$

The variables r and v_d^{sim} are negative in half of the amplification region [-0.35,0] cm (r=0 cm at the anode wire plane). In the reconstruction, an average constant efficient drift velocity v_{dE}^{eff} has to be determined for the full range, amplification and drift region:

$$|r(t)| = \int_{t_0}^{t} v_{dE}(t) \cdot dt \approx v_{dE}^{eff} \cdot (t - t_0) \tag{1.20}$$

The velocity v_d^{eff} is not simply the overall average drift velocity in the direction of the drift electric field. An other effect is included in Eq. 1.20: electrons starting from both side of the anode wires plane in the amplification region (-0.35 cm and 0.35 cm for example) arrive approximately at the same time. The resulting reconstructed signal is the superposition of two different points along the track. Since the amplification region is small (0.7 cm) compared to the drift region (3 cm), the expected deterioration of the y and ϕ resolution is reasonable. The unisochronity, as well as residual signals from electrons arrived before the time t (Time Response Function TRF) reduces the r resolution. The sigma σ_r is estimated to be of the order of 2000 μm.

In the $r\phi$ direction The readout cathode plane is segmented in the z direction, along the anode wires (beam direction), and in the perpendicular $r\phi$ direction. The size of the pads is given in Table 1.6.

Layer	0	1	2	3	4	5
Pad width W [cm] ($r\phi$)	0.635	0.665	0.695	0.725	0.755	0.785
Pad length l [cm] (z)	7.5/9.0	7.5/9.0	8.0/9.0	8.5/9.0	9.0/9.0	9.0/9.0

Table 1.6: Size of the cathode pads for the stacks (0-1-3-4)/(2)

In the $r\phi$ direction, the pad width is small and the signal created by an avalanche is shared over about three pads. The $r\phi$ position of the particle can be then reconstructed from the spread of the signal. The Pad Response Function (PRF) gives the fraction of the cluster charge deposited on the readout pad as a function of the position of the cluster with respect to the middle of the pad y_p.

$$\mathrm{PRF}(y_p) = \int_{y_p - W/2}^{y_p + W/2} \sigma_{ch}(y^{'}) dy^{'} \tag{1.21}$$

where σ_{ch} is the induced charge in the cathode plane. The PRF can be measured experimentally and compared to the Mathieson parametrization [17] (initially for Multiple Wires Proportional Chambers) or exact calculations performed with GARFIELD [18]. The distribution is found to be approximately Gaussian (see Fig. 1.11). About 80 % of the signal is collected on the central pad and 10 % on each of the two neighbor pads, depending on the width W. The final $r\phi$ position resolution, below 300 μm, is much better than the width W of the pad.

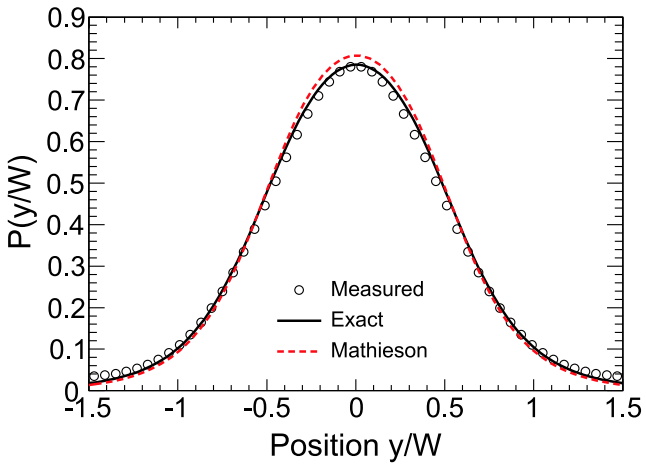

Figure 1.11: Pad Response Function for W=0.75 cm [18].

In the z direction the length l of the readout cathode pads are larger (see Table 1.6) so that most of the time the signal is spread over one pad row only. A priori the resolution is then given by $\frac{l}{\sqrt{12}}$ (about 2.6 cm). To optimise it, the pads are slightly tilted by an angle β_{tilt}=$\pm$2° with respect to the z-axis. This is done in opposite direction for consecutive layers of the TRD. A correlation between the y and z position is introduced:

$$y = y_{measured} + (z - z_{row}) \cdot tan(\beta_{tilt}) \tag{1.22}$$

where z_{row} is the known z-position of the middle of the current pad. The matching of the tracks from the different TRD-layers allows to determine the z-positions by a minimization procedure during a track model fit (helix). The final z resolution is of the order of 1 mm.

Part I

Calibration of the Transition Radiation Detector

Chapter 2

Calibration

2.1 What has to be calibrated?

The calibration constants are related to the two main functions of the TRD, the tracking and the identification of charged particles.
The three dimensional reconstruction of the particle trajectory implies the knowledge of:

- the drift velocity, v_{dE} (and the Lorentz angle α_L, which can be deduced from v_{dE} and E).
- the time reference or time-offset, t_0.
- the width of the PRF, σ_{PRF}.

These variables are expected to vary over the time and the detectors. Time variations of T and P will affect the drift velocity in time, whereas static mechanical and electronic (t_0) imperfections are responsible for non-uniformities over the detectors.
The Particle Identification (PID) is based on the energy deposited in the chamber by the particle. This is measured by looking at the amplitude of the signal, which depends strongly on the gas gain. Thus the signal has to be corrected for the variation of the gain over the 540 detectors due to mechanical non-uniformities within the chambers and for the variation of the gain in time due to changes of the pressure and temperature.

2.2 Expected variations

Two kinds of variations of the calibration constants can occur:

- fluctuations as a function of time due to variations of atmospheric conditions (temperature, pressure and gas composition).
- static variations over the chambers because of some geometrical imperfections.

Gain The expected static variations of the gain factor have been estimated with the results of the gain calibration procedure on test-beam data in this thesis. During the construction of the chambers, tests are also performed to minimize the variations within the chamber [19]. Parabolic shapes of the gain distribution were observed with smooth variations of the order of $\pm 10\,\%$. The overall variations are expected to be about $\pm 20\,\%$.

Drift velocity Static variations of the drift velocity have been seen for different chambers working in the same conditions (temperature, pressure, gas composition, drift voltage) in test-beam data. The spread was below $10\,\%$. Variations due to changes of the temperature (day/night effect) and pressure were smaller.
At Point 2, possible gradients of the temperature and pressure over the $\pm 370\,\mathrm{cm}$ in the radial direction and $\pm 3.5\,\mathrm{m}$ in the beam direction can be reflected in the drift velocity. Nevertheless the gas system has been optimised to reduce the pressure gradient by segmentation of the pressure regulation along slices in height of the detectors. Therefore the overall variations are estimated to be of the order of $10\,\%$.

Time-offset t_0 Very small variations of the time-offset were observed in test-beam data. An upper conservative limit has been estimated at 0.2 timebin (tb), that means $20\,\mathrm{ns}$. These variations are mainly due to the electronic response of the Pre-Amplifier-Shaper (PASA) for different capacitance of the pads.

Width of the PRF The width of the Pad Response Function has been studied with test-beam data, together with the y-position resolution. It was found by minimizing the resolution of the angle with respect to the normal of the chambers, that some chambers show deviations from the theoretical value [20]. The maximal deviation was in the order of $3.2\,\%$. This observation motivated the idea to calibrate the width σ_{PRF}.

2.3 The global strategy with physics events

Physics events, *pp* and *PbPb* collisions, will be used for the calibration. In a first pass, the events will be reconstructed without any calibration correction. The calibration constants are determined from the distribution in amplitude and in time of the signal. In a second pass (and maybe more), the calibration can be improved.

2.3.1 Reconstruction of the events

Each detector (ITS, TPC or TRD) has a dedicated algorithm to track the charged particle without using information from other detectors. This allows to reconstruct the event even if some detectors are not operational. This kind of reconstruction is called *local reconstruction*. The *global reconstruction* aims to match the local tracks (ITS track, TPC track, TRD track, TOF track) together and reconstruct a global track.

In both cases the input of the reconstruction framework are the raw data or digits, which correspond to the detector signal in ADC counts. The first necessary step is the clusterizing. The clusters are sets of adjacent (in space for the TRD) digits that were presumably generated by the same particle. After the tracking algorithm, the output consists of reconstructed tracks. One track is identified with a state vector of five parameters (y,z,$\sin(\phi)$,$\frac{dz}{dl}$,$1/p_T$) at a given position in space. The corresponding error covariance matrix measures the estimated accuracy of the state estimate.

Local tracking In the TRD, the local tracking is based on the linear Riemann sphere fit. In the transverse plane (x,y), the particle's trajectory is fitted by a circle of radius R and origin (x_0,y_0):

$$(x - x_0)^2 + (y - y_0)^2 = R^2 \tag{2.1}$$

The initial number of fitting parameters is three corresponding to R, x_0 and y_0. Since the pads are tilted in the z direction, the measured $y_{measured}$ coordinate of the clusters is correlated with their z position. The unknown z positions are assumed to depend linearly on the radial position of the track. Therefore the slope $\frac{dz}{dr}$ and the z position at a reference point are two additional parameters in the linear Riemann fit (5 parameters in total). The stand-alone tracking code of the TRD was tested with simulated and real (cosmic-ray) data [21].

Global tracking The Global tracking is based on the Kalman filter algorithm. Two distinct phases are present in the recursive algorithm:

- the prediction or extrapolation using the state vector of the track estimated from the previous step.
- the update of the track, onces a measured cluster has be found to match more or less with the prediction.

The choice of the Kalman-filtering approach in ALICE has been motivated by the possibility to handle multiple scattering and energy losses in a simple way. At each step, the material budget is calculated and the mean correction is computed. The correction factors are not negligible for some of the tracking detectors (ITS and TRD), which have a significant radiation thickness.

Online, during data taking, the local tracking will be performed on the TRD data at the High-Level-Trigger (HLT). A first estimation of the calibration constants is stored in the offline condition database. Offline, after the data have been migrated to the storage elements, the global tracking will be run on the ITS, TPC, TRD and TOF data available. A better calibration will be achieved.

2.3.2 Determination of the calibration constants

In *pp* and *PbPb* collisions, the produced particles are mostly pions. In a first order, they are uniformly distributed over the rapidity range $|\eta|<0.9$, covered by the TRD.

- From the average integral deposited energy dE/dx, the gain factor will be relatively calibrated over the chambers. By comparing the dE/dx distributions of different runs, one can also correct for the time variations of the gain.
- From the detector signal as a function of time, the drift velocity and the time-offset are calibrated. The time window corresponding to the drift region can be easily recognized and used to estimate the drift velocity.
- From the spread of the signal over adjacent pads, the width of the PRF is determined.

A certain amount of statistics has to be first accumulated before the detectors can be fully calibrated. The distributions of different detectors are added to reduce the minimal number of collisions needed to calibrate. Ideally each 10 minutes, the calibration constants are extracted for each of the 18 TRD supermodules. This allows to correct for variations within one run at LHC. Nevertheless the calibration framework doesn't provide the possibility to correct for temperature or pressure variations during a run yet. For each run (about 3 hours), the calibration procedures produce calibration constants for each of the 540 individual detectors. Thus time variations run by run and variations over the detectors can be corrected. Finally for static variations, the statistics of one year is accumulated (10^9 *pp* events) to see the profiles of each detector, pad per pad. A total number of 1181952 pads have to be calibrated.

2.4 Expected accuracy of the calibration constants

The final accuracy of the calibration constants expected to be achieved is:

- 1 % for the drift velocity
- 0.02 timebin for the time-offset
- 1 % for the relative gain calibration

The remaining effect is called the residual decalibration. As for the fully decalibrated detectors, residual decalibrated detectors are simulated to see the degradation in tracking efficiencies and resolutions and in the particle identification. Random values have been implemented over the detectors following a Gaussian distribution with the corresponding width for each parameter (drift velocity, time-offset and gain factor). The resulting effect of a such residual calibration has been found to be negligible.

Chapter 3

Gain calibration

3.1 Use of the energy loss

The gas gain of the detector is calibrated on relative basis assuming that all the chambers are equally exposed to the charged particles produced in hadron-hadron collisions. In pp and $PbPb$ collisions, the $\frac{dN_{ch}}{d\eta}$ distribution is quasi flat over the pseudo-rapidity-range covered by the TRD ([-0.9,0.9]). Most of produced particles are pions and their momentum distribution is in this region in a good approximation independent on their pseudo-rapidity. Therefore the energy loss distributions deposited in each chamber or part of chamber should be the same. A comparison of the dE/dx spectra allows to calibrate relatively the gas gains.

3.1.1 Fluctuations of the energy loss

The mean dE/dx energy loss for pions is described by the Bethe-Bloch formula. It corresponds to the average of discrete interactions which can be closed collisions resulting in ionization of the gas molecules, or distant collisions resulting in excitation of the gas molecules. These interactions have a very wide range of possible energy transfers, which leads to a particular shape of the energy loss distribution. In thin gas sheets, the distribution is a Landau distribution [13].

$$f(\lambda) = \frac{1}{\sqrt{2\pi}} e^{-0.5(\lambda + e^{-\lambda})} \tag{3.1}$$

The variable λ is the normalised deviation from the most probable energy loss $(\Delta E)_{mp}$.

$$\lambda = \frac{\Delta E - (\Delta E)_{mp}}{\langle E \rangle} \tag{3.2}$$

where ΔE is the actual energy loss. The average energy loss is larger than the most probable value. The Landau distribution presents a long tail towards higher energy losses due to δ-electrons, ionization electrons, which are energetic enough to ionize the gas themselves and may produce secondary tracks in the detector. The Most Probable Value (MPV) of the distribution is easier to estimate than the mean value. The final dE/dx spectra obtained in pp and $PbPb$ collisions are the convolution of the dE/dx Landau distribution at a given momentum and the

momentum distribution of the pions. As a first approximation, the momentum spectrum has a thermal form $\exp(-\frac{M_T}{T})$ at low p_T, where $M_T=\sqrt{M_{\pi^\pm}^2+p_T^2}$ is the transverse mass of the pion and T the corresponding temperature at freeze-out. At higher p_T, a QCD-inspired power-law function is expected.

3.1.2 The calibration procedure

The calibration procedure is divided in two parts:

- the dE/dx spectra are populated by accumulating the data of many pp or $PbPb$ events.
- the relative gas gains are extracted from the distributions for the given time period.

These procedure is performed at a certain granularity level of the detector: during the online processing of the data the relative gas gain is determined for each detector, in a second pass the calibration accuracy is improved by looking at the amplification factor profile within each chamber. The granularity is given by the number of *calibration groups*. Table 3.1 summarizes the different possibilities.

Mode column / row	1	2	3	4
1	(2·2)	(2·4)	(2·(N_{row}/2))	(2·N_{row})
2	(4·2)	(4·4)	(4·(N_{row}/2))	(4·N_{row})
3	(8·2)	(8·4)	(8·(N_{row}/2))	(8·N_{row})
4	(16·2)	(16·4)	(16·(N_{row}/2))	(16·N_{row})
5	(36·2)	(36·4)	(36·(N_{row}/2))	(36·N_{row})
6	(144·2)	(144·4)	(144·(N_{row}/2))	(144·N_{row})

Table 3.1: Number of *calibration groups*, (groups in pad column)·(groups in pad row), according to the pad column and pad row mode, where N_{row}=12 for chambers of stack 3 and N_{row}=16 otherwise.

Filling of the dE/dx distributions

For each *calibration group*, the dE/dx distribution is stored. To save memory, a two dimensional histogram contains all the information: the y axis is the *calibration group* number, the x axis the energy loss distribution. The dE/dx spectra are obtained by projections on the x axis. Fig. 3.1 shows one example of such a 2D histogram.

By filling the 2D histogram, the deposited charge has to be corrected for:

- the angles of the track, so that it corresponds to the energy loss per unit length. Otherwise a systematic higher amplification factor is reconstructed for the chambers at large pseudo-rapidity (stack 0 and 5). For these detectors, the tracks originating from the primary

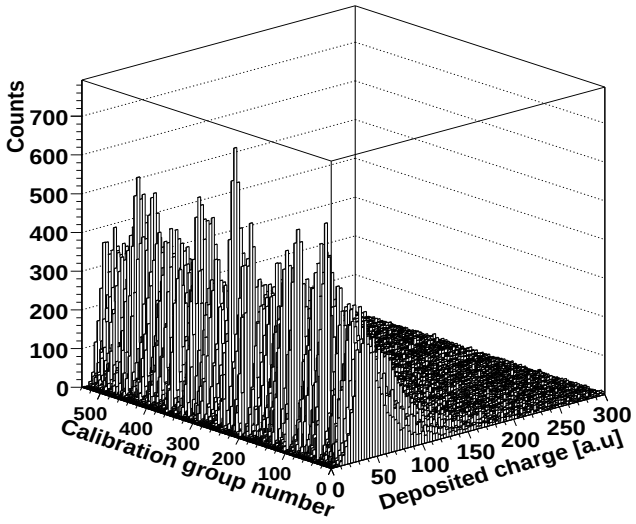

Figure 3.1: A 2D histogram containing the dE/dx distributions of each calibration group (here detector). These were produced with *decalibrated* simulated *pp* events.

vertex are more inclined in θ (the polar angle) and as a consequence depose more energy in each timebin. A better correction is achieved when the particle is also tracked in the TPC. The angles are then determined with more accuracy.

- previous gas gain corrections. The cluster charge is eventually already corrected for non-uniform gains during the tracking. Thus it is crucial to know which database was used to reconstruct the event and retrieve the initial energy loss without any correction. An other possibility would have been to multiply the relative amplification factor found with the previous correction factor. This has nevertheless the disadvantage to make impossible the accumulation of statistics (addition of the 2D dE/dx histograms) from run to run, since different databases could have been used.

- the presample and tail of the signal. Contributions from noisy clusters before the start of the physical signal (at time t_0) reduce in principle the dE/dx resolution. The effect is however very small, when the chambers are running in good conditions (not too much noise). In addition, fluctuations of the drift velocity lead to a systematic effect: the signal is stretched over a longer time for small drift velocities. The dE/dx is calculated over the amplification and drift regions. The number of clusters used in the computation of the dE/dx, which belongs to the tail of the signal, can eventually bias the gain calibration if the drift velocities are quite different and the tail of the signal is truncated for small drift velocities. Thus the boundaries of the amplification and drift regions have to be correctly defined. The clusters are tagged *to be within the chamber border*, when their timebin t_{cl} fulfills the conditions:

$$t_{cl} > t_0 \tag{3.3}$$

$$(t_{cl} - t_0) < \frac{d}{v_{dE}^{eff}} \tag{3.4}$$

The distance d corresponds approximately to the drift and amplification region length (d_{DR},d_{AR}) and is $d_{DR}/2+d_{AR}$=0.7/2+3=3.35 cm. If the calibration constants v_{dE}^{eff} and t_0 are not yet properly determined and taken as constant default values for all the chambers, the time window can correspond to different parts of the signal. Therefore for a first calibration, the energy loss is integrated over the full timebin range. For enough timebins, the resulting error on the amplification factor is small since all the tail of the signal is included in the calculation of the dE/dx for all detectors. In a second pass, only clusters, which are tagged *to be within the chamber border*, are considered.

Finally a track can be rejected due to the following reasons:

- at least one cluster attached to the track is masked (noisy pad).
- the track has a very small (*flowlimit*) or too large number (*fhighlimit*) of clusters. The two variables, *flowlimit* and *fhighlimit*, have to be tuned and as default taken to be 0 and the total number of timebins, respectively.

Fitting of the spectra and extraction of the relative gas gains

Onces the dE/dx spectra are populated and present enough statistics, they can be compared. The distributions can be well fitted with the convolution of a Gaussian and a Landau distribution. To characterize the amplification factor, the Most Probable Value (MPV) is the most appropriate value. It is less sensitive to the long tail of the distribution than the mean value. The following methods were implemented:

- mean value: the mean value of the spectra is taken.
- fit1: the sum of a Gaussian and a Landau function is used to fit the spectra.

$$f_{k_G,\sigma_G,k_L,\sigma_L,m}(x) = k_G \cdot G_{\sigma_G,m}(x) + k_L \cdot L_{\sigma_L,m}(x) \tag{3.5}$$

  The symbols $G_{\sigma_G,m}$ and $L_{\sigma_L,m}$ are for a Gaussian function (width σ_G, mean value m) and a Landau function (width σ_L, MPV m). The fit function has 5 fit parameters: k_G and k_L two normalization constants, m the common MPV of the Gaussian and the Landau distribution and σ_G, σ_L their widths. The MPV gives the relative amplification factor.

- fit2: the convolution of a Gaussian and a Landau function is used to fit the spectra.

$$f_{k_1,\sigma_G,\sigma_L,m}(x) = k_1 \int G_{\sigma_G,0.0}(x-z) L_{\sigma_L,m}(z) dz \tag{3.6}$$

  The function has 4 fit parameters: k_1 a normalization constant, σ_G the width of the Gaussian distribution, σ_L and m the width and MPV of the Landau distribution. The variable m allows to determine the relative amplification factor.

- weighted mean: the measured dE/dx distribution can be written as a function $N(\Delta E)$. The number of tracks $N(\Delta E)$ correspond to the number of particles found, that have the energy loss ΔE in the chamber. The weighted mean is defined as :

$$wm = \frac{\int_0^{\Delta E_{max}} f_w(\Delta E) \cdot N(\Delta E) \cdot \Delta E \cdot d\Delta E}{\int_0^{\Delta E_{max}} f_w(\Delta E) \cdot N(\Delta E) \cdot d\Delta E} = \frac{\sum_i f_w(\Delta E_i) \cdot N(\Delta E_i) \cdot \Delta E_i}{\sum_i f_w(\Delta E_i) \cdot N(\Delta E_i)} \tag{3.7}$$

where $f_w(\Delta E)$ is a positive weight function ($0.0 \leq f_w(\Delta E)$). Only the relative values of the weights matter in determining the value of wm. In other words, $k \times f_w(\Delta E)$ gives the same result if k is a positive constant. For $f_w(\Delta E)$=1.0, the weighted mean is simply the mean value of the distribution. The weight function has to be first determined with a typical measured dE/dx distribution. A polynomial parameterization with 5 parameters (a,b,c,d,e) is fitted to give the same result as a fit with a convolution of a Gaussian and a Landau distribution.

$$f_w(\Delta E) = a + b \cdot f_r(\Delta E) + c \cdot (f_r(\Delta E))^2 + d \cdot (f_r(\Delta E))^3 + e \cdot (f_r(\Delta E))^4 \tag{3.8}$$

$$f_r(\Delta E) = \frac{\int_0^{\Delta E} N(\Delta e) d\Delta e}{\int_0^{\Delta E_{max}} N(\Delta e) d\Delta e} = \frac{\sum_{i=bin(0)}^{bin(\Delta E)} N(\Delta e_i)}{\sum_i N(\Delta e_i)} \tag{3.9}$$

The weighted function is shown in Fig. 3.2

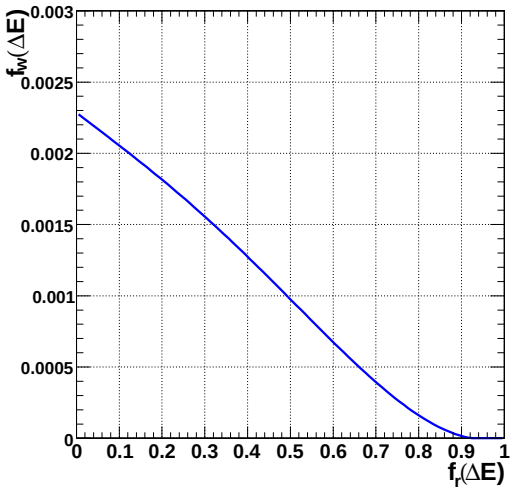

Figure 3.2: Weighted function used to extract the Most Probable Value of the dE/dx distribution.

The decisive points for the choice of one of these methods are the achieved accuracy, the stability (maximum deviation) and the CPU time needed. Results on simulations allowed to study them comparatively. The weighted mean was finally chosen as the default method.

3.2 Simulated data

To test the relative gas gain calibration, *pp* collisions at $\sqrt{s}$=14 TeV are simulated. The detector is artificially *decalibrated* using a database, in which each chamber has a constant amplification factor different from the others. To follow the expected variations, the gas gain distribution is taken as a Gaussian distribution centered around 1.0 with a width of 20 %. For each chamber, the energy loss distribution of the charged particles crossing the gas volume is measured and stored. The relative amplification factors are then extracted from the dE/dx spectra. The quality of the calibration procedure is determined by comparing the reconstructed coefficients with those used in the simulation. The number of accumulated *pp* events plays an important role, since the particle energy loss fluctuates around a mean value. Thus the study is done as a function of the mean number of tracks found per chamber. The performances of the four different fitting methods are evaluated by looking at the relative gain $\frac{\Delta g}{g}=\frac{g_{rec}-g_{sim}}{g_{sim}}$.

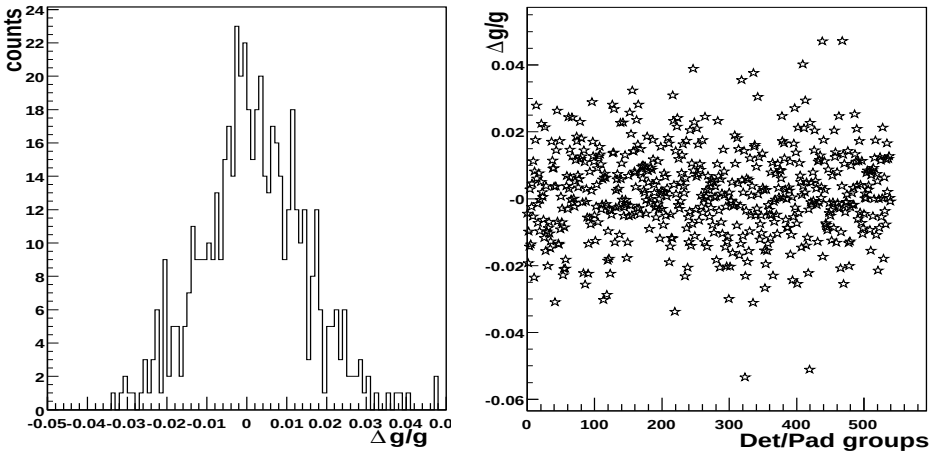

Figure 3.3: Distribution (left panel) and dependence on the detector number (right panel) of $\frac{\Delta g}{g}=\frac{g_{rec}-g_{sim}}{g_{sim}}$. The weighted mean was used with about 6000 tracks per detector.

Fig. 3.3 shows such a distribution using the weighted mean method. The mean number of entries (tracks) per dE/dx spectra is in the order of 6000, which corresponds to about 62500 *pp* collisions (N_{pp}). The number N_{pp} can be estimated with the charge particle multiplicity at mid-rapidity of about $\frac{dN_{ch}}{dy}\approx 6$ and a tracking efficiency around 80 %. The $\frac{\Delta g}{g}$ distribution is approximately Gaussian with a width of 1.13 % (left panel). No systematic effects are seen in the right panel of Fig. 3.3, where $\frac{\Delta g}{g}$ is plotted as a function of the detector number.

The criteria to judge the quality of the procedure are the width of the $\frac{\Delta g}{g}$ distribution ($\sigma_{\text{relative gain}}$) and the maximum deviation (the worse result obtained). These two variables are shown in Fig. 3.4 as a function of the mean number of tracks per detector (N_{mean}) for the four fitting methods.
The relative error $\sigma_{\text{relative gain}}$ decreases exponentially with N_{mean} to reach an asymptotic value

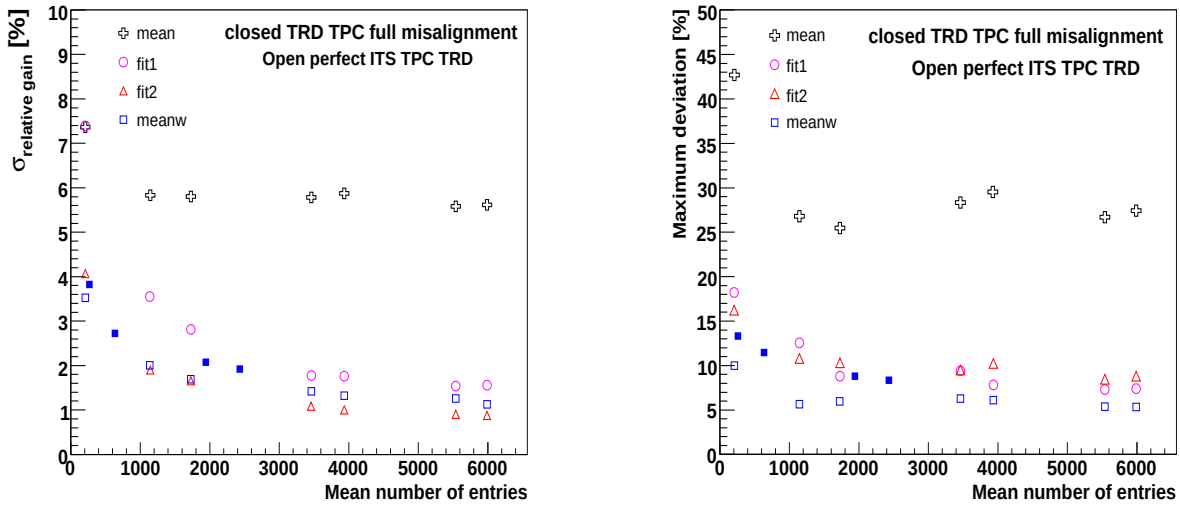

Figure 3.4: Accuracy (left panel) and maximum deviation of the reconstructed gain as a function of the mean number of tracks per calibration group.

(left panel Fig. 3.4). Whereas the fit2 method presents the best accuracy below 1 % for N_{mean}=4000 (N_{pp}≈41700), the mean value method quickly saturates at 5.8 %. Clearly the mean value of the dE/dx contains less direct information about the gas gain than the Most Probable Value. For N_{mean}=300 (N_{pp}≈3200), $\sigma_{\text{relative gain}}$ is already in the order of 4 % for the weighted mean and the fit2. The goal value of 1 % is nevertheless not really achieved by the weighted mean, which reaches an accuracy of about 1.5 % for N_{mean}=3000 (N_{pp}≈31300). To achieve the good accuracy, a minimum of 3000 tracks per *calibration group* is needed (N_{pp}≈31300). With a data taking rate of 100 Hz, 10^5 *pp* collisions correspond to 1000 s running time, about 20 min. Thus Offline the variations of the amplification factors per detector can be estimated each 20 min during a *pp* run.
The maximum deviation saturates quickly with N_{mean}. With a maximum error of 5 %, the weighted mean is the most performant method. The fit2 method is the less robust fit function. The mean value is still the least accurate method with a maximum deviation reaching 25 %.
The effect of full misalignment of the TPC and the TRD was also studied. The detectors are placed inside a space frame. Due to the gravitational force and mechanical imperfections, the position of the chambers are slightly different from the ideal ones. The discrepancy influences the tracking procedure and has to be corrected for. As a consequence the maximum deviation and $\sigma_{\text{relative gain}}$ are larger for the same mean number of entries.

The fit procedures fit1 and fit2 are not always successful. To check if the measured dE/dx distribution is well reproduced by the fit function, the χ^2 can be used:

$$\chi^2 = \sum_{i=minbin}^{maxbin} \left(\frac{f(\Delta E_i) - N(\Delta E_i)}{\sigma_i} \right)^2 \tag{3.10}$$

where $[minbin, maxbin]$ is the range over which the measured dE/dx distribution ($N(\Delta E_i)$) is

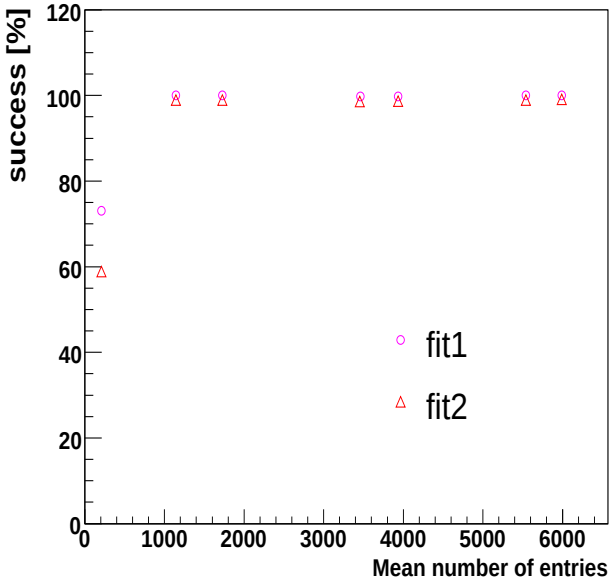

Figure 3.5: Percentage of successful fits for the two methods as a function of the mean number of tracks per calibration group.

fitted by the fit function $f(\Delta E)$. The variables σ_i are errors of the measured $N(\Delta E_i)$ and taken equal to $\sqrt{N(\Delta E_i)}$. The number of degrees of freedom *ndf* is (*k*-*c*), where k is the number of non-empty bins used for the fit and c is the number of fit parameters. If $\frac{\chi^2}{ndf}$ is below an adjustable limit, the fit is said successful. A minimum of entries in the dE/dx spectra is also required (default 1000). An example of fit1 and fit2 is shown with the test-beam data of 2007 (Fig. 3.11). In Fig. 3.5 the percentage of successful fits is presented as a function of N_{mean} for simulated *pp* collisions. Here also one can see that the fit1 is more robust than the fit2, even if it gives results with a smaller accuracy.
Finally a last non negligible criterion for the online calibration is the CPU time needed to extract the 540 relative amplification factor (one per detector). The weighted mean is comparable to the mean value, since the computation is straightforward (see Table 3.2). The fit1 and fit2 requires much more CPU time. Therefore the weighted mean is the default method used for the gas gain calibration.

Method	mean value	fit 1	fit 2	weighted mean
CPU time [s]	0.540	11.940	390.05	0.510

Table 3.2: CPU time needed to fit 540 dE/dx distributions with different fit methods.

3.3 Test-beam data

A last test-beam was organized at the Proton Synchrotron CERN accelerator from the 30/10 to the 12/11/2007. The motivations were the following:

- Sophisticated methods were developed to identify electrons with momentum above 1 GeV/c since the last test-beam at CERN in 2004. As expected the test-beam data were found to be very useful to improve the Particle Identification algorithms and provide reference data. Nevertheless the simulations done within the AliRoot framework show performances better by a factor two than the real data. Thus a new test-beam helps to understand this discrepancy and accumulate the statistics needed for the reference histograms of the PID.

- The trigger system (Global Tracking Unit) of the TRD was never tested in reality, as well as the High Level Trigger (HLT) and the data format containing the trigger information (*online tracklets*). This test-beam gave the opportunity to get ready for the final online configuration of the TRD in ALICE.

- Test-beam data constitute a testbench for the standalone reconstruction algorithm and for the calibration procedures.

The third supermodule (SM 3) built in Muenster was brought to the T10 area at CERN and used for the test-beam. A beam of π^- and e^- with momentum from 1 GeV/c to 6 GeV/c was aimed at one stack of the supermodule. The setup is sketched in Fig 3.6. To give a first trigger signal, 2 Scintillator detectors (S1,S2) are placed in the beam line. The position of the beam is studied with two Silicon detectors (Si1 and Si2), whereas the Cherenkov and the lead-glass calorimeters provide information to identify the e^- and π^- independently from the TRD.

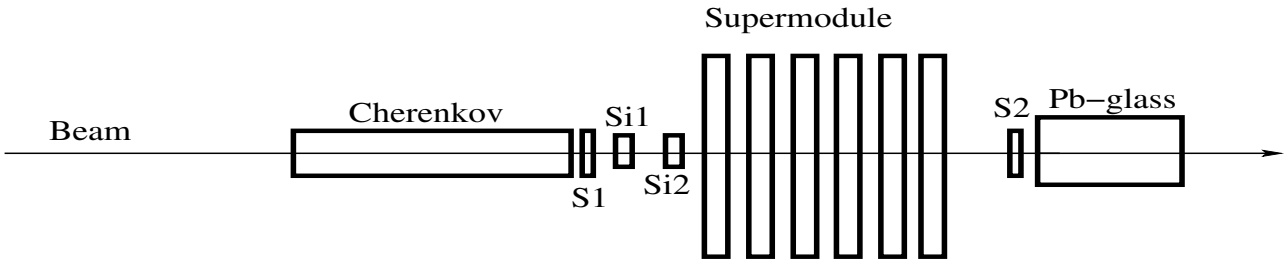

Figure 3.6: Schema of the setup.

One supermodule weights about 1650 kg. Therefore it was not particularly easy to transport it to its final position (see Fig. 3.7), where it was just fitting in the space available.

From the right to the left, one can recognize one part of the Cherenkov detector, the S1, Si1, Si2 detectors and the SM 3 on the photo in the left panel of Fig. 3.7. The lead-glass calorimeter is also visible behind the SM.

Figure 3.7: Left panel: the supermodule 3 (SM 3) having a lift. Right panel: SM 3 at its final position in the test-beam area.

In this work, we focus on the run 387 at 4 GeV/c. The supermodule was at that time filled with 83 % Xe and 17 % CO_2.

3.3.1 Particle Identification

Electrons are separated from the pions with the correlated signals of the lead-glass calorimeter and the Cherenkov detector (see Fig. 3.8).

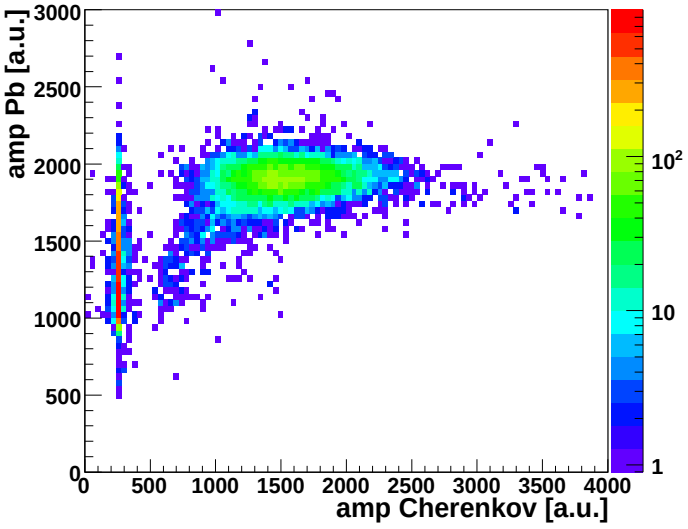

Figure 3.8: Cherenkov and lead glass signals for π^- and e^- at 4 GeV/c.

Since the e^- loose all their energy through electromagnetic showers in the lead-glass detector, the signal amplitude is larger than for the π^-. The Cherenkov detector is based on the emission of Cherenkov radiation light by the charged particles, which have a velocity higher than the speed of light in the medium. Due to the larger π^- mass ($M_{\pi^\pm}$=139,6 MeV/c^2, $M_{e^\pm}$=0.511 MeV/c^2), π^- have a smaller Cherenkov signal. Thus e^- and π^- can be separated with cuts on the Cherenkov and lead-glass signal amplitude. For 4 GeV/c, the values are given in Table 3.3. A similar amount of e^- and π^- were found. Only π^- are useful for the calibration procedures. The e^- produce transition radiation in the radiator in front of the chambers. Therefore the Most Probable Value of their energy loss distribution can not be as well determined as for π^- with the methods described before.

Particle	amp Cherenkov [a.u.]	amp Pb [a.u.]
electron	[900,2200]	[1600,2500]
pion	<500	<1700

Table 3.3: Cuts on the Cherenkov and lead glass amplitudes to identify pions and electrons.

3.3.2 Events quality

The data were reconstructed with the standalone tracking algorithm. The left panel of Fig. 3.9 shows the probability to find a given number of tracks in pion and electron events.

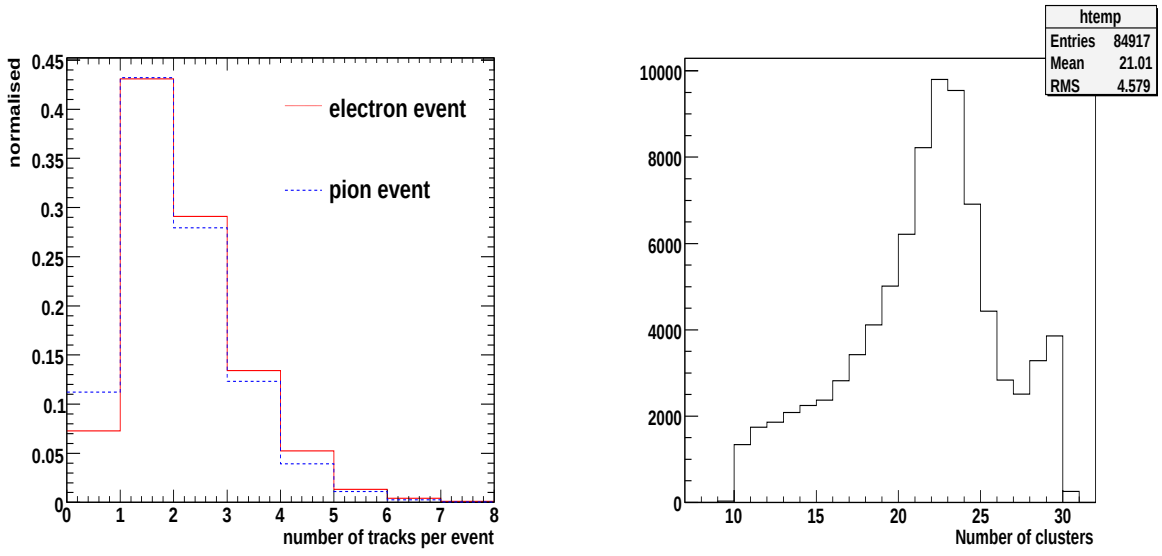

Figure 3.9: Left panel: Number of tracks found per event for *pion* and *electron* event. Right panel: Number of clusters attached to a track.

The tracking efficiency is around 92 % for e^-, which have a better signal-to-noise ratio, and 89 % for π^- at 4 GeV/c. Due to secondary interactions and δ ray electrons, some events contain

more than one track. Their fraction is higher than expected and not completely understood. Only events with one track can be used for the calibration, since π^- have to be selected and the identities of the additional tracks are not known. 43 % of the pion events fulfill the criterion.

The distribution of the number of clusters attached to the tracks is presented in the right panel of Fig. 3.9. A peak at around 29 timebins is most likely due to noisy pads or to 2(3) tracks. Tracks with a number of clusters between 20 and 25 were used for the calibration.

3.3.3 Relative gas gain calibration

Fig. 3.10 shows the π^- and e^- energy loss distributions in the 6 planes of the stack.

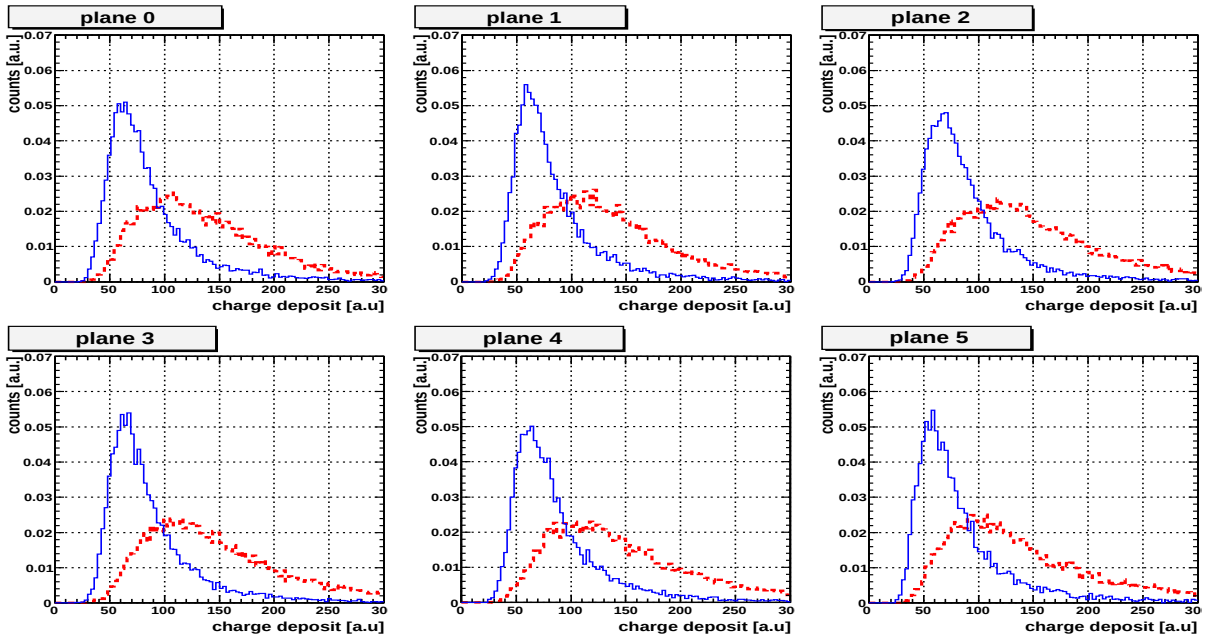

Figure 3.10: Energy loss distributions of pions (blue full line) and electrons (red dashed line) of 4 GeV/c in the 6 planes of the stack. One reconstructed track per event is required.

The curves are normalized to their integral. Whereas the π^- loose energy in the gas according to a dE/dx Landau distribution, the e^- energy loss distribution is much broader due to the additional contribution of TR photons absorbed at the entrance of the drift region. Moreover the e^- dE/dx energy loss alone is already larger than that of the π^-, since the factor $\gamma\beta$ is higher for e^- than for π^- at the same momentum. The 4 GeV/c e^- are already in the Fermi plateau, while the π^- are in the relativistic rise regime.

To calibrate the amplification factor of the 6 chambers, the Most Probable Value of the π^- energy loss distribution is determined for the 6 chambers of the stack. The fit1 and fit2 are shown in Fig. 3.11 for the plane 4. They are very similar with a slightly better description of the tail by the fit2.

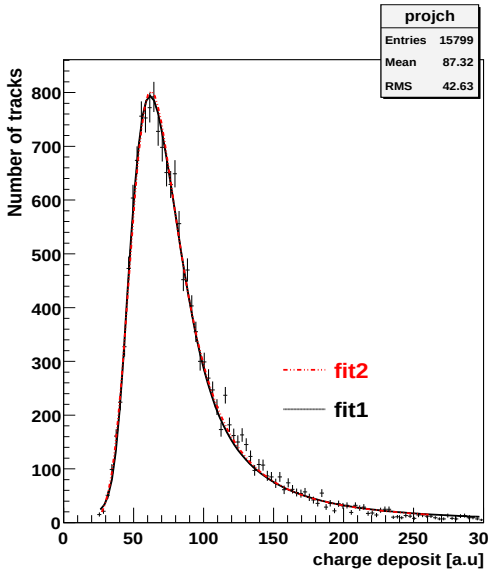

Figure 3.11: fit1 and fit2 for plane 4 (counting from 0 to 5).

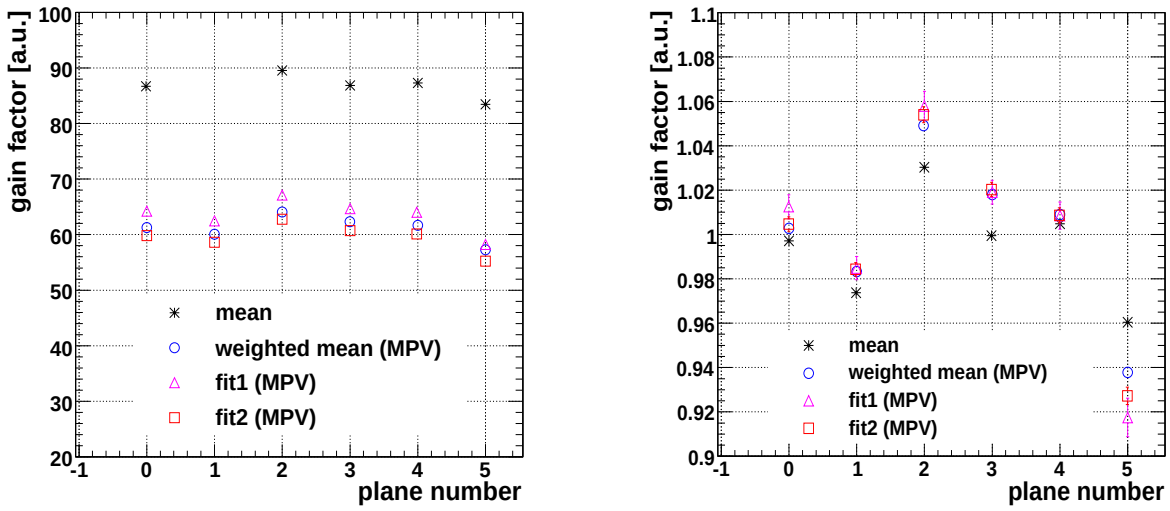

Figure 3.12: Gain factor of the six detectors of the stack determined with the different fitting methods. The absolute values are shown in the left panel, the values normalized to the mean in the right panel.

The mean and MPV values of the distributions are given for the 6 chambers in the left panel of Fig. 3.12. As expected from the long tail of the Landau dE/dx spectra, the mean value is larger than the MPV. The MPV is extracted with the three different methods: weighted mean, fit1 and fit2. Each method has the tendency to reconstruct a larger or smaller value. Since the gas gain is calibrated only relatively, this effect should not play a role as long as the methods give proportional results. To compare the final relative gain calibration, the values have been normalized to their average over the 6 chambers (right panel of Fig. 3.12). According to all

the methods, the gas gain variation is below ±10 %. The anode voltage U_a of each chamber was nevertheless adjusted to have similar signal amplitudes. If the chambers were exactly identical, the small voltage differences (see Table 3.4) would lead to a rather large variation of the amplification factors (in the order of 30 % for plane 3 compared to plane 0). The weighted mean method gives similar results as the fit1 and fit2 methods, with a maximum deviation of 2.2 % and 1.12 % respectively.

Plane number	0	1	2	3	4	5
U_a [keV]	1.55	1.53	1.52	1.50	1.54	1.54

Table 3.4: Anode voltage of the different chambers.

3.4 Cosmic-ray data

During the construction of the supermodules in Muenster, measurement with cosmic rays are performed. For triggering, scintillator detectors are placed below and above the supermodule. After the test-beam in October 2007, the SM 3 was sent back to Muenster to find and repair a gas leak. Several cosmics runs were taken with different anode and drift voltages. The gas mixture used was composed of Ar (≈63 %) and CO_2 (≈37 %).

3.4.1 Gas gain as a function of the anode voltage

To study the amplification factor dependence on the anode voltage, runs with different U_a were analyzed. The raw data were reconstructed with the standalone tracking algorithm.

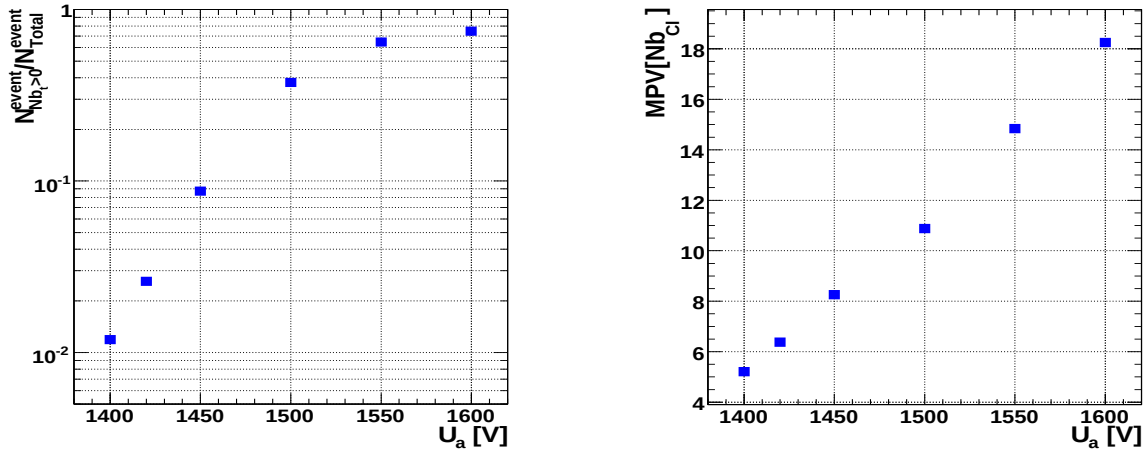

Figure 3.13: Fraction of events with at least one reconstructed track (left panel) and most probable number of clusters attached to one tracklet (right panel) as a function of the anode voltage.

The left panel of Fig. 3.13 shows the fraction of events with at least one found track. The ratio $N^{event}_{Nb_t>0}/N^{event}_{Total}$ increases exponentially with U_a before beginning to saturate at about 1550 V to reach 75 % at 1600 V. This quantity corresponds to the combined trigger and tracking efficiency. The most probable number of clusters attached to the tracklets MPV[Nb_{Cl}] are quite small compared to the total number of timebin, 30 tb (see right panel of Fig. 3.13). At low U_a, the signal suffers from noise contamination.

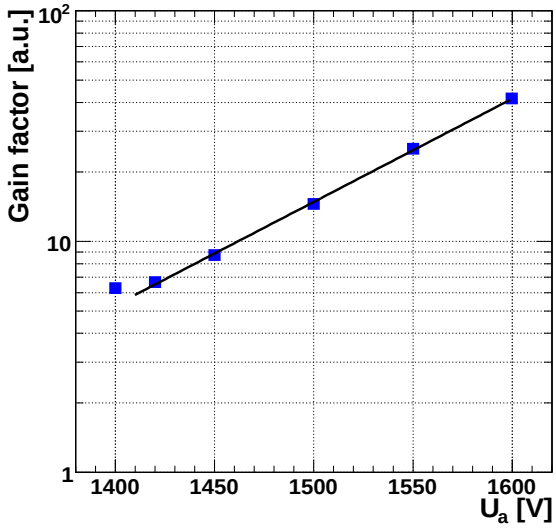

Figure 3.14: Gain factor as a function of the anode voltage.

The dE/dx spectrum was integrated over the complete supermodule with the total number of events available in each run. Fig. 3.14 shows the extracted gain factor as a function of U_a. The expected exponential behaviour can be seen except from the lowest value of U_a, for which the noise contamination is probably responsible.

3.4.2 Systematic effect of the drift velocity

The previous results were all from runs, for which the drift voltage was set to -1900 V. Four runs were taken with a lower drift velocity. The voltages were U_d=-1600 V and U_a=1500 V. Their reconstructed amplification factors are compared in Fig. 3.15 with data taken at the same anode voltage U_a=1500 V but at a higher drift velocity U_d=-1900 V. To compute dE/dx of one tracklet, the deposited charged is integrated over the total number of timebins. Since for U_d=-1600 V ($v_d \leq 1.39\,\mathrm{cm}/\mu\mathrm{s}$), the tail of the signal begins to be truncated, the extracted gain factors are systematically lower. Other effects (like the variations of the gas composition...) may also play a role.

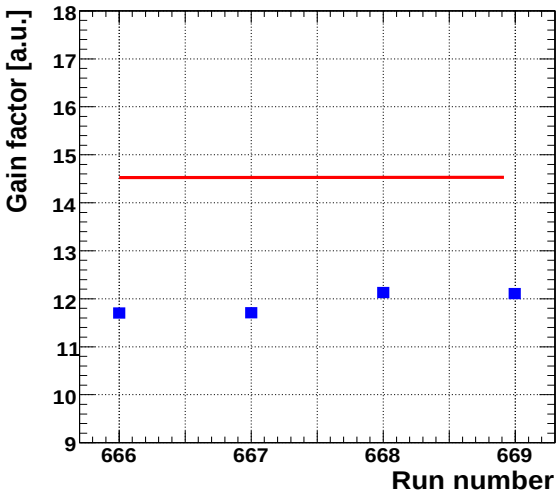

Figure 3.15: Extracted gain factor for the runs 666 to 669 with U_a=1500 V and U_d=-1600 V (blue full squares), compared to the amplification factor of run 660 with U_a=1500 V and U_d=-1900 V (red line).

3.4.3 Gain factor dispersion and systematic effect of the trigger

For the runs 666, 667 and 669, the amplification factor of each chamber (30 chambers in one supermodule) has been determined. The particle species, which crosses the chambers, are mainly $\mu^{\pm}$ (80 %) with an average mean energy of 4 GeV/c. They are assumed to be uniform over the all supermodule for the calibration. Nevertheless the trigger can introduced some bias. Coincidences between scintillator detectors below and above the supermodule lead to the trigger signal (see Fig. 3.16). Since the scintillator detectors above cover between one and two stacks depending on their z position, some stacks are privileged (see Table 3.5).

Run / Stack number	0	1	2	3	4
666	526	852	2352	12048	11958
667	13261	8756	1826	937	585
668	438	4036	5621	3215	396
669	14226	13644	9799	16200	12938

Table 3.5: Mean number of reconstructed tracks per chamber for runs 666 to 669.

For the run 666, the dispersion of the gain factor over the chambers was found below 10 % ($\sigma_g \approx 9.6$ %). This proves that the detectors are quite identical because the anode voltage has not been tuned chamber per chamber but is the same for all the chambers, . The σ_g is smaller than the expected value of about 20 %.

One way to see if the trigger influences the gain calibration, is to compare the gain profile of the supermodule for different runs. In case of a good calibration, they should be similar with

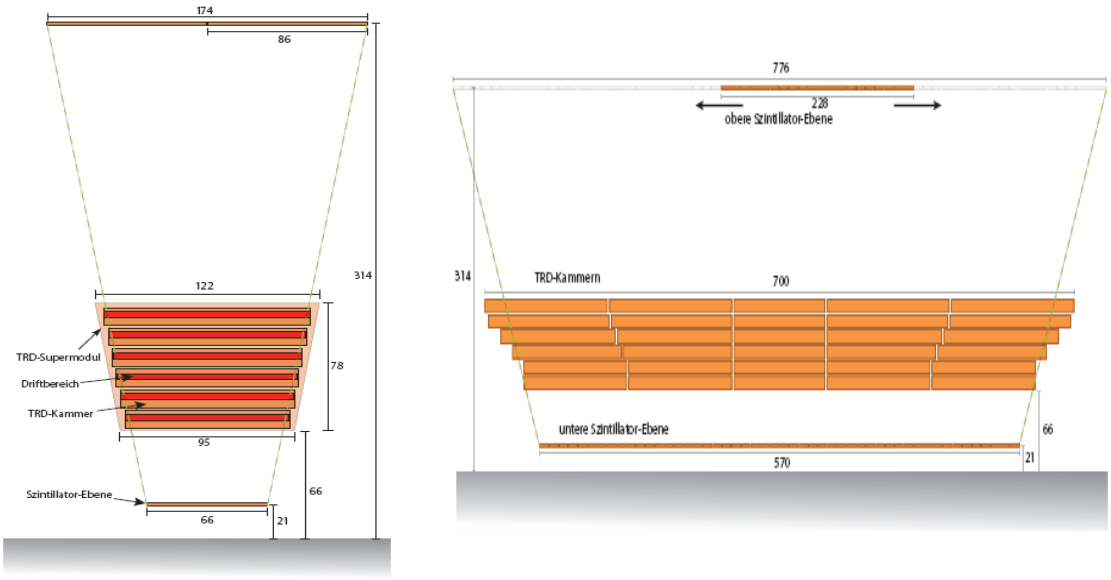

Figure 3.16: Setup to take cosmic-ray data with one supermodule [22].

an overall proportional constant. The amplification factors obtained for the run 667 and 669 are compared in Fig. 3.17. The gain factors of each run has been previously normalized to their mean value. No big systematic bias due to the different triggered stacks are observed. The difference from run to run is in the order of 3 %.

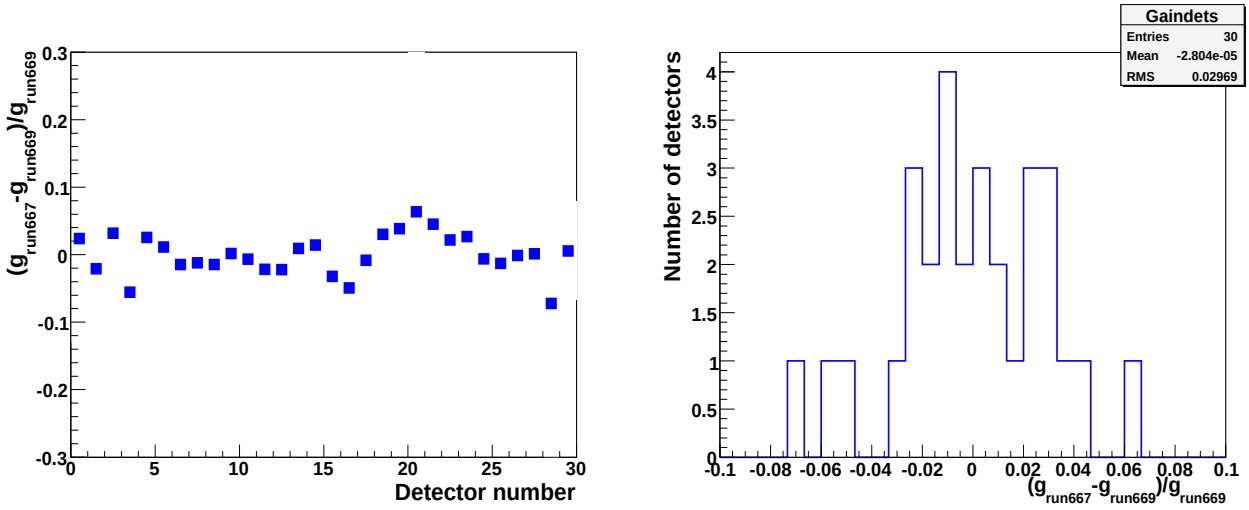

Figure 3.17: Relative comparison of the gains obtained for the runs 667 and 669: the distribution (right panel) and as a function of the detector number (left panel).

In Fig. 3.18, the gain maps of the run 666 and 667 are compared. Whereas the scintillator detectors are placed above the stack 4 in the run 666, they are at the opposite side of the SM 3 in run 667. The reconstructed gain factor is larger for chambers, which were not in the range

of the trigger detectors. To overcome this bias, the three runs can be simply added since the running conditions were otherwise quite similar. The dispersion was then found to be in the same order as previously, about 9 %.

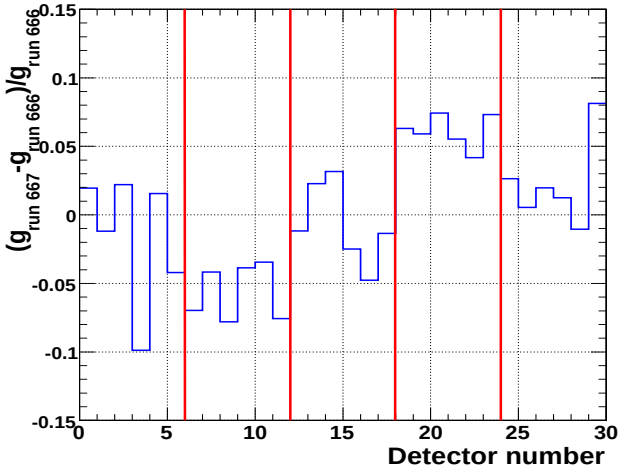

Figure 3.18: Relative comparison of the chamber gains obtained for runs 666 and 667.

3.5 First gain calibration of the four supermodules installed at CERN

Cosmic-ray data were also taken with the four supermodules installed in the ALICE setup at CERN (SM 0 from the chamber 0 to 30, SM 8 from the chamber 240 to 270, SM 9 from the chamber 270 to 300, and SM 17 from the chamber 510 to 540).

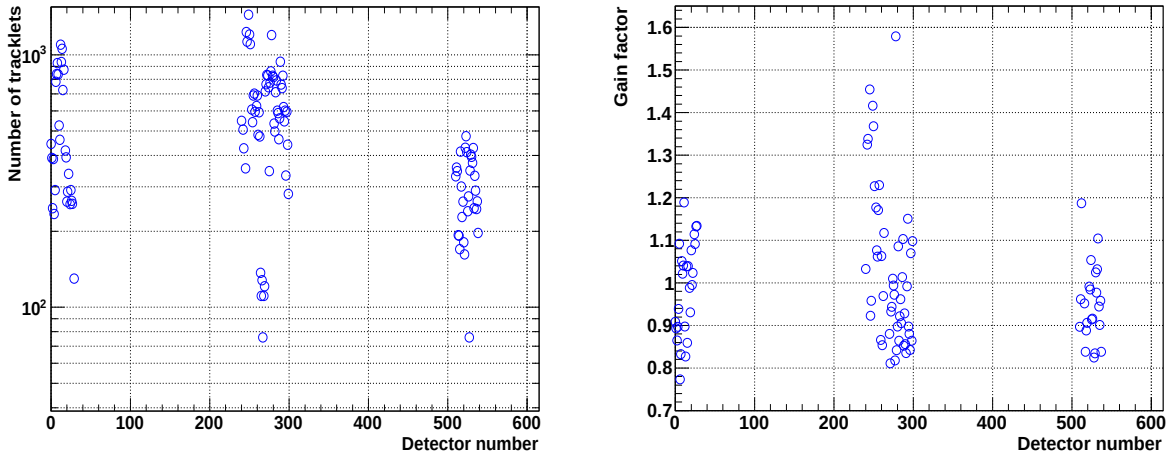

Figure 3.19: Number of reconstructed tracklets (left panel) and normalized gain factor (right panel) as a function the detector number.

The runs were reconstructed with the offline central barrel tracking (when the TPC was also part of the same trigger cluster), or the TRD standalone tracking. Only one run out of the 24 runs used for the calibration was without the TPC. All runs were triggered by the TRD L1. The left panel of Fig. 3.19 shows the number of tracklets found per detector. The differencies between detectors can come from half chambers switched off. This has to be still investigated. Since the reconstructed gain factors are quite similar excepting for some chambers in the SM 8 (see right panel of Fig. 3.19), the different number of reconstructed tracks per detector can not be explained by different gas gains. The sigma of the gain factor distribution is in the order of 16 %. All detectors were nevertheless not running at exactly the same anode voltage (the nominal value for the 82-18 % Ar-CO_2 mixture is 1450 V).

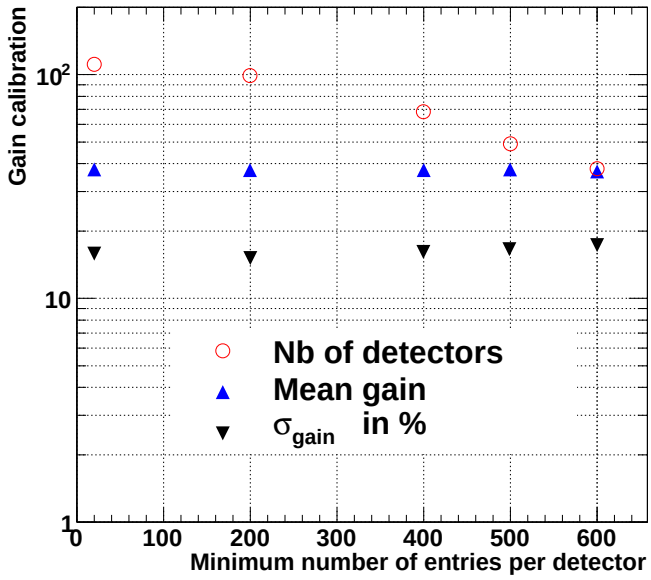

Figure 3.20: Number of detectors for which the dE/dx spectrum is fitted, and mean and sigma of the detector gain factor distribution as a function of the minimum number of entries required per detector.

To evaluate the role played by the Landau fluctuations of the energy loss and the non-uniformity of the charged particles crossing the chambers, the fit of the dE/dx spectra was performed for different minimum number of entries in a detector. The mean number of entries in each detector is indeed well below the threshold of 1000-3000 entries. This number was evaluated for *pp* collisions at 14 TeV in order to reach an accuracy of the order of a few % for the gain calibration. Fig. 3.20 shows the number of detector passing the minimum entries cut, the mean and sigma of their gain factor distribution as a function of the minimum number of entries required in the dE/dx spectrum to be fitted. Only 48 detectors have more than 600 entries. The mean of the gain distribution is constant, while the sigma increases slightly from 16 % to 18 %. The main variations of the gain factor from one detector to the other doesn't come from the statistics.

Chapter 4

The calibration of the drift velocity

Two algorithms were developed to calibrate the electron drift velocity in the gas: one, which doesn't require necessarily tracking, another, which, on the contrary, can be performed only with the global tracking and the information of the TPC or eventually the local tracking.

4.1 Algorithm with or without tracking

4.1.1 Use of the average pulse height

The average pulse height $\langle PH \rangle$ as a function of the time can be used to estimate the drift velocity. As for the relative gas gain calibration, the $\langle PH \rangle$ of each calibration group are stored in a 2D profile histogram (see Fig.4.1).

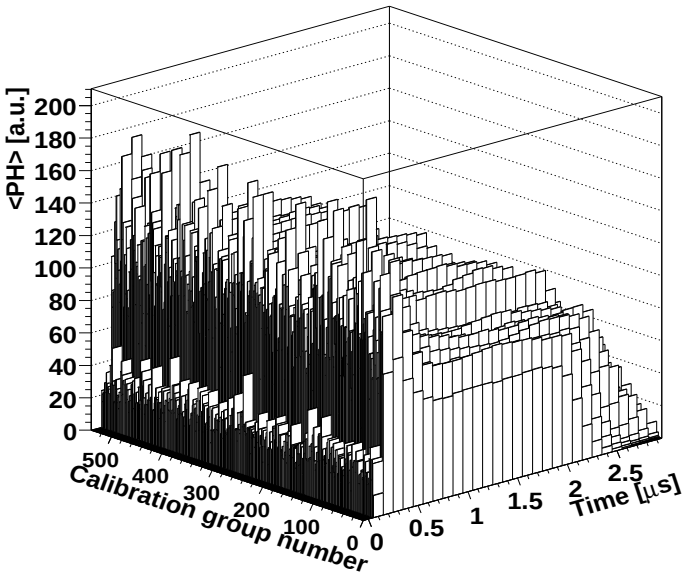

Figure 4.1: 2D histogram containing the average pulse height distributions of each calibration group (here detector), produced with *decalibrated* simulated *pp* events (see below).

The mean signal of a charged particle crossing the chamber is characterized by:

- a first peak due to the amplification region, as contributions of ionization electrons, which come from both sides of the anode wire plane, are overlapping.
- a flat plateau, that results from the electrons in the drift region.
- a tail because of the Time Response Function (TRF).

From the shape of $\langle PH \rangle$, three points in time are extracted: the start of the signal t_B, the end of the amplification region t_{AR} and the end of the amplification region t_{DR}. One sophisticated method consists in fitting $\langle PH \rangle$ with an appropriate function. The TRF $f_{TRF}(t)$ is the detector response for a single electron, which arrives at the time t=0 at the anode wire plane. On average, the ionization electrons are uniformly distributed along the particle path. Thus $\langle PH \rangle$ is the sum of the electron signal arriving at time t_i:

$$\langle PH \rangle(t) = \sum_i f(t-t_i) = \begin{cases} a \cdot \int_{t_B}^{t} f_{TRF}(t-t')dt' & \text{for } t_B \leq t \leq t_{AR} \\ a \cdot \int_{t_B}^{t_{AR}} f_{TRF}(t-t')dt' + b \cdot \int_{t_{AR}}^{t} f_{TRF}(t-t')dt' & \text{for } t_{AR} \leq t \leq t_{DR} \\ a \cdot \int_{t_B}^{t_{AR}} f_{TRF}(t-t')dt' + b \cdot \int_{t_{AR}}^{t_{DR}} f_{TRF}(t-t')dt' & \text{for } t_{DR} \leq t \end{cases} \tag{4.1}$$

where the fraction a/b determines the ratio of the signal amplitude at the amplification peak and in the drift region plateau. Fig. 4.2 shows the TRF used in the simulation of the detector response and the analytical function, which has been fitted to it.

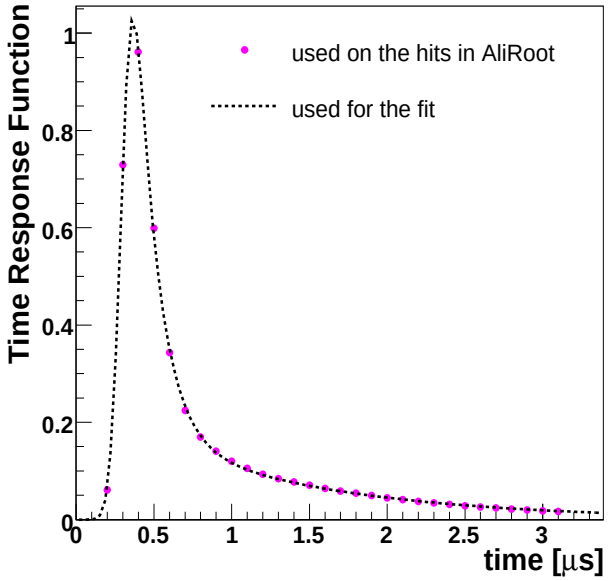

Figure 4.2: Time Response Function used in the simulation of the detector response and function used in the fit of the average pulse height.

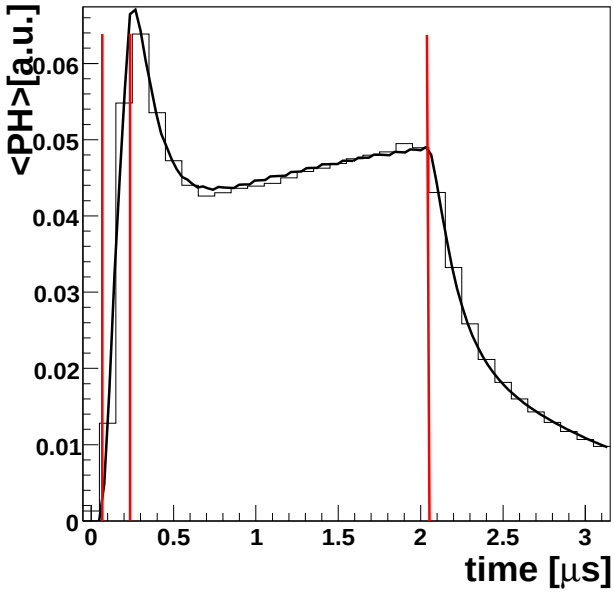

Figure 4.3: Example of a fit of the simulated average pulse height for $\pi^{\pm}$ at 1 GeV to determine the times t_B, t_{AR} and t_{DR} (see text for definition).

The final fit function inspired from Eq. 4.1 has 5 parameters: t_B, t_{AR}, t_{DR}, a/b, an overall scale factor and the baseline, which can be constrained to zero if the baseline subtraction has been performed in the front end electronics. In the left panel of Fig. 4.3, one can see an example of such a fit. The three fit parameters t_B, t_{AR} and t_{DR} are indicated by the vertical lines. No tail cancellation is performed for this $\langle PH \rangle$ of 4 GeV/c $\pi^{\pm}$.

The fit has the disadvantage of not always converging. That is why a more simple method has been developed in parallel. The times t_B, t_{AR} and t_{DR} are identified as:

- the maximum positive slope of $\langle PH \rangle$, $\frac{d\langle PH \rangle}{dt}(t_B)$=Max$[\frac{d\langle PH \rangle}{dt}(t)]$.
- the maximum of $\langle PH \rangle$, $\langle PH \rangle(t_{AR})$=Max$[\langle PH \rangle(t)]$.
- the maximum negative slope of $\langle PH \rangle$, $\frac{d\langle PH \rangle}{dt}(t_B)$=Min$_{(t_{AR}+0.4\,\mu s)\leq t}[\frac{\langle PH \rangle}{dt}(t)]$, after the time $t_{AR} + 0.4\,\mu$s.

Fig. 4.4 shows $\frac{d\langle PH \rangle}{dt}$ of the particular $\langle PH \rangle$ of Fig. 4.3 and the time t_B and t_{DR} found (vertical lines). The values of t_B, t_{AR} and t_{DR} are interpolated between timebins using Lagrange polynomial functions. For n points $(t_1,\langle PH \rangle(t_1))$, $(t_2,\langle PH \rangle(t_2))\cdots$ $(t_n,\langle PH \rangle(t_n))$, there exists only one polynomial function of degree n-1, which fits the points:

$$P(t) = \sum_{i=1}^{i=n} \langle PH \rangle(t_k) \cdot \prod_{i \neq k} \left(\frac{t - t_i}{t_k - t_i} \right) \tag{4.2}$$

Onces the polynomial function $P(t)$ has been determined for 4 or 3 points around t_B, t_{AR} or t_{DR}, its maximum is found numerically by sampling the time t. The procedure is not always successful. To consider the result as reasonable, the following conditions have to be fulfilled:

- The mean signal $\langle PH \rangle$ should have enough accumulated statistics. In particular, the statistical errors should not be larger than the natural variation of the signal. That means for example for $\langle PH \rangle(tbin_{AR}))$ where $tbin_{AR}$ is in timebin that:

$$\langle PH \rangle(tbin_{AR} - 1) + E(\langle PH \rangle(tbin_{AR} - 1))) \leq \langle PH \rangle(tbin_{AR}) \tag{4.3}$$

$$\langle PH \rangle(tbin_{AR} + 1) + E(\langle PH \rangle(tbin_{AR} + 1))) \leq \langle PH \rangle(tbin_{AR}) \tag{4.4}$$

- the found $tbin_B$ and $tbin_{DR}$ should not be at the limit of the signal (first and last timebin), otherwise the interpolation is not possible.

- the time t_{AR} should be larger than t_B

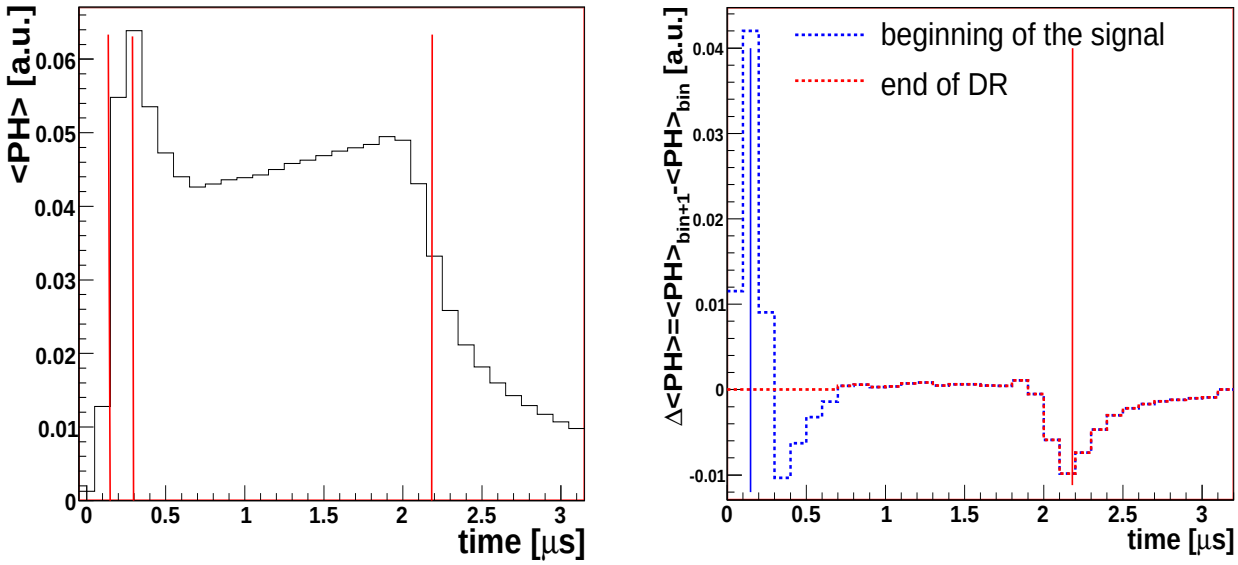

Figure 4.4: Determination of the times t_B, t_{AR} and t_{DR} with the *slope method* (see text for definition) Simulated average pulse height (left panel) and $\frac{d\langle PH \rangle}{dt}$ for simulated $\pi^{\pm}$ at 1 GeV.

	t_B [μs]	t_{AR} [μs]	t_{DR} [μs]	v_d [μs]	$(v_d^{rec}$-$v_d^{sim})/v_d^{sim}$ [%]
slope method	0.15	0.30	2.18	1.59	-1.5
fit	0.06	0.17	1.99	1.65	+2.5

Table 4.1: The different times (beginning, end of amplification region and end of drift region) found with the two different methods. The resulting drift velocity is also given together with its error.

The two methods are compared in Table 4.1. The *slope method* gives systematically larger times t_B, t_{AR} and t_{DR}, but the final reconstructed drift velocity is very similar.

$$v_{dE}\,(\mathrm{cm}/\mu\mathrm{s}) = \frac{d_{DR}}{t_{DR} - t_{AR}} = \frac{3\,(\mathrm{cm})}{(t_{DR} - t_{AR})(\mu\mathrm{s})} \tag{4.5}$$

For the calibration of the time-offset, the time t_B or t_{AR} can be used. Independently on the algorithm and chosen time, the reconstructed t_0 is always positive and shifted by a constant value compared to that used in the simulation. Thus the relative calibration of t_0 relies on the measured $\langle PH \rangle$, whereas the absolute value comes from the comparison with simulated $\langle PH \rangle$.

4.1.2 Calibration using simulated events

As for the relative gas gain calibration procedure, the drift velocity calibration algorithm has been tested with *pp* collisions at 14 TeV (B=0.5 T), for which the detector was *decalibrated*. Each chamber has a constant uniform drift velocity v_{dE} and time-offset t_0, but v_{dE} and t_0 follow a Gaussian distribution around 1.5 cm/μs and 1 tb, respectively. According to the expectations, the widths of the Gaussian are 10 % and 0.2 tb. After reconstruction of v_{dE} and t_0 from $\langle PH \rangle$, the values are compared with those used in the simulation. The accuracy and stability of the procedure have been evaluated with the σ of the $\Delta v_{dE}/v_{dE}$=(v_{dE}^{rec}-v_{dE}^{sim})/v_{dE}^{sim} and Δt_0=(t_0^{rec}-t_0^{sim}) distributions and the maximum deviations Max[$\Delta v_{dE}/v_{dE}$] and Max[Δt_0].

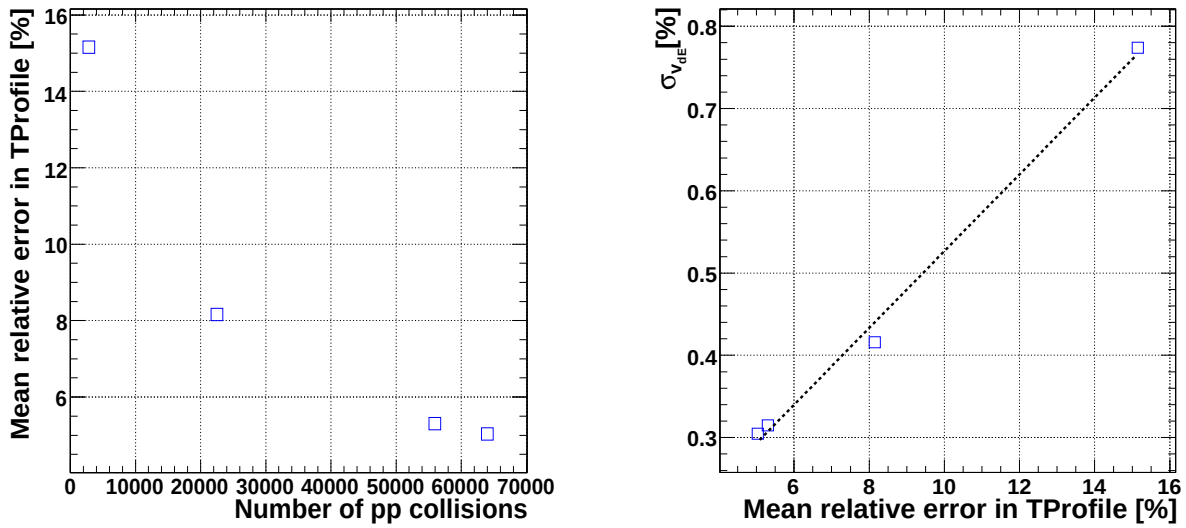

Figure 4.5: Left panel: mean statistical error in the average pulse height as a function of the number of *pp* collisions accumulated. Right panel: relative error of the extracted drift velocity as a function of the statistical error in the average pulse height.

It was found in the simulations, that $\sigma_{v_{dE}}$ scales approximately linearly with the mean relative error in $\langle PH \rangle$ (see Fig. 4.5). Since the signal amplitude is characterized by large event-by-event fluctuations, one has first to accumulate a certain statistics before the average pulse height looks like the typical $\langle PH \rangle$ shown in Fig. 4.3 for simulated data. The mean relative error in $\langle PH \rangle$ is the statistical error of each bin averaged over all the timebins. It decreases with the number of *pp* collisions used in the calibration. Assuming no statistical error, the extrapolated lower limit of σ_{vdE} is about 0.06 %. Already with 3100 *pp* collisions, $\sigma_{v_{dE}}$ is below the goal accuracy

of 1 %. It has to be nevertheless stressed out that in the simulation the noise is modelled by a Gaussian distribution of width 1.2 ADC counts. In reality the width is even smaller (see next chapter) but correlated noise and data corruption can constitute a serious problem.

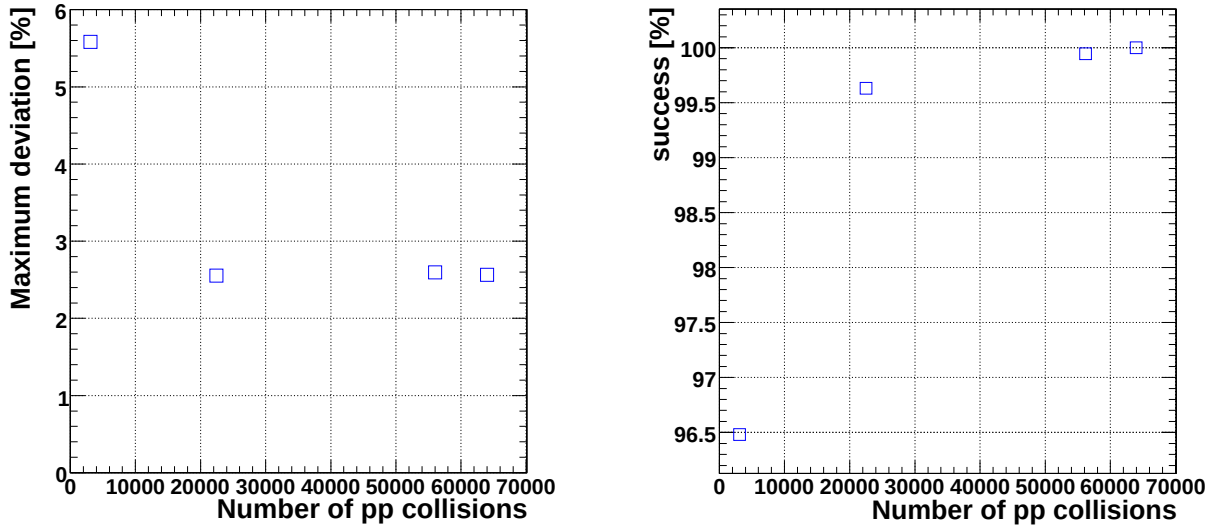

Figure 4.6: Maximum deviation of the extracted v_{dE} (left panel) and percentage of successful fits (right panel) as a function of the number of pp collisions accumulated.

The left panel of Fig. 4.6 shows the maximum deviation of the reconstructed v_{dE} with respect to the simulated value as a function of N_{pp}. A saturation is observed at Max$[\Delta v_{dE}/v_{dE}]\approx$2.5 %. The number of successful fits increases with N_{pp} to achieve 100 % for 64000 pp collisions (right panel of Fig. 4.6). However the upper limit of 100 % is reached only in the best conditions, when the total number of timebins is large enough so that the tail of $\langle PH \rangle$ is always contained in the measurement. A simple calculation allows to estimate the minimum number of timebins required to be able to calibrate all the chambers for a given drift velocity distribution. From simulations, the amplification peak was found to be at about 2.7 tb for t_0=0 tb. The signal is then contained in $(2.7+\frac{d_{DR}}{v_{dE}})$ tb. At least one timebin is needed after $tbin_{DR}$ for the extrapolation procedure. The minimum number of timebins is therefore about 25 tb for v_{dE}=1.35 cm/μs.

For a calibration of t_0 using t_B, σ_{t_0} and Max$[\Delta t_0]$ are shown in Fig. 4.7. The variable σ_{t_0} saturates at about 0.02 tb, the wished accuracy, whereas Max$[\Delta t_0]$ decreases up to 0.12 tb. In the simulations, better results are obtained with t_B than with t_{AR}, which leads to a minimum σ_{t_0} of 0.07 tb. The maximum positive peak of $\frac{d\langle PH \rangle}{dt}$ is sharper than the maximum peak of $\langle PH \rangle$.

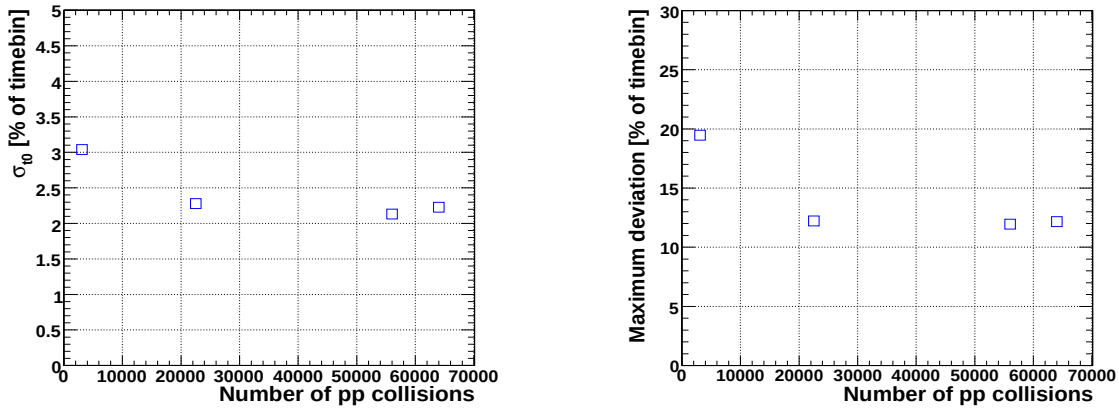

Figure 4.7: Relative error (left panel) and maximum deviation (right panel) of the extracted t_0 as a function of the number of pp collisions accumulated.

4.1.3 Calibration using the Test-beam 2007 data

The v_{dE} and t_0 calibration procedure was tested on test-beam data acquired in 2007. The average pulse heights of e^- and π^- of momentum 4 GeV/c are shown in Fig. 4.8 for the six planes of the stack exposed to the beam (B=0 T and v_d=v_{dE}).

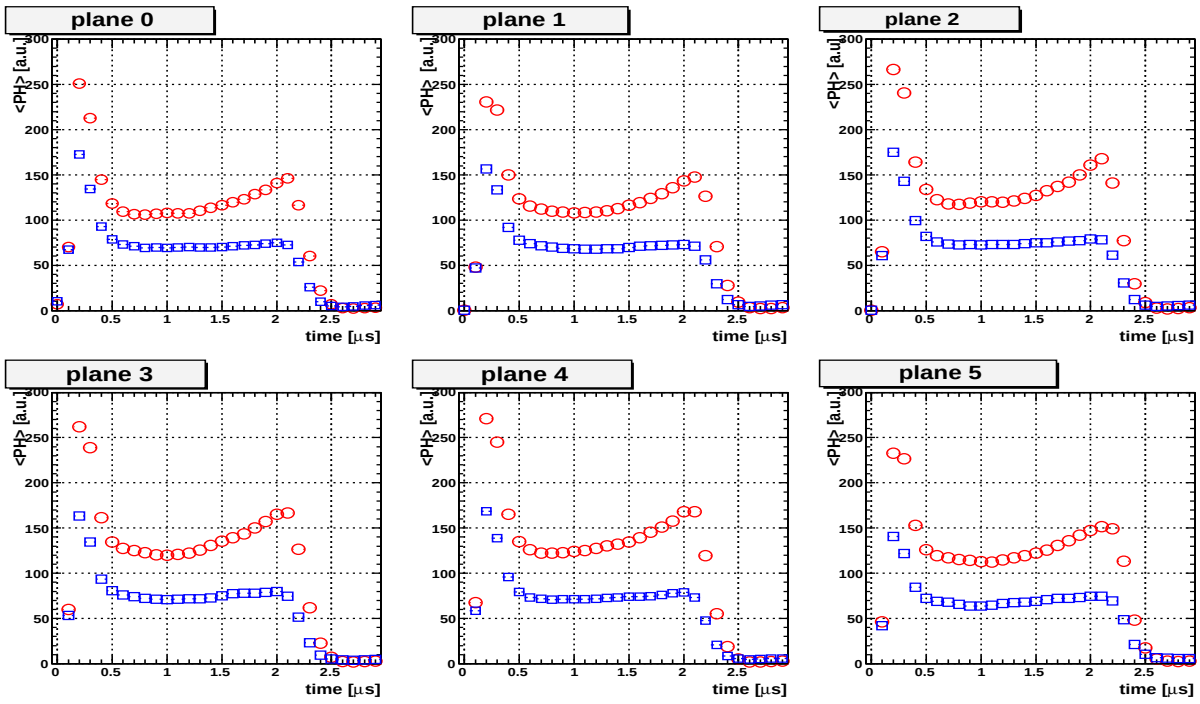

Figure 4.8: Average pulse height of pions and electrons with momentum 4 GeV/c in the 6 planes of the stack. Tail cancellation was performed at reconstruction.

Like before, exactly one reconstructed particle per event is required and each tracklet is required to have between 20 and 25 clusters. Due to the absorption of TR photons

at the entrance of the gas volume, the e^- $\langle PH \rangle$ presents a second peak at the end of the drift region. Only π^- are used for the calibration of v_d, whereas e^- can also help to determine t_0.

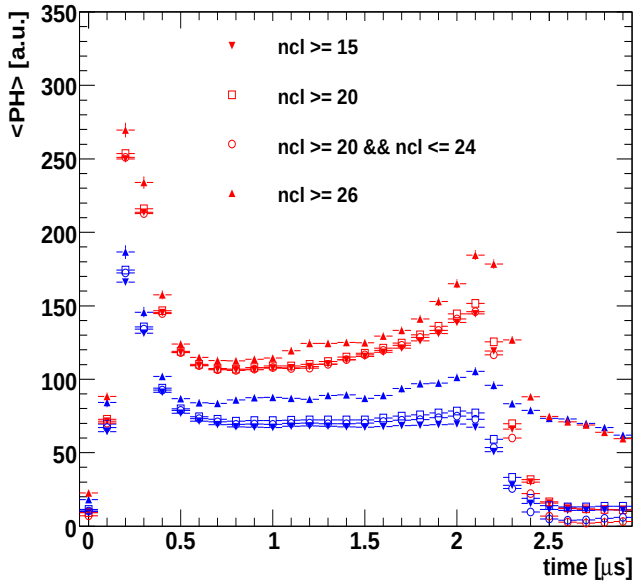

Figure 4.9: Average pulse height of pions and electrons (4 GeV/c) with different cuts on the number of clusters attached to the track.

The effect of the cut on the number of clusters attached to the track has been evaluated in Fig. 4.9. The distribution of the number of clusters attached to tracks was first shown in Fig. 3.9. Tracks with more than 26 clusters have a large tail in $\langle PH \rangle$, suggesting the presence of some noisy pads or multiple tracks. The exclusion of tracks with more than 25 clusters allows to come back to the expected baseline value null at the end of $\langle PH \rangle$. The differences are otherwise not so important.

The extracted v_d and t_0 are plotted as a function of the plane number in Fig. 4.10. The chambers were filled with a mixture of Xe 83 % and CO_2 17 %. As for the gas gain, they were adjusted to have approximately the same drift velocity in each chamber. The resulting drift field (in case of a perfect drift region of 3 m) is between 0.62 V/cm and 0.68 V/cm (Table 4.2).

Plane number	0	1	2	3	4	5
$-U_d$ [kV]	1.86	1.96	1.90	2.03	1.90	1.93
E [kV/cm]	0.62	0.65	0.63	0.68	0.63	0.64

Table 4.2: Drift voltages and fields in the six planes of the stack.

From GARFIELD simulations, the expected v_d should be comprised between 1.254 cm/μs and 1.536 cm/μs for Xe/CO_2 (85 %/15 %). Since the amount of CO_2 was slightly larger than 15 %,

v_d should be a little bit smaller. The found values of about 1.48 cm/μs lies in the expected range, even if no obvious correlation between U_d and v_d can be seen.

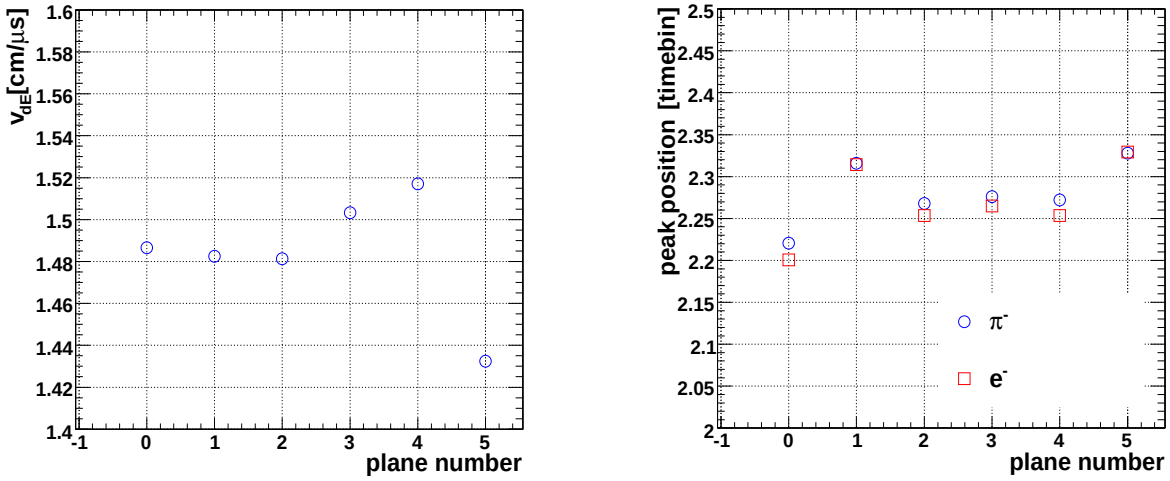

Figure 4.10: Drift velocities (left panel) and time-offsets (right panel). The drift velocities are extracted from the π^- average pulse heights, whereas the time-offsets can be determined by the π^- or e^- average pulse heights

The position of the beam in the chambers is shown in Fig. 4.11 in the z direction (Row) and $r\phi$ direction (column) in the ALICE global coordinates. Since the beam is spread over at least 3 pad columns (≈1.9 cm), the unisochronity can not be responsible for the differences in extracted v_d. Thus local deformations or wire imperfections of the chambers are the most probable candidates.
In the right panel of Fig. 4.10, on can see the position of the amplification peak for the e^- and π^- $\langle PH \rangle$ in the 6 planes. The reconstructed t_0 is systematically smaller with e^- by up to 0.02 tb. This is at the limit of the desired accuracy. The reason is related to the TRF, which leads to an asymmetric amplification peak. Due to the larger signal for e^-, the asymmetry is more pronounced, shifting the extrapolated peak position to smaller values. The overall observed t_0 variations are smaller than the expectations: about 0.1 tb.
Finally the relative gas gain calibrated $\langle PH \rangle$ are shown in Fig. 4.12. Since the calibration was done with π^-, the heights of the drift amplification plateau are identical. One recognizes clearly the chamber (at plane 5) with a smaller drift velocity. For e^-, the amplitudes of $\langle PH \rangle$ are in the plane number order. Bremsstrahlung in the detector material and TR in the radiator result in a small correlation between the deposited energies in the different planes. Photons, that are produced in one plane, have a certain probability to propagate up to the next plane and be absorbed in the gas volume. Due to this effect, the $\langle PH \rangle$ shows an increase with the plane number.

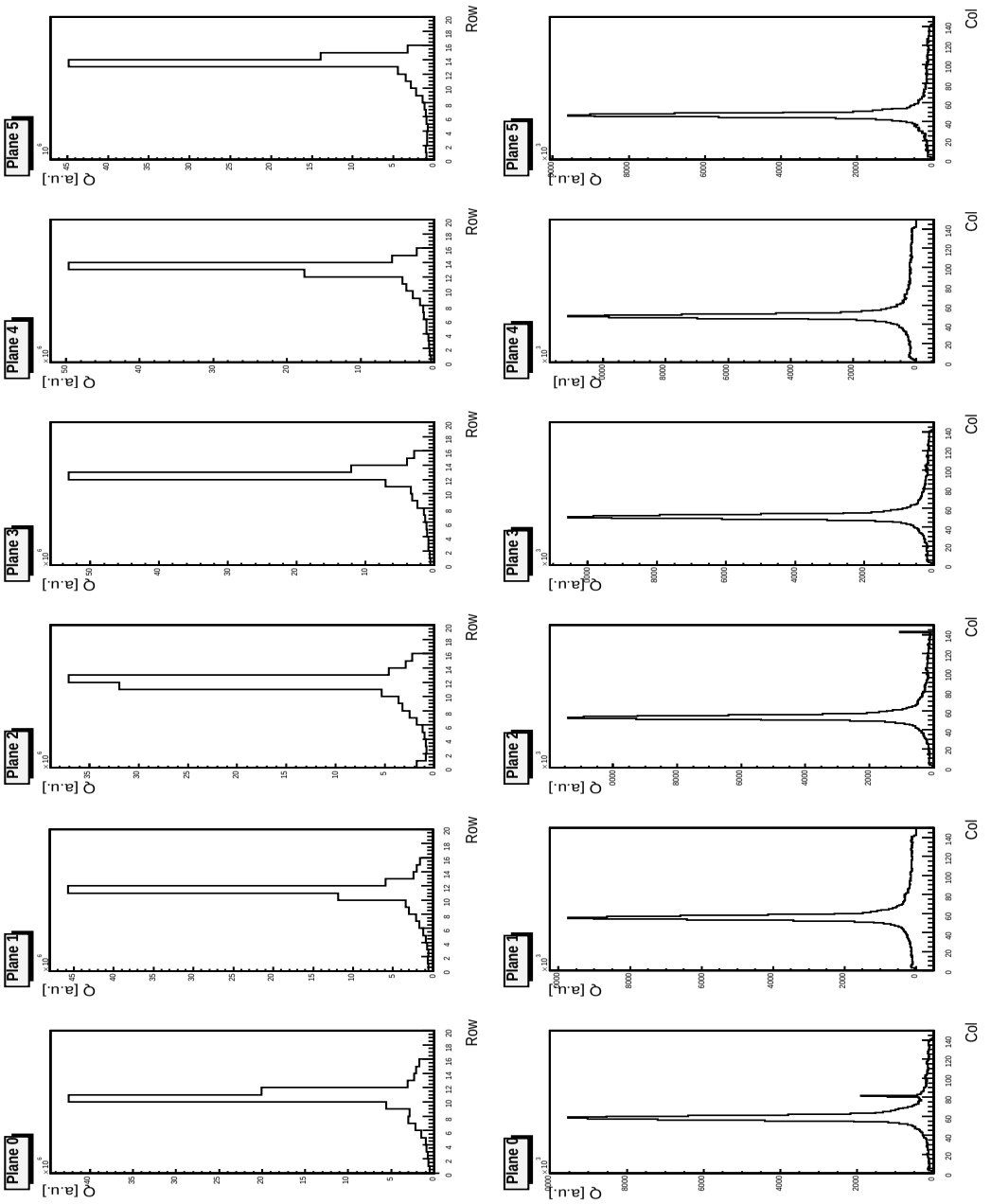

Figure 4.11: Integrated deposited charge as a function of the pad row (upper panel) and pad column (lower panel) in the 5 plane. The position of the beam can be clearly identified.

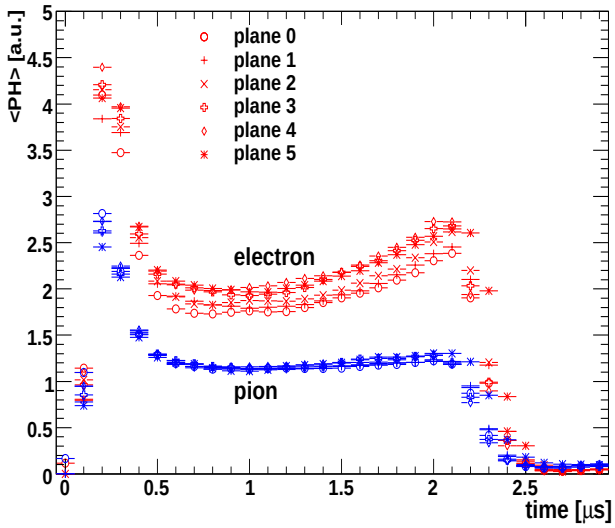

Figure 4.12: Comparison of the π^- and e^- average pulse heights of the 6 planes after gain calibration.

The average pulse height is very useful for monitoring, since some problems like space charge or electron attachment can be easily recognized. For instance, after reducing the overpressure in the supermodule from 0.4 mb to 0 mb, the $\langle PH \rangle$ showed electron attachment in plane 5 (see Fig. 4.13). The reason was a gas leak in the vicinity of this plane. The leak amounted to 17 l/h at an overpressure of 0.2 mb and 30 l/h at 0.4 mb, which is a lot given the price of Xe on the market. During the test-beam, a small overpressure was kept to avoid electron attachment and the supermodule was repaired afterwards.

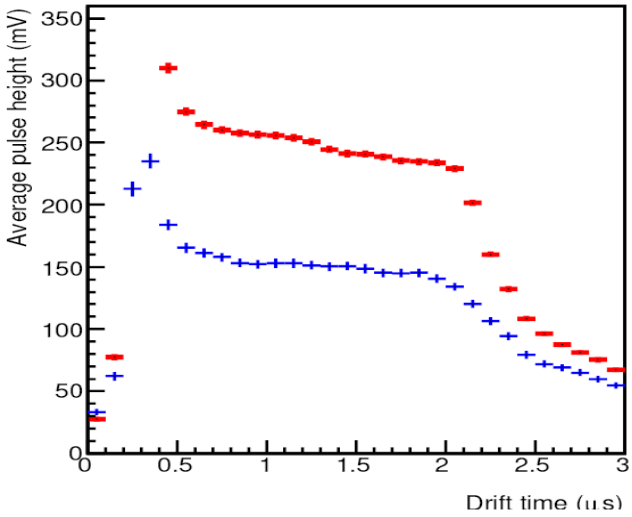

Figure 4.13: $\langle PH \rangle$ for plane 5 showing attachment after one hour running at 0 overpressure.

4.1.4 Calibration using the Test-beam 2004 data

In 2004, six final chambers built in Heidelberg were already tested with π^-/e^- beams of 1 GeV/c to 10 GeV/c at CERN (B=0 T and v_{dE}=v_d). The gas mixture used was composed of Xe (85 %) and CO_2 (15 %). The drift velocity was measured during a momentum scan (see Table 4.3).

Run number	425	426	428	429
Beam momentum [GeV/c]	10	8	6	4
T [°C]	18.1	18.0	17.6	18.1
P [mb]	964	964	964	962

Table 4.3: Momentum scan from run 425 to 429.

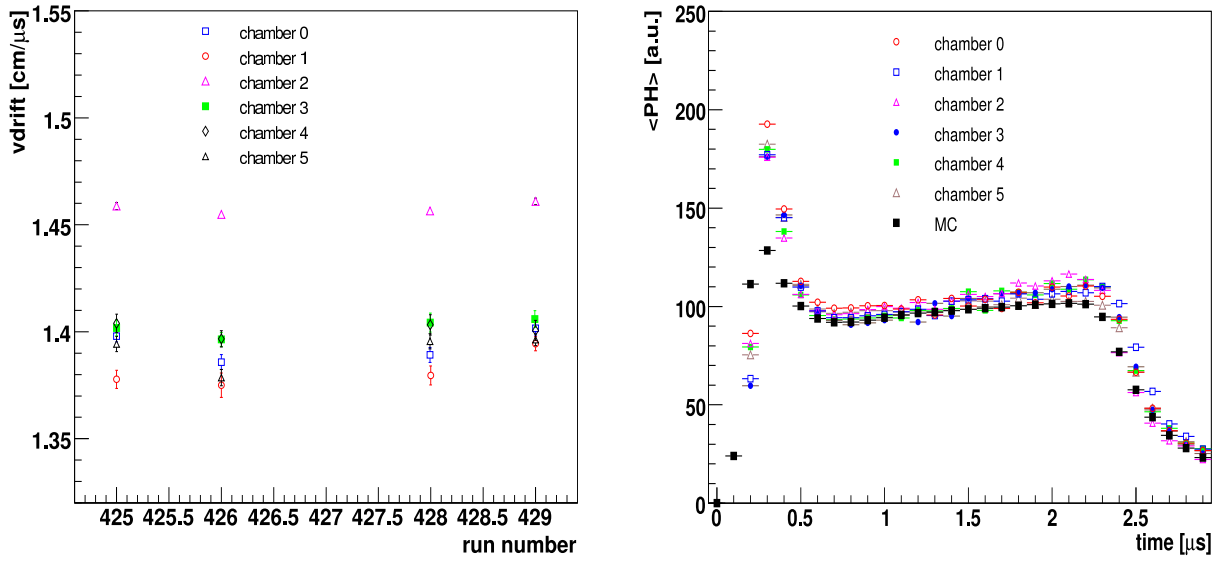

Figure 4.14: Left panel: drift velocities of the chambers for different runs. Right panel: comparison of the π^- average pulse heights at 10 GeV/c (run 425) of the different chambers and simulations (MC) done with v_d=1.4 cm/μs.

In the left panel of Fig. 4.14, v_d is plotted as a function of the run number of the six chambers. No tracking was applied but a simple algorithm looking for maxima was used. One chamber presents a larger reconstructed drift velocity, even through its drift voltage is smaller than for some other chambers (see Table 4.4).

Due to the smaller values of U_d (≈1.8 kV instead of 2.1 kV), the drift velocity is smaller than in the nominal conditions (≈1.4 cm/μs compared to 1.5 cm/μs). Qualitatively the decrease of v_d for the runs 425 and 426, and the runs 429 and 428, can be understood with the small variations of air temperature and pressure, as given in Table 4.3 corresponding to the beginning

Plane number	0	1	2	3	4	5
-U_d [kV]	1.85	1.80	1.80	1.85	1.80	1.80

Table 4.4: Drift voltage of the different chambers.

of each run. The reconstructed drift velocity should follow the fluctuations of T/P.

The $\langle PH \rangle$ have been compared with simulations for π^- of 10 GeV/c in the right panel of Fig. 4.14. The position of the amplification peak has been used to *align* the signals. Unfortunately the simulations don't describe very well the amplification peak. The plateau of the drift region was also found more flat in the simulation than in the data. The reconstructed drift velocities make nevertheless sense.

4.1.5 Calibration using cosmic-ray data

Cosmic measurements with different drift voltages were performed with the SM 3 at IKP in Muenster. Four runs from 666 to 669, with a low drift velocity (U_d=1600 V, U_a=1500 V) can be compared to a run with a higher drift velocity (U_d=1900 V, U_a=1500 V, run 660). The left panel of Fig. 4.15 shows the ratio $N^{event}_{Nb_t>0}/N^{event}_{Total}$ for the low v_d runs (blue full squares) together with the value obtained for the high v_d run (red line) (B=0 T and v_{dE}=v_d).

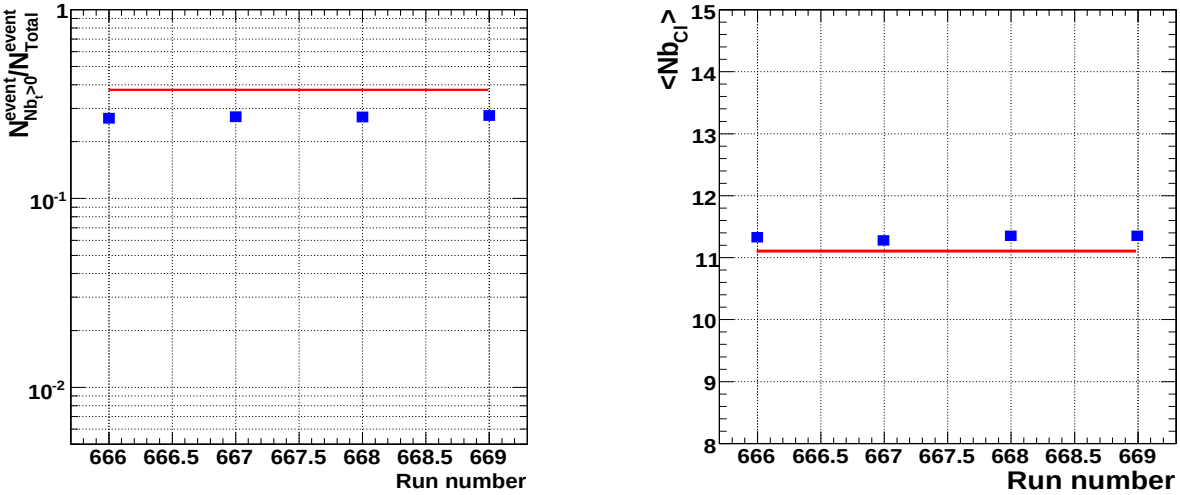

Figure 4.15: Fraction of events with at least one reconstructed track (left panel) and mean number of clusters attached to the tracklet for low (blue squared symbols) and high (red line) drift velocity runs.

The efficiency is smaller for low v_d, since the amplitude of the clusters decreases and the signal-to-noise ratio is consequently worse. The mean number of clusters attached to the tracklet should be on the contrary larger for low v_d, because the signal is spread over a longer

time interval. The effect is nevertheless very small (see right panel of Fig. 4.15). This could be due to the fact that the $\langle PH \rangle$ is truncated at the end for the low v_d runs.

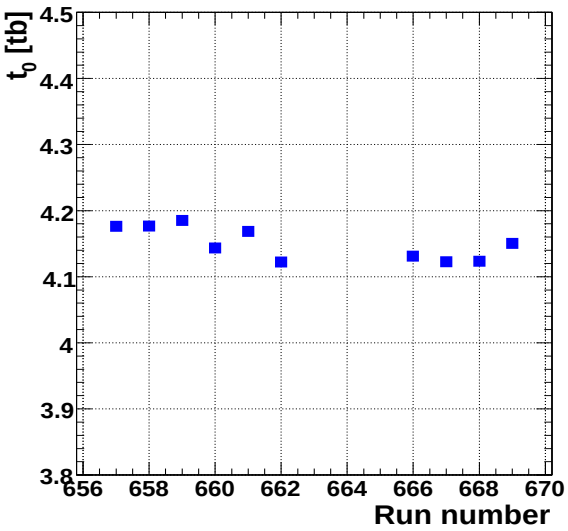

Figure 4.16: Time-offset as a function of the run number.

The noise in the presample region ($t \leq t_0$) and in the tail of the $\langle PH \rangle$ is too high in these data set to determine with accuracy automatically the drift velocity. Most of the time, the fit procedure fails and one has to tune it manually. Nevertheless v_d was found to be about 1.65 cm/μs for U_d=1900 V and around 1.37 cm/μs for U_d=1600 V. Since the tail of the $\langle PH \rangle$ was partially truncated for U_d=1600 V, the found value of v_d was first taken as an upper limit. The gas composition used was estimated to be (Ar/CO_2 (63 %/37 %)). For this gas mixture, drift velocities of the order of 1.3 cm/μs and 1.1 cm/μs are expected for U_d=1900 V and U_d=1600 V respectively, based on GARFIELD simulations. The extracted v_d are about 25 % above the expected values. The drift velocity is sensitive to the amount of CO_2 in the gas, which has a quite large uncertainty in the measurement [23]. The latter could be the reason of the discrepancy between simulated and extracted v_d.
The time-offset was evaluated with the peak of the amplification region in the $\langle PH \rangle$. Contrary to the drift velocity, t_0 should be constant over the runs taken with different drift voltage. The overall variations are indeed small below 0.1 tb (see Fig. 4.16).

4.2 The algorithm with global tracking

A second procedure was developed to measure the electron drift velocity in the gas. A good knowledge of the track angles is required. Therefore the combined tracking in the TPC and the TRD (global tracking) is mandatory.

4.2.1 Principle

The algorithm is based on the relation between the y-coordinate of the clusters and the drift velocity v_{dE}.

The y position of the clusters

The y position of a cluster can be reconstructed from the knowledge of the σ_{PRF}. Nevertheless it has to be corrected for the $E{\times}B$ effect and the tilting of the pads in the z direction.

$E{\times}B$ correction Due to the magnetic field perpendicular to the drift field **E**, the ionization electrons don't drift exactly in the direction of **E** but their drift velocity forms an angle α_L with the vector **E**. The Lorentz angle α_L leads to a biased reconstructed y position of the clusters along the track and thus a biased reconstructed ϕ angle of the track ($\phi{>}0$ and $\alpha_L{<}0$ in Fig. 4.17). The incident angle ϕ of the track is directly related to the y reconstructed position

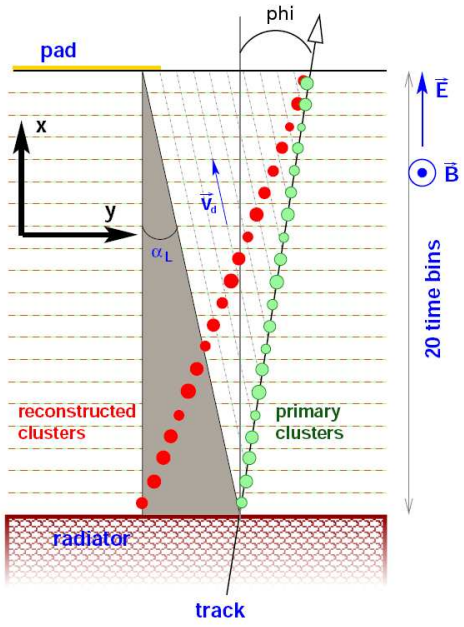

Figure 4.17: Fake angular reconstruction of the track due to the $E{\times}B$ effect.

of the clusters. The measured y cluster positions can be expressed as a function of the arrival time of the clusters t, the average drift velocity v_{dE} in the **E** direction, the time-offset t_0 and the angle ϕ of the track (with the convention of Fig. 4.17):

$$y_{measured} = y_0 - v_{dE} \cdot (t - t_0) \cdot \tan(\phi) \tag{4.6}$$

where y_0 is the position of the track at the end of the chamber (in the amplification region). With the magnetic field, this relation is not true anymore, and a correction term as to be added ($\alpha_L{<}0$ here):

$$y_{measured} = y_0 - v_{dE} \cdot (t - t_0) \cdot (\tan(\phi) - \tan(\alpha_L)) \tag{4.7}$$

Tilted Pads A correlation between the y and z positions of the clusters is moreover introduced due to the tilting of the pads:

$$y = y_{measured} + (z - z_{row}) \cdot \tan(\beta_{tilt}) \tag{4.8}$$

where y and t are the cluster position and its measured timebin, $\tan(\phi)$ the angle of the associated track. The value of $\tan(\phi)$ is taken from the parameters of the Kalman track associated to the cluster ($\sin(\phi)$). The constants z_{row} and $\tan(\beta_{tilt})$ are known from the pad row of the cluster and its chamber (β_{tilt}=$\pm 2°$).

Measurement of the drift velocity

The drift velocity is determined from the derivative dy/dt. For this purpose, the z position of the cluster is assumed to be linearly dependent on the x position of the track:

$$z = z_0 + \frac{dz}{dx} \cdot \frac{dx}{dt} \cdot (t - t_0) = z_0 - \frac{dz}{dx} \cdot v_{dE} \cdot (t - t_0) \tag{4.9}$$

The track position at the anode wire is (t_0,y_0,z_0). From Eq. 4.8, Eq. 4.7 and Eq. 4.9, one can deduce an expression of the derivative dy/dt:

$$\frac{dy}{dt} = -[\tan(\phi) + \tan(\beta_{tilt})\frac{dz}{dx}]v_{dE} + \tan(\alpha_L)v_{dE} \tag{4.10}$$

Since the position of the clusters are already corrected from the $E\times B$ effect with an assumed v_{dE}^{ideal} and $\tan(\alpha_L^{ideal})$, Eq. 4.11 becomes:

$$\frac{dy}{dt} = -[\tan(\phi) + \tan(\beta_{tilt})\frac{dz}{dx}]v_{dE} + \tan(\alpha_L)v_{dE} - \tan(\alpha_L^{ideal})v_{dE}^{ideal} \tag{4.11}$$

In this equation, the term $[\tan(\phi)+\tan(\beta_{tilt})\frac{dz}{dx}]$ depends on the Kalman track parameters $\sin(\phi)$ and dz/dl.

$$\tan(\phi) = \frac{\sin(\phi)}{\sqrt{1 - \sin^2(\phi)}} \tag{4.12}$$

$$\frac{dz}{dx} = \frac{dz}{dl}\frac{1}{\cos(\phi)} = \frac{dz}{dl}\frac{1}{\sqrt{1 - \sin^2(\phi)}} \tag{4.13}$$

All the other factors are calibration constants. Thus a linear fit of dy/dt as a function of $[\tan(\phi) + \tan(\beta_{tilt})\frac{dz}{dx}]$ allows to extract the drift velocity v_d and the $\tan(\alpha_L)$ as soon as the database used during the reconstruction is known ($\tan(\alpha_L^{ideal})v_{dE}^{ideal}$).
The variable $\tan(\alpha_L)$ will not be calibrated but will be directly computed from v_{dE}:

$$\tan(\alpha_L) = \mu B \approx \frac{v_{dE}^{eff}}{E} B \tag{4.14}$$

where μ is the electron mobility. The calibration procedures of the average drift velocity and σ_{PRF} (see next chapter) allow to check in two independent ways if the mean $\tan(\alpha_L)$ measured is consistent with the calculations.

4.2.2 Algorithm

The procedure is the following:

- For each tracklet, dy/dt is determined by a linear fit ($y{=}a_0 \cdot t + a_1$) of the (t,y) coordinates of the clusters. The fit is considered successful if the estimated error of the slope parameter ($E(a_0)$) is below an established value. The fit procedure returns a computed error of the fit parameters a_i determined by the so called covariance matrix V_{ij}:

$$(V^{-1})_{ij} = \frac{1}{2}\frac{\partial \chi^2}{\partial a_i \partial a_j} \tag{4.15}$$

  The diagonal elements V_{ii} correspond to the variances of a_i and the off-diagonal elements V_{ij} the covariance between a_i and a_j. Thus $E(a){=}\sqrt{\frac{1}{V_{00}^{-1}}}$. A upper threshold is applied on this variable.
  In a second calibration path, clusters can be excluded from the fit if they are calculated to be outside of the chamber borders.

- Onces dy/dt is computed, the point ($\Gamma{=}[\tan(\phi) + \tan(\beta_{tilt})\frac{dz}{dx}]$,$dy/dt$) is added in the two dimensional histograms of the corresponding chamber (see Fig. 4.18).

- After having accumulated enough *tracklet points*, the correlation between Γ and dy/dt is fitted for each chamber to extract its calibration constants v_{dE} and $\tan(\alpha_L)$. Here a cut on the $\sqrt{\frac{\chi^2}{ndf}}$ value of the linear fit is applied before finally filling a database with the found values. This time, ndf is the number of tracklets in the two dimensional histogram minus the two parameters of the linear fit.

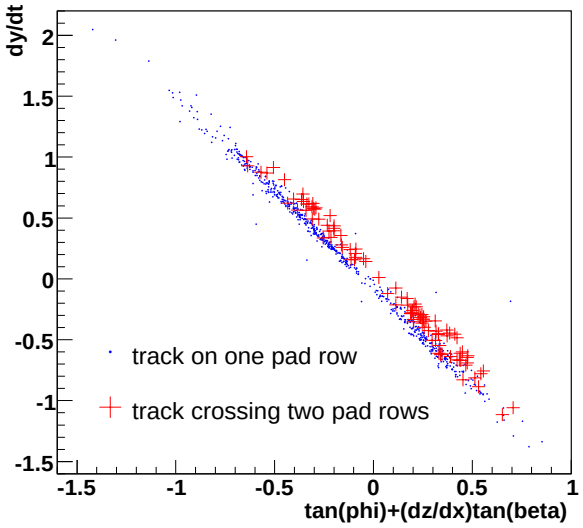

Figure 4.18: The correlation between dy/dt and $\tan(\phi)+(dz/dx)\tan(\beta_{tilt})$ for the reconstructed track in one chamber. The tracks crossing at least two pad rows are in red crosses and those crossing one pad row in blue points.

Not all tracklets are used. Beside the fact, that the cluster fit of the tracklet may be not successful, there are other conditions, for which a tracklet can be rejected:

- if some clusters belonging to the tracklet are masked (noisy pads or pads connected to the neighbor).
- if the tracklet crosses two pad rows. In this case, Eq. 4.8 is still true for each cluster but the variable z_{row} is not a constant anymore for the tracklet and changes at the crossing. Such tracklets can be easily recognized in the two dimensional histogram (Γ,dy/dt) as outliers (see Fig. 4.18). The number of tracklets crossing pad rows increases with θ and therefore the percentage of accepted tracks is slightly smaller for the stacks 0 and 4. Nevertheless for $p_T > 1\,\mathrm{GeV/c}$, this is a small effect ($\approx$5 %), since the maximal spread of the track in the z direction is for a straight track about $(d_{DR} + d_{AR})/\tan(\theta_{Max})$=3.7 cm and the pad length is 7.5-9 cm.

4.2.3 Results on simulated data

The procedure was tested on simulated pp collisions at 14 TeV with B=0.5 T, for which the chambers were decalibrated in the same way as before with a v_d Gaussian distribution ($\langle v_{dE} \rangle$=1.5 cm/μs and $\sigma_{v_{dE}}$=10 %).

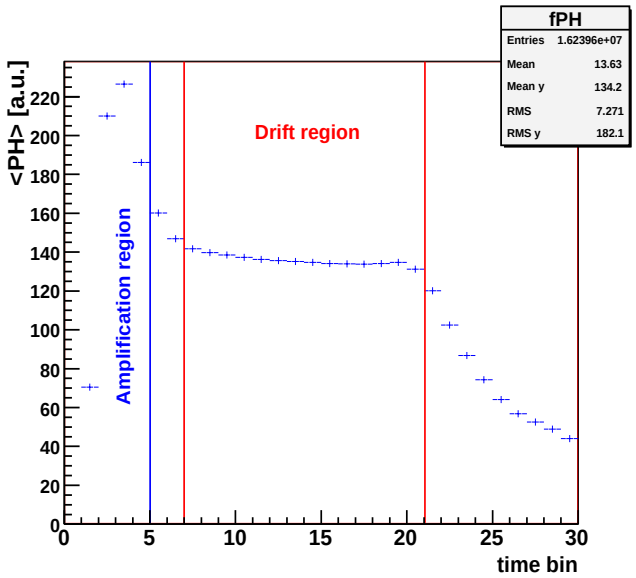

Figure 4.19: Average pulse height and limit of the definition in the amplification region and in the drift region.

The mean number of reconstructed tracks per chamber was in the order of 1000. Since the ionization electrons drift from both side of the anode wire plane in the amplification region, the amplitudes are added together and dy/dt doesn't depend linearly on t anymore. Moreover the drift velocity in the amplification region is not constant and is much higher than in the drift

region. In principle, it doesn't make sense to fit the (t,y) positions of the clusters in this region. To extract the physical drift velocity v_{dE} of the electrons in the drift region, the linear fit has to be performed with clusters belonging to this region only. However the drift velocity used in the tracking is a mean effective drift velocity, which includes clusters from the amplification region. That is why, the two regions are taken in the fit. To quantify the influence of the signal range in time, the extracted v_{dE} values were compared for a fit done with all the clusters attached to the tracklet and only clusters from the drift region. The drift region was defined as the region between timebin 7 and 21 (see Fig. 4.19).

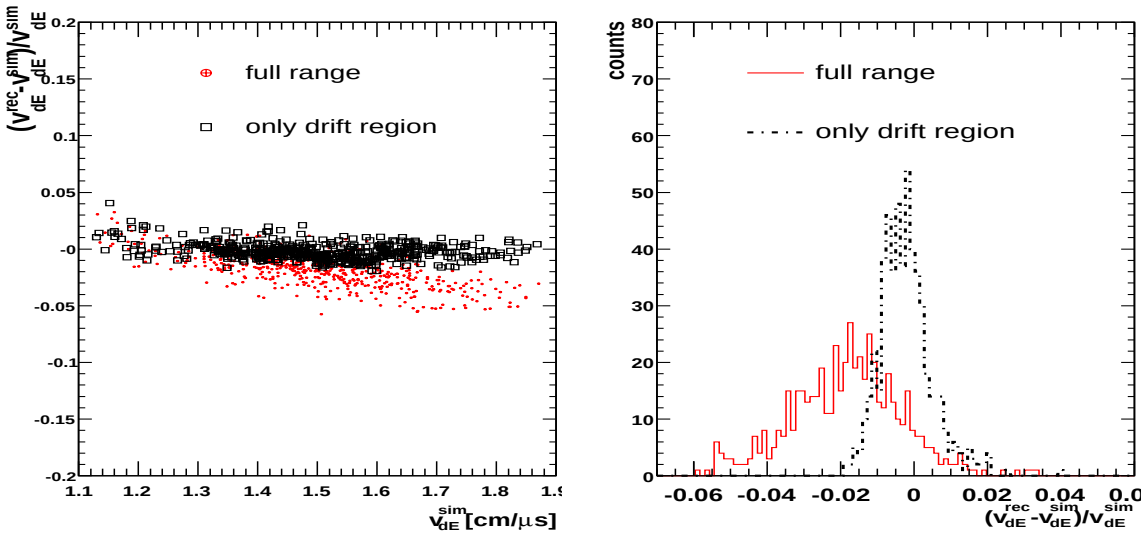

Figure 4.20: The $\Delta v_{dE}/v_{dE}$ distribution (right panel) and $\Delta v_{dE}/v_{dE}$ as a function of v_{dE}^{sim} for a track fit over the full range (30 tb) or only the drift region.

The right panel of Fig. 4.20 shows the $\Delta v_{dE}/v_{dE}$ distributions. With only the drift region, $\Delta v_{dE}/v_{dE}$ is centered at 0.0 and $\sigma_{v_{dE}}$≈0.61 %. For all the time range, the reconstructed drift velocity, v_{dE}^{rec}, is smaller than that simulated, v_{dE}^{sim}, by about 1.8 % and $\sigma_{v_{dE}}$≈1.5 %. The left panel of Fig. 4.20 shows that for high v_{dE}^{sim}, v_{dE}^{rec} is systematically smaller than expected, whereas for low v_{dE}^{sim} it is the contrary. The inclusion of all the clusters in the tracklet fit leads to the tendency to reconstruct a more uniform drift velocity over the chamber with an absolute mean value smaller than expected.

Since the procedure allows also to look at the $\tan(\alpha_L)$, the $\Delta\tan(\alpha_L)/\tan(\alpha_L)$ distributions are plotted in the right panel of Fig. 4.21. The sigma of the distribution (≈1.4 %) is quasi independent on the time range. Nevertheless the distribution is slightly shifted towards lower values in both cases but the shift is more important when the fit is performed over the full range (≈0.5 %).

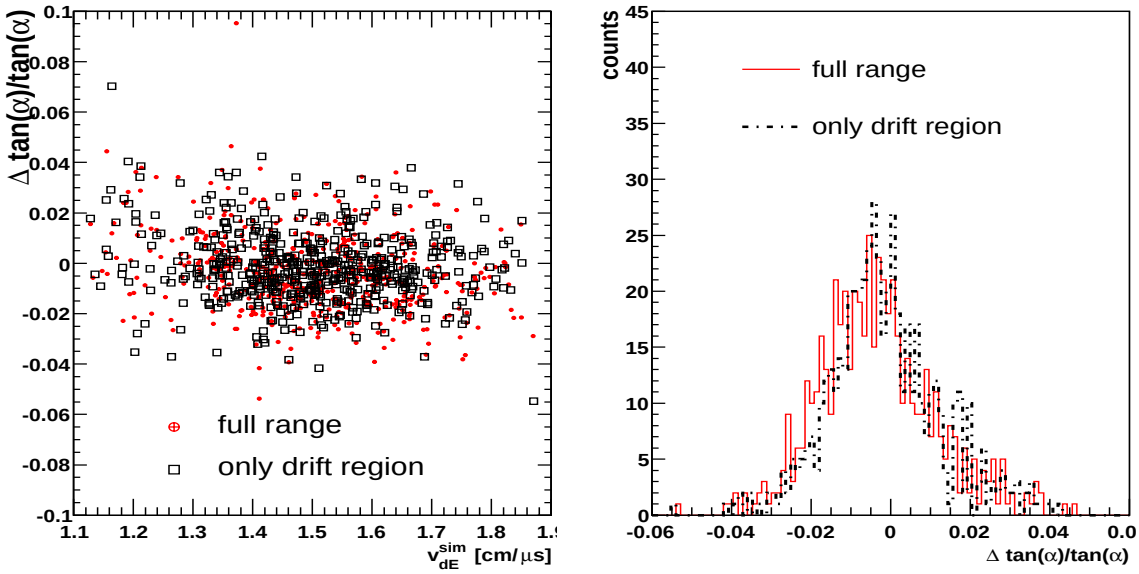

Figure 4.21: The $\Delta\tan(\alpha_L)/\tan(\alpha_L)$ distribution (right panel) and $\Delta\tan(\alpha_L)/\tan(\alpha_L)$ as a function of v_{dE}^{sim} for a track fit over the whole range or only over the drift region.

Chapter 5

The calibration of the Pad Response Function

The width of the Pad Response Function plays an important role in the reconstruction of the y position of the clusters. First it will be shown how from the sharing of the clusters charge and the ϕ track angle, the width of the PRF σ_{PRF} is measured. Then the performances of the algorithm will be illustrated with simulated pp collisions at 14 TeV.

5.1 Algorithm

The y position of the cluster has to be first determined independently on the width σ_{PRF}. The charge distribution of the cluster over the adjacent pads as a function of y corresponds then to the PRF. The width has to be nevertheless corrected from the effect of the TRF.

5.1.1 Independent determination of the y cluster coordinate

To reconstruct the distance y of a cluster to the middle of the central pad, one uses the signal amplitudes Q_{i-1}, Q_i and Q_{i+1} of the cluster on the readout pads $i-1$, i and $i+1$. There are three possibilities: by using the Center of Gravity (*CoG*) of the deposited cluster charge, by assuming a Gaussian PRF (*PRF1*), or by assuming a Gaussian PRF with a known width (*PRF2*). In AliRoot the last method is used together with a look up table to spare CPU time. The CoG method gives the worse position resolution. Assuming a Gaussian PRF, the pulse height are correlated to the y coordinate of the cluster by:

$$\frac{Q_{i-1}}{Q_{i-1}+Q_i+Q_{i+1}} = A\, e^{-\frac{(y+W))^2}{2\sigma^2_{PRF}}} \tag{5.1}$$

$$\frac{Q_{i}}{Q_{i-1}+Q_i+Q_{i+1}} = A\, e^{-\frac{y^2}{2\sigma^2_{PRF}}} \tag{5.2}$$

$$\frac{Q_{i+1}}{Q_{i-1}+Q_i+Q_{i+1}} = A\, e^{-\frac{(y-W)^2}{2\sigma^2_{PRF}}} \tag{5.3}$$

A is proportional to the total charge of the avalanche. To derive a measure of y independent on σ_{PRF}, we have first to calculate the ratios:

$$\frac{Q_i}{Q_{i-1}} = e^{\frac{2yW+W^2}{2\sigma^2_{PRF}}} \tag{5.4}$$

$$\frac{Q_{i+1}}{Q_i} = e^{\frac{2yW-W^2}{2\sigma^2_{PRF}}} \tag{5.5}$$

then the quantities:

$$\frac{Q_{i+1}}{Q_{i-1}} = e^{\frac{2yW}{\sigma^2_{PRF}}} \tag{5.6}$$

$$\frac{Q_i^2}{Q_{i-1}Q_{i+1}} = e^{\frac{W^2}{\sigma^2_{PRF}}} \tag{5.7}$$

and finally we can estimate the y position (*PRF1*):

$$y = \frac{W}{2}\frac{ln(\frac{Q_{i+1}}{Q_{i-1}})}{ln(\frac{Q_i^2}{Q_{i-1}Q_{i+1}})} \tag{5.8}$$

This formula can be used only for three pads clusters since it requires that Q_{i-1}, Q_i and Q_{i+1} are different from zero. Nevertheless it allows a calibration of σ_{PRF}, which can be extracted from a Gaussian fit of the Q_i/Q_{total} distribution (PRF) as a function of y.
Onces σ_{PRF} is calibrated, it can be used to determine y with a better resolution. With the signals on the pad $i-1$ and i:

$$y = \frac{\sigma^2_{PRF}}{W}ln(\frac{Q_i}{Q_{i-1}}) - \frac{W}{2} \tag{5.9}$$

or, alternatively, on the pads i and $i+1$:

$$y = \frac{\sigma^2_{PRF}}{W}ln(\frac{Q_{i+1}}{Q_i}) + \frac{W}{2} \tag{5.10}$$

The best results are obtained by a combination of these two measurements of y to a weighted average with weights w_1 and w_2:

$$y = \frac{1}{w_1+w_2}[w_1(-\frac{W}{2} + \frac{\sigma^2_{PRF}}{W}ln(\frac{Q_i}{Q_{i-1}})) + w_2(+\frac{W}{2} + \frac{\sigma^2_{PRF}}{W}ln(\frac{Q_{i+1}}{Q_i}))] \tag{5.11}$$

Since the measurement error is roughly inversely proportional to the recorded pulses on the readout pads, one uses as weights w_1=Q^2_{i-1} and w_2=Q^2_{i+1} for the *PRF2* method [14].

5.1.2 Systematic effect of the Time Response Function

The width σ_{PRF} is not directly measured by fitting the cluster charge distribution Q_i/Q_{total} as a function of y. The found σ^2 has to be first corrected from the ϕ angle effect, which comes from the Time Response Function (TRF). The response of a point-like charge absorbed in the drift region is spread in time due to the slow drift of the positive ions produced in the

avalanche. The time distribution is given by the TRF. Since the tail of the TRF is much longer (300 ns) than one time bin (100 ns), the signal of subsequent avalanches will be added, leading to a strong correlation between timebin measurements (clusters). For an inclined track, a large charge deposition due to Landau fluctuations or Transition Radiation absorption will pull away the position of the following clusters. This results in a deterioration of the reconstructed y positions of the following clusters. Thus the measured width of the clusters σ^2, is the quadratic sum of the PRF width and an angular term:

$$\sigma^2 = \sigma^2_{PRF} + k_1^2 \times \tan(\phi)^2 \tag{5.12}$$

With the presence of the magnetic field, the minimum width is found at the Lorentz angle α_L:

$$\sigma^2 = \sigma^2_{PRF} + k_1^2 \times (\tan(\phi) - \tan(\alpha_L))^2 \tag{5.13}$$

As a consequence, The measurement of σ^2 as a function of $\tan(\phi)$ allows to extract σ_{PRF}, k_1 and $\tan(\alpha_L)$.

5.1.3 Measurement of the Pad Response Function

The clusters are classified according to the $\tan(\phi)$ of their associated track and used to determine PRF(y).

$$\mathrm{PRF}(y) = \langle \frac{Q_i}{Q_{\mathrm{total}}} \rangle \tag{5.14}$$

where Q_{total}=$Q_{i-1} + Q_i + Q_{i+1}$. The PRF as a function of $\tan(\phi)$ are stored in a 2D profile for all the calibration groups. Fig. 5.1 shows one example of a such 2D profile.

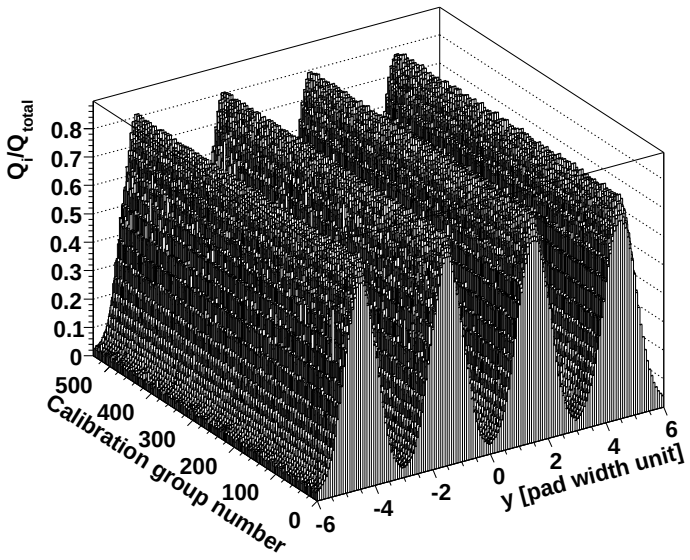

Figure 5.1: 2D profile containing the PRF distributions of each calibration group (here detector) as a function of $\tan(\phi)$ (see text for more explanations). These are simulated data.

One axis contains the *calibration group* numbers (calibration per detector here), whereas the variable plotted on the other axis is related to y. The example corresponds to four bins in $\tan(\phi)$ placed successively in the histogram.

Fits of the PRF(y) distributions allows to determine σ^2 as a function of $\tan(\phi)$ for each group. The relation .5.13 is then used to determine σ_{PRF}. Therefore the algorithm is composed of the following steps:

- The y positions of the three pad clusters attached to the tracklet are fitted by a straight line. The linear fit allows to extrapolate a y position for the two pad clusters, for which Eq.5.8 can not be used. Tracklets with less than 5 associated three pad clusters are rejected. The clusters are required to be in the drift region, since in the amplitude region there is a superposition of clusters coming from both sides of the anode wire plane.

- Onces the y positions are extrapolated for the two pad clusters, the PRF(y) of the tracklet $\tan(\phi)$ bin is updated. Each cluster belonging to the tracklet provides three measurements ((-y-1), ($Q_{i-1}/(Q_{total})$)), (y, ($Q_i/(Q_{total})$)), ((1-y), ($Q_{i+1}/(Q_{total})$)) used for the computation of the average PRF(y) in the range $y \in$ [-1.5,1.5]. The number of $\tan(\phi)$ bins 0.2 wide can be chosen between 1 and 8. For 8 bins, σ is measured from $\tan(\phi)$= -0.8 to 0.8. This is the best case but needs a large amount of accumulated *pp* collisions, because most of the tracklets are such that $\tan(\phi)\approx 0$. Low momentum tracks provide the main source of statistics above $|\tan(\phi)|>0.2$.

- For each $\tan(\phi)$ bin, σ is determined by a Gaussian fit of PRF(y).

- The dependence of σ^2 on $\tan(\phi)$ is finally fitted by a polynomial of a second degree. The width σ_{PRF} corresponds to the minimum.

A lot of Gaussian fits have to be performed. For a calibration per chamber and 8 $\tan(\phi)$ bins, 4320 fits are required. The Minuit package in ROOT finds the best fit parameters by minimizing the χ^2, which can be time-consuming. In the case of functions linear in their fit parameters:

$$g(y) = a_1 g_1(y) + \cdots + a_n g_n(y) \tag{5.15}$$

the problem can be solved analytically by inversion of a matrix. The convergence is then guaranteed and no starting values are needed. Since the Gaussian Minuit fits are practically always successful, the last mentioned points are not particularly crucial. The principal advantage of a linear fit to determine σ is the substantial increase in speed in comparison to non-linear techniques. Instead of fitting PRF(y) with a Gaussian:

$$PRF(y) = \frac{1}{\sqrt{2\pi\sigma^2}} \exp(-\frac{(y-b)^2}{2\sigma^2}) \tag{5.16}$$

where b should be found consistent with 0.0, the logarithm $\ln(f(y))$ is fitted with a polynomial of a second degree, $a_0+a_1y+a_2y^2$. The width σ can be then computed according to:

$$\sigma = -\frac{1}{\sqrt{2 \cdot a_2}} \tag{5.17}$$

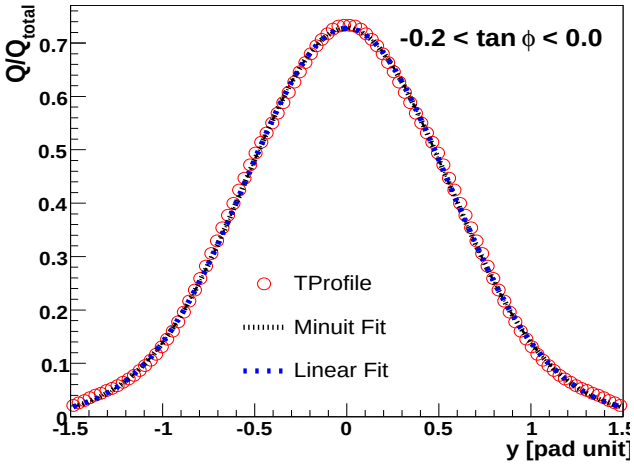

Figure 5.2: Comparison of a Minuit Gaussian fit based on the minimalization of χ^2 and a linear fit of the PRF for simulated pp collisions at 14 TeV.

Fig. 5.2 shows a comparison of the two methods for simulated pp collisions at 14 TeV. The Minuit fit is plotted together with the linear fit. The curves are identical.

5.2 Results on simulated data

The algorithm was tested on simulated pp collisions at 14 TeV with B=0.5 T. The two steps, the straight line fit of the three pad clusters attached to the tracklet and the final polynomial fit, were studied in detail.

5.2.1 The straight line fit of the tracklet

The y position resolution is characterized by the residual Δy: the distance between the position of the reconstructed three-pad cluster computed with Eq.5.8 and the fit result.

The width σ_y=$\sigma(\Delta y)$ should fulfill the equation:

$$\sigma_y^2 = \sigma_0^2 + (\tan(\phi) - \tan(\alpha_L))^2 \cdot k_0^2 \tag{5.18}$$

where σ_0 is the intrinsic y resolution due to electronic noise and k_0 corresponds to the convolution of the TRF and the unisochronity effects for non zero inclination angles.
In the left panel of Fig. 5.3, the charge distribution of the clusters is shown. Clusters with small amplitudes are more affected by the electronic noise, which is simulated with a Gaussian shape of width 1.2 ADC counts. To study its contribution in σ_y, a minimum cut on the total cluster charge Q_{cl} was required at 55 ADC counts (30 % of the clusters are rejected), 83 ADC counts (50 %), 101 ADC counts (60 %) or 129 ADC counts (70 %). The three last cases (blue lines) rejecting 80 %, 90 % and 95 % of the clusters suffered from

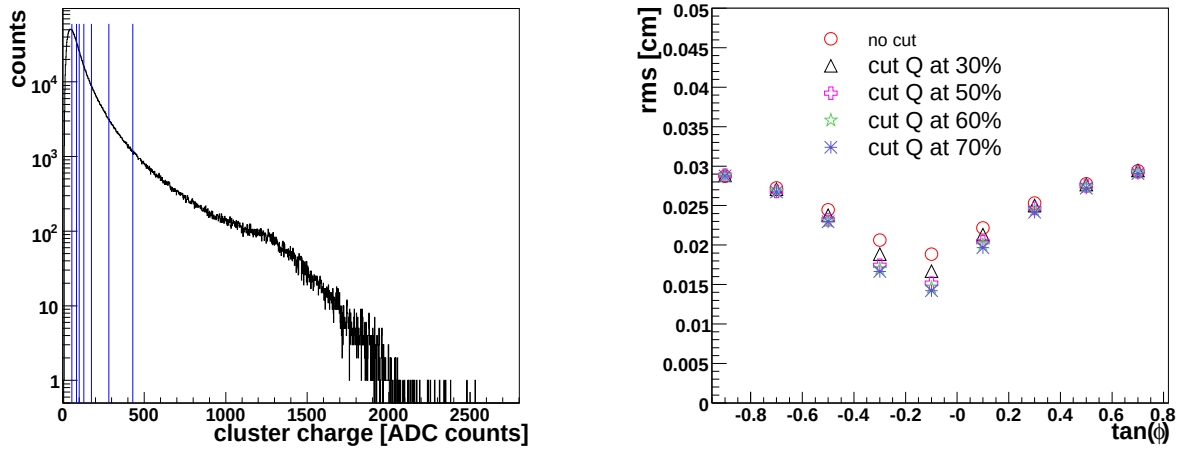

Figure 5.3: Left panel: cluster charge Q_{cl} distribution and low Q_{cl} cuts (blue lines) for which 30 %, 50 %, 60 %, 70 %, 80 %, 90 % and 95 % of the clusters are rejected. Right panel: width of the residual Δ_y (see text) as a function of tan(ϕ) for different low Q_{cl} cuts.

lack of statistics. In the right panel of Fig. 5.3, σ_y is plotted as a function of tan(ϕ). The behavior of σ_y at large tan(ϕ) is not influenced by the Q_{cl} cut, as the angular term (tan(ϕ)-tan(α_L))$^2\cdot$ k_0^2 in Eq. 5.18 becomes namely dominant. An increase of the Q_{cl} low cut reduces σ_0 only for angles around α_L (corresponding to drift parallel to **E**), but the effect is rather small.

Fig. 5.4 shows the y distributions for all the clusters (full line), three pad clusters (dashed line) and two pad clusters (points) in different tan(ϕ) bins. The three pad clusters are mostly populating the region around y=0.0 and the equivalent regions around -1 (-y-1) and 1 (1-y). Without two pad clusters, the measured PRF(y) presents holes around -0.5 and 0.5. Only for zero-inclination tracks (tan(ϕ)=tan(α_L)≈-0.17 corresponding to B=0.5 T), the statistics is still poor in this region after including the two pad clusters. The y distributions of two and three pad clusters are not symmetric for large tan(ϕ) due to the following reasons:

- A three pad cluster with a charge amplitude will bias the following two pad clusters. For tan(ϕ)>0.0, y is more populated in the negative values. For tan(ϕ)<0.0, y is more populated in the positive values.

- For tan(ϕ)>0.0, the three pad clusters with $y \in$ [-0.5, 0.0] are followed in time by two pad clusters, so that Landau fluctuations don't influence the y distribution of three pad clusters. On the contrary, those with $y \in$ [0.0, 0.5] shift the following three pad clusters towards positive y. Thus more three pad clusters with $y \in$ [0.0, 0.5] are found.

The sum of the two effects gives a symmetric y distribution.

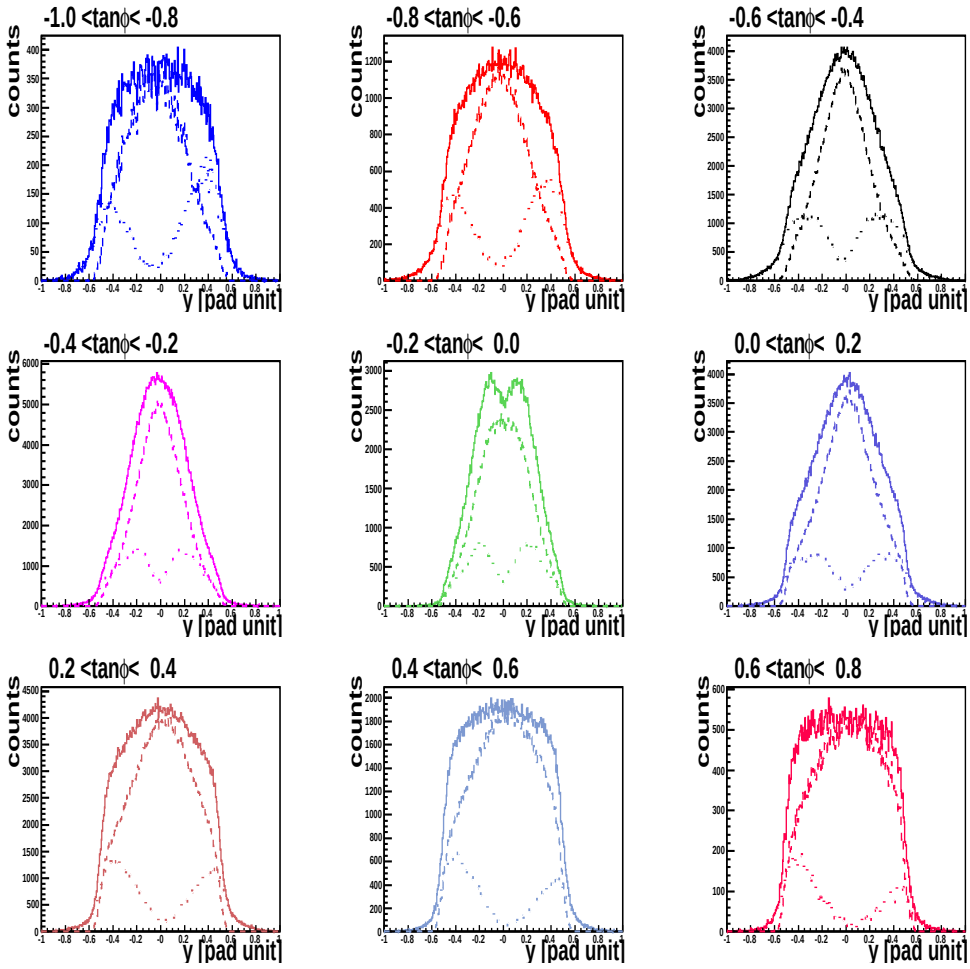

Figure 5.4: y distributions of three (dashed line) and two (dotted line) pad clusters, together with the sum (full line) for different tan(ϕ) bins.

5.2.2 The width of the PRF

Fig. 5.5 shows σ^2 as a function of tan(ϕ) after the Gaussian fits of PRF(y) for each tan(ϕ) bin. For chambers within a plane, the statistics has been added. The width σ depends on tan(ϕ) according to Eq. 5.13 and the plane dependence arises, since the pads have an increasing width W with the plane number. The variable σ_{PRF} is larger.

The angle factor k_1=σ_x was found to be of the order of 2 mm (see left panel of Fig. 5.6). Its value rises slightly with the low Q_{cl} cut, since for clusters with larger deposited charge, the correlation between timebins is higher due to the TRF. From the minimum of the σ^2 versus $tan(\phi)$ distributions, the tan(α_L) can be extracted. The chambers were nevertheless decalibrated so that the 10 % variations of the drift velocity leads to a certain uncertainty band of tan(α_L). This is represented with two horizontal blue lines (10 % v_d) and a red line (v_d=1.5 cm/μs). The reconstructed tan(α_L) lie within the band and doesn't depend on the low Q_{cl} cut.

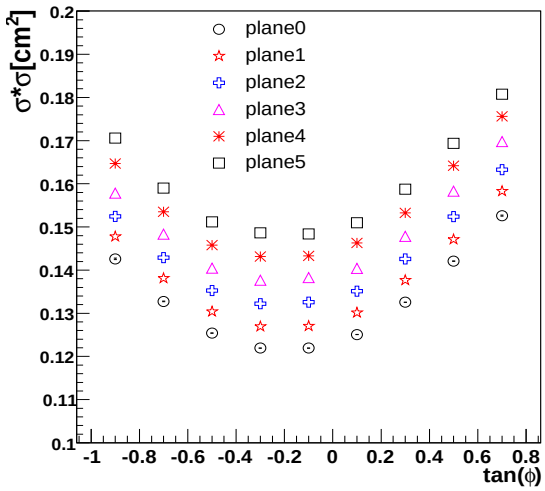

Figure 5.5: The width σ^2 of the cluster charge spread distribution as a function of tan(ϕ) for the six planes of the TRD.

The found σ_{PRF} were compared to the values used in the simulations. To reproduce the detector response in simulation, the total charge of an avalanche is spread over three pads i-1, i and i+1 in the column (y) direction using the PRF$_{sim}$:

$$Q_{i-1} = PRF_{sim}(-(y+1)) \cdot Q_{total} \tag{5.19}$$

$$Q_i = PRF_{sim}(y) \cdot Q_{total} \tag{5.20}$$

$$Q_{i+1} = PRF_{sim}(1-y) \cdot Q_{total} \tag{5.21}$$

In the PRF algorithm we assume that the total induced charge is distributed only over three pads:

$$(PRF(-(y+1)) + PRF(y) + PRF(1-y)) = 1.0 \tag{5.22}$$

This is not exactly true according to the PRF used in the simulation:

$$(PRF_{sim}(-(y+1)) + PRF_{sim}(y) + PRF_{sim}(1-y)) \leq 1.0 \tag{5.23}$$

The resulting effect on the reconstructed $PRF(y)$ can be seen in the left panel of Fig. 5.7. For the tan(ϕ) bin corresponding to the minimum σ, PRF$_{rec}(y)$=PRF$_{sim}(y)$/(PRF$_{sim}(-y-1)$+PRF$_{sim}(y)$+PRF$_{sim}(1-y)$) is compared to PRF$_{sim}(y)$. The function PRF$_{rec}(y)$ has a higher peak and bigger width than PRF$_{sim}(y)$. This effect can nevertheless not explain the wider PRF(y) found after complete reconstruction.

In the right panel of Fig. 5.7 $\sigma_{PRF_{sim}}$ and $\sigma_{PRF_{rec}}$ are called *database direct* and *database reconstructed*. Their values are plotted together with the extracted σ^{rec}_{PRF} for different low Q_{cl} cuts as a function of the plane number. For more than 30 % rejected clusters, σ^{rec}_{PRF} saturates at a value about 2 % above $\sigma_{PRF_{rec}}$. This last systematic discrepancy is still under investigation. It was checked that beside the 2 % shift, the relative error on σ^{rec}_{PRF}, $\Delta\sigma_{PRF}$=(σ^{rec}_{PRF}-$\sigma_{PRF_{rec}}$)/$\sigma_{PRF_{rec}}$, has a width of less than 0.6 % for about 1000 tracks per calibration groups (here chambers).

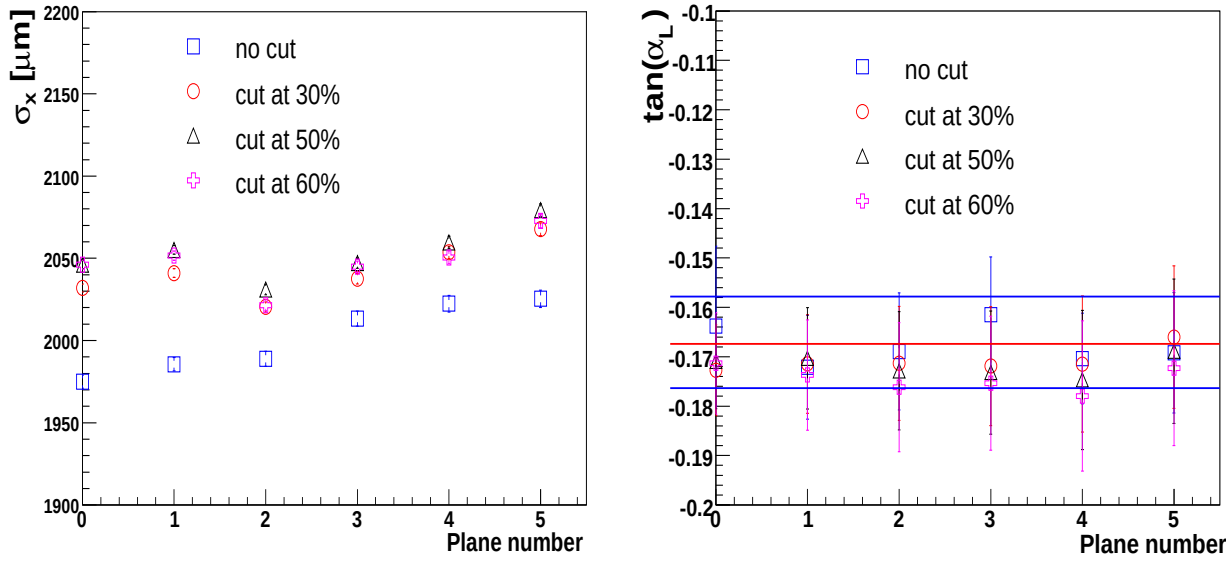

Figure 5.6: Extracted k_1=σ_x (left panel) and tan(α_L) (right panel) from the parabola fit of σ^2(tan(ϕ)) for the six planes. The simulated tan(α_L) is spread around the value given by horizontal red line within the zone limited by the blue lines.

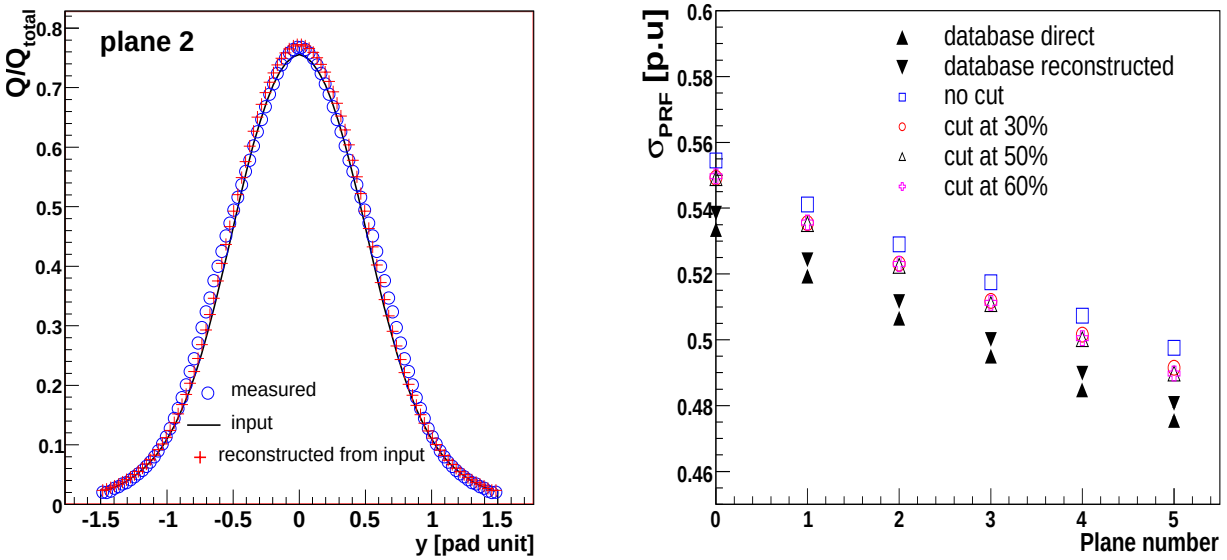

Figure 5.7: Left panel: reconstructed PRF (for -0.2<$tan(\phi)$<-0.1) compared with that used in the simulation PRF$_{sim}$ and the PRF directly computed from PRF_{sim} (see text). Right panel: reconstructed σ^{rec}_{PRF} for different low Q_{cl} cuts, together with the width of PRF_{sim} (*database direct*) and PRF_{rec} (*database reconstructed*).

Chapter 6

Online Calibration

This chapter is dedicated to the online calibration framework. The idea is to run the calibration procedures presented in the previous chapter in a transparent way, independent whether online or offline. Therefore we will not focus on the calibration methods themselves, except for the PEDESTAL algorithm which was not yet described. After a brief introduction to the online architecture, it will be explained on which systems the calibration algorithm is performed and how the data are transferred from online to offline worlds.

6.1 Introduction to the online architecture

The different online systems of the ALICE experiment are the Experimental Control System (ECS), the trigger (TRG), the Detector Control System (DCS), the Data Acquisition (DAQ [24]) and the High Level Trigger (HLT [25]). The online architecture is presented in Fig. 6.1.

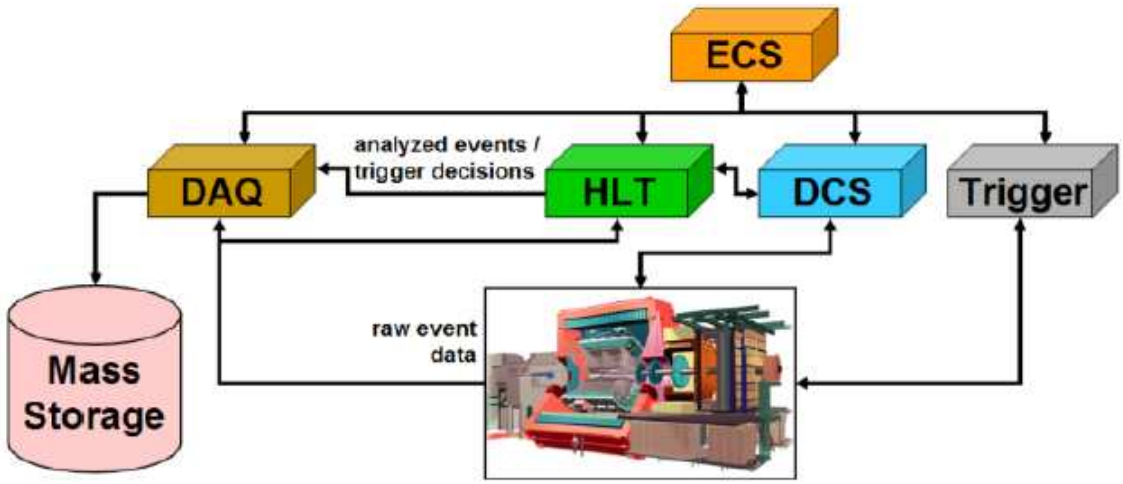

Figure 6.1: Schema of the online ALICE architecture.

- The ECS is the top level of control of the experiment. It provides a framework with an unified view of all online systems and allows to perform operations on individual or a set of detectors. The experiment can be splitted into trigger partitions, containing one or more detectors, which can be operated independently and concurrently during the runs, defined as periods of about three hours of data-taking without any interruption.

- The TRG allows to select specific events. Trigger subdetectors, like the TRD, provides a trigger signal to the Central Trigger Preprocessor (CTP), which takes finally the decision to record the event. During the data taking, data are acquired with different trigger types.

- The supervision and operation of the detectors take place in the DCS, where for instance front-end electronics are configured. The anode and drift voltages are set through Process Visualization and Steering System panels [26]. The DCS is connected to sensors, I/O interfaces and fieldbuses giving the anode and drift currents, the temperature and the status (STAND-BY, CONFIGURED, READY,...) of the chambers as well as other relevant information.

- The role of the DAQ system is to build the events and archive the data to permanent storage tapes. In addition it also provides an efficient access to the data for execution of calibration algorithms online.

- After triggering, the data rate for some triggers is expected to be still higher than what can be transferred to the permanent storage. The HLT allows in this case to reject fake triggered events by using better (but slower) Particle Identification and tracking algorithms, and more sophisticated algorithms like jet or V0 (like $K^0 \rightarrow \pi^+\pi^-$ decays) finders. The main differences with the L1/L2 trigger is that the HLT machines are the place where the information of all ALICE detectors (ITS/TPC/TRD/TOF$\cdots$) can be combined, allowing a global reconstruction of the events. In the case of a L1 or L2 trigger, only the trigger signals of the trigger subdetectors are combined together at the CTP to take the final decision.
  The HLT receives a copy of the events from the DAQ, which are then analyzed and compressed. In the case the HLT is part in the run, the data are submitted to the DAQ event builders for permanent storage only for events accepted by the HLT, otherwise the event is discarded. Besides its trigger role, the HLT framework provides the possibility to monitor online the data-taking and to run calibration algorithms.

All the online machines are in a special network protected by a firewall. Therefore to retrieve offline data, which are produced from the raw or reconstructed events in the online systems (DCS/DAQ/HLT), a special framework, called Shuttle, has been developed for the ALICE experiment. Its role is to store relevant information in the Offline Conditions Data Base (OCDB) available for the offline access via Grid.

6.2 Calibration on DAQ

6.2.1 DAQ architecture

When the CTP gives a positive trigger signal, the data produced by the detectors are injected on the Detector Data Link (DDL). To link the detectors to the DAQ machines several hundred meters apart, optical fibers (DDL) are used. The event fragments are received in the Local Data Concentrators (LDCs). For the TRD, 3 LDCs are available corresponding to the following blocks of supermodules (SMs):

- 0-1-2-9-10-11
- 3-4-5-12-13-14
- 6-7-8-15-16-17

Event fragments (sub-events) are then shipped to a farm of machines called Global Data Collectors (GDCs), where the complete events are built. Whereas the LDCs are detector specific, the GDCs are event specific: for a given event, all LDCs of different detectors send the data to the same GDC machine. Finally the events are sent to the mass storage system.

6.2.2 Algorithms on DAQ for the TRD

Calibration algorithms, so called Detector Algorithms (DA), are executed on DAQ machines for a first online calibration on raw data, without any reconstruction. The DAQ machines can be:

- the LDCs, which are part of the dataflow. In this case, the algorithm is executed at the end of the run on sub-events.
- the GDCs, which are also part of the dataflow. The algorithm is in this case performed at the end of the run on full events, containing data of all SMs available during the run.
- the monitoring servers, which are not part of the dataflow but can access data from any LDC or GDC. The algorithm is executed continuously during the run on full events.

Two algorithms were implemented for the TRD: one to evaluate the noise (pedestal algorithm), and one for the reconstruction of the drift velocity and time-offset in case the HLT is not taking part in the run (vdrift algorithm). Both produce a file with the so called reference data used to extract the calibration constants. The file is exported to the DAQ File Exchange server (FXS) at the end, from where it can be picked up by the Shuttle.

The pedestal algorithm The pedestal algorithm runs on LDCs. When the shift crew starts a PEDESTAL run, the data-taking stops automatically after 100 events. The chambers should be so configured that the data is without zero suppression. At the end of the PEDESTAL run, the DA starts and runs on the LDC machines. The data present on the machines are read and

analyzed to produce the output file exported afterwards to the DAQ FXS. One output file per LDC machine is transferred on the DAQ FXS. The person on shift can check if no problem occurred by looking at the DAQ electronic logbook. The reference data are picked up by the Shuttle afterwards and the noise level of the 1181952 pads for the full TRD is stored in the OCDB.

The drift velocity algorithm The vdrift algorithm is executed on a dedicated monitoring server for the TRD. The procedure starts at the beginning of a PHYSICS run. The shift crew decides how long the run is. The end of the run is automatically detected by the DA, which produces the output file and exports it to the DAQ FXS. Only one file is transferred on the DAQ FXS. The file contains the 2D TProfile with the average pulse height spectrum of each chamber. The calibration online is done chamber per chamber. The v_d and t_0 are extracted at the Shuttle from the 2D TProfile and saved in the OCDB.

6.3 Pedestal algorithm

6.3.1 Algorithm

To determine the noise level of each pad, the ADC amplitude distributions around the baseline are stored for each chamber in a 2D histogram.

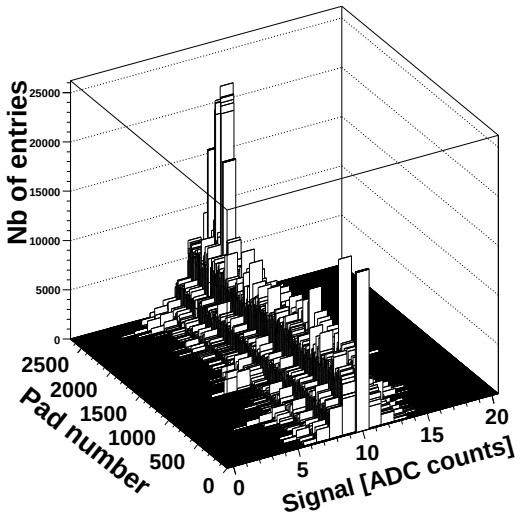

Figure 6.2: 2D histogram of the detector 0 (SM 0, S0, L0) with the ADC value distributions around the baseline (10 ADC counts) for each pad (PEDESTAL run 34510).

Such a histogram is shown in Fig. 6.2 for chamber 0 (SM 0 Stack 0 Layer 0). The number of pads in this chamber is (144 pad column) $\times$ (16 pad row) = 2304 pads. However the pad number goes from 0 up to 2688. Some pads are read two times by two different Multiple-Chip-Modules (MCMs) for the trigger. One MCM processes the signal of 21 pads in a pad row. The

first and the two last MCM channels (0, 19 and 20) are used only for searching the trigger online tracklets at the boundary between two MCMs. They are read by the neighbor MCMs as well. Table 6.1 gives the correspondence between the MCM channel and the pad column (col) number.

pad column	MCM number / MCM channel	MCM number / MCM channel	MCM number / MCM channel
17	**m-1 / 18**	m / 0	-
18	m-1 / 19	**m / 1**	-
19	m-1 / 20	**m / 2**	-
20	-	**m / 3**	-
...	-	...	-
35	-	**m / 18**	m+1 / 0
36	-	m / 19	**m+1 / 1**
37	-	m / 20	**m+1 / 2**

Table 6.1: The correspondence between pad column number and MCM channel. The MCM channels read per default are in bold characters.

The calibration software takes the values from the MCM channels 1 to 18 as default. It may happen that one MCM fails to read properly these channels, in which case there is the possibility for the MCM channels 1, 2 and 18 to read the channel 0, 19 and 20 of the neighbor MCMs. That is why the pedestal algorithm doesn't estimate the noise pad-wise but for each MCM channel.
For the MCM channels read per default (from 1 to 18 included), the pad column (*iCol*) and pad row number (*iRow*) are used to compute the pad number (*iCh*) in the 2D histogram:

$$iCh = iRow + iCol \times rowMax \tag{6.1}$$

where *rowMax* is the total number of pad row in the chamber, 12 for chambers in the stack 2 and 16 for the others. The ADC value distributions of the MCM channels 0, 19 and 20, are placed in the 2D histogram after all the pads. These channels are identified with a *iCcol* number (0 for 0, 1 for 19 and 2 for 20), the MCM number *iMcm* in the pad row ($iMcm \in [0,8]$) and the row number *iRow*:

$$iCh = rowMax \times colMax + [iRow + (iCcol \times mcmMax + iMcm) \times rowMax] \tag{6.2}$$

where *colMax* and *mcmMax* are the total number of pad column (144) and MCMs per pad row (8).

The 2D histogram of each chamber is filled with 100 events of non-zero-suppressed data. For a total number of 30 timebins, 30×100 = 3000 entries per pad are accumulated. Then the 2D

histogram is projected in each *pad number* bin to obtain the ADC value distribution for each MCM channel. By fitting them with a Gaussian, the baseline (mean value of the Gaussian) and noise (sigma of the Gaussian) are extracted.

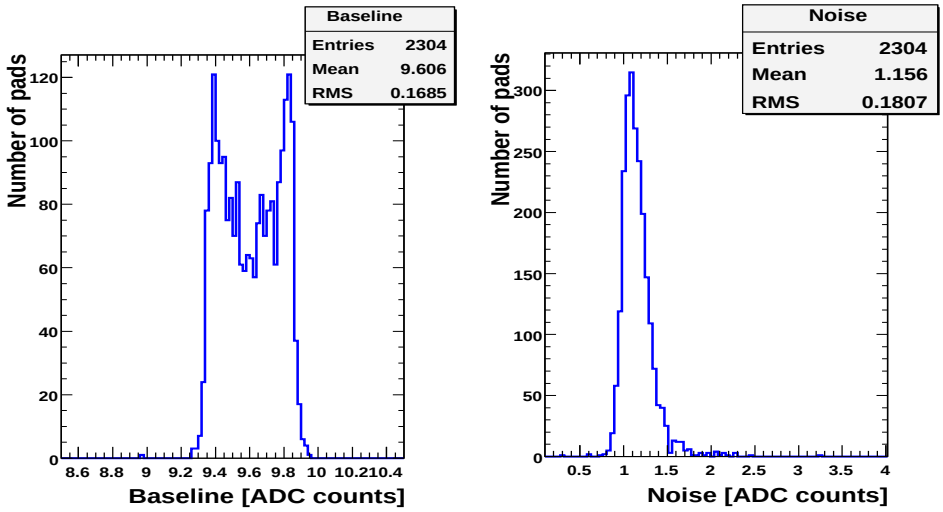

Figure 6.3: Baseline (left panel) and noise (right panel) distributions in chamber 0 (PEDESTAL run 34510).

InRange	ADC input range (input charge)	2000 mV
OutRange	ADC output range (number of channels)	1023
chg	Electronic gain	12 mV/fC
e	Electron charge	$1.602 \cdot 10^{-4}$ fC

Table 6.2: Variables of the electronics for the conversion of the signal from ADC counts to mV or number of electrons.

Fig. 6.3 shows the baseline and noise distributions in ADC counts for the detector 0. The baseline is slightly below the nominal value of 10 ADC counts and has a typical two peaks structure for all chambers. The presence of the two peaks is not completely understood. The mean noise $\sigma_{\text{noise}}^{\text{ADC counts}}$ is about 1.16 ADC counts. Using Table 6.2, the noise can be converted into electrons:

$$\sigma_{\text{noise}}^{\text{electrons}} = \sigma_{\text{noise}}^{\text{ADC counts}} \times \frac{\text{InRange}}{\text{OutRange}} \times \frac{1}{chg \cdot e} \approx 1132\,\text{electrons} \tag{6.3}$$

The noise is in agreement with the expected value of about 1000 electrons.

Fig. 6.4 shows the baseline and noise as a function of the pad column and pad row number in detector 0. In this case for the pad (*iRow*=8, *iCol*=72), the fit procedure results in a particularly low baseline and high noise. It indicates that the fit probably failed because the distribution is not Gaussian. Such pads are marked with a particular flag in the variable *pad status*.

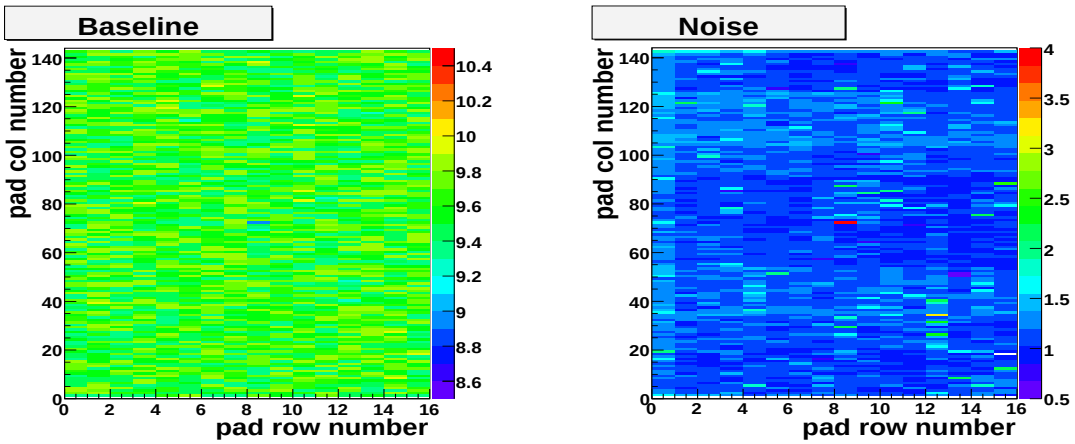

Figure 6.4: Baseline (left panel) and noise (right panel) as a function of the pad column and pad row number in the detector 0 (PEDESTAL run 34510).

6.3.2 Pad capacitance and noise

Fig. 6.5 shows the noise in ADC counts in SM 0.

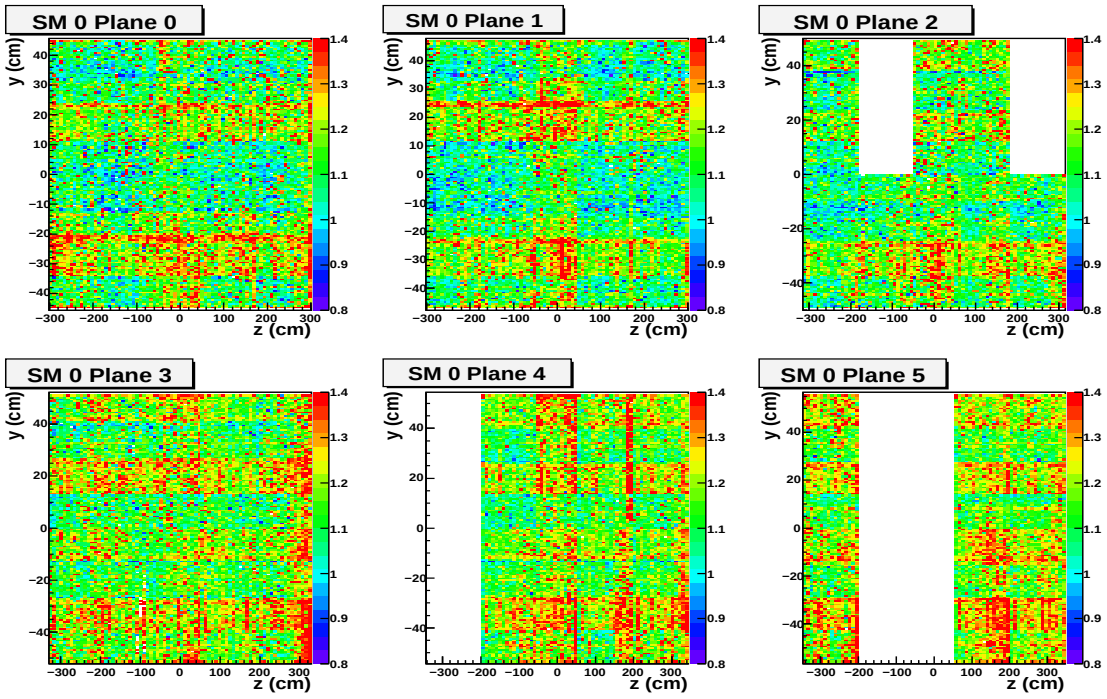

Figure 6.5: Noise in the six planes of SM 0 (PEDESTAL run 38125). The five stacks in each layer are in the z direction.

Some Optical Readout Interfaces (ORI), mounted on the TRD chambers, do not send data. The corresponding half chambers are represented in white. Clearly the noise plot shows stripe patterns of higher noise in the z-direction. Along a pad row (z direction), the shape of the noise distribution is correlated to the static pad capacitance of the pad plane, which can be

considered independent on the row number.

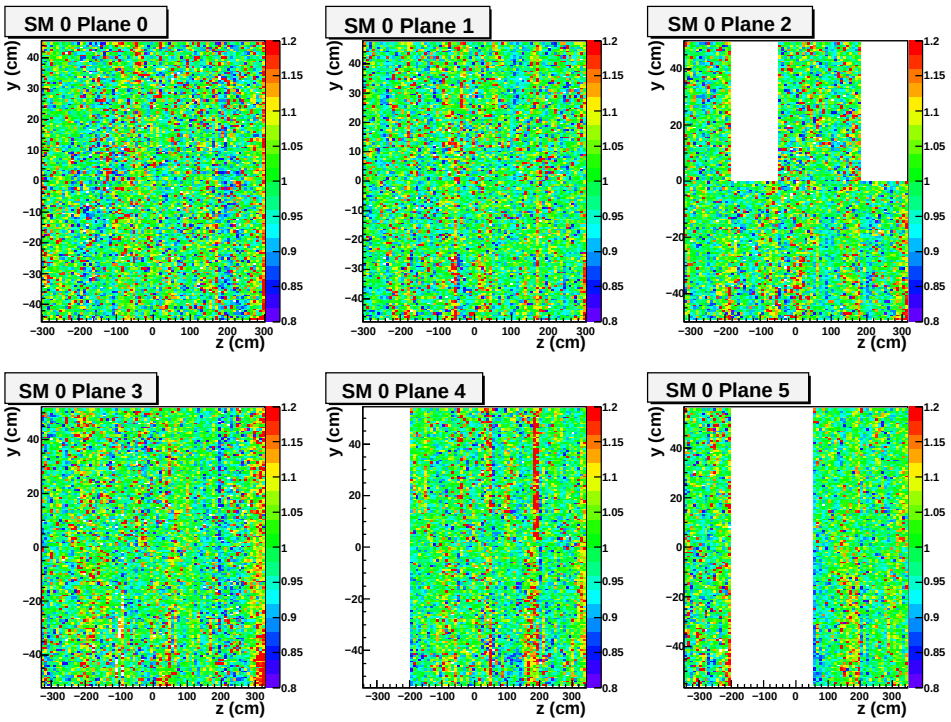

Figure 6.6: Unfolded noise distributions (see text for explanation) in the SM 0 (PEDESTAL run 38125).

To identify possible noisy spots in the SM, the noise distributions can be corrected for the expected noise variations induced by the pad capacitance. Noisy pads are excluded from the unfolding procedure with the condition ($0.6 \leq \sigma_{\text{noise}}^{\text{ADC counts}} \leq 1.5$). The noise of a full layer is then projected onto the pad column axis: the noise is averaged over the pad rows $\langle \sigma_{\text{noise}} \rangle_{\text{pad row}}$. The unfolded noise, $\sigma_{\text{unfolded noise}}$, corresponds to:

$$\sigma_{\text{unfolded noise}} = \sigma_{\text{noise}} / \langle \sigma_{\text{noise}} \rangle_{\text{pad row}} \tag{6.4}$$

Fig. 6.6 shows the unfolded noise in SM 0, where only a moderate number of noisy spots are seen.

6.3.3 Pad status

The baseline and unfolded noise are used to detect unreliable pads, which can then be excluded from the reconstruction. According to the situation, different status are attributed to the pads:

- the noisy pad are masked. They are identified using the mean baseline $\langle b \rangle$, the rms of the baseline σ_{baseline} in the chamber. Per definition, the unfolded mean noise $\langle \sigma_{\text{unfolded noise}} \rangle$ must be close to unity. All pads with baseline b and unfolded noise $\sigma_{\text{unfolded noise}}$ are masked if they fulfill Eq. 6.5 and . 6.6.

$$|b - \langle b \rangle| > 5 \cdot \sigma_{\text{baseline}} \tag{6.5}$$

$$\sigma_{\text{unfolded noise}} > 5.0 \tag{6.6}$$

- the disconnected pads are recognizable by a small noise.

$$\sigma_{\text{unfolded noise}} < 0.5 \tag{6.7}$$

- a pad can be connected to the neighbor pad on the left or on the right. They are then called bridged left or bridged right. By comparing the baseline and noise of the neighbor pads, they can be identified.

- for the special case of the MCM channels 0, 19 and 20, corresponding to pads read by two different MCMs, the pad can be noisy or disconnected for one MCM but correctly read by the other MCM. The PASA channel is not the same. In this case, the pad is characterized as *readsecond* and it means that the data reader class will take the value from the other MCM.

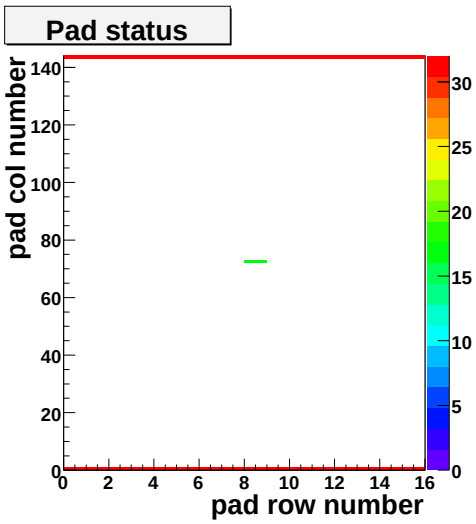

Figure 6.7: Pad status in the detector 0 (PEDESTAL run 34510). See Fig. 6.4 for the corresponding baseline and noise distribution.

As an illustration of the above discussion, Fig. 6.7 shows the resulting pad status for the detector 0. The pad status is stored as a character and is plotted as kMasked = 2, kPadBridgedLeft = 4, kPadBridgedRight = 8, kReadSecond = 16, kNotConnected = 32. The pad ($iRow$=8, $iCol$=72) was found as *readsecond*. In the pad row 8, this pad is read per default from the channel 1 of the MCM 4. The ADC value distribution around the baseline is stored in the bin iCh_d=1160 of the 2D histogram of the detector 0 (see Eq. 6.1). In the left panel of Fig. 6.8, one can see a double peak structure, which indicates some big fluctuations of the baseline. In addition, the pad can be also read from the channel 19 ($iCcol$=1) of the MCM 3 in the pad row 8. The corresponding ADC value distribution is stored in the bin iCh_s (see Eq. 6.2):

$$iCh_s = 16 \times 144 + [8 + (1 \times 8 + 3)] \times 16 = 2488 \tag{6.8}$$

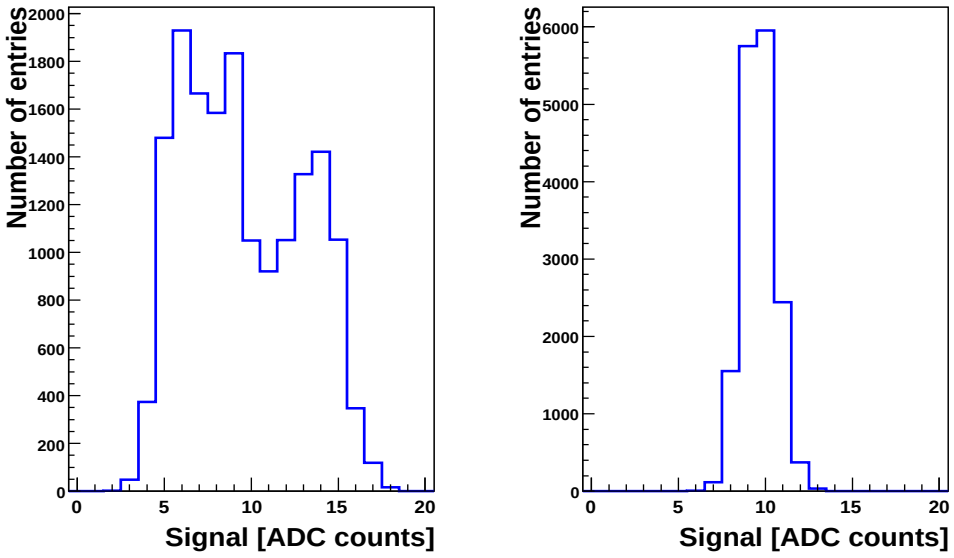

Figure 6.8: The ADC value distributions of the pad (*iRow*=8, *iCol*=72) read from the default MCM (on the left) and the neighbor MCM (on the right). This pad is flagged as *readsecond*.

The second MCM doesn't suffer from baseline fluctuation, as one can see in the right panel of Fig. 6.8.
It may happen that one ORI does not send any data during a PEDESTAL run due to malfunctioning. All pads from this half chamber will be flagged as disconnected. At the end of the run, the Offline Configuration Database (OCDB) is updated and filled with the pad noise and pad status. The new database entry is valid for all following runs, as long as a new PEDESTAL run is not taken.

6.3.4 Dependences of the noise on the running conditions

It is important to know what could affect the noise. The configuration of the electronics plays a role. In ref. [27], the noise level was measured during the construction of SM 3 for different configurations:

- without any filter switched on (nf).
- with pedestal subtraction (p).
- with pedestal subtraction, gain correction and tail cancellation (pgt).

The configurations nf and p give the same level of noise. Adding the gain correction factors per pad and the tail cancellation increases σ_{noise} by about 16 %. The digital power consumption of the electronic rises, which may lead to higher noise due to parasitic couplings. The tail cancellation applied on pedestal data leads also to enhanced fluctuations.
The effect of the high voltage (HV) was studied by comparing the PEDESTAL runs 49552 and 51586. The running conditions are summarized in Table 6.3. Fig. 6.9 shows a small increase of

the noise of about 2 % with the high voltage switched on. The fact that the high voltage has a negligible influence on the noise level compared to the electronic configuration, indicates that most of the noise is genuine noise and doesn't come from parasitic couplings with HV in the chamber.

run number	number of timebins	electronic configuration	U_a [V]	U_d [V]
49552	16	p	1480	1200
51586	16	p	0	0

Table 6.3: Running conditions of the PEDESTAL run 49552 and 51586. No magnetic field was on.

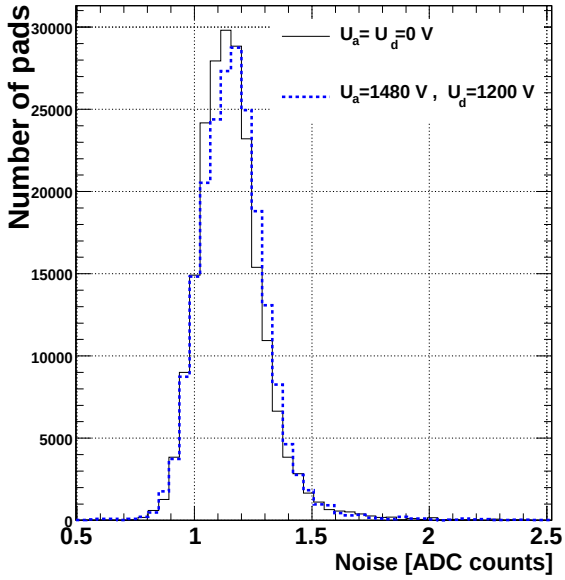

Figure 6.9: Noise distribution for the PEDESTAL run 49552 (with high voltage) and 51586 (without high voltage).

6.3.5 Noise and pad status in the reconstruction

The noise and pad status are used during the reconstruction during the clusterization algorithm. A cluster is defined as a local maximum over three neighbor pads (amp[0],amp[1],amp[2]). The ADC signals have to fulfill:

$$\text{amp}[1] \geq \text{amp}[0] \quad \text{and} \quad \text{amp}[1] \geq \text{amp}[2] \tag{6.9}$$

$$\text{amp}[1] \geq \text{fClusMaxThresh} \tag{6.10}$$

$$\text{amp}[0] \geq \text{fClusSigThresh} \quad \text{and} \quad \text{amp}[1] \geq \text{fClusSigThresh} \tag{6.11}$$

fClusMaxThresh and fClusSigThresh are two thresholds belonging to the reconstruction parameters. The parameters are all stored in the AliTRDrecoParam class and have to be tuned. Table 6.4 gives the relevant ones for the noise and pad status.

symbol	name
fClusMaxThresh	threshold value for the middle pad
fClusSigThresh	threshold value for the neighbor pads
fMinMaxCutSigma	threshold sigma noise for the pad middle
fMinLeftRightCutSigma	threshold sigma noise for the three pad sum

Table 6.4: Relevant reconstruction parameters.

In order to limit the number of noisy clusters, two conditions are imposed on the cluster amplitudes:

$$\text{amp}[1] \geq \text{fMinMaxCutSigma} \times \sigma_{\text{noise}}[1] \tag{6.12}$$

$$(\text{amp}[0] + \text{amp}[1] + \text{amp}[2]) \geq \text{fMinLeftRightCutSigma} \times \sigma_{\text{noise}}[1] \tag{6.13}$$

where $\sigma_{\text{noise}}[1]$ is the noise level for the middle pad. Moreover the pad status is also propagated from the pad signals to the cluster. Two cases have a special treatment:

- if one of the neighbor pads is bridged with the middle pad, its signal is considered zero, with the signal assigned to the middle pad.
- if the middle pad is flagged as noisy, then its signal is considered equal to fClusMaxThresh.

Such clusters are used in the reconstruction of tracklets. During the analysis they can be eventually excluded.

6.4 The Drift velocity algorithm

6.4.1 Algorithm

No tracking procedure is executed on DAQ. As a consequence, the drift velocity algorithm is based on a simple tracklet finder procedure optimized for a low charged particle multiplicity environment. A maximum of one tracklet can be found in each chamber for each event. The steps are the following:

- the algorithm looks for one possible seed inside the chamber. The signal amplitudes are summed over two pad rows and two pad columns to form online clusters. The online clusters are integrated over all timebins for each pad. The position of the maximum gives the position of the seed. Since one expects cases where no track crosses the chamber, the seed is rejected if less than 60 % of the online clusters at the seed position are below a certain threshold (20 ADC counts after baseline subtraction).

- for each seed, the average pulse height is filled with the amplitude of the online clusters as a function of time.

6.4.2 Results

The algorithm was tested on the four supermodules installed in ALICE during the LHC08d cosmic-ray data taking period from September 2008 to the middle of October 2008.

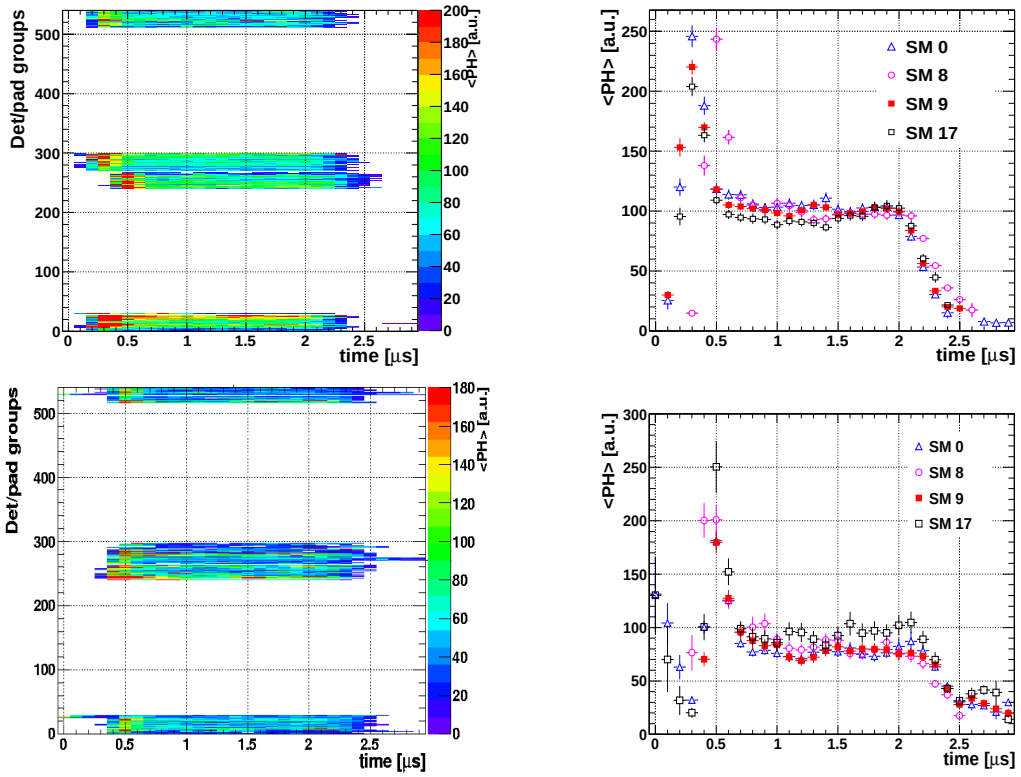

Figure 6.10: Average pulse height of each detector (left panels) and integrated over the chambers belonging to the same supermodule (right panels) for two different runs: in the top panels the run 60283 (19/09/2008 with 2613 reconstructed tracks), in the bottom panel the run 60691 (24/09/2008 with 699 reconstructed tracks).

The average pulse height of each detector shows variations of the time-offset from one run to the other, that could be related to the pretrigger signal. This observation was confirmed afterwards by the offline calibration with reconstructed tracks. The offline average pulse heights for two different runs are plotted on Fig. 6.10. All runs were triggered by the TRD itself (TRD L1 trigger).

Since 15 runs, from the run 60904 (26/09/2008) to the run 61857 (06/10/2008), present similar average pulse heights, there were added together to allow a determination of the drift velocity and time-offset for each individual detector (B=0 T for these runs, v_{dE}=v_d). The results ob-

tained with the online algorithm are compared with the ones obtained offline after tracking. In addition to the very different algorithms, the tail cancellation is applied only offline on the data. The offline clusters are also the sum of the ADC signals over one pad row and three pad columns and therefore they have smaller amplitudes than the online clusters. The number of found offline tracklets in each detector is very similar to the number of entries online (see Fig. 6.11). There are nevertheless differences.

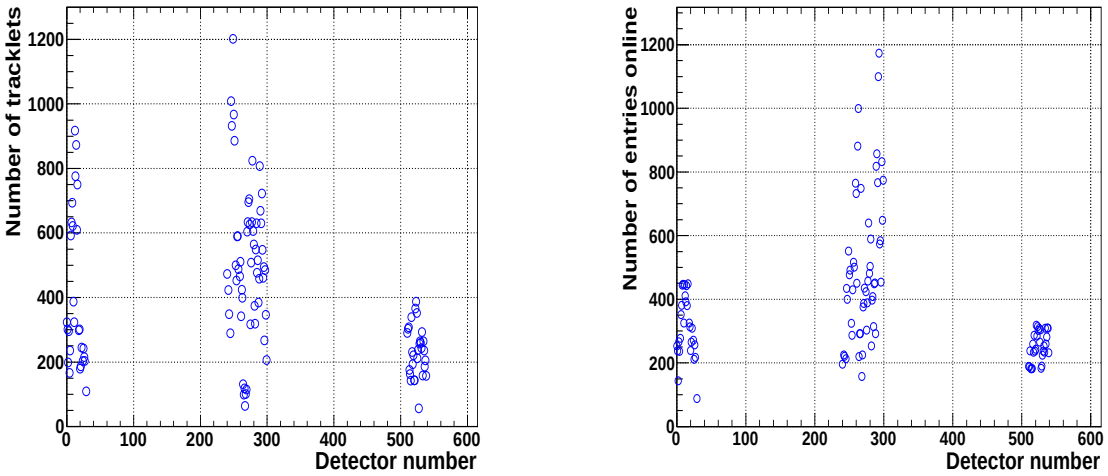

Figure 6.11: Number of offline tracklets (left panel) and entries found online (right panel) in the average pulse height histograms of each detector of the 4 SMs in operation in ALICE.

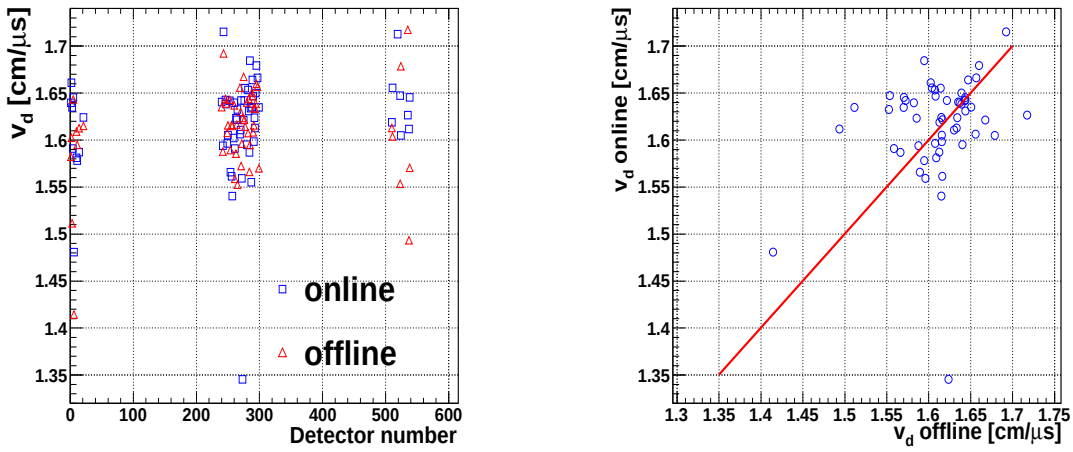

Figure 6.12: Left panel: drift velocity as a function of the detector number found by the online and offline calibration procedures; right panel: correlation between the drift velocities found online and offline.

The drift velocity as a function of the detector number is plotted in the left panel of Fig. 6.12. The values obtained with the online and offline calibration procedures are compared. A mean

drift velocity of 1.615 cm/μs was found in both cases with a sigma of about 3.3 %. The anode voltage was set to 1200 V for all the chambers and the magnetic field was off for these runs. The found mean drift velocity is in agreement with Garfield simulations for the gas composition used, a mixture of Ar and CO_2 with a CO_2 content between 18 % (v_d=1.7 cm/μs) and 20 % (v_d=1.5 cm/μs). The correlation between the online and offline v_d is not as good as one would expect (see right panel of Fig. 6.12). The statistics is also quite small, below 400 tracklets per detector for the SM 17 and for most of the chambers in SM 0.

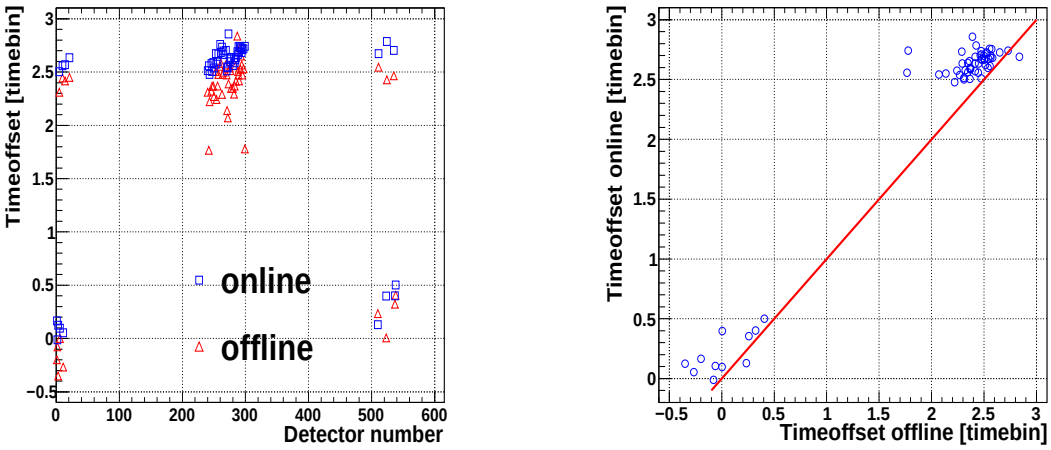

Figure 6.13: Left panel: time-offset as a function of the detector number found by the online and offline calibration procedures; right panel: correlation between the time-offset values found online and offline.

The time-offset is shown as a function of the detector number in the left panel of Fig. 6.13. Some chambers have smaller t_0 in the SM 0 and SM 17. The results of the online algorithm suggest an increasing t_0 with the detector number in the SM 8 and SM 9. The tendency is not so clear with the offline calibration procedure. A shift of about 0.2 timebins is observed between the online and offline reconstructed t_0 (see Fig. 6.13). This is well above the desired t_0 resolution of 0.1 timebin and is still under investigation.
A first calibration of the gain, drift velocity and time-offset has been performed for the runs of the LHC08d period. The raw data have been reconstructed in a second path with the correct calibration constants. The tracking efficiency increased: for the run 60283, 2613 tracks were found with the default database, after calibration 3422 were reconstructed.

6.5 Calibration using the HLT

The HLT has the big advantage to provide an online reconstruction of the events in an equivalent way as in the offline framework. After receiving the TRD Raw data from the DAQ, the cluster finder followed by the TRD standalone tracking algorithm are executed in parallel in the HLT cluster. A global event reconstruction (with the TPC) is in the future also envisaged. The

produced TRD tracklets are then used to fill the reference histograms for the calibration: the dE/dx distributions, the average pulse heights and the PRF. For the calibration framework, it doesn't make any difference if the TRD tracklets are the result of the TRD standalone tracking executed online or offline, or the global tracking executed online or offline. However, the quality of the tracklets and, as a consequence, that of the calibration will differ. At the end of each run the reference data are exported to the HLT FXS and picked up by the Shuttle. Finally, after fitting, a new set of calibration constants are stored in the Offline Conditions Database.
The HLT offers the possibility to use the latest set of calibration parameters valid for the ongoing run through a special framework (called the *taxi*). At the beginning of each run, a local copy of the OCDB is updated on the HLT cluster: the HCDB (HLT Condition Database). This will improve the tracking if the conditions didn't dramatically change compared to the previous run.
The reference data of the calibration are planed to be used for monitoring of the chambers in addition with other histograms related to the tracking. The HLT Online Monitoring Environment including ROOT (HOMER) interface provides a connection to the Alice Event monitoring framework (AliEve). The reconstruction of the events can be monitored in the AliEve 3D vizualization framework together with ROOT structures, like the reference histograms of the calibration.

6.6 The TRD preprocessor at the Shuttle

The role of the Shuttle is described in appendix. At the Shuttle the TRD preprocessor is executed for the run types:

- PEDESTAL: empty events (also called black events) taken with the TRD alone and a random trigger.
- STANDALONE: data taking with the TRD alone and a random trigger. These runs are mainly to check the data integrity or the correlated noise.
- DAQ: test runs.
- PHYSICS: global run including more than one detector and different trigger clusters. One trigger cluster is defined by the way the events are triggered. Different trigger types can be active simultaneously.

Table 6.5 summarizes the tasks executed by the preprocessor for each run type.

The DCS data points allow to check the currents, voltages, temperatures of the chambers. The measured datapoints saved in the DCS Archive DB during the run are made available at the Shuttle by AMANDA. On the DCS FXS one file gives information about the electronic configuration (number of timebins, p/pgt $\cdots$). These two first sources of information are converted to ROOT format in the TRD preprocessor and stored in the OCDB. The datapoints

run type	DCS data points temperatures voltages, etc $\cdots$	DCS FXS electronic configuration	DAQ FXS calibration DA noise/(v_{dE}/t_0)	HLT FXS calibration DA $g/(v_{dE}/t_0)/\sigma_{PRF}$
DAQ	yes	yes	no	no
PEDESTAL	no	yes	yes (noise)	no
STANDALONE	yes	yes	no	no
PHYSICS	yes	yes	yes (v_{dE}/t_0)	yes

Table 6.5: Tasks performed by the TRD preprocessor for every run type.

are received as time-stamp value pairs, which are used to build graphs for the time dependence of the parameters.
The file on the DAQ FXS contains either the result of the pedestal DA or the result of the drift velocity DA. The reference data for the calibration of the relative gain (the dE/dx distributions per chamber saved in a 2D histogram), the v_{dE}/t_0 (the average pulse height per chamber saved in a 2D TProfile) and the σ_{PRF} (the PRF per chamber saved in a 2D TProfile) are taken from the HLT FXS. After the fit procedures to extract the calibration constants (g,v_{dE},t_0 and σ_{PRF}), the reference data are stored in the Grid reference database and the calibration coefficients in the OCDB. During the fit of the distributions, it is checked if the histograms contain enough statistics and if the result is reasonable. In case of failure the default value is stored. For the calibration of v_{dE} and t_0, the results from the HLT are per default used. If the HTL does not take part in the run, the results of the VDRIFT algorithm executed on the DAQ are used.
The possible exit states of the TRD preprocessor are:

- Preprocessor Done: the preprocessor ended successfully.
- DCS Error: the retrieving of the DCS archive data by AMANDA failed. In this case the TRD preprocessor is not called by the Shuttle.
- FXS Error: a problem occurred during the connection to one of the FXSs.
- Preprocessor Error: the fit procedures or conversion to ROOT format failed in the TRD preprocessor.
- Preprocessor TimeOut: the preprocessor exceeded the allowed processing time.
- Preprocessor OutOfMemory: the preprocessor exceeded the allowed memory usage.
- Store Error Status: a problem occurred during the transfer of the data to the OCDB and/or reference database.

If the Shuttle fails processing one of the 20 preprocessors, the run is to be reprocessed at a later stage. The maximum number of iterations is three in case of a Preprocessor Error, Preprocessor TimeOut, Preprocessor OutOfMemory states. Otherwise the Shuttle tries to query the data

from the DCS archive database (DCS Error), FXSs (FXS Error) until the retrieval is successful. The transfer to the Grid is also retried as long as the data are still available on the local disc.

Part II

Feasibility study of $Z^0 \rightarrow e^+e^-$ measurement with the ALICE central barrel in pp collisions at $\sqrt{s}$=14 TeV

Introduction

The $W^{\pm}$ and Z^0 bosons are the elementary particles that mediate the weak nuclear force. They have been discovered at CERN in 1983. It was a major success for the standard model of particle physics that predicted their existence. In this section, after a brief historical introduction, we will give some physics motivations to look at the Z^0 production in ALICE.

Direct observation of Z^0 and $W^{\pm}$

In 1983, the $W^{\pm}$ [28, 29] and Z^0 boson [30, 31] were discovered at the CERN $p\bar{p}$ collider. The CERN's Super Proton Synchrotron (SPS) accelerator was operated as a proton-antiproton collider at a center-of-mass energy of about 600 GeV. The Leading Order (LO) for the Z^0 production process is represented in Fig 6.14.

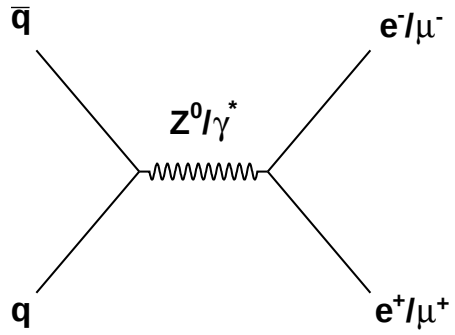

Figure 6.14: LO process to produce Z^0 in $p\overline{p}$ collisions.

The quarks (antiquarks) in the proton (antiproton) carry about 1/6 of its momentum each. That is why, the minimal collision energy $\sqrt{s}$ to produce Z^0 is about 600 GeV.

$$\sqrt{s} = 6 \times m_{Z^0} \approx 600\,\text{GeV} \tag{6.14}$$

The observation of the Z^0 boson provided a direct confirmation of the unified model of the weak and electromagnetic interactions, which is now called, together with the QCD, the standard model. The Z^0 and $W^{\pm}$ bosons were identified by their leptonic decays ($Z^0 \rightarrow l^+l^-$ and $W^{\pm} \rightarrow l\nu_l$). The UA1 and UA2 experiments used calorimeters to detect the electrons; the neutrinos were detected indirectly through the measurement of missing transverse momentum. The

production and decay properties of the intermediate vector bosons were found to be consistent with the theoretical expectations. They are summarized in Table 6.6. Z^0 and $W^{\pm}$ are produced by Drell-Yan mechanism (see fig.6.14) modified by higher order QCD corrections [32, 33, 34, 35]; their decay properties are predicted by the SU(2)×U(1) standard model [36, 37, 38].

	M [GeV/c^2]	Br(e) [%]	σ×Br(e) [pb]
Z^0	91.19	3.363	60
$W^{\pm}$	80.42	10.72	600

Table 6.6: Mass, electronic branching ratio and cross-section for production in $p\overline{p}$ collisions at 600 GeV of Z^0 and $W^{\pm}$.

Studies of Z^0 properties

Many intrinsic properties of the Z^0 boson have been examined in great detail in e^+e^- collisions at the Large Electron Collider (LEP) at CERN and the Stanford Linear Collider (SLC) at SLAC. The mass of Z^0 has been determined to high precision [39]. In 1989, studies of Z^0 decay performed at LEP demonstrated that there is only three ν families.
In e^+e^- collisions, the experiments focused on the electroweak character of the Z^0 boson. In hadron colliders the production properties are presumably characterized by QCD. A little bit later, the Z^0 boson were studied in $p\bar{p}$ collisions at much higher energies ($\sqrt{s}$≈1.8-1.96 TeV) by the experiments of the Fermilab Tevatron. The Z^0 served as a clean probe of the strong interaction. Its large mass assured a large energy scale (Q^2=M_Z^2) for probing perturbative QCD with good reliability.

Motivation for Z^0 measurements at the LHC with ALICE

In pp collisions at the LHC, the stability of the predictions offers the possibility to use the total Z^0 cross-section for a better understanding of the luminosity of the collider, and the acceptance and efficiency of the detectors [40]. The decay of Z^0 bosons into electrons provides an experimental measurement of its production rate. Experimentally, the cross-section times branching ratio is calculated from

$$\sigma_{Z^0} \cdot Br(Z^0 \rightarrow e^+e^-) = \frac{N_{Z^0}^{obs} - N_{Z^0}^{bck}}{A_{Z^0} \cdot \epsilon_{Z^0} \cdot \int Ldt} \tag{6.15}$$

$N_{Z^0}^{obs}$ is the number of Z^0→e^+e^- candidates observed in the data; $N_{Z^0}^{bck}$ is the number of expected background events in the Z^0→e^+e^- candidate samples; A_{Z^0} is the acceptance of the Z^0 decays, given by the geometrical acceptance of the central barrel of ALICE and the kinematic constraints of the selection criteria; ϵ_{Z^0} is the efficiency to identify the Z^0 decays

falling within the acceptances; $\int Ldt$ is the integrated luminosity of the data samples used. A comparison between the experimental results and the theoretical calculations allows to check the understanding of the detectors.
Z^0, with a 3.37% branching ratio to lepton pairs [1], is a source of high p_T electrons. The decay electrons have a transverse momentum between 30 GeV/c and 50 GeV/c, with a peak at half the mass of the vector boson ($cM_{Z^0}/2 \approx 45$ GeV/c). The measurement of Z^0 through its electronic decay channel gives the possibility to check the p_T resolution of the central barrel of ALICE above 30 GeV/c, important for high p_T studies.

In heavy ion collisions the Z^0 has been proposed as a reference to measure the effect of the transition to a deconfined phase on the production of quarkonia. At the CERN SPS energies the J/Ψ has been normalized to the Drell-Yan continuum ($q\bar{q} \rightarrow l^+l^-$) in the lepton pair mass range $2.9 < M < 4.5$ GeV/c^2. At the LHC energies the dilepton continuum in this region will be dominated by decays of $c\bar{c}$ and $b\bar{b}$, whose production in nuclear collisions has large uncertainties. Despite the large mass differences, $M_Z \gg M_{J/\Psi}$, and the difference in production mechanisms, mainly $q\bar{q}$ for Z^0 and gg for quarkonium, the Z^0 is a good candidate for an alternative reference to quarkonium study. The Z^0 boson will probe the nuclear modification of the quark Parton Distribution Functions (PDF) at high Q^2 ($Q^2 \approx c^2 M_{Z^0}^2$), whereas the quarkonium will probe the nuclear modification of gluon PDF at smaller Q^2 (see Appendix A). The Z^0 properties should be hardly affected by the presence of a Quark Gluon Plasma. The Z^0 is formed approximately $1/(c^2 M_{Z^0}) = 0.002$ fm/c after the collision and decays inside the medium with a (vacuum) lifetime of 0.08 fm/c [41] i.e. before the expected formation time of a Quark Gluon Plasma (≈ 0.1 fm/c). As a consequence, only the nuclear modification of the PDFs have to been known in order to use Z^0 as a reference for quarkonium studies.

Chapter 7

Z^0 production in hadron collisions

7.1 Physics Processes

In hadron-hadron collisions at high energies, massive e^+e^- pairs are produced via the Drell-Yan process. Quark-antiquark annihilations form an intermediate γ^* or Z^0 (γ^*/Z^0 interference) vector boson which then decays into an e^+e^- pair. In the dielectron invariant mass region of the Z^0 mass ($M_{Z^0}\approx 91\,\mathrm{GeV/c^2}$), they are predominantly from the resonant production and decay of the Z^0. Given the large virtualities that characterize the production of Z^0 ($Q^2=\mathrm{c}^2{M_{Z^0}}^2$), the differential inclusive cross-section for producing Z^0 in proton-proton collisions can be calculated in the framework of pertubative QCD (pQCD).

$$\frac{d^2\sigma_{ij\to Z^0}}{dp_T^2 dy} = \sum_{i,j}\int dx_i dx_j f(x_i) f(x_j) \frac{d^2\hat{\sigma}_{ij\to Z^0}}{dp_T^2 dy} \tag{7.1}$$

where p_T and y are the transverse momentum and the rapidity of the Z^0 boson; x_i and x_j are the longitudinal momentum fractions of the protons carrying by the colliding partons; f(x_i) and f(x_j) are the parton distribution functions (PDF's) for the incoming partons inside the proton; and $\hat{\sigma}_{ij} \to Z^0$ is the partonic cross-section for production of Z^0. The subscripts i and j denote the contributing parton flavors (i.e, up, down, etc.). The sum is over all flavors.

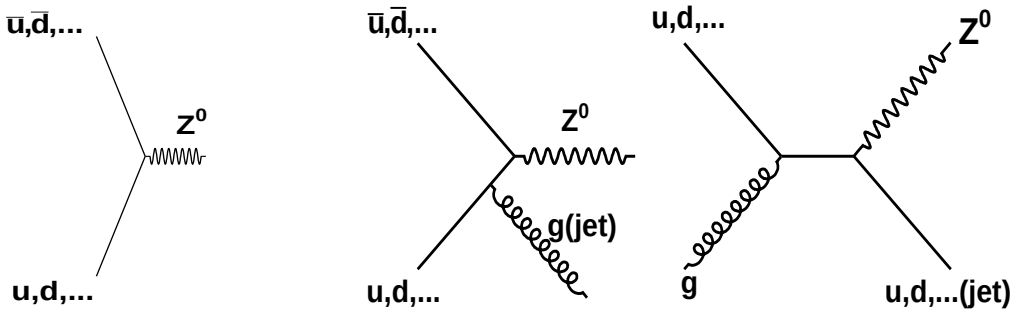

Figure 7.1: Feynman diagrams for Z^0-boson

The PDF's are related to non-perturbative effects and can not be calculated analytically but only parametrized and fitted to the deep inelastic and hard scattering data. The partonic cross-sections are calculated in standard pQCD by expanding in powers of the strong coupling constant, α_s. At α_s^0, the Z^0 boson is produced via the 2→1 Born process, $q+\bar{q}\rightarrow Z^0$ (see Fig. 7.1). At α_s^1, the one loop correction of the Born process has to be taken into account, together with the 2→2 processes, $q+\bar{q}\rightarrow Z^0+g$ and $q(\bar{q})\rightarrow Z^0+q(\bar{q})$. The computation of the inclusive cross-section implies the knowledge of the quark and anti-quark PDF's at leading order and gluon PDF for Z^0+jets production. Calculations for Tevatron and LHC energies have been carried out in next-to-leading order (NLO) and next-to-next-leading order (NNLO). The cross-sections are dominated by the leading-order $q+\bar{q}\rightarrow Z^0$ processes. $u\bar{u}$, $d\bar{d}$, $s\bar{s}$ and $c\bar{c}$ contribute respectively to 40 %, 38 %, 15 % and 6 % of the LO cross-section [42]. The NNLO error band is a little bit larger than at the Tevatron because the partons are probed at smaller Bjorken-x values where the PDF's are less well known from deep inelastic and hard scattering data. Nevertheless the convergence of the NLO and NNLO calculations is good and leads to a total cross-section times branching ratio of about 1.96 nb [43, 44].
By assuming leading order kinematics ($q\bar{q}\rightarrow Z^0$), the x range probed by the measurement of Z^0 can be calculated as a function of the centre-of-mass (c.m.s) energy per nucleon pair $\sqrt{s_{NN}}$, the mass M_{Z^0}, and the rapidity y_{Z^0} (see Appendix A).

$$x_{1,2} = \frac{\mathrm{c}^2 M_{Z^0}}{\sqrt{s_{NN}}} e^{\pm y_{Z^0}} \tag{7.2}$$

The x values probed at mid-rapidity (y_{Z^0}=0.0) are summarized in Table.7.1 for pp collisions at 14 TeV and $PbPb$ at 5.5 TeV. For comparison, the results are also shown for charm and bottom productions. While Z^0 allows to explore the quark and antiquark PDFs at x values of the order of 10^{-3}-10^{-2}, $c\bar{c}$ and $b\bar{b}$ productions probe the gluon PDF at smaller x.

System	$PbPb$ 5.5 TeV	pp 14 TeV
$c\bar{c}$	$x\approx 4\times10^{-4}$	$x\approx 2\times10^{-4}$
$b\bar{b}$	$x\approx 2\times10^{-3}$	$x\approx 6\times10^{-4}$
Z^0	$x\approx 1.66\times10^{-2}$	$x\approx 6.5\times10^{-3}$

Table 7.1: The x-range probed at mid-rapidity and $p_T\rightarrow 0$ by the charm, bottom and Z^0 productions for $PbPb$ and pp collisions.

7.2 PYTHIA Generation

The leading order event generator PYTHIA 6.326 [45] was used to simulate the production of Z^0. Only the leading order Born processes were generated. PYTHIA offers the possibility to take into account the contributions of 2→2 processes, $q+\overline{q}\rightarrow\gamma^*/Z^0+g$ and $q(\overline{q})+g\rightarrow\gamma^*/Z^0+q(\overline{q})$, where the vector boson is recoiling against a jet. The calculations work well when p_T is of the

order of Q^2. However, as $p_T \to 0$, correction terms that are proportional to $\alpha_s \ln(Q^2/\mathrm{p}_T^2)$ become significant for all values of α_s and the cross-sections diverge. Thus, a cut-off on p_T has to be carefully chosen in PYTHIA. Physically, the divergences are due to the presence of collinear and low-p_T gluons that are not properly accounted for in the standard perturbation expansion. At leading order, it is better to use the parton showers algorithms of PYTHIA in addition to the Born processes to simulate the inclusive Z^0 production. This produces initial- and final-states QCD radiations that generate additional jets. To avoid double-counting the $2 \to 2$ processes have to be completely turned off. The CTEQ5L PDF's [46] are used together with some tuned parameters [47]. With the parameter MSTP(44) one can choose to simulate the complete γ^*/Z^0 interference or the pure Z^0 component. The γ^*/Z^0 interference leads to an enhancement of about 1.85 % of the dilepton yield in the mass range $66 < M_{e^-e^+} < 116\,\mathrm{GeV/c^2}$ for pp collisions at 14 TeV and reduces considerably the statistics in the high mass region. Pure Z^0 was simulated for this work.

The ROOT [48] interface to PYTHIA 6, originally written in FORTRAN code, allows to program in C++. Moreover, to check the fast parametrized response of the detectors, the interface in AliRoot [49] was also used. In this way, the particles generated by PYTHIA are propagated through a realistic implementation of the ALICE detectors with Geant 3 [50], producing secondary particles. The QCD process was defined in AliRoot/PYTHIA6/AliPythia. To force the electronic decay of the produced Z^0, a AliDecayer case was added.

7.2.1 Comparison with total $W^{\pm}$ and Z^0 cross-sections at CERN Collider and Tevatron

Since their discovery by the UA1 and UA2 collaborations the intermediate Z^0 and $\mathrm{W}^{\pm}$ vector bosons have been copiously observed at higher energies in $p\bar{p}$ collisions. They have been detected through their leptonic decay channels ($Z^0 \to l^- l^+$) and semi-leptonic channels ($W^{\pm} \to l\nu_l$) using calorimeters.

$\sqrt{s}$ [GeV]	experiment	$\sigma(p\overline{p} \to Z^0 X \to e^+e^- X)$ [nb]
546	UA1[51]	$0.042 \pm^{0.033}_{0.020} \pm 0.006$
546	UA2[52]	$0.116 \pm 0.039 \pm 0.011$
630	UA1[51]	$0.071 \pm 0.011 \pm 0.011$
630	UA2[52]	$0.0656 \pm 0.004 \pm 0.0038$
1800	D0[53]	$0.221 \pm 0.003 \pm 0.004 \pm 0.010$
1800	CDF[54, 55, 56]	$0.248 \pm 0.004 \pm 0.003 \pm 0.010$
1960	D0[53, 57, 58, 59]	$0.2649 \pm 0.0039 \pm 0.0085 \pm 0.0051 \pm 0.0172$
1960	CDF[54, 55, 56]	$0.2549 \pm 0.0033 \pm 0.0046 \pm 0.0152$

Table 7.2: Z^0 production in cross-section $\sigma(p\overline{p} \to Z^0 X \to e^+e^- X)$ measured for different center-of-mass (c.m.s) energies.

Table 7.2 and 7.3 summarize the inclusive Z^0 and $W^{\pm}$ cross-sections times the electronic ($Z^0 \rightarrow e^+e^-$ Br=3.363 % [1]) and semielectronic ($W^{\pm} \rightarrow e\nu_e$ Br=10.72 % [1]) branching ratio that have been experimentally found at different c.m.s energies. Due to the l-ν lepton universality in $W^{\pm}$ and Z^0 decays, the measured cross-sections in the muonic decay channels are very similar. At a given energy, the $W^{\pm}$ cross-section is about 10 times higher than the Z^0's.

$\sqrt{s}$ [GeV]	experiment	$\sigma(p\overline{p} \rightarrow W^{\pm}X \rightarrow e\nu_e X)$ [nb]
630	UA1[51]	0.63±0.04±0.10
630	UA2[51]	0.682±0.012±0.040
1800	D0[60]	2.310±10±50±100
1800	CDF[61, 62]	2.49±0.12
1800	CDF[61, 62]	2.19±0.04±0.21
1960	D0[60]	2.8652±0.0083±0.0628±0.0404±0.1862
1960	CDF[56]	2.749±0.010±0.053±0.165

Table 7.3: $W^{\pm}$ production in $\sigma(p\overline{p} \rightarrow W^{\pm}X \rightarrow e\nu_e X)$ measured for different c.m.s energies.

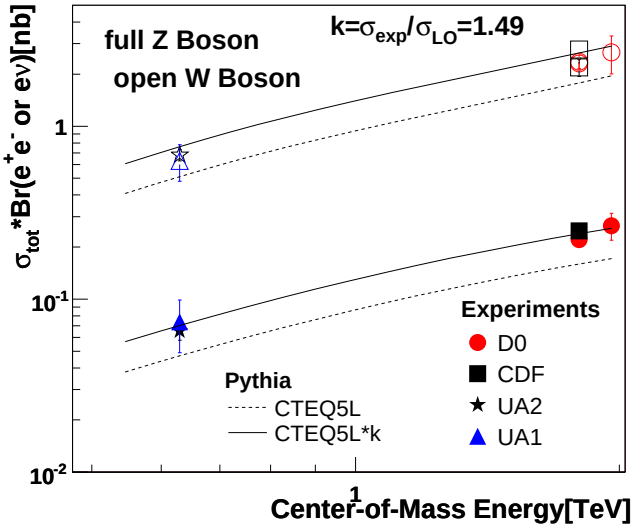

Figure 7.2: Production cross-section times branching ratio into electrons for Z^0 and $W^{\pm}$-boson in $p\overline{p}$-collisions as a function of the c.m.s energy.

Fig. 7.2 illustrates the Tables. The inclusive Z^0 and $W^{\pm}$ cross-sections times branching ratio are shown as a function of the c.m.s energy. The measurements of the UA1, UA2 [51], CDF [54] [61], and D0 [53] [60] experiments are compared with the PYTHIA results without a scale factor (dashed line) and with a scale factor of 1.49 (full line). Since the lowest-order processes contribute to a large percent of the total $W^{\pm}$ and Z^0 production, the higher-order corrections can be approximated by an effective k factor, that depends weakly to the c.m.s energy. Moreover the ratio $\frac{\sigma_{tot}(Z^0) \times Br(e^+e^-)}{\sigma_{tot}(W^{\pm}) \times Br(e\nu_e)}$ is well reproduced by PYTHIA.

7.2.2 Comparison with p_T- and y-spectra at Tevatron

The transverse momentum (p_T) spectrum of the Z^0 boson has been measured by the CDF[54] and the D0[53][60] collaborations in $p\bar{p}$ collisions at 1800 GeV c.m.s energy. In the parton model, at lowest order, Z^0 bosons are produced in head-on $q\bar{q}$ collisions. The vector boson cannot have any transverse momentum. The formation time is proportional to $1/(cM_{Z^0})=1/Q$. As Q increases, the size of the colliding parton system decreases. By the uncertainty principle, the momentum distribution of the partons broadens. This can be interpreted by the radiation of gluons within the color field of the nucleon, that carry away transverse momentum from the quarks. As a consequence the observed p_T distribution of any dielectron system produced at a scale $Q{\approx}cM_{e^+e^-}$ gets broader when Q increases. The average p_T of the Z^0 boson ($M_{Z^0}{\approx}91\,\mathrm{GeV/c^2}$) is also expected to be higher than the average p_T of the $W^{\pm}$ boson ($M_{W^{\pm}}{\approx}80\,\mathrm{GeV/c^2}$).

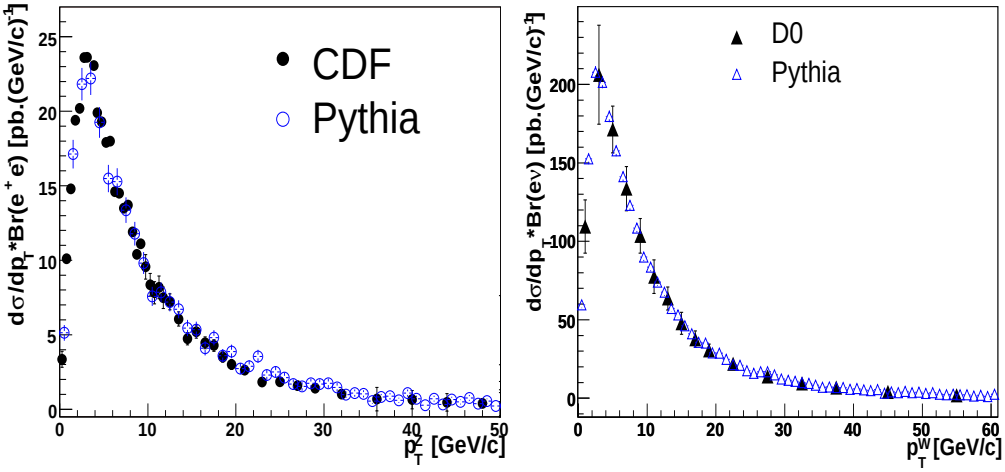

Figure 7.3: Transverse momentum spectra of Z^0 (left) and $W^{\pm}$ (right) from $p\bar{p}$ collisions at $\sqrt{s}$=1800 GeV, compared to PYTHIA simulations.

Fig. 7.3 shows the transverse momentum spectra of the Z^0 boson, $p_T^{Z^0}$ (left), and the $W^{\pm}$ boson, $p_T^{W^{\pm}}$ (right), as they are respectively obtained by the CDF and D0 collaborations. Z^0 boson is measured in the mass range $66{<}M_{e^-e^+}{<}116\,\mathrm{GeV/c^2}$. The average p_T is found to be about 6 GeV/c for the Z^0 and 5 GeV/c for the $W^{\pm}$ boson. The p_T distributions are compared with our PYTHIA simulations. The simulations have been normalized to the measured inclusive cross-section, $\sigma_{tot}(p\overline{p}{\rightarrow}Z^0\,{\rightarrow}e^+e^-){=}252$ pb and $\sigma_{tot}(p\overline{p}{\rightarrow}W^{\pm}\,{\rightarrow}e\nu_e){=}2.31$ nb at $\sqrt{s}$=1800 GeV. A good agreement is achieved. The initial and final state QCD radiations, simulated via the parton shower algorithms of PYTHIA, allow to reproduce the measured data even in the tail of the spectrum.

The rapidity (y), spectrum of the Z^0 has been measured up to $|y|$=2.8 by the CDF collaboration[54] in $p\bar{p}$ collisions at 1800 GeV. The momentum fraction x_1 (x_2) of the partons in the proton (antiproton) is related to the rapidity of the dileptons through the relation.7.2.

Thus the Z^0 bosons produced at large rapidity originate from events in which one parton is at large x and the other parton is at very small x. The kinematic limit is given by the case x=1.0:

$$y_{MAX} = \pm \ln(\frac{\sqrt{s}}{c^2 M_{Z^0}}) \tag{7.3}$$

At the Tevatron, where $\sqrt{s}$=1800 GeV, $|y|$<3.0. Therefore the CDF experiment covers nearly the entire kinematic region of rapidity. This is remarkable since most measurements at high energy proton-antiproton collisions are performed only in the central rapidity production region and model dependent extrapolation for forward rapidities is needed to extract the total cross-section for hard processes. This is not the case of the CDF Z^0 results which provide a test of the theory. Fig. 7.4 shows the measured differential y cross-section in $p\bar{p}$ collisions at 1800 GeV compared with PYTHIA simulations. The agreement is good.

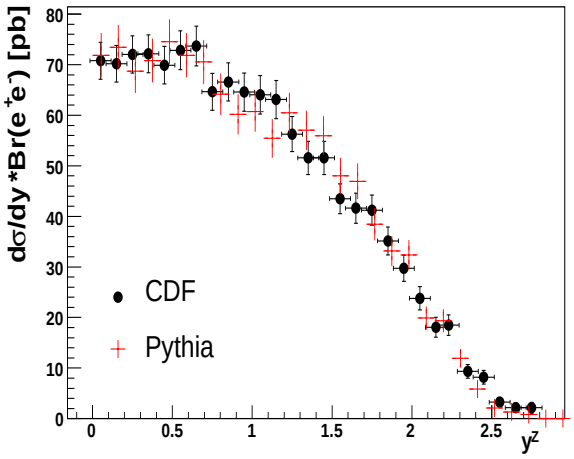

Figure 7.4: Rapidity distribution of Z^0 measured by the CDF collaboration in $p\bar{p}$ collisions at 1800 GeV[54] and compared with PYTHIA simulations.

7.2.3 Predictions for pp collisions at the LHC energy

The cross-section at the LHC, calculated with an inelastic pp cross-section of 79 mb and PYTHIA assuming the same k-factor as at lower energies, are shown in Table 7.4.

14 [TeV]	$\sigma^{X_{pp}} \times Br(e)$ [nb]	NNLO [nb][43]	$N^{X_{pp}}$
$Z^0 \rightarrow e^+e^-$	≈2.4	≈1.84	3×10^{-8}
$W^{\pm} \rightarrow e\nu_e$	≈23.8	≈19.8	3×10^{-7}

Table 7.4: Extrapolated inclusive cross-sections with PYTHIA and a k factor of 1.5 for pp collisions at 14 TeV compared with NNLO calculations

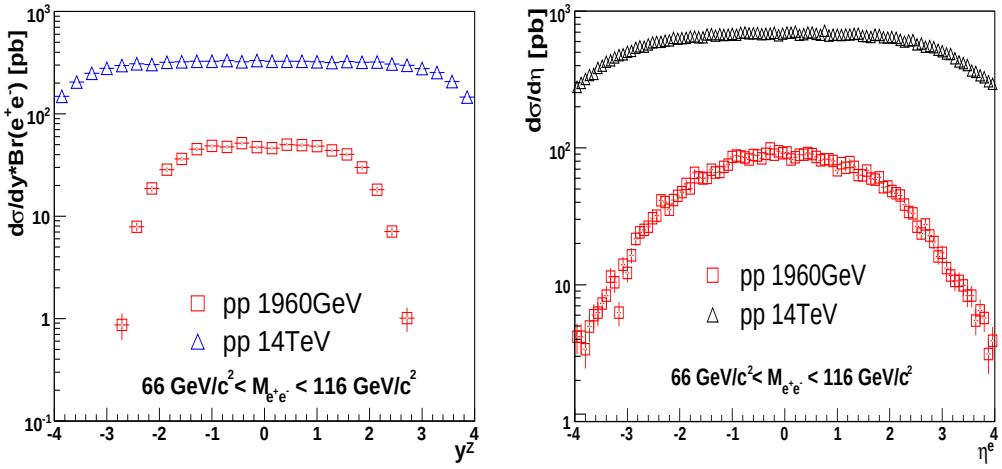

Figure 7.5: Rapidity distributions of Z^0 (left) and its decay electrons (right) for pp collisions at 1.96 and 14 TeV c.m.s energy.

In Fig. 7.5 the Z^0 and electrons differential cross-sections are presented respectively as a function of the rapidity y and the pseudo-rapidity η for pp collisions at 14 TeV. For comparison the same differential cross-sections are shown for pp collisions at 1.96 TeV. The simulations are normalized to the inclusive cross-sections times electronic branching ratio evaluated with PYTHIA and a scale factor of 1.5. At the LHC, the kinematic limit of the Z^0 rapidity, given by Eq. 7.3, is about 5 ($|y|$<5), compared to 3 at Tevatron energies. The y and η distributions are therefore wider for increasing $\sqrt{s}$. As a consequence, at higher energy a smaller relative fraction of Z^0 are in the geometrically acceptance of detectors covering the same rapidity range.

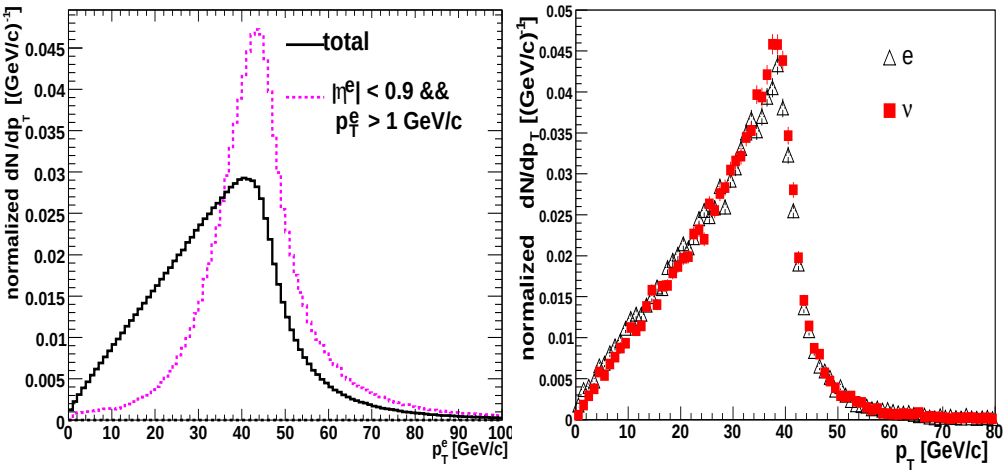

Figure 7.6: p_T normalized distributions of electrons from Z^0 decays in the total phase space (solid) and inside the acceptance (dotted) of the central barrel (left) and normalized p_T distributions of electrons and neutrinos from $W^{\pm}$ weak decays in the total phase space (right), simulated for pp collisions at 14 TeV.

The left panel of Fig. 7.6 shows the transverse momentum distributions of electrons emitted in Z^0 decays in the total phase space and within the acceptance of the central barrel. The distributions are normalized to unity. The p_T distribution in the total phase space shows a peak in the region between 38 and 50 GeV/c, corresponding to about half the mass of the intermediate vector boson, $cM_{Z^0}/2$ (45 GeV/c). The central barrel acceptance ($|\eta|<0.9$) has the effect to select electrons with small longitudinal momentum component, p_L.

$$\eta = -\ln(\tan(\frac{\theta}{2})) = \frac{1}{2}\ln(\frac{p+p_L}{p-p_L}) \tag{7.4}$$

As a consequence the high p_T electrons are favored. The normalized p_T distribution within the detectors acceptance is harder. In the right panel of Fig. 7.6 the p_T normalized distributions of electrons and neutrinos coming from $W^{\pm}$ weak decays in the total phase space are represented. The distributions peak at about $cM_{W^{\pm}}/2$ (40 GeV/c) and are similar with the one of electrons from Z^0 decays.

Chapter 8

Z^0 production in heavy-ion collisions

Concerning particle production via hard processes, a nuclear collision, in first order, is a superposition of independent nucleon-nucleon collisions. The differential yields scale from pp to $PbPb$ proportionally to the number of inelastic nucleon-nucleon collisions. The number of binary collisions can be estimated with the Glauber model[63]. However, there are two sorts of effects that can break the binary scaling.

- Initial-state effects, like modification of the Parton Density Functions (PDF's) in the nucleus. This effects can be studied by comparing pp collisions and pA collisions.
- Final-state effects, particularly interesting for partonic QCD final-states. The partons, interacting with the medium formed in the collision, probe its properties (temperature, volume, gluon density).

For Z^0 production in $PbPb$ collisions, only initial-state effects are relevant.

8.1 Number of nucleon-nucleon collisions

The Glauber model describes the nucleus-nucleus interactions as a superposition of independent nucleon-nucleon interactions. It assumes that the nucleons suffering several collisions don't deflect from their incident straight-line trajectory and don't loose energy. The nucleon-nucleon collisions are treated incoherently and thus are unaffected by any other scattering taking place before (initial-state) or after (final-state effects). At high energy the straight-line trajectory (eikonal limit) is a very good approximation. A schematic view of the geometry of the collision between two nuclei with mass numbers A and B is shown in Fig. 8.1. The physical variables in the Glauber formalism are:

- σ_{NN}, the inelastic nucleon-nucleon cross-section.
- the nucleon density distributions inside the nuclei, $\rho_A(\mathbf{s_A}, z_A)$ and $\rho_B(\mathbf{s_B}, z_B)$.

$$\int \rho_A(\mathbf{s_A}, z_A) d\mathbf{b_A} dz_A = 1 \tag{8.1}$$

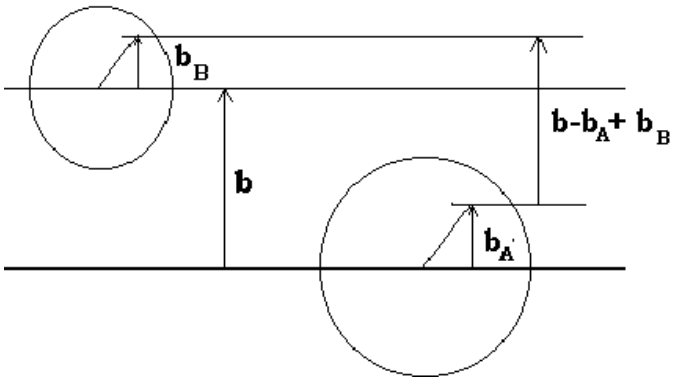

Figure 8.1: Collision of two nuclei at an impact parameter b

For a nucleus-nucleus collision at an impact parameter $\mathbf{b}$, the probability, $p(\mathbf{b})$, that a pair of nucleons undergoes a collision is:

$$p(\mathbf{b}) = \int \rho_A(\mathbf{s}, z_A) \cdot \rho_B(\mathbf{s} - \mathbf{b}, z_B) d\mathbf{s} dz_A dz_B \cdot \sigma_{NN} \tag{8.2}$$

$p(\mathbf{b})$ can be expressed in terms of the nucleus-nucleus overlap function $T_{AB}(\mathbf{b})$.

$$T_{AB}(\mathbf{b}) = \int \rho_A(\mathbf{s}, z_A) \cdot \rho_B(\mathbf{s} - \mathbf{b}, z_B) d\mathbf{s} dz_A dz_B \tag{8.3}$$

$$p(\mathbf{b}) = T_{AB}(\mathbf{b}) \cdot \sigma_{NN} \tag{8.4}$$

$T_{AB}(\mathbf{b})$ represents the nucleon density per surface unit and is normalized to unity if integrated over all impact parameters.

$$\int T_{AB}(\mathbf{b}) d\mathbf{b} = 1 \tag{8.5}$$

If the two nuclei are not deformed or oriented, $T_{AB}(\mathbf{b})$ depends only on the magnitude of $\mathbf{b}$.

The number of inelastic nucleon-nucleon collisions can be as high as $A \times B$. If they are considered independent, with the probability $p(\mathbf{b})$ to occur for each nucleon pair, the probability of occurrence of n inelastic nucleon-nucleon collisions follows a binomial distribution:

$$P(n, \mathbf{b}) = \binom{AB}{n} (p(\mathbf{b}))^n (1 - p(\mathbf{b}))^{AB-n} \tag{8.6}$$

The mean number of nucleon-nucleon collisions at fixed $\mathbf{b}$ is then given by:

$$\langle N_{coll} \rangle(\mathbf{b}) = \sum_{n=0}^{AB} nP(n, \mathbf{b}) = AB \cdot p(\mathbf{b}) = \sigma_{NN} \cdot AB \cdot T_{AB}(\mathbf{b}) \tag{8.7}$$

From this last expression the nuclear overlap function $T_{AB}(\mathbf{b})$ $[\mathrm{mb}^{-1}]$ can be thought as the time integrated luminosity (reaction rate per unit cross-section) per AB collision at a given impact parameter.

The participants are the nucleons of A and B which have undergone at least one inelastic collision. It is obtained from the following equation[64]:

$$\langle N_{part}(\mathbf{b})\rangle = \int d^2s\{AT_A(\mathbf{s})[1-(1-\sigma_{NN}T_B(\mathbf{b}-\mathbf{s}))^B]+BT_B(\mathbf{b}-\mathbf{s})[1-(1-\sigma_{NN}T_A(\mathbf{s}))^A]\} \quad (8.8)$$

The number of spectators can then be calculated as:

$$\langle N_{spect}(\mathbf{b})\rangle = A + B - \langle N_{part}(\mathbf{b})\rangle \quad (8.9)$$

Experimentally the number of participants can be extracted from the energy deposited by the spectators. The measurement of the energy carried by the non-interacting nucleons in the forward direction, at zero degree relative to the beam direction gives an estimation of $\langle N_{spect}\rangle$. In ALICE, spectator nucleons are detected by means of Zero-Degree Calorimeters (ZDC's) [9], placed at 116 m from the Interaction Point (IP). Another way to access the collision centrality is via the charged particle multiplicity. The latter can be determined via tracklets in the two innermost layers of the Inner Tracking System (ITS) ($|\eta|<2$), the tracks reconstructed by the full tracking procedure in ITS and Time Projection Chamber (TPC) ($|\eta|<0.9$) or the energy deposited in the pads of the Forward Multiplicity Detector (FMD) ($-3.4<\eta<-1.7$).

8.2 Application of Glauber Model to hard processes

In the same way as one obtains the expression for the mean number of binary collisions, $\langle N_{coll}\rangle(b)$, in a nucleus-nucleus reaction with impact parameter b, the average yield for a hard process in a nucleus-nucleus collision at a given impact parameter can be expressed as a function of the nuclear overlap function $T_{AB}(b)$:

$$\langle N_{AB}^{hard}\rangle(b) = \frac{d\sigma_{AB}^{hard}}{db}/\frac{d\sigma_{AB}^{inel}}{db} = \sigma_{NN}^{hard}\cdot AB\cdot T_{AB}(b) \quad (8.10)$$

where σ_{NN}^{hard} is the production cross-section of the hard process in nucleon-nucleon collision. From Eq. 8.7 and 8.10, we get the so-called binary collision scaling formula for the hard scattering yields in heavy-ion collisions.

$$\langle N_{AB}^{hard}\rangle(b) \approx \langle N_{coll}\rangle(b)\cdot N_{NN}^{hard} \quad (8.11)$$

The way to compute $\langle N_{AB}^{hard}\rangle$ (b) for a given hard process is first to determine, via a Glauber Monte Carlo calculation, the average number of inelastic NN collisions corresponding to a centrality class using Eq. 8.7, and then to deduce $\langle N_{AB}^{hard}\rangle$ (b) from the corresponding yield in pp collisions via Eq. 8.11.

Hard scattering is more enhanced for increasingly central reactions, with large number on N_{coll}, as compared to the total reaction cross-section, which includes soft (i.e scaling with the number of participant nucleons) as well as hard contributions.

8.3 Z^0 production in $PbPb$ collisions at 5.5 TeV

8.3.1 Geometrical scaling

We investigated the cases of a minimal-bias, central (0-10 %) and very central (0-5 %) $PbPb$ collisions at 5.5 TeV. To estimate the number of nucleon-nucleon collisions we used the program [65]. The nucleon density in Pb is described by a Woods-Saxon distribution:

$$\rho(r) = \frac{n}{1 + exp(\frac{r-r_0}{d})} \tag{8.12}$$

It is normalized to the number of nucleons and the respective values of the parameters r_0 and d are 6.49 fm ($\approx$1.12·A$^{1/3}$-0.86·A$^{-1/3}$) and 0.54 fm with A=208[66]. The factor n is given by the normalization, n= 7.69 (1/(fm^3*A)). From Eq. 8.12 and 8.3, the nucleus-nucleus overlap function $T_{AB}(\mathbf{b})$ can be evaluated for a given impact parameter. The nucleon-nucleon inelastic cross-section, σ_{NN}, is about 70 mb at 5.5 TeV. Using Eq. 8.7 and 8.8, the number of nucleon-nucleon collisions and participants can be calculated and averaged over the impact parameter range. Table 8.1 summarizes our results.

	5 %	10 %	Min-Bias
b_{Max} [fm]	3.5	5.1	100
$\langle N_{coll} \rangle$	1669	1498	353
$\langle N_{part} \rangle$	374	344	102
$\langle N^{Z^0}_{PbPb} \rangle$	1.836×10^{-5}	1.648×10^{-5}	3.883×10^{-6}

Table 8.1: Mean number of nucleon-nucleon collisions ($\langle N_{coll} \rangle$) and participants ($\langle N_{part} \rangle$) for $PbPb$ collisions at 0-5 % and 0-10 % centrality and minimum-bias with $\sqrt{s}$=5.5 TeV and the resulting Z^0 yield.

The yield in nucleon-nucleon collisions has been estimated with PYTHIA and a scaling factor of 1.5 (see Table 8.2). Finally the Z^0 yields were computed using the binary scaling (Eq. 8.11). They are given in Table 8.1.

$\sqrt{s}$ [TeV]	σ_{pp} [mb]	$\sigma^{Z^0_{pp}} \times Br(e)$ [pb]	$\langle N^{Z^0_{pp}} \rangle$
5.5	69	758	1.1×10^{-8}

Table 8.2: The Z^0 yield per pp collision at 5.5 TeV.

The expected number of Z^0 events at 0-10 % is about 286 events in one ALICE running year (10^6). We assume a data acquisition bandwidth of 20 Hz for central collisions, which gives a total number of recorded events of 2×10^7 events. The total acceptance of Z^0 in the detector is

estimated to be about 5 % at 5.5 TeV. Finally we expect about 16 Z^0 recorded by the ALICE central barrel per year.

8.3.2 Break of the binary collision scaling

Cold and hot nuclear effects can break the geometrical scaling. By the uncertainty principle Z^0 bosons are created approximately $1/(c^2 M_{Z^0}) \approx 0.002$ fm/c after nuclear contact and decay with a vacuum lifetime of 0.08 fm/c. They are moreover produced with a relative small velocities. Thus they will decay in a dense environment of quarks and gluons. The decay particles of the Z^0 boson are therefore expected to cross the QGP, but the leptons will exhibit no QGP effect. Due to the weak coupling with the medium, the expected change of the width is of the order of 1 MeV, which is negligible compared to the natural total width of the Z^0 (2490 ± 7 MeV)[41]. The mass shift is even smaller. The Z^0 boson should not be affected by the presence of a Quark Gluon Plasma.

However cold nuclear effects have to be considered. A broadening of the intrinsic transverse momenta of the partons is expected in the initial state from nuclear effects. The k_T broadening is due to the partons being confined in the initial-state nucleons, gluon Bremsstrahlung, as well as multiple soft scattering of the nucleons prior to the hard scattering. This will influence the p_T distribution of the vector boson but not its total cross-section.
A second cold nuclear effect, called nuclear shadowing, comes from the modification of the Parton Distribution Functions (PDF's) inside the nucleus, $f_{q_i}^A$, compared to the nucleon, $f_{q_i}^N$ (see appendix C). These are due to non-perturbative effects. Therefore the modifications are parametrized through the ratio $S = \frac{f_{q_i}^A}{f_{q_i}^N}$. The factor $S(x, Q^2, A, b)$ depends on the Bjorken value x of the parton, the energy scale Q^2, the number of nucleons inside the nucleus (A=208) and the impact parameter of the collision. At very low x the magnitude of PDF's is generally reduced through shadowing. The magnitude of the reduction of the total Z^0 cross-section is expected to be about 10 % from NLO calculations[67]. For comparison it amounts to about 35 % for $c\bar{c}$ pairs and 15 % for $b\bar{b}$ pairs using the EKS98 parametrization[68].

Chapter 9

Response of the ALICE central barrel

9.1 Fast Simulation

9.1.1 Why Fast Simulation?

To study the possibility to detect the Z^0 in the ALICE central barrel, detailed simulations of the detector signals are needed. AliRoot [49] is an object oriented framework, that describes the ALICE detector. It contains a detailed description of the geometry of all sub-detectors. It enables the three different steps of the simulation:

- **Generation of *pp* or *PbPb* collisions**: hadron and heavy-ion collisions are simulated with the help of event generators. AliRoot includes interfaces to several event generators. The most important ones are PYTHIA 6 [45] and 8 [69], and HIJING (Heavy-Ion Jet INteraction Generator) [70]. PYTHIA is a Leading Order perturbative QCD generator, used for simulation of nucleon-nucleon interactions. HIJING is a QCD-inspired model of jet production. It has been developed and systematically compared with data, by taking particularly into account the role of mini-jets in *pp*, pA and AA reactions at collider energies. Binary scaling with the Glauber model is used to extrapolate *pp* collisions to pA and AA collisions. Jet quenching, related to the energy loss of partons in nuclear matter, and shadowing are moreover implemented. The simulation of heavy-ion collisions with HIJING takes a considerable amount of computing time. That is why, a parameterized version of this generator, AliGenHIJINGpara, is also part of AliRoot. It is based on parametrized pseudo-rapidity density and transverse momentum distributions of charged and neutral pions and kaons.
  The output of the generation step consists of the expected particles produced in the collisions with their initial momenta and energies.

- **Propagation of all particles through the detectors**: the particles created in the collision can decay, interact with the detector material and produce additional secondary particles, which will also propagate through the detectors. The final amount of particles is of the order of three to four times the number of particles generated initially in the interaction. This is characterized by the so-called material budget of the detectors. All

tracking detectors around the interaction point are designed such that their respective performance is optimized keeping a reasonable amount of material quantified in terms of the radiation length. The production of too many secondary particles has to be avoided, otherwise the tracking efficiency is reduced and the initial signal is deteriorated and finally destroyed.
In AliRoot, particles are propagated through the detectors using interfaces to transport packages. Geant 3 [50] is the one commonly used but the framework gives also the possibility to use Geant 4 [71] or Fluka [72]. Interactions with the detector material produce hits, which represent the intermediate output. Each sub-detector collaboration is then responsible for the simulation of the corresponding digital output of the detector electronics. The final output is the sub-detector digits. Under digits, we simply understand the detector signal as it is recorded in reality. Thus the first and second steps are pure simulation, whereas the last step (reconstruction of the events) is common to simulated and real data.

- **Reconstruction of the events**: the detector signal is analyzed to identify tracks and reconstruct their momenta and particle types. The particle identification is given as probabilities for several particle types ($e^{\pm}$, $\mu^{\pm}$, $\pi^{\pm}$, $K^{\pm}$, $(p,\bar{p})$). The primary vertex and secondary decay vertices are determined by algorithms on tracks. The final output is the ESD (Event Summary Data), which contains all the information of the reconstructed events.

This kind of simulations consumes a considerable amount of computing time (about 2-3 min per event in pp collisions at $\sqrt{s}$=14 TeV). Therefore it is called slow simulation. The vector boson Z^0 is a rare probe and its production cross-section times electronic branching ratio is about 10^{-8} smaller than the total inelastic cross-section in pp collisions. This means that one has to simulate about 10^9 inelastic pp collisions to have 100 produced $Z^0 \rightarrow e^+e^-$. A huge among of events are needed to gather enough statistics to study the sources of background with much higher cross-sections. Thus it is impossible to carry out reliable simulations with conventional methods. Therefore the propagation of the particles through the detectors and the reconstruction of the events are replaced by a parametrization prepared specifically for individual sub-detectors (e.g. the muon-arm or the detectors in the ALICE Central Barrel (ACB)).

9.1.2 The concept of Fast Simulation

The Fast Simulation of the ACB does not perform the whole cycle described before, but produces directly from the particles generated in hadron collisions the tracks reconstructed in the central barrel. Two points have to be underlined. First, since the generated particles are not propagated through the detectors, the secondary particles are not taken into account. Then, only the reconstructed vector momentum at the primary vertex and the particle identification probabilities of the track are stored. No information about the impact parameter of the track

is available at the end. Fast Simulation is therefore not suitable for studies implying impact parameter cuts or reconstruction of secondary vertices. Onces these simplifications are taken into account, the questions, one has to answer for each generated particle, are:

- if the particle is reconstructed as a track.
- what is the resolution of its reconstructed vector momentum.
- if the particle type is correctly identified.

The answers of these three questions are contained in so-called response functions or lookup tables (LUTs). They are generated by analysing a small but significant number of slow simulated events for a given running condition (given multiplicity and magnetic field). They should give the same final answer as the full chain of simulation but in a much smaller time.

9.2 Response Functions

9.2.1 What has to be parametrized?

To reproduce the behaviour of the detector, the following has to be known:

- **The single particle reconstruction efficiency**: the efficiency, ϵ, gives the probability that the particle is detected and tracked in the ALICE central barrel. It includes the acceptance of the central barrel and the tracking efficiency. The acceptance, *acc*, is defined by the dead areas and support structures, that might stop the particles. All particles in the acceptance produce hits in the detectors and have a given probability, the tracking efficiency ϵ_{tr}, to be tracked by the detector algorithms. The main restricting factor comes from the acceptance. The reconstruction probability is stored in the response functions.
- **The resolution**: the resolution describes the accuracy of the reconstructed transverse momentum p_T, polar angle θ and azimuthal angle ϕ of the tracks at their production vertex. More precisely the probability distributions of $\Delta x = x_{generated}$-$x_{reconstructed}$, where x is one of the three physical variables, p_T, θ or ϕ, are needed. Most of the time they correspond to a Gaussian function around zero and can be completely characterized by their width σ. A more complicated probability distribution has to be parametrized for the p_T resolution of electrons, due to Bremsstrahlung. The parameters of the fit functions are stored in the resolution LUTs.
- **The PID**: to identify electrons emitted in Z^0 electronic decays, the dE/dx information of the Time Projection Chamber (TPC) and the transition radiation produced in the radiators of the Transition Radiation Detector (TRD) are used. The main difficulty comes from the much more numerous $\pi^{\pm}$, that can be misidentified as electrons. At such high p_T ($30\,\mathrm{GeV/c} \leq p_T \leq 50\,\mathrm{GeV/c}$), the dE/dx energy loss measurement in the TPC brings only little information. Thus the main task of the TRD is to differentiate electrons from pions

using transition radiation. The percentage of misidentified $\pi^{\pm}$ is quantified by the $\pi^{\pm}$ efficiency, ϵ_{π}, for a given electron efficiency, ϵ_e, taken equal to 90 %. Other particles, such as kaons or protons, may also be mis-identified as electrons. Their rate are nevertheless much lower than the rate of pions. That is why they can be neglected. The probability for a pion to be misidentified as an electron is stored in the response functions.

9.2.2 What does it depend on?

Different kinds of dependencies have to be taken into account. First the LUTs are built for particular running conditions and types of analysis. Then the response functions themselves depend on the kinematic variables and the type of generated particles.

Global dependencies

Dependencies on the running conditions The tracking efficiency depends on the multiplicity of charged particles in the physics events. For instance the large multiplicities expected in *PbPb* collisions at 5.5 TeV put demanding and different requirements on the tracking code compared to the small multiplicity in *pp* collisions at 14 TeV. This will influence mainly the reconstruction efficiency but also the p_T, θ and ϕ resolution. As a consequence the LUTs have to be generated for a given multiplicity.
The nominal value of the magnetic field B is 0.5 T. A priori there is no plan to run at different values of B. Nevertheless, since p_T is determined by the curvature r_c of the tracks in the magnetic field ($p_T[GeV]$=0.3 q $B[T]$ $r_c[m]$, qe is the total particle charge), its resolution depends on B. A smaller value of B decreases the p_T resolution. In this work, one considers only the case of nominal magnetic field.
Dependencies on the event and track quality cuts The track quality cuts play not only a role in the p_T, θ and ϕ resolution, but also decrease the reconstruction efficiency. That is why the same cuts applied in the physics analysis are mandatory to build the LUTs.

Dependencies on the primary generated particle

Dependencies on the particle vector momentum The reconstruction efficiency and resolution depend naturally on the geometry of the central barrel. Therefore their parametrizations are functions of the form F(p_T,θ,ϕ). The production of transition radiation depends on the γ factor of the particle. The final ϵ_{π} of the ACB is parametrized as a function of the momentum p of the pions.
Dependencies on the particle type Whereas the tracking efficiency, and θ and ϕ resolutions can be, in a good approximation, considered independent of the particle type, the p_T resolution of the electrons is worse than for the other types of particles. The electron energy loss by Bremsstrahlung results in a smaller reconstructed p_T at its production vertex. In cases where the electron is highly energetic, the photon will be emitted in the direction of the electron momentum and Bremsstrahlung in the ITS affects only the measurement of $\Delta\phi$ given by

the smaller curvature of the track in the magnetic field. The variables ϕ and θ are correctly reconstructed at the production vertex. Therefore in a first approximation only p_T resolution LUTs have to be built separately for electrons and pions.

9.2.3 How can the dependencies be optimized?

Functions of the form F(p_T,θ,ϕ) require the analysis of a non-negligible amount of slow simulated events. In theory the values of the variables have to be evaluated over a discrete 3D (p_T,θ,ϕ) map covering the geometrical acceptance of the ACB in θ ($40°\leq\theta\leq140°$) and ϕ ($0\leq\phi\leq2\pi$), and the p_T range of interest (here $1\,\mathrm{GeV/c}\leq p_T\leq100\,\mathrm{GeV/c}$). Assuming that about 1,000 generated particles are needed for each (p_T,$p_T+\Delta p_T$; θ,$\theta+\Delta\theta$; ϕ, $\phi+\Delta\phi$) bin, equidistant bins with bin widths of Δp_T=10 GeV/c, $\Delta\theta=\frac{\pi}{150}$ rad and $\Delta\phi=\frac{\pi}{45}$ rad lead to the necessity of about 10^8-10^9 primary particles. To reduce this number, one can take advantage of two particular properties of the response functions.

Separation of the θ and ϕ variables

If the θ and ϕ variables can be separated, then the response functions F can be written as:

$$F(p_T,\theta,\phi)=\frac{F_1(p_T,\theta)\times F_2(p_T,\phi)}{C(p_T)} \tag{9.1}$$

$$F_1(p_T,\theta)=\int F(p_T,\theta,\phi)d\phi \tag{9.2}$$

$$F_2(p_T,\phi)=\int F(p_T,\theta,\phi)d\theta \tag{9.3}$$

$$C(p_T)=\int F_1(p_T,\theta)d\theta=\int F_2(p_T,\phi)d\phi \tag{9.4}$$

F is the function that has to be known. Instead of storing its value in a 3D discrete $p_T\times\theta\times\phi$ maps, it can be calculated from the functions F_1 and F_2, that depend only on two variables and whose values can be stored in two 2D discrete $p_T\times\theta$ and $p_T\times\phi$ maps. The factor C will then appear as the projection of F_1 and F_2 on the p_T axis. This reduces the number of necessary primary particles by a factor 100. Nevertheless one has to check if the response functions fulfill the (θ,ϕ) separation condition. It was also shown in the reference [73] that the response functions created by using the separation produce the same final signal as with the full reconstruction chain. As a conclusion, the efficiency and resolution response functions are stored in 2D $p_T\times\theta$ and $p_T\times\phi$ maps.

Use of the detector symmetry

Still the F_1 and F_2 functions require about 10^6-10^7 primary particles to be built. Another way to reduce this number is to use the geometrical symmetries of the ITS-TPC-TRD. The central barrel presents a periodic symmetry of $\frac{2\pi}{18}$ in ϕ and a symmetry in θ relative to the mid-rapidity plane. Thus statistical errors can be improved by projecting the ϕ-space in the interval $[0,20°]$

and the θ-acceptance-space ($40\,°<\phi<140\,°$) in the interval [40 °,90 °]. The range in p_T, θ and ϕ of the 2D maps are respectively [10 GeV/c,100 GeV/c] (or [1 GeV/c,10 GeV/c] for low p_T studies) , [0.69 rad,1.57 rad] and [0 rad,0.35 rad].

9.3 Build of response functions

9.3.1 Simulated events

The LUTs are built by analyzing events produced within the AliRoot framework using the slow simulation procedure. Low- and High- multiplicity events were considered. However since this thesis is dedicated to the study of Z^0 in pp collisions, only a few High-multiplicity events were simulated to compare the integrated performances as a function of p_T, θ or ϕ with the Low-multiplicity case. Only a few particles have a transverse momentum above 10 GeV/c in pp collisions at 14 TeV. The response functions have to be created for particles with momentum between 10 and 100 GeV/c. That is why, instead of using pp collisions, a flat distribution of $\pi^{\pm}$ and $e^{\pm}$ over the p_T range [10 GeV/c,100 GeV/c] is generated in the geometrical acceptance of the central barrel with the AliGenBox event generator. It is important that this artificial particle distribution does not increase significantly the multiplicity of the events and as a consequence the occupancies of the detectors. It was shown in the reference [73] that 1,000 embedded particles per event with p_T momentum between 1 GeV/c and 10 GeV/c increase the TRD occupancy by only 3 %. We chose to simulate 60 π^+, 60 π^-, 60 e^+ and 60 e^- per events. For the High-multiplicity performances, the simulation of the heavy-ion collisions was carried out using the parametrized version of the HIJING generator, AliGenHIJINGPara, for a charged multiplicity at mid-rapidity per pseudo-rapidity unit of 4000 ($\frac{dN_{ch}}{d\eta}$). The expected multiplicity in $PbPb$ at 5.5 TeV is based on extrapolations from lower energy data and has big uncertainties [9]. It lies between 3000 and 4000. The same distribution and multiplicity of $\pi^{\pm}$ and $e^{\pm}$ were embedded to the physics events. All the simulations were performed with the nominal magnetic field of 0.5 T. For the creation of the response functions respectively 40,000 and 10,000 events at Low- and High- multiplicity were simulated. This corresponds to 2,400,000, and respectively 600,000, π^+, π^-, e^+ and e^-. The mean size of the reconstructed and MC information per event is of the order of 11.6 MB for Low-multiplicity and 84.9 MB for High-multiplicity. This implies a total needed disk space of about 455 GB, respectively 166 GB.

9.3.2 Analysis

The matching between generated primary particles and reconstructed tracks is assessed using the libraries of the ALICE Physics Working Group 1. They allow to see if a particle has been reconstructed in the different parts of the detector, what is the quality of the corresponding track and what is the resolution on the kinematic variables extrapolated to the primary vertex. Different quality cuts are applied at the event and track level.

Primary Vertex

The proton LHC beams cross each other at a very small angle of 300 μrad=0.0172°. As a consequence the Interaction Point (IP) is situated in the so-called interaction diamond (see Fig. 9.1).

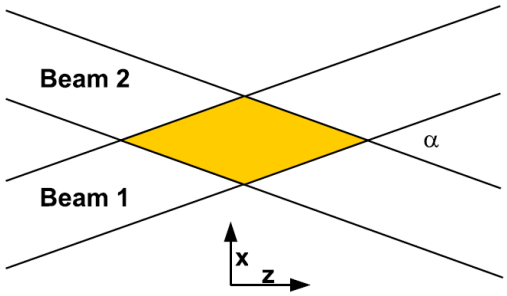

Figure 9.1: The Interaction Point (colored area) is situated in the interaction diamond due to the geometry of the beams crossing. In the xy direction, σ_{xy}≈50 μm, whereas in the z direction σ_z≈5.3 cm.

Its position is very well defined in the transverse directions x and y, orthogonal to the beam direction. On the contrary, parallel to the beam, the z coordinate of the IP is smeared out. The resulting x, y and z position distributions are Gaussian with σ_{xy}≈50 μm and σ_z≈5.3 cm. Events with generated primary vertex more than $3\times\sigma_z$ away from the nominal z-position (15.9 cm) are removed. In this work, no requirement is done on the reconstructed primary vertex. Indirectly the distance of closest approach to the reconstructed primary vertex (or its nominal position (0,0,0) if not reconstructed) is imposed to be less than $6\times\sigma_z$ (≈±32 cm in z) in the z direction. This requirement, together with the $3\times\sigma_z$ cut, ensures that pp interactions are well contained within the geometrical acceptance of the detectors. Thus the efficiency doesn't fluctuate too much in p_T,θ, and ϕ from event to event due to the position of the production vertex.

Track coming from the primary vertex

The response functions are a parametrization for particles which were created in the interaction point. Other particles created when primary particles interact with the detector material can falsify the result. They have to be removed. Fig. 9.2 shows the production vertices of the particles produced in pp events at 14 TeV in the rz plan.

The beam pipe is located at a radius of 3 cm. The low atomic number Z of beryllium (Z=4) results in a big radiation length X_0. The interaction with primary particles is small but nevertheless present. The innermost layer of the ITS is segmented in ϕ and is situated at a radius of about 3.8 cm and 4.2 cm depending on the ϕ position. It leads to a big amount of particle creations, mainly conversion electrons. Most of the conversion electrons are low-energetic, i.e.

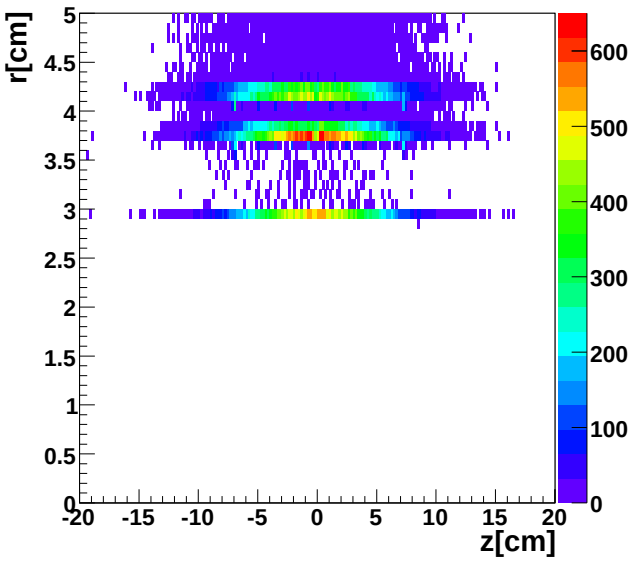

Figure 9.2: Production vertices of secondary particles, that are reconstructed and refitted in the TPC and ITS, in r (radial) and z position.

low p_T particles and can be suppressed in the analysis with a low p_T cut. A cut, performed on the distance in x, y and z directions of the particle production vertex to the MC primary vertex at $\pm 0.1\,\mathrm{cm}$, removes all secondary particles.

Track Quality

The track quality cuts should reflect the cuts applied in the analysis, here the quality cuts performed on the reconstructed electrons from Z^0 decays and background sources.
The main tracking detector is the TPC. The ITS provides useful information for the reconstruction of the particle momenta at their production vertex, since energy loss in the different ITS layers reduces the resolution of the TPC alone.
The role of the TRD is principally to identify high energetic electrons from pions. For this purpose, the particle has to be reconstructed in at least 5 planes of the TRD, otherwise the probability to misidentify a pion as an electron increases dramatically.
Strict track quality cuts will affect the reconstruction efficiency but improve the p_T,θ and ϕ resolutions and PID. The influence of different quality requirements has been studied and is presented in the next section. For the analysis related to the reconstruction of the Z^0 boson in the central barrel, the track has to be refitted from the outermost TRD detector towards the ITS during the tracking procedure (ITS-TPC-TRD refitted) and reconstructed in at least 5 planes of the TRD to assure a good PID.

9.4 Results at Low-multiplicity

9.4.1 Efficiency

The efficiency corresponds to the ratio of reconstructed particles to generated particles. It depends strongly on the track quality cuts applied. Although 2D-histograms are needed for the response functions, plots as a function of only one variable are more suggestive. In the following, ϵ as a function of θ, ϕ and p_T will be presented for different track quality cuts.

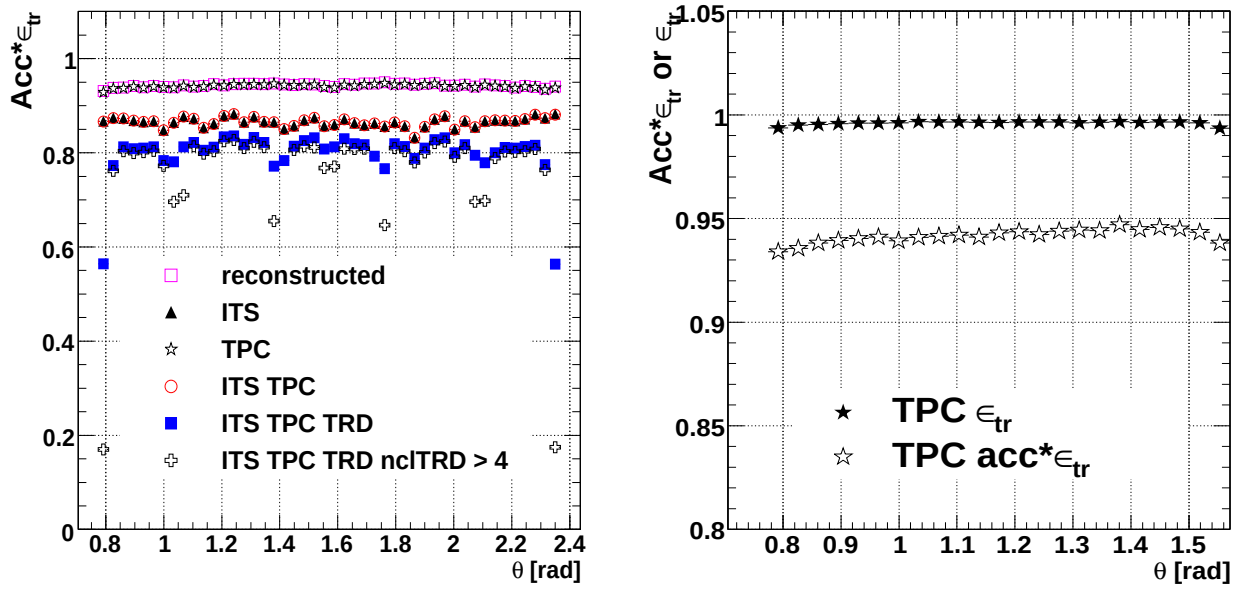

Figure 9.3: Reconstruction efficiency for different track quality cuts (left), and tracking efficiency and reconstruction efficiency of the TPC (right) as a function of the polar angle.

The left panel of the Fig. 9.3 shows the reconstruction efficiency as a function of θ integrated over p_T ([10 GeV/c,100 GeV/c]) and ϕ ([0 rad,2π rad]). If no particular track quality is applied, the particle is reconstructed in at least one detector. To improve the p_T, θ and ϕ resolutions, the track is required to be ITS-TPC refitted or ITS-TPC-TRD refitted. The cases of ITS, TPC refitted tracks are also plotted. Finally for the identification of electron at high momenta, the track has to be reconstructed in at least 5 TRD planes (ITS TPC TRD ncl TRD>4). The efficiency for reconstructed and TPC refitted tracks is flat as a function of θ and falls to 0 outside of the acceptance range. For the TPC refitted tracks, no granularity is expected in θ excepted from the central electrode, that separates the gas volume of the TPC in two parts at mid-rapidity. A slight drop of about 1 %, more pronounced for the ITS-TPC, ITS-TPC-TRD refitted and ITS-TPC-TRD ncl TRD>4 tracks, can be seen. It is caused by particles absorbed or diverted by the central electrode. The reconstructed and TPC refitted efficiencies are quasi on top of each other, which underlines the fact that the TPC is the main tracking detector in the ACB. The ITS refit requirement reduces ϵ by about 7 %. The efficiency decreases more or

less uniformly by about 5 % with the TRD refit condition. The stack structure of the TRD in θ introduces dead zones, that are more visible for tracks reconstructed in at least 5 TRD planes.

The right panel of Fig. 9.3 illustrates the difference between reconstruction efficiency and

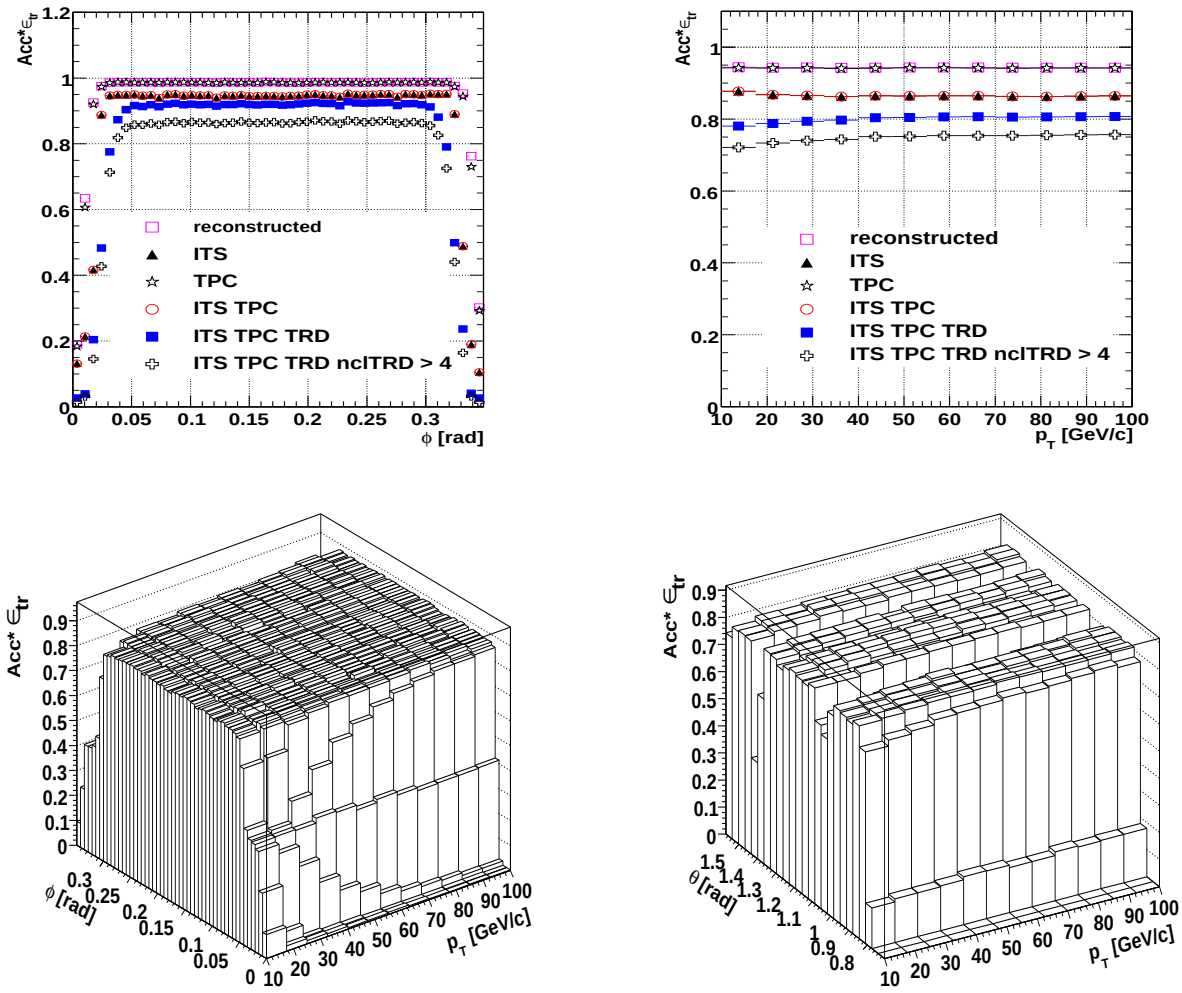

Figure 9.4: Top panels: reconstruction efficiency for different track quality cuts as a function of the azimuthal angle (left panel) and the transverse momentum (right panel). Bottom panels: 2D $p_T \times \phi$ (left panel) and $p_T \times \theta$ (right panel) efficiency maps for tracks refitted in the ITS, TPC and TRD and reconstructed in more than 5 TRD planes.

tracking efficiency. The first includes the geometrical acceptance of the detector and the fluctuations of the deposited energy loss ($acc*\epsilon_{tr}$), whereas the second is a test of the tracking algorithm (ϵ_{tr}). A particle is considered to be reconstructible if it lets at least 50 signal digits over the 500 time samples in the TPC. The tracking efficiency is then of the order of 99 %. For this figure, the symmetry relative to the mid-rapidity plane has been used.

The top left panel of Fig. 9.4 shows the efficiency as a function of ϕ, integrated over p_T ([10 GeV/c,100 GeV/c]) and θ ([0.69 rad,1.57 rad]). The ϕ interval [0 rad, $\frac{2\pi}{18}$ rad] corresponds to one sector of the TPC and one supermodule of the TRD. The requirement of at least 5 TRD planes reduces the probability to reconstruct the particle by about 6 %. Contrary to the θ de-

pendence, for which it only increases the dead zone effect, the efficiency is uniformly reduced. The main decrease comes from tracks that cross TRD stacks in the pseudo-rapidity direction and loose energy by Bremsstrahlung or scatter in the material of the support structure. The tracks crossing several supermodules in the $r\phi$ plan are rare since the bending radius for particles with a p_T above 10 GeV/c is bigger than 66 m in the nominal magnetic field (0.5 T). The maximal deviation over the total radial length of the TRD ($\approx$ 76 cm), amounts to less than 4.3 mm. It is negligible compared to the width of the chambers ($\approx$118 cm).
The efficiency as a function of p_T and integrated over θ ([0.69 rad,1.57 rad]) and ϕ ([0 rad,2π rad]) is presented on the top right panel of Fig. 9.4. It doesn't change significantly for high p_T due to already nearly straight tracks at 10 GeV/c.
The 2D ϵ-maps shown in Fig. 9.4 were built with the requirement that the track is refitted in the ITS, TPC and TRD and reconstructed in at least 5 TRD planes.

9.4.2 Transverse momentum resolution

The p_T resolution is determined by the distribution of:

$$\Delta p_T/p_T = \frac{p_T^{Generated} - p_T^{Reconstructed}}{p_T^{Generated}} \tag{9.5}$$

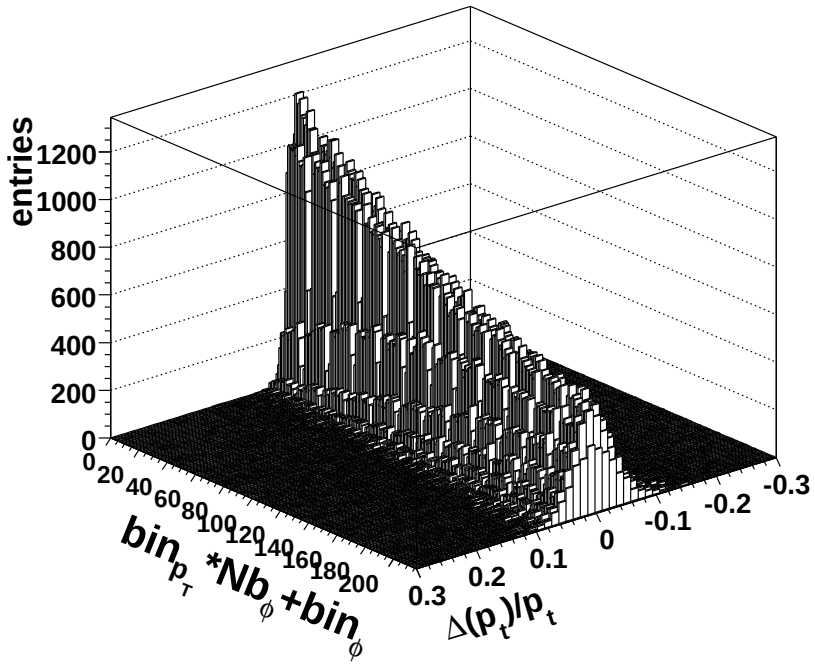

Figure 9.5: Relative p_T resolution distributions for charged pions stored in 2D histograms for the $p_T \times \phi$ resolution map.

The $\Delta p_T/p_T$ distributions are stored for each $p_T \times \theta$ and $p_T \times \phi$ bin in two 2D histograms. One example is shown on the Fig. 9.5. On the X-axis, $\Delta p_T/p_T$ is plotted, whereas the Y-axis

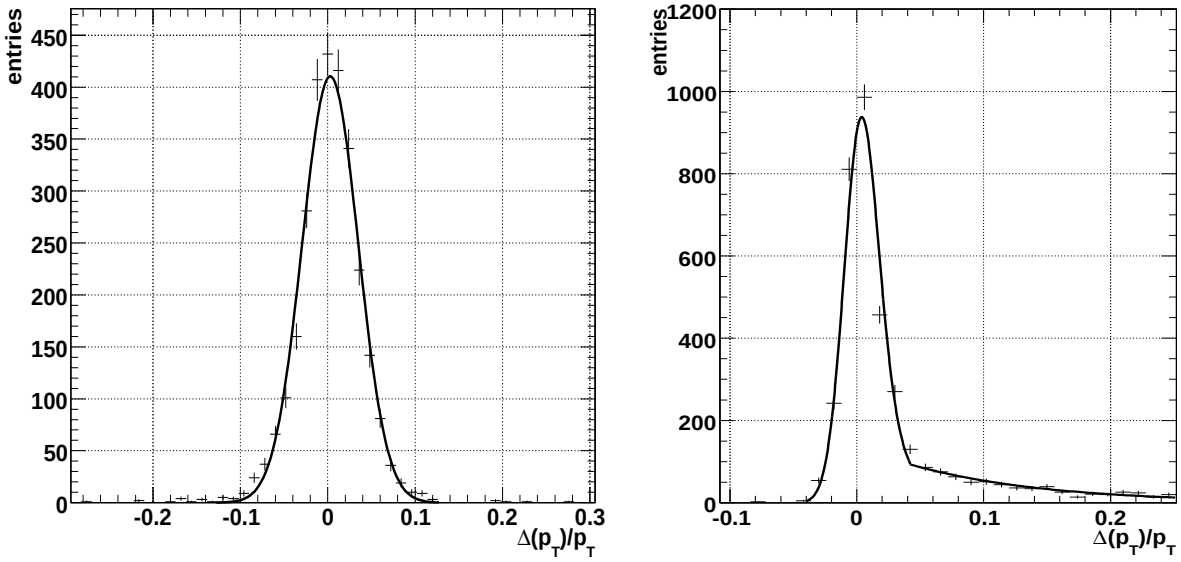

Figure 9.6: Example of fits of the relative p_T resolution for $\pi^{\pm}$ (left panel) and $e^{\pm}$ (right panel).

corresponds to the $p_T \times \theta$ or the $p_T \times \phi$ bin. A typical binning needs about 20 X-bins and $10_{p_T} \times 25_{\theta\, or\, \phi}$=250 Y-bins. Instead of storing the two big 2D histograms directly into the LUTs, the $\Delta p_T/p_T$ distributions in each Y-bin are fitted with an appropriate function. The function parameters are stored in 2D $p_T \times \theta$ and $p_T \times \phi$ maps like for the efficiency. The number of parameters needed to fit the distributions determine the number of 2D $p_T \times \theta$ and $p_T \times \phi$ maps. For Gaussian distributions, like it is the case for the pions p_T resolution, this reduces the size of the histograms by a factor 20, since only one parameter is stored out of the three fit parameters of the Gaussian function. Since the $\Delta p_T/p_T$ Gaussian distribution is centered around zero, the mean value is not stored. Then the resolution response functions are used as probability distributions and therefore the absolute scaling is not important. The total integral is always normalized to one. An example of such a Gaussian fit of pion $\Delta p_T/p_T$ distributions is shown on the left panel of Fig. 9.6.

As it can be seen on the right panel of Fig. 9.6, the electron $\Delta p_T/p_T$ distributions present a tail towards positive values ($p_T^{Generated} > p_T^{Reconstructed}$) due to Bremsstrahlung. This is superimposed with the Gaussian smearing from multiple scattering. A Landau function convoluted with a Gaussian can well reproduce the $\Delta p_T/p_T$ distribution in the region around 0, whereas an exponential function describes the tail. The following formula is used for fitting:

$$g_{k_1,\sigma_g,\sigma_l,M_l,k_2,\alpha,b}(x) = \begin{cases} f_{k_1,\sigma_g,\sigma_l,M_l}(x), & \text{for } x \leq b \\ k_2 exp(-\alpha x), & \text{for } x \geq b \end{cases} \tag{9.6}$$

$$f_{k_1,\sigma_g,\sigma_l,M_l}(x) = k_1 \int G_{\sigma_g}(x-z) L_{\sigma_l,M_l}(z) dz \tag{9.7}$$

Below x=b, the distribution is parametrized by a constant k_1, the Gaussian width σ_g, the Landau width σ_l and the Landau Most Probable Value M_l. Above x=b, the fit parameters are

a constant k_2 and the exponential slope α. Out of these 7 parameters (the border between the functions, b, is also a parameter), only 6 have to be saved. Analogous to before, the absolute scaling is not important since the resolution response functions are used as probability distributions and therefore normalized to one. Nevertheless the relative scaling between the two parts of the function is stored as k_1/k_2. Six 2D $p_T \times \theta$ and $p_T \times \phi$ maps constitute the LUTs for the electron p_T resolution.

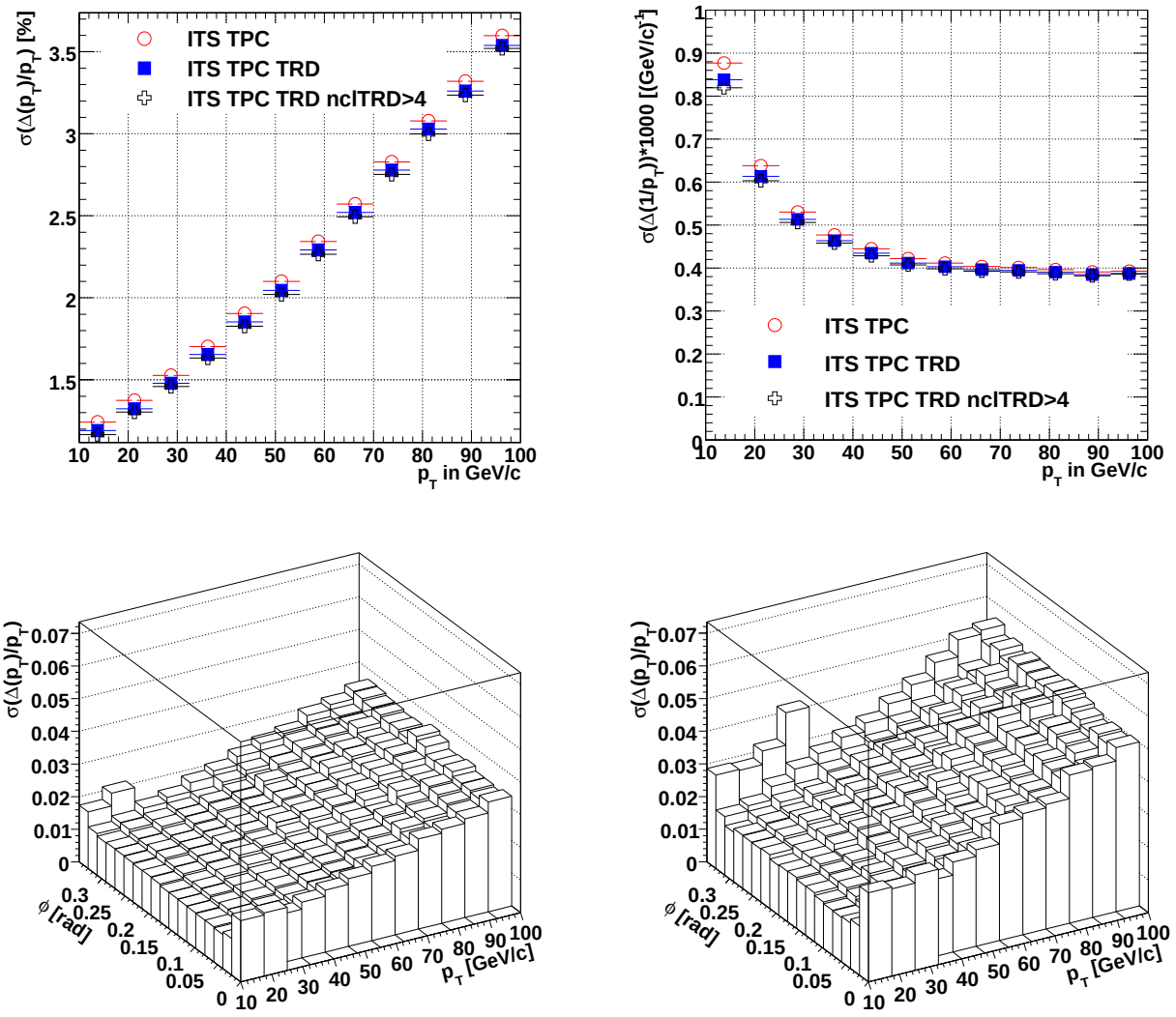

Figure 9.7: Top panels: p_T (left panel) and $1/p_T$ (right panel) resolution as extracted with Gaussian fits for $\pi^{\pm}$ as a function of p_T. Bottom panels: 2D $p_T \times \phi$ p_T resolution maps for $\pi^{\pm}$ (left panel) and $e^{\pm}$ (right panel) for ITS-TPC-TRD refitted tracks with at least 5 TRD planes.

The top panels of the Fig. 9.7 show the p_T resolution of pions as a function of p_T. In the left panel, the width of the Gaussian distribution is plotted. It has a constant term, an offset at p_T=0 GeV/c that can not be seen on the figure, and a slight linear increase. The first is caused by multiple scattering, the latter by the increasing uncertainty of the p_T measurement.

Coulomb scattering and strong interactions with nuclei contribute to multiple scattering. The charged particle is deflected by many small-angle scatterings. The final Coulomb deflection can be described by the theory of Moliere. As a good approximation, the resulting projected deflection-angle, θ_0, has a more or less Gaussian distribution with a width, that can be expressed as a function of the medium properties (thickness of the scattering medium in radiation lengths x/X_0) and the charged particle properties (momentum p, velocity βc, charge number z).

$$\sigma_{\theta_0} = \frac{13.6\,\mathrm{MeV}}{\beta cp} z\sqrt{x/X_0}[1 + 0.038\ln(x/X_0)][39] \tag{9.8}$$

The width σ_{θ_0} is inversely proportional to the momentum particle. Thus multiple scattering affects principally the p_T resolution at low momentum. The decrease of the p_T resolution due to multiple scattering can also be seen on the $\sigma(\Delta(1/p_T))$ distribution as a function of p_T, shown on the right panel of Fig. 9.7. This results in an increase of $\sigma(\Delta(1/p_T))$ at low p_T.
The p_T-determination is based on the measurement of the track curvature, r_c, in the magnetic field ($p_T[GeV]$=0.3 q $B[T]$ $r_c[m]$, qe is the total particle charge). The decrease of r_c with p_T is responsible for the linear increase of $\sigma(\Delta p_T/p_T)$. The ITS improves the resolution of the TPC alone by providing information on the particle momentum before (or *during*) Bremsstrahlung inside the material of the ITS layers. The information of the TRD improves slightly the p_T resolution by reconstructing the track over a bigger visible track length. As a consequence the curvature is better estimated ($\Delta p_T/p_T^2 \approx 0.0003(\mathrm{GeV/c})^{-1}$).

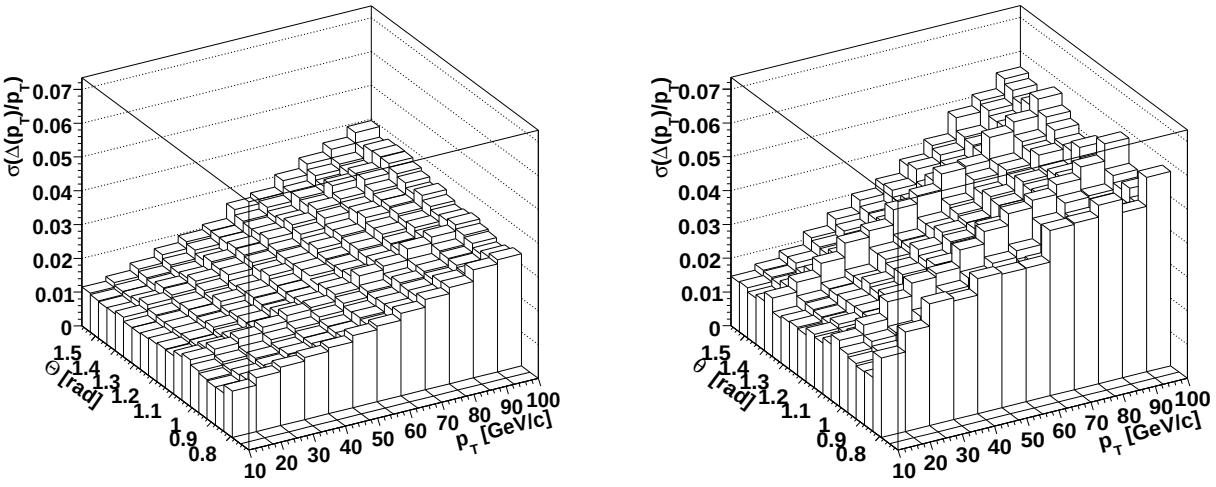

Figure 9.8: 2D $p_T \times \theta$ p_T resolution maps for $\pi^{\pm}$ (left panel) and $e^{\pm}$ (right panel) for ITS-TPC-TRD refitted tracks with at least 5 TRD planes.

Displaying the six fit parameters is not very suggestive for the electron p_T resolution. That is why, Gaussian fits of the $\Delta p_T/p_T$ distributions are performed and shown as a function of p_T and ϕ, or p_T and θ. The 2D $p_T \times \phi$ maps are presented in Fig. 9.8 for pions (left

panel) and electrons (right panel). The track quality required is the final one (ITS-TPC-TRD ncl TRD>4 tracks). The linear slope is clearly steeper for electrons than for pions due to Bremsstrahlung. The energy loss by Bremsstrahlung depends on $\frac{1}{M^2}$. It affects by a factor 78400 ($M_{\pi^\pm}/M_{e^\pm}\approx(140\,\mathrm{MeV/c^2})/(0.5\,\mathrm{MeV/c^2})$ more the electrons than pions, for which it stays negligible. The energy loss by Bremsstrahlung is given by the radiation length X_0 of the material:

$$|\frac{dE}{dx}|_{Br} = \frac{E}{X_0} \tag{9.9}$$

The radial length of the TRD was found to correspond to about 20 % X_0[74]. The ITS contributes also to the electron energy loss in detector material. Bremsstrahlung in the ITS affects more the p_T resolution than in the TRD since no p_T measurement is possible before the ITS. The p_T resolution at p_T=100 GeV/c is found to be about 3.5 % for pions and 5.7 % for electrons. As a function of ϕ, $\sigma(\Delta p_T/p_T)$ is higher in the gaps between the modules of the TRD. If no track has been reconstructed in the $p_T\times\phi$ bin (the reconstruction efficiency is zero), $\sigma(\Delta p_T/p_T)$ is null. As a function of θ (Fig. 9.8), the boundary of the two and a half TRD stacks in half of the total θ acceptance can also be seen.

9.4.3 Polar angle resolution

The θ resolution at the production vertex is determined by $\Delta\theta$:

$$\Delta\theta = \theta^{Generated} - \theta^{Reconstructed} \tag{9.10}$$

The $\Delta\theta$ distributions are Gaussian for pions and electrons and taken identical at first approximation.

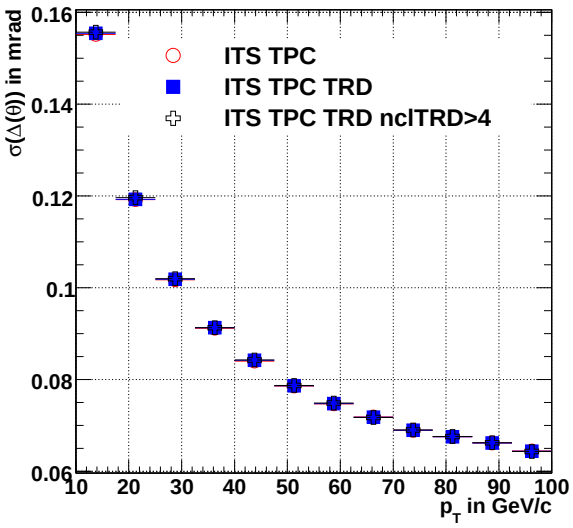

Figure 9.9: The θ resolution extracted with a Gaussian fit as a function of p_T for different track quality cuts.

Fig. 9.9 shows the width $\sigma(\Delta\theta)$ of the Gaussian fits as a function of p_T for different track quality cuts. The TRD doesn't improve the θ resolution since θ is not related to the curvature of the tracks in the transverse xy plane, but to the momentum component in the longitudinal rz plane. The width $\sigma(\Delta\theta)$ decreases with p_T due to less multiple scattering.

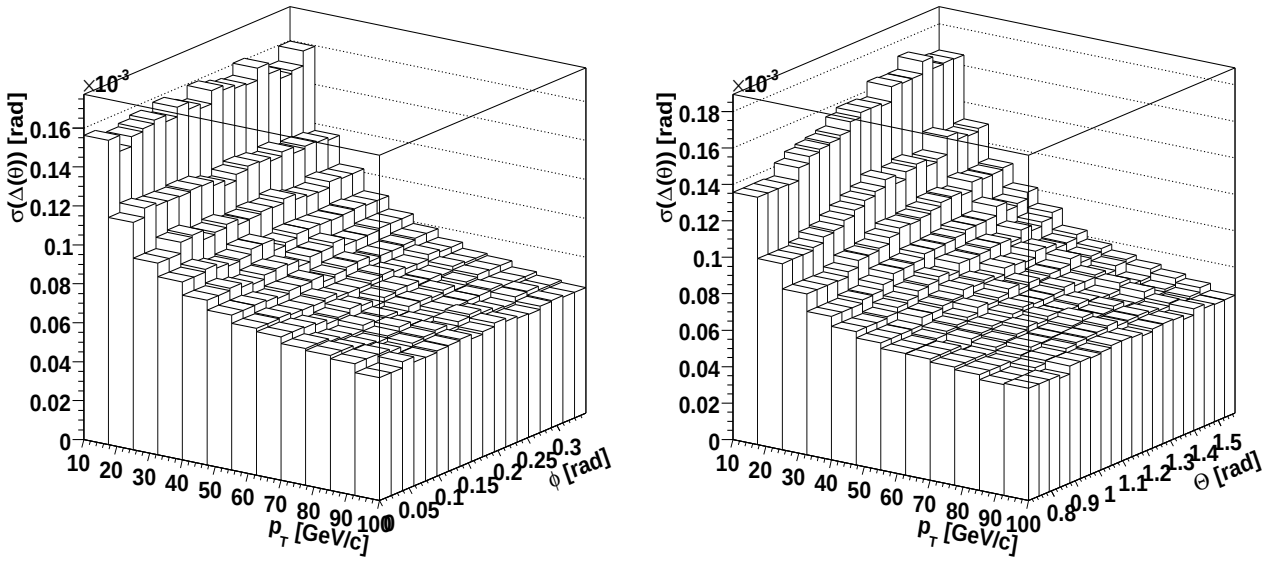

Figure 9.10: Resolution of the polar angle plotted in 2D $p_T \times \phi$ (left panel) and $p_T \times \theta$ (right panel) $\sigma(\Delta\theta)$ maps for ITS-TPC-TRD refitted tracks reconstructed in at least 5 TRD planes.

The 2D $p_T \times \theta$ and $p_T \times \phi$ resolution maps are presented in Fig. 9.10. In θ (right panel), the resolution decreases at mid-rapidity (σ increases with θ). Two effects have to be taken into account as a function of θ:

- far from mid-rapidity the particles have a longer path through the TPC and the ITS. They suffer more from Bremsstrahlung and multiple scattering. This will decrease the resolution far from mid-rapidity (increase $\sigma(\Delta\theta)$ for small θ angles in the 2D $p_T \times \theta$ map). This effect should decrease with the particle momentum.

- near mid-rapidity the electrons produced by ionization in the TPC gas along the track have to drift for a longer time through the TPC. At mid-rapidity the total length in the z direction (time direction) is equal to half of the TPC length, 2.5 m. The longitudinal and transverse diffusion are approximately the same and characterized by the diffusion constant $D_T \approx D_L \approx 220\,\mu\text{m}/\sqrt{cm}$. For electrons coming from the central electrode, the diffusion spreads the cloud laterally over 3.4 mm and causes an arrival time spread of 120 ns. The Δt-measurement of the drifting charge is specially affected. This will decrease the resolution at mid-rapidity (increase $\sigma(\Delta\theta)$ at large θ angles in the 2D $p_T \times \theta$ resolution map).

The second effect plays an more important role since θ is directly related to the Δt measurement and the θ resolution is worse at mid-rapidity. The $\sigma(\Delta\theta)$ values have been taken from the

neighborhood bin when no track was reconstructed in the $p_T \times \phi$- or $p_T \times \theta$-bin. This procedure is also applied for the p_T and ϕ resolution maps to avoid no-physical $\sigma(\Delta\theta)$.

9.4.4 Azimuthal angle resolution

The ϕ resolution at the production vertex is determined by $\Delta\phi$:

$$\Delta\phi = \phi^{Generated} - \phi^{Reconstructed} \tag{9.11}$$

Analogous to the θ resolution, the $\Delta\phi$ distributions are Gaussian and quasi identical for pions and electrons. Fig. 9.11 shows the width of the Gaussian fit as a function of p_T for different track quality cuts.

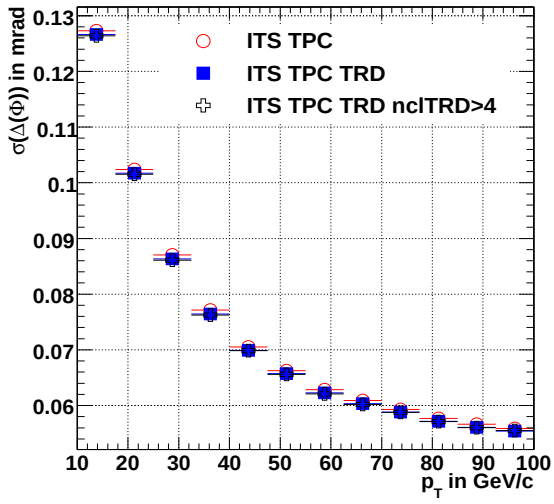

Figure 9.11: The ϕ resolution as a function of p_T for different track quality cuts.

The resolution decreases with p_T but not as significantly as for the θ resolution. The improvement due to less multiple scattering at high momentum has to be convoluted with the negative effect of the smaller track curvature in the transverse plane at high p_T. This produces less global curvature $\delta\phi$ used for the p_T determination. The information of the TRD improves slightly the resolution since the track is reconstructed over a longer path length and $\delta\phi$ increases.
The 2D $p_T \times \theta$ and $p_T \times \phi$ resolution maps are presented in Fig. 9.12. In θ (right panel), the resolution decreases far from mid-rapidity. This is due to a longer path through the TPC, that bears more Bremsstrahlung and multiple scattering. The effect of the diffusion in the transverse plane is less important.

9.4.5 Results at lower transverse momentum

The lower p_T range [1 GeV/c,10 GeV/c] is less important for the Z^0 study since the p_T of the electrons emitted in Z^0 decays is of the order of $\frac{cM_{Z^0}}{2}$=45 GeV/c. A p_T cut at 10 GeV/c reduces

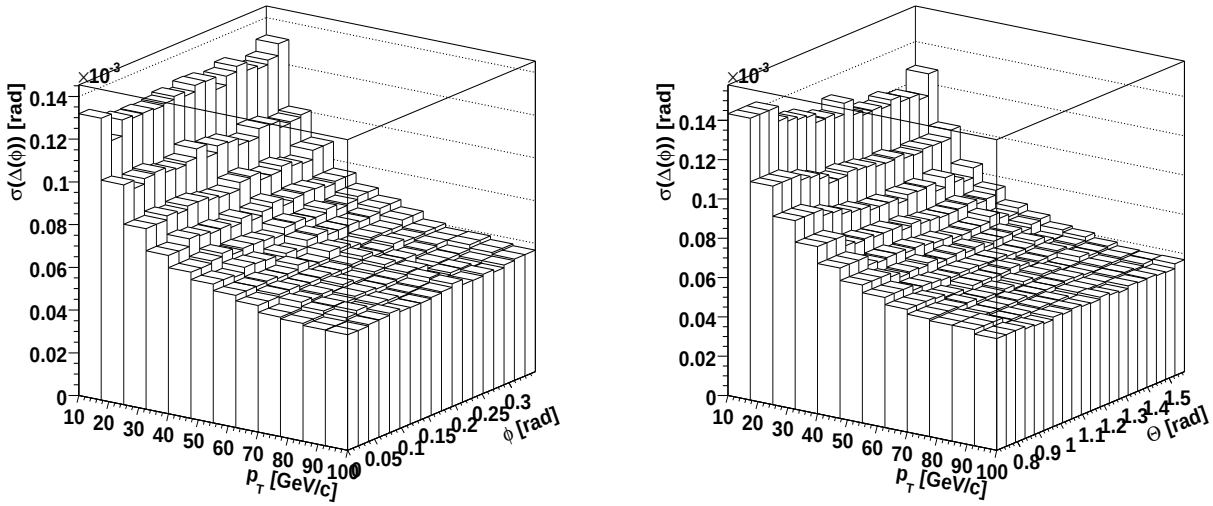

Figure 9.12: The 2D $p_T \times \phi$ (left panel) and $p_T \times \theta$ (right panel)ϕ resolution maps for ITS-TPC-TRD refitted tracks reconstructed in at least 5 TRD planes.

the Z^0 acceptance by less than 0.1 % as shown in the next section. Nevertheless about 25,000 events have been generated, as for the p_T range [10 GeV/c,100 GeV/c], with flat p_T distributions of 80 π^+, 80 π^-, 80 e^+ and 80 e^- per event. This corresponds to 8,000,000 particles and a disk space of about 320 Bb.

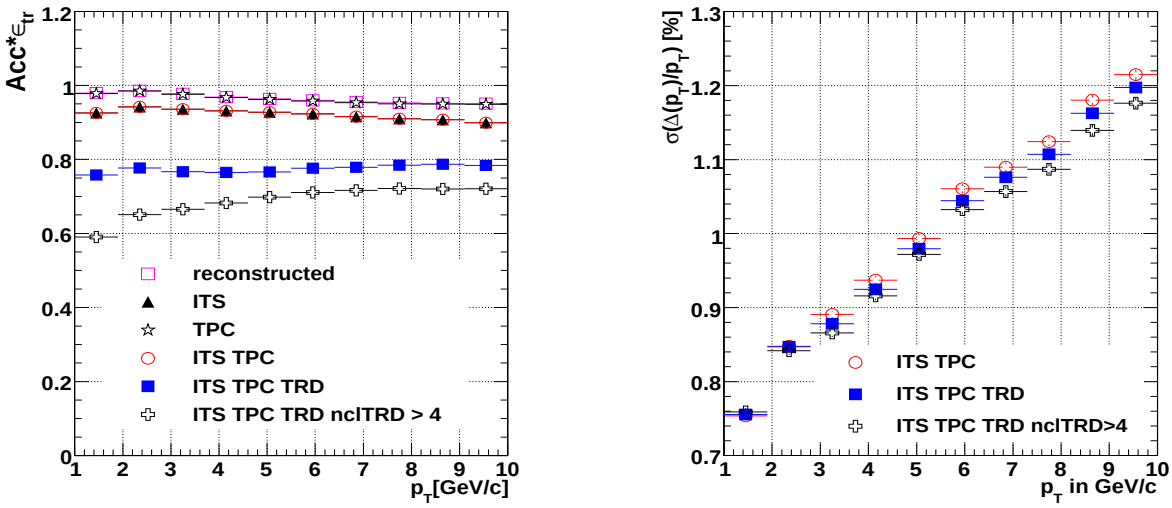

Figure 9.13: Left panel: reconstruction efficiency as a function of p_T for different track quality cuts; Right panel: p_T resolution as a function of p_T for different track quality cuts.

The left panel of Fig. 9.13 shows the reconstruction efficiency as a function of p_T for different track quality cuts. The reconstruction efficiency is higher at lower p_T for ITS, TPC and ITS-TPC refitted tracks and decreases by about 4 % between 2 GeV/c and 6 GeV/c. This is a

consequence of the higher influence of dead zones with increasing momentum. Particles with low p_T have a smaller curvature and propagate out of dead zones, producing enough hits in the detector to be tracked. Particles with high p_T have quasi straight trajectory and stay in the dead zones. For TRD refitted tracks, the probability to reach the TRD without being absorbed before has to be also considered. This requirement is even more strict for the tracks flagged as ITS-TPC-TRD ncl TRD>4 tracks. The probability to be not absorbed increases with p_T and wash out the dead zones effect.
In the right panel of Fig. 9.13 the p_T resolution is shown as a function of p_T. Like for the high p_T case, it contains an offset due to multiple scattering and a linear component due to the determination of the track curvature. The two are found similar to the high p_T case so that the p_T resolution is continuous. The information of the TRD improves the resolution because of the longer reconstructed path length.

9.5 Results at High-multiplicity

The comparison of the reconstruction efficiency and the pion p_T resolution at two different multiplicities can be seen in Fig. 9.14. The efficiency clearly decreases with the multiplicity. Nevertheless the pion p_T resolution is not as much affected. The reconstruction efficiency is reduced by about 2 % from the multiplicities 0 to 4000. This factor doesn't depend on p_T, ϕ or θ above p_T=10 GeV/c.

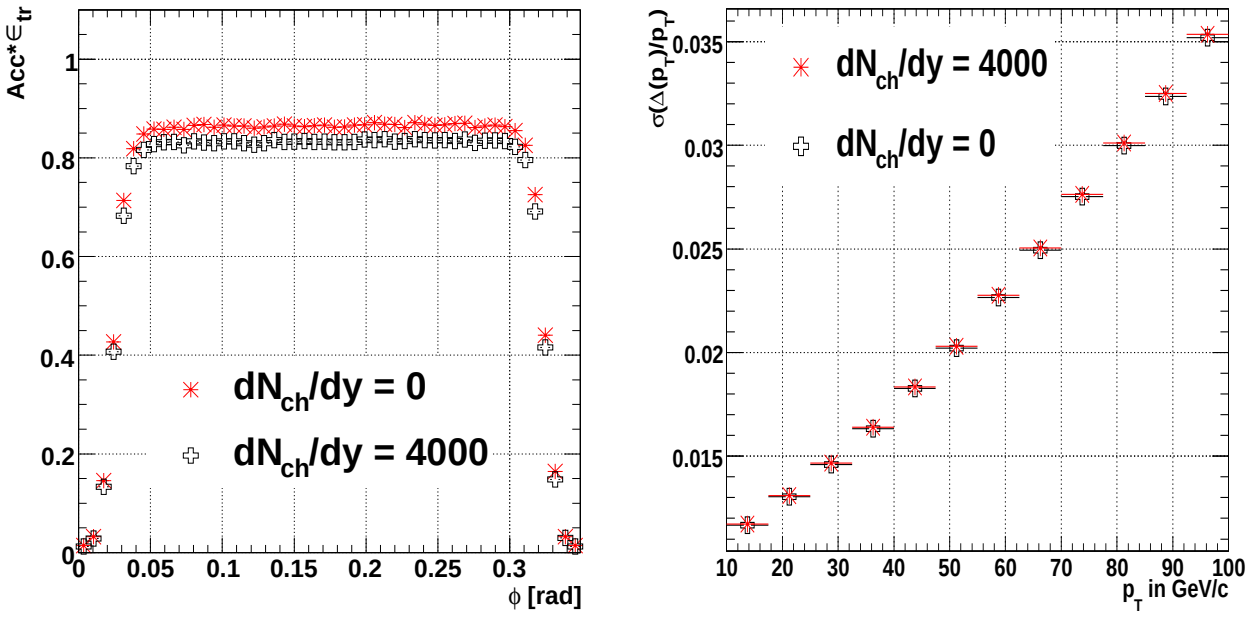

Figure 9.14: Reconstruction efficiency as a function of ϕ (left panel) and p_T resolution as a function of p_T for different multiplicities, for ITS-TPC-TRD refitted tracks reconstructed in at least 5 TRD planes.

9.6 Parametrization of the Particle Identification

The probability for a pion to be misidentified as an electron, the pion efficiency, has to be parametrized as a function of the $\pi^{\pm}$ momentum. The pion efficiency depends on the electron efficiency, ϵ_e, which gives the percentage of correctly identified electrons. The variable ϵ_e is usually fixed to 90 % for each detector contributing to the PID (the TPC and TRD). The final combined ϵ_e is therefore $\epsilon_e^{TPC} \times \epsilon_\pi^{TRD}$=81 %.

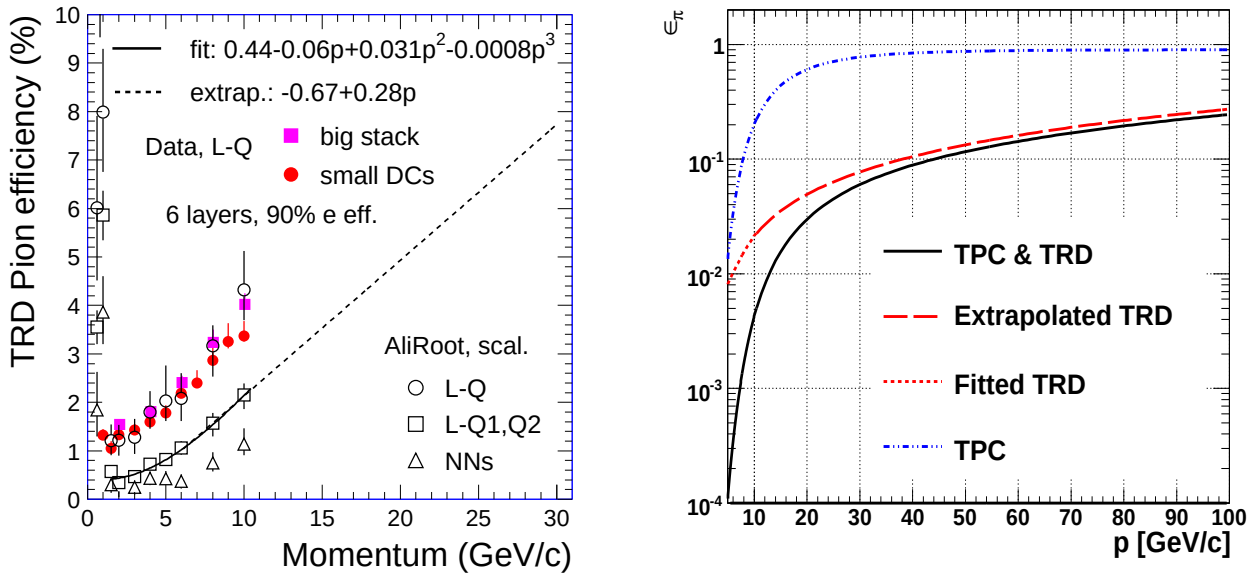

Figure 9.15: Probability to misidentify a pion with the TRD (ϵ_π^{TRD}) as a function of momentum extracted from test beam data compared with simulations within the AliRoot framework and extrapolated to high p (left). Calculated ϵ_π^{TPC}, extrapolated ϵ_π^{TRD} and combined ϵ_π as a function of momentum

In the left panel of Fig. 9.15, the pion efficiency of the TRD alone is shown as a function of momentum[75, 76, 77, 78]. The electron identification with the TRD has been studied in a dedicated TRD test-beam in 2004 using a e^-/π^- beam of 1 GeV/c to 10 GeV/c at CERN. The results of data analysis of small prototype chambers (*small DCs*) and real size chambers (*big stack*) are compared with simulations done within the AliRoot framework for a one dimensional likelihood method, L-Q. This method uses only the total deposited energy inside the chamber. Due to the smaller electron mass, $e^{\pm}$ are already in the Fermi plateau at 1 GeV/c and loose more energy per ionization than $\pi^{\pm}$. The difference in deposited energy is enhanced by the presence of the radiator in front of the chamber, in which only $e^{\pm}$ produce transition radiations. The AliRoot results have been scaled with a factor 2 to match the measurements. This discrepancy is still under investigation. Nevertheless the shape of the ϵ_π^{TRD} momentum dependence is well reproduced. Some improvements can be achieved by using a two dimensional method, *L-Q1,*

Q2 or a neural network, *NNs*[75]. These last methods make use of the small absorption length of the Xe gas. The transition radiation photons are absorbed at the entrance of the chamber. As a consequence the average $e^{\pm}$ signal as a function of time presents a peak at the end, whereas the mean $\pi^{\pm}$ signal stays flat over the drift region. A fit of the L-Q1, Q2 performances allows to extrapolate ϵ_{π}^{TRD} to the momentum range of interest for the Z^0. In the right panel of Fig. 9.15, the TPC pion efficiency has been estimated with simulations for a TPC electron efficiency of 90 %[79]. The TPC PID capability is combined to the extrapolated TRD pion efficiency. The final ϵ_{π} for 81 % electron efficiency is also plotted in Fig. 9.15. At p_T=$\frac{cM_{Z^0}}{2}$=45 GeV/c, the expected probability to misidentify a $\pi^{\pm}$ as an $e^{\pm}$ is about 10 %.

9.7 User package

The 2D $p_T \times \theta$ and $p_T \times \phi$ efficiency and resolution maps are provided together with a User package. The package, called ACBRESPONSE, was already existing [73] and only updated during this work. It provides an interface to the LUTs and can be used together with AliRoot. The class *AliResponses* rebuilds the response functions from the fit parameters stored in the LUTs and gives the user the answer of the questions about the reconstruction efficiency, the resolutions and the electron-pion separation efficiency. It is possible to get the answer directly from the response functions, as the probability to be reconstructed for example, or query random distributions based on the response functions.
The main update done in this work, was to introduce the particle dependence for the p_T resolution, to update the pion efficiency at low p_T and extrapolate it for high p_T, and to build the LUTs (efficiency and resolution) for the appropriate track quality cut (ITS-TPC-TRD refitted tracks reconstructed in at least 5 TRD planes) with the latest version of AliRoot. The p_T resolution had improved meanwhile due to software development in the tracking algorithm. This work focuses on high p_T $\pi^{\pm}$ and $e^{\pm}$ ([10 GeV/c,100 GeV/c]), contrary to the previous one, for which the main statistics to build the LUTs were for $\pi^{\pm}$ and $e^{\pm}$ below 10 GeV/c.

Chapter 10

Z^0 acceptance in the ALICE central barrel

The $Z^0 \rightarrow e^+e^-$ acceptance in the ALICE central barrel is estimated for pp collisions at 14 TeV.

10.1 Selection criteria

The $Z^0 \rightarrow e^+e^-$ events are selected looking for two energetic, isolated electrons. The reconstructed dielectron invariant mass is then required to lie within a mass window consistent with the measured Z^0 boson mass. The complete set of selection criteria used to identify $Z^0 \rightarrow e^+e^-$ are summarized here. They correspond to the ones used to build the LUTs for the fast simulation program plus an isolation cut.

Track selection

The tracking is mainly done by the TPC but the ITS improves the p_T resolution at the production vertex of the electrons since the kinematic variables of the reconstructed track can be corrected from the energy loss in the ITS layers. The TRD improves also the p_T and ϕ resolution because of the longer reconstructed path length of the track. That is why the track is required to be refitted in the TRD, TPC and ITS. In addition the TRD particle probabilities to be $e^{\pm}$,$\mu^{\pm}$,$\pi^{\pm}$,$K^{\pm}$, or (p,$\bar{p}$) have to be calculated with at least five TRD planes. The pion efficiency decreases approximately as a logarithm with the number of TRD planes used [75].
To restrict ourselves to a region of high track reconstruction efficiency, we require that the distance of closest approach to the reconstructed primary vertex (or its nominal position (0,0,0) if not reconstructed) in the z direction is imposed to be less than $6\times\sigma_z$ ($\approx\pm 32$ cm in z).

Electron selection

At high momenta (about 45 GeV/c), the TRD gives the possibility to separate $e^{\pm}$ from $\pi^{\pm}$ with an expected probability to misidentify a $\pi^{\pm}$ as an $e^{\pm}$ of the order of 10 %. The $\pi^{\pm}$ and $e^{\pm}$

can not be well separated with the dE/dx TPC information since they are both in the Fermi plateau and have therefore similar energy loss in the TPC gas. The TPC and TRD electron efficiencies are required to be above 90 %, which leads to a total efficiency of $\epsilon_{TPC} \times \epsilon_{TRD}$=81 %.

$Z^0 \rightarrow e^+e^-$ selection

We select events which contain electron(s) and positron(s), that pass the track quality cut and electron selection described before. The electrons from decays of Z^0 bosons have a high transverse momentum. Thus the reconstructed $e^{\pm}$ are required to have a minimum p_T. Moreover $e^{\pm}$ from Z^0 are often isolated from hadronic jets, in contrast to misidentified $\pi^{\pm}$ from jets and $e^{\pm}$ originating from decays of heavy-flavor hadrons. We therefore require in addition that no high p_T track j is found in the neighborhood of the reconstructed $e^{\pm}$. This consists to reject the reconstructed $e^{\pm}$, for which there is at least one track j with:

- $p_T^j > 2\,\mathrm{GeV/c}$
- $|\eta_{e^{\pm}} - \eta_j| \leq 0.1$ and $|\phi_{e^{\pm}} - \phi_j| \leq 0.1\,\mathrm{rad}$

This *isolation cut* works well in *pp* collisions since the mean number of charged tracks inside the TPC is about 12 for minimum-bias events. For *PbPb* collisions at 5.5 TeV, about 8000 charged tracks are expected from the *underlying event*. These are mainly low p_T tracks but an isolation cut will nevertheless affect the signal acceptance.
The invariant mass, M_{inv}, is then computed for each isolated electron-positron pair inside the event (see Appendix B):

$$M_{e^+e^-} = M_{inv} = \sqrt{2. \times p_{Te^+} \times p_{Te^-} \times (cosh(\eta_{e^+} - \eta_{e^-}) - cos(\phi_{e^+} - \phi_{e^-})} \tag{10.1}$$

M_{inv} is required to be between 66 and 116 $\mathrm{GeV/c^2}$.

10.2 Signal acceptance

The total acceptance, A_{total}, is defined as the fraction of $Z^0 \rightarrow e^+e^-$ events that satisfy the selection criteria. A_{total} is the product of two factors:

$$A_{total} = A_{geo} \times \epsilon_{total} \tag{10.2}$$

- A_{geo} is related to the geometrical acceptance of the central barrel and constitutes the main limit on the total number of reconstructed Z^0. The electron reconstruction in the ACB is restricted to the finite fiducial coverage of the ITS-TPC-TRD tracking system ($|\eta_{e^{\pm}}|$<0.9). A_{geo} corresponds to the requirement that both electrons have $|\eta_{e^{\pm}}|$<0.9.
- ϵ_{total} is a correction for additional inefficiencies from the event selection criteria. It can be written as a product of squared efficiencies, that are applied twice, for each electron:

$$\epsilon_{total} = (Acc \times \epsilon_{tr})^2 \times \epsilon_{pid}^2 \times \epsilon_{p_T}^2 \times \epsilon_{iso}^2 \tag{10.3}$$

The factor *Acc* describes the reduction from the geometrical acceptance within $|\eta|<0.9$ due to support structures, while ϵ_{tr} is the tracking efficiency. The product $Acc \times \epsilon_{tr}$ corresponds exactly to the reconstruction efficiency maps, that were presented in the previous section. The particle identification efficiency is fixed to $\epsilon_{PID}=0.81$. The efficiency of the low p_T cut, ϵ_{p_T}, depends on the minimum p_T required. Finally the effect of the isolation cut is described by ϵ_{iso}. The correlation between different criteria is taken into account by having a specific order in which individual efficiency estimations are made. Each efficiency term is an efficiency for the subset of $Z^0 \rightarrow e^+e^-$ events that satisfies the geometrical criteria of the samples as well as the requirements associated with each of the efficiency terms to the left of the term under consideration. No trigger efficiency is included.

$\|\eta_{e^\pm}\|<0.9$	8.58 % ±0.01 %
$A_e \times \epsilon_e^{tr} \times \epsilon_e^{pid}$ MC p_T	3.63 % ±0.07 %
$A_e \times \epsilon_e^{tr} \times \epsilon_e^{pid}$	3.52 % ±0.08 %
$A_e \times \epsilon_e^{tr} \times \epsilon_e^{pid}$ $p_{Te^\pm}>10$ GeV/c	3.52 % ±0.08 %
$A_e \times \epsilon_e^{tr} \times \epsilon_e^{pid}$ $p_{Te^\pm}>25$ GeV/c	3.21 % ±0.07 %
$A_e \times \epsilon_e^{tr} \times \epsilon_e^{pid}$ $p_{Te^\pm}>25$ GeV/c iso cut	3.19 % ±0.07 %

Table 10.1: Acceptance and reconstruction efficiency for Z^0 in the mass range $66\,\mathrm{GeV/c^2}<M_{e^+e^-}<116\,\mathrm{GeV/c^2}$ for different single track cuts

The signal acceptance depends on the specific invariant mass range, 66 GeV/c^2-116 GeV/c^2. Table 10.1 summarizes the efficiency of the different cuts applied. The statistical errors are below 0.1 %. The geometrical acceptance of the central barrel implies that both of the electrons have $|\eta_{e^\pm}|<0.9$. This reduces the Z^0 yield by more than 10. With the tracking and PID efficiencies, the acceptance of Z^0 is 3.6 %. This corresponds to an average single particle reconstruction efficiency of about 80 % and a PID efficiency of 81 %. The reconstructed $p_{Te^\pm}$ is shifted towards lower values due to the Bremsstrahlung. That is why, the low mass invariant cut at 66 GeV/c^2 reduces slightly the acceptance to 3.5 % for the reconstructed $p_{Te^\pm}$,$\theta_{e^\pm}$ and $\phi_{e^\pm}$. The effect of further $p_{Te^\pm}$ cuts is not very important, as one can expect from Fig. 7.6. The isolation cut does not affect the signal and 99 % of Z^0 pass the cut.
Fig. 10.1 illustrates the results of Table 10.1. The generated dielectron invariant mass yield (m_{sim}) is shown in the total phase space and in the geometrical acceptance of the ITS-TPC-TRD with and without tracking and PID efficiencies together with The reconstructed dielectron invariant mass yields (m_{rec}) for different $p_{Te^\pm}$ cuts. The yields are computed for minimum-bias *pp* collisions. The m_{rec} spectra have a tail towards low values of M_{inv} resulting from the Bremsstrahlung of the electrons.

The generated shape (m_{sim} distributions) is not exactly symmetric around the mass of the Z^0 boson and presents higher yields in the lower mass region. This can be better seen in Fig. 10.2,

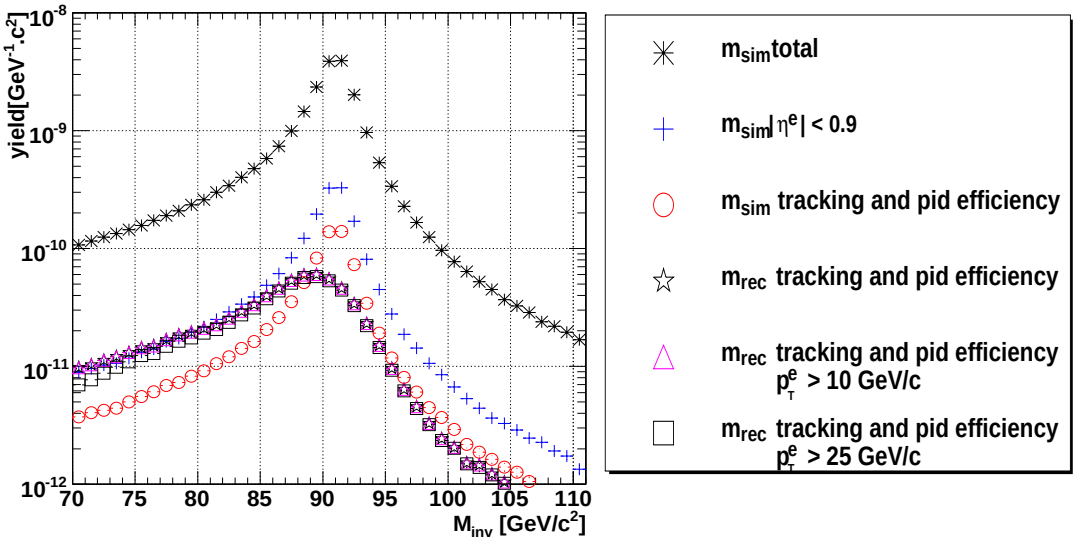

Figure 10.1: Generated (m_{sim}) and reconstructed (m_{rec}) dielectron invariant mass yield from Z^0 in the total phase space and within the central barrel acceptance for different p_T^e cut.

where the invariant mass yield in the total phase space is plotted for Z^0/γ^* interference, pure Z^0 and Drell-Yan processes ($q\bar{q}\rightarrow\gamma^*\rightarrow e^+e^-$). The total Drell-Yan cross-section is proportional to $\frac{4\pi\alpha^2}{3s}$, where α is the finestructure constant ($\alpha=\frac{e^2}{4\pi\epsilon_0\hbar c}$) and $\sqrt{s}$, the c.m.s energy. At LHC it becomes very small and its yield in the high invariant mass region can not explain the asymmetry of the Z^0 invariant mass. It comes from final states radiations (i.e. internal Bremsstrahlung).

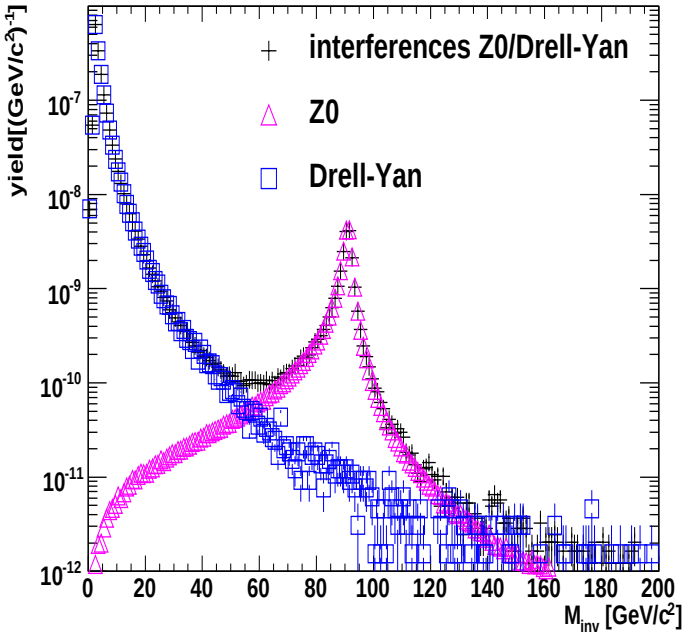

Figure 10.2: Dielectron invariant mass yield in all phase space for Z^0/γ^* interference, pure Z^0 and Drell-Yan process.

Chapter 11

Background studies

The background was studied for pp collisions at 14 TeV.

11.1 Background at lower energies

The UA1 and UA2 experiments at CERN's Super Proton Synchroton (SPS) accelerator measured for the first time the Z^0 through its muonic and electronic decay channels. The SPS was operating as a proton-antiproton collider at $\sqrt{s}$=600 GeV. The particularity of the Z^0 signal was, that it was a very clear signal quasi free of background. The electrons were identified with calorimetry techniques [51]. Events containing a Z^0 decay in the e^+e^- channel were selected by requiring the presence of two isolated electrons with transverse energy in excess of 15 GeV, and two-electron mass in excess of 70 GeV/c^2.
At the Tevatron, the D0 and the CDF experiments have measured Z^0 in the same decay channels (e^+e^- and $\mu^+\mu^-$). The detectors have a cylindrical layout centered on the accelerator beam-line containing electromagnetic calorimeters followed by hadronic calorimeters in the radial direction for the $e^\pm$ identification. Tracking detectors are installed in the region directly around the interaction point to reconstruct charged-particle trajectories inside a uniform magnetic field of 1.4 T for CDF and 2 T for D0 along the proton beam direction. The invariant mass of the electron-positron pair is calculated with the formula:

$$M_{inv}^2 = 2 \times E_1 E_2 \left(1 - cos\left(\psi\right)\right) \tag{11.1}$$

where ψ is the opening space-angle of the electron-positron pair, and E_1 and E_2 their energy measured in the electromagnetic calorimeters. The CDF and the D0 used the information on impact parameters only in the muonic decay channel to reduce the background from cosmic rays and $\pi^\pm/K^\pm$ weak decays [54] [53]. In the electronic decay channel the signal was already very clean without any cut on the track impact parameter to suppress remaining electrons coming from secondary vertices. As an example, in the CDF analysis cuts are performed at the event level, single track level and on the invariant mass, that has to lie within the mass range corresponding to the Z^0 mass.

- At the event level a cut was applied on the reconstructed z position of the primary vertices to be in a region of high track reconstruction efficiency.
- At the single track level, the cuts were related to:
  - the track quality (χ^2, matching of the track reconstructed in the inner tracking system with the clusters in the electromagnetic calorimeter)
  - the Particle Identification (deposited energies in the hadronic and electromagnetic calorimeters, energy-to-momentum ratio, profile of the shower)
  - the two characteristics of the electrons coming from Z^0 (high p_T and E_T, and isolation cut)

With this, the biggest contribution to the background was found to come from jet events, in which one or both electrons were either real or fake electrons from hadronic jets. Electroweak processes were also investigated, such as $Z^0 \rightarrow \tau^+\tau^-$ decays, in which $\tau^\pm$ is misidentified as an electron or decays in an electron, and $W^\pm \rightarrow e\nu_e$, in which the electron is associated with a misidentified jet. The final total background amounted to less than 1.5 % of the signal. Table 11.1 summarizes the different contributions to background at Tevatron.

	Nb of events	% of the signal
total candidates $Z^0 \rightarrow e^+e^-$	4242	
Multi-jets	41±18	≈1.0
$Z^0 \rightarrow \tau^+\tau^-$	3.7±0.4	≈0.1
$W^\pm \rightarrow e\nu_e$	16.8±2.8	≈0.4

Table 11.1: Background to $Z^0 \rightarrow e^+e^-$ in $p\bar{p}$ collisions at $\sqrt{s}$=1.96 TeV as measured by the CDF Collaboration [54]

11.2 Background sources studied in pp collisions at 14 TeV

The different sources of background that are investigated for pp collisions at $\sqrt{s}$=14 TeV are:

- reconstructed dielectrons from jets, that can be real electrons or pions misidentified as electrons.
- $W^\pm \rightarrow e\nu_e$ events with an associated hadronic jet that results in a second reconstructed electron ($\mathrm{Br}_{W^\pm \rightarrow e\nu_e}$=10.75 % [1]).
- $Z^0 \rightarrow \tau^+\tau^-$ events, in which electrons or misidentified pions from $\tau^\pm$ decays ($\tau^- \rightarrow e^-\bar{\nu}_e\nu_\tau$, $\mathrm{Br}_{e\nu_e\nu_\tau}$=17.36 % [1] and $\mathrm{Br}_{\tau \rightarrow e/\pi+X}$=44.0850 % [1]) are combined.

- electrons and misidentified pions from $t\bar{t}$ events. The top quark decays into a $W^{\pm}$ boson and a b quark. Simultaneous semielectronic decays of b or $W^{\pm}$ lead to correlated background.
- simultaneous semielectronic decays of D and $\bar{D}$ charm mesons ($\mathrm{Br}_{c\to eX}\approx 9.6\,\%$ [1]).
- simultaneous semielectronic decays of B and $\bar{B}$ beauty mesons ($\mathrm{Br}_{b\to eX}\approx 10.86\,\%$ [1]).

The two first sources of background can be considered as uncorrelated background, whereas the other sources result in correlated background. Jet events include a priori $c\bar{c}$, $b\bar{b}$ and $t\bar{t}$ events but for more accuracy these contributions have been simulated separately. The cross-sections are summarized in Table 11.2. For comparison they are also given for $p\bar{p}$ collisions at $\sqrt{s}$=1.96 TeV. Their relative ratios to the signal are also mentioned. No big changes are expected between the Tevatron and the LHC, except that the p_T spectra will be harder at the higher energy. In the following, we will describe more in details each source of background.

σ	$p\bar{p}$ at 1.96 TeV	pp at 14 TeV
$Z^0\to e^-e^+(Z^0\to \tau^-\tau^+)$	255.8 pb [54]	1.84 nb [43]
$W^{\pm}\to e\nu_e$	2.77 nb [61] (*10*)	19.8 nb [40] (*10*)
$t\bar{t}$	6.7 pb [80, 81] (*0.026*)	833 pb [82] (*0.45*)
$b\bar{b}$	50 μb (2.10^5)	0.51 mb [68] (2.10^5)
$c\bar{c}$	$\approx$500 μb (2.10^6)	11.2 mb [68] (5.10^6)

Table 11.2: Total production of different sources of background and (in parentheses)their relative ratio to the signal. The branching ratios $\mathrm{Br}_{\tau\to e/\pi+X}$=44.0850 %, $\mathrm{Br}_{c\to e}\approx 9.6\,\%$ and $\mathrm{Br}_{b\to e}\approx 10.86\,\%$ have moreover to be taken into account.

11.3 Jets

The inclusive jet production and the jet structure have been intensively studied by the CDF and D0 collaborations in $p\bar{p}$ collisions at 1.96 TeV. It was first shown that PYTHIA 6.115 describes fairly well some high transverse momentum charged jet observables with its default parameters, like the multiplicity and momentum distributions of charged particles inside the jet or the size of the leading charged jet. However the soft component of the event was not reproduced correctly [83].
The total cross-section (σ_{total}) of a hadron-hadron collision can be decomposed in elastic scattering, single diffraction, double-diffraction and hard QCD processes (Hard Core):

$$\sigma_{total} = \sigma_{EL} + \sigma_{SD} + \sigma_{DD} + \sigma_{HC} \tag{11.2}$$

The jet events (HC) can be artificially decomposed into a hard scattering component and an

underlying event (see left panel of Fig. 11.3). The hard scattering component contains particles that originate from two large p_T outgoing partons plus initial and final-state radiations. The underlying event consists of particles that come from the breakup of the proton and antiproton and some contributions from initial- and final-state radiations. The way Pythia simulates the all event is illustrated in the right panel of Fig. 11.3. The underlying event is modelled by including multiple parton interactions, adding sometimes a second semi-hard 2-to-2 parton-parton scattering to the hard 2-to-2 parton-parton collision.

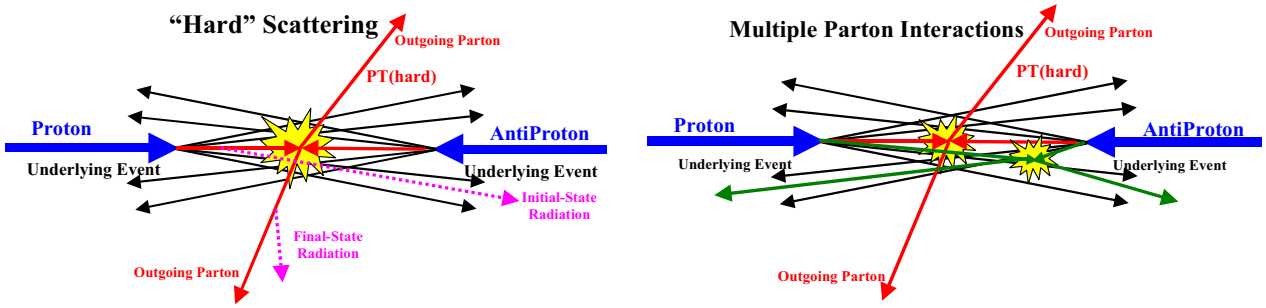

Table 11.3: Left: the way QCD Monte-Carlo models simulate a proton-antiproton collision in which a *hard* 2-to-2 parton scattering occurred. Right: the way Pythia models the underlying event in proton-antiproton collision by including multiple parton interactions [83].

Experimentally the hard scattering component can be studied by looking at the jets properties. The definition of a jet depends on the jet reconstruction algorithm used. A *cone-like* typed algorithm was developed, where a jet is defined as a circular region in η-ϕ space with a radius $R=\sqrt{(\delta\eta)^2+(\delta\phi)^2}=0.7$. Some jets observables, like the leading charged jet multiplicity or the radial distribution of charged particles within the leading charged jet, were found to be in fair agreement with the results of PYTHIA [83]. The direction of the leading charged particle jet in each event allows to separate the *underlying* event from the hard scattering component and study its properties. The CDF collaboration defined three regions of the η-ϕ space: a *toward* region containing the charged particle jet, a *away* region containing the away-side jet (for two jets production) and a *transverse* region perpendicular to the plane of the hard 2-to-2 scattering and sensitive to the underlying event. The properties of the *transverse* region were poorly reproduced by the PYTHIA calculations done with its default multiple interaction model.

For the structure of the multiple interaction PYTHIA proposes different models. The Model 3 (MSTP(82)=3) was developed to reproduce the UA5 data. It assumes a varying impact parameter between the two colliding particles. The hadronic matter overlap is described by a Gaussian matter distribution. In the default Model 4 (MSTP(82)=4), the hadronic matter overlap is consistent with a double Gaussian of the form:

$$\rho(r) \propto \frac{1-\beta}{a_1^2}\exp\left(-\frac{r^2}{a_1^2}\right)+\frac{\beta}{a_2^3}\exp\left(-\frac{r^2}{a_2^2}\right) \tag{11.3}$$

This corresponds to a distribution with a small core region, of radius a_2 containing a fraction β of the total hadronic matter, embedded in a larger hadronic matter of radius a_1. $\frac{a_2}{a_1}$ and β can be tuned with the PARP(84) and PARP(83) variables. This model was chosen to fit the CDF data and some parameters, PARP(83) and PARP(84) together with other variables determining the multiple parton interactions, were tuned to describe correctly the transverse region. This resulted in the so-called PYTHIA Tune A CDF [84, 83] with the CTEQ 5L PDF.

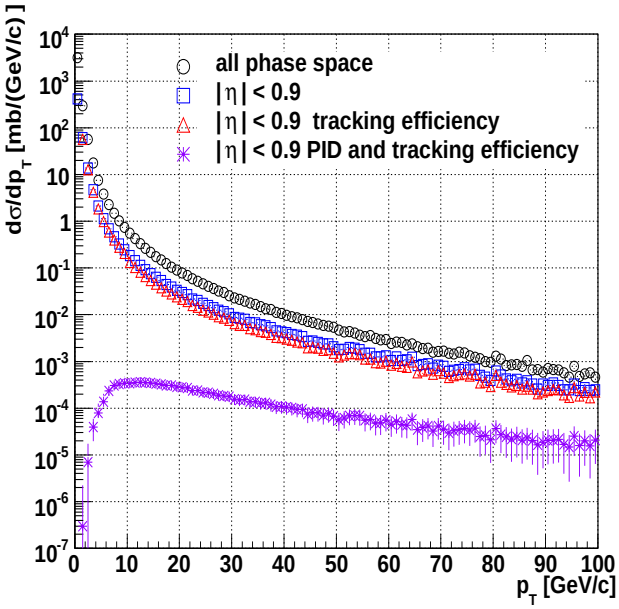

Figure 11.1: p_T-distribution of $\pi^{\pm}$ from HC pp collisions at 14 TeV in the total phase space and in the acceptance of the ACB. The resulting misidentified $e^{\pm}$ p_T spectrum is also plotted

Fig. 11.1 shows the $\pi^{\pm}$ p_T distributions obtained for HC pp collisions at 14 TeV. The PYTHIA cross-section of 54.7 mb was taken for the normalization. The p_T spectrum in the total phase space is plotted together with the p_T spectrum in the geometrical acceptance of the ACB ($|\eta|$<0.9). They are falling quasi exponentially with p_T. The resulting misidentified $e^{\pm}$ p_T spectrum can be calculated by applying first the tracking efficiency (open red triangle) and then the probability to misidentify the $\pi^{\pm}$ as an $e^{\pm}$ (magenta crosses). The p_T shape of the misidentified $e^{\pm}$ comes from the convolution of the falling $\pi^{\pm}$ p_T spectrum and the pion efficiency $\epsilon_{\pi^{\pm}}$, that increases with momentum.

11.4 $D\bar{D}$ and $B\bar{B}$ simultaneous semi-electronic decay

Heavy quarks are produced in initial hard pp collisions through primary partonic scatterings. The minimum virtuality Q_{min}=2c$M_{q_{hv}}$ for the production of a $q_{hv}\bar{q_{hv}}$ pair implies a space time scale of $\approx 1/(2c^2 M_{q_{hv}})$. Thus the formation time is about $\approx$0.1 and 0.02 fm/c for charm and beauty respectively. The large virtualities that characterize the production of heavy quarks allows to calculate the $c\bar{c}$ and $b\bar{b}$ production cross-sections in QCD perturbation theory. Moreover

the time to build up the wave functions of mesons including open charm and open beauty is of the order of 1 fm/c. Thus the heavy quark production and the heavy-flavored hadron production can be estimated decoupled. As a consequence the inclusive D and B mesons production cross-section can be calculated in the framework of collinear factorisation and perturbative QCD. The expression for the single-inclusive differential cross-section for the production of a heavy-flavour hadron $H_{q_{hv}}$ (D or B mesons) is then:

$$d\sigma^{pp\to H_{q_{hv}}X}\left(\sqrt{s}, M_{q_{hv}}, \mu_F^2, \mu_R^2\right) = \sum_{i,j} f_i\left(x_1, \mu_F^2\right) \otimes f_j\left(x_2, \mu_F^2\right) \otimes d\sigma^{ij\to q_{hv}\bar{q_{hv}}}\left(\alpha_s(\mu_F^2), \mu_F^2, M_{q_{hv}}, x_1x_2s\right) \otimes D_{q_{hv}}^{H_{q_{hv}}}\left(z, \mu_F^2\right) \tag{11.4}$$

where α_s, μ_F and μ_R are the strong coupling constant, the factorization scale and renormalization scale. The different terms of the convolution are:

- $f_i\left(x_1, \mu_F^2\right)$, the nucleon Parton Distribution Function for the parton of type i at momentum fraction x_1 of the proton, and renormalization scale μ_F. The concept of PDF is explained in the appendix C. This term is a non-perturbative term, that is parametrized. The $c\bar{c}$ and $b\bar{b}$ productions probe mainly the gluon PDF at a Bjorken scale x equal to $\approx 1.7\times10^{-4}$ and $\approx 6.4\times10^{-4}$ respectively. The uncertainties on the gluon PDF at these small x will introduce uncertainties in the final cross-section. Moreover the density of low-x gluons will be closed to saturation of the available phase-space. Gluon-recombination effects ($gg\to g$) could result in a higher gluon PDF in the x and Q range of interest for $c\bar{c}$ and $b\bar{b}$ production and leads to an enhancement of $q_{hv}\bar{q_{hv}}$ at low p_T.

- $d\sigma^{ij\to q_{hv}\bar{q_{hv}}}\left(\alpha_s(\mu_F^2), \mu_F^2, M_{q_{hv}}, x_1x_2s\right)$ is the partonic cross-section calculable in pQCD as a power series of the strong coupling constant α_s.

- $D_{q_{hv}}^{H_{q_{hv}}}\left(z, \mu_F^2\right)$ is the fragmentation function. This non-pertubative term parametrizes the probability for the heavy quark q_{hv} to fragment into a hadron $H_{q_{hv}}$ with momentum fraction $z{=}p_{H_{q_{hv}}}/p_{q_{hv}}$.

The first and last term are related to non-perturbative processes and are parametrized. Since we are interested in simultaneous semi-electronic decay of $D\bar{D}$ and $B\bar{B}$, the last step consists to let decay the D and B mesons. In the following, we will first focused on the production of $c\bar{c}$ and $b\bar{b}$ (first two terms in the convolution) and then study the resulting D and B mesons p_T distributions as well as the final $e^{\pm}$ p_T distributions.

11.4.1 $c\bar{c}$ and $b\bar{b}$ production

$c\bar{c}$ and $b\bar{b}$ are produced at leading order through pair creation: predominantly $gg\to q_{hv}\bar{q_{hv}}$ with a small contribution of $q\bar{q}\to q_{hv}\bar{q_{hv}}$. Moreover the Q^2 evolution equation of the PDF's, given by the DGLAP equation, leads to the possible presence of heavy quarks at the Q^2 scale of the hard interaction. Thus flavor excitations ($qq_{hv}\to qq_{hv}$) give rise to contributions at higher order, together with gluon splitting ($g\to q_{hv}\bar{q_{hv}}$) in initial- and final-state shower. The cross-sections of these higher-order processes are calculated using mass-less matrix elements in PYTHIA and

diverge when $p_T^{hard} \to 0$. A choice of a low p_T^{hard} cut-off has been previously done with the CTEQ 5L PDF's [68] to reproduce the NLO predictions (HVQMNR program [85]). In Fig. 11.2 the p_T distributions of the c and b quarks at NLO are compared with the PYTHIA results. Calculations are performed up to next-to-leading order according to the factorisation theorem. The CTEQ 4M PDF's are used together with the following set of parameters: for charm, M_c=1.2 GeV/c^2 and μ_F=μ_R=2μ_0, for beauty, M_b=4.75 GeV/c^2 and μ_F=μ_R=μ_0. μ_F, μ_R are respectively the factorisation scale and the renormalisation scale, μ_0=$\sqrt{(\mathrm{c}M_{q_{hv}})^2 + (p_{T,q_{hv}}^2 + p_{T,q_{\bar{hv}}}^2)/2}$. To obtain good statistics at high transverse momentum with PYTHIA, $c\bar{c}$ and $b\bar{b}$ were simulated in p_T^{hard} bins. Each bin was afterwards scaled by its corresponding cross-section. Beyond about 40 GeV/c, the c and b quarks production rates are similar. The p_T range of interest is above $\approx$ 80 GeV/c since only very high p_T quarks can produce after fragmentation into heavy-flavored mesons and their three body decays high p_T electrons ($p_{Te^\pm} \approx 45$ GeV/c=$\frac{\mathrm{c}M_{Z^0}}{2}$). In this region the c and b production rates are similar because the c and b masses become negligible. However the NLO calculations are found to be harder up to a factor 5. This would result in a contribution of $c\bar{c}$ and $b\bar{b}$ about 25 higher in the invariant mass yield.

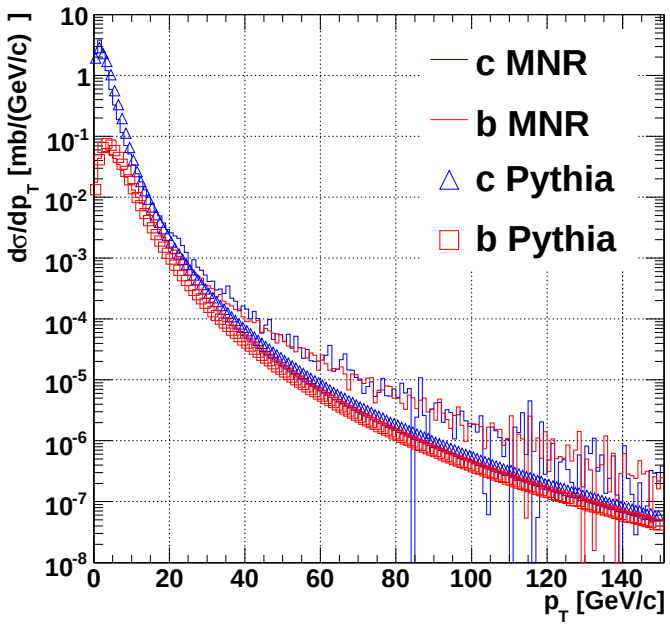

Figure 11.2: p_T distributions of the c and b quarks in the total phase space as they are calculated with the HVQMNR program [85] at NLO, compared with a tuned PYTHIA.

11.4.2 Fragmentation of c and b quarks and decay electrons

The c and b quarks produced in high energy event will lose a fraction of their momentum when picking up a light quark from the vacuum in order to hadronize into a heavy D or B meson. The non-perturbative fragmentation function is usually extracted from e^+e^- data.

Experiments like CLEO [86] at the Cornell Electron Storage Ring, BELLE [87] at the B factory of the KEKB electron-positron collider in Japan, or ALEPH [88], DELPHI [89] and OPAL [90] installed at the large electron-positron collider (LEP) at CERN, provide useful data for the study of the fragmentation of heavy quarks into D and B mesons ($e^+e^- \rightarrow q_{hv}X \rightarrow H_{q_{hv}}X$). The non-perturbative contributions are expected to be a small correction to pQCD results of the order of $O(\Lambda_{QCD}/M_{q_{hv}})$, where Λ_{QCD} is the QCD scale. The fragmentation should be a little bit harder for the b quarks than for the c quarks. The high-accuracy experimental data were found to be compatible with expectations and allowed to implement precisely a parametrization of the heavy quarks fragmentation function. At large p_T the corrections can be nevertheless large.

In PYTHIA the c and b quarks are hadronized with the default Lund String fragmentation model. The left panel of Fig. 11.3 shows the p_T spectra of c and b quarks, as well as D and B mesons obtained with PYTHIA after normalization to the NLO total $c\bar{c}$ and $b\bar{b}$ cross-sections. The results are in rough agreement with the expectations.

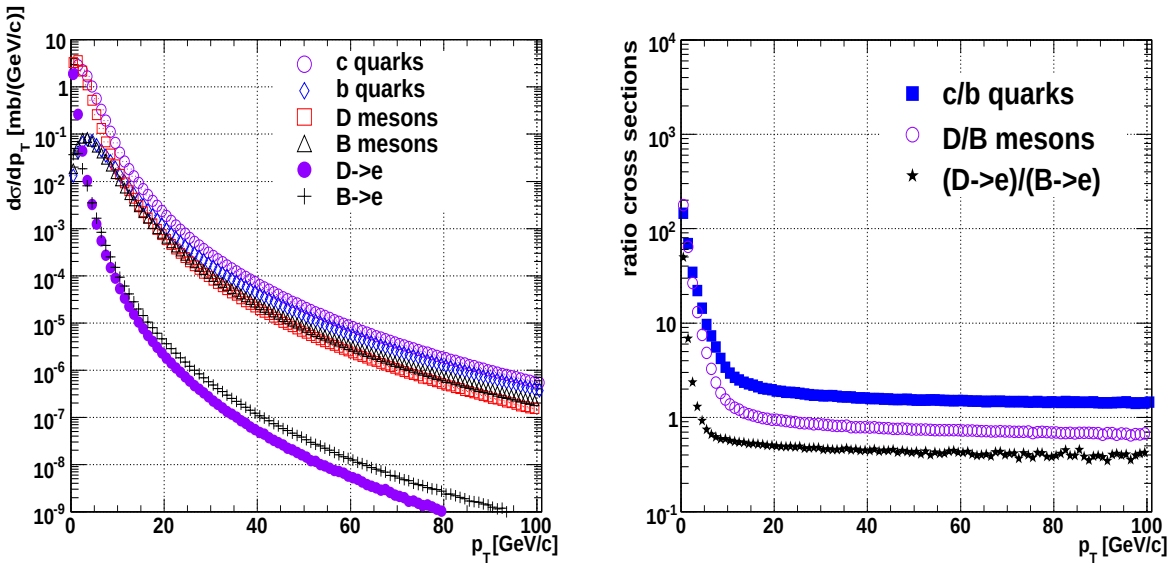

Figure 11.3: p_T distributions (left) and ratio of cross-sections (right) for c and b quarks, D and B mesons, and electrons from D and B.

Nevertheless, in PYTHIA charm quarks are assumed to fragment to D and D^* mesons according to the number of available spin states. D mesons are pseudoscalars with spin equal to 0, whereas D^* mesons are vectors with spin equals to 1. Thus the primary number of D^0,D^+,D^{*0} and D^{*+} are in the proportion 1:1:3:3. The resonances D^* mesons decay then to D mesons with a preference to D^0 due to the slightly larger mass of the D^+. The final ratio $N(D^0)/N(D^+)$ can be easily calculated with the corresponding branching ratios:

$$\frac{N(D^0)}{N(D^+)} = \frac{N(D^0_{primary}) + N(D^{*+}) \times Br(D^{*+} \to D^0) + N(D^{*0}) \times Br(D^{*0} \to D^0)}{N(D^+_{primary}) + N(D^{*+}) \times Br(D^{*+} \to D^+) + N(D^{*0}) \times Br(D^{*0} \to D^+)} \approx 3.08 \tag{11.5}$$

Experimentally this idea works only for B mesons. The ratio D^0/D^+ was namely found to be less than 3, about 2.4 by the ALEPH experiment [91]. An eventual explanation is the bigger mass difference between D^+ and D^0 (M_{D^+}≈1869.3 MeV/c^2, M_{D^0}≈1864.5 MeV/c^2) than between B^+ and B^0 (M_{B^+}≈5279.0 MeV/c^2, M_{B^0}≈5279.4 MeV/c^2). This would lead to an *enhancement* of $e^\pm$ from c compared to the simulations with PYTHIA, since D^+ has a much higher semielectronic branching ratio than D^0 (see Table 11.4). Thus for our study we decided to normalize the background contributions of simultaneous semi-electronic decay of D or B mesons to the NLO cross-sections and the branching ratios $\mathrm{Br}_{c\to e}$ and $\mathrm{Br}_{b\to e}$ taken from the reference [1].

The D and B mesons are forced to decay in their semileptonic channel. These are three body decays, for example $D^+ \to \bar{K}^0 e^+ \nu_e$. The different branching ratios are summarized in Table 11.4. The contribution of $b\to((D\to e+\mathrm{X})+\mathrm{X})$ is neglected here. The p_T final distributions are shown on the left panel of Fig. 11.3 after normalisation to the NLO cross-sections taking into account the branching ratios, $\mathrm{Br}_{c\to e}$≈9.6 % and $\mathrm{Br}_{b\to e}$≈10.86 %. The decay contributes also to the fact that most $e^\pm$ comes from b at high p_T. It can be seen on the right panel of the Fig. 11.3, where the ratios c/b, D/B and ($e^\pm$ from D)/($e^\pm$ from B) have been plotted.

	decay channels l+X
$D^0/\bar{D}^0$	6.7 %
D^+/D^-	17.2 %
D_s^+/D_s^-	8 %
$B^0/\bar{B}^0$	10.4 %
B^+/B^-	10.9 %

Table 11.4: semi-electronic branching ratios for D and B mesons.

To describe the underlying event, multiple parton interactions have been moreover turned on with the ATLAS setting [92].

11.5 Weak processes

11.5.1 $Z^0 \to \tau^+\tau^- \to (e^\pm/\pi^\pm)(e^\pm/\pi^\pm)+X$

Pure Z^0 was simulated like described before and forced to decay into $\tau^+\tau^-$. The $\tau^\pm$ was then forced to decay into channel where at least one $e^\pm$ or one $\pi^\pm$ are present.

11.5.2 $W^{\pm}\rightarrow e\nu_e$

The lowest order process for $W^{\pm}$ production ($q\bar{q'}\rightarrow W^{\pm}$) has been simulated with initial- and final-state radiations. In this way PYTHIA reproduces very well the $W^{\pm}$ p_T distribution in $p\bar{p}$ collisions at 1.8 TeV (see Fig. 7.3). The additional hadronic jets have to be also properly simulated since the contribution to the background comes mainly from the association of a $e^{\pm}$ from $W^{\pm}$ decay ($\mathrm{Br}_{W^{\pm}\rightarrow e\nu_e}$=10.75 % [1]) and a misidentified $\pi^{\pm}$ from a jet. The initial- and final-state showers algorithm of PYTHIA allows to generate these additional jets and mimic the higher orders.

11.5.3 $t\bar{t}$

The dominant lowest-order processes, mainly $gg\rightarrow t\bar{t}$ but also $q\bar{q}\rightarrow t\bar{t}$, have been simulated taking into account the quark masses. These are the same processes as for $c\bar{c}$ and $b\bar{b}$ production. However as $\sqrt{s}$ increases, the higher processes gain in importance relative to the lowest-order production graphs. Only about 10 %-20 % of the b production come from the lowest-order processes at LHC energies. The fraction is even smaller for charm. The large mass of the t quark (M_t≈174 GeV/c^2) compared to the mass of the c and b quarks (M_c≈1.2 GeV/c^2, M_b≈4.75 GeV/c^2) leads to a much larger fraction, well above 50 %. In this case, the higher-order corrections can be approximated by an effective k factor. That is why only the lowest-order processes were simulated for $t\bar{t}$ production. The spectra are normalized with the NLO cross-section.
All decay channels have been let open. According to the Cabibbo-Kobayashi-Maskawa Matrix, the t quark decays weakly with a quasi 100 % branching ratio to a $W^{\pm}$ boson and a b quark. Its width can be estimated with the following formula [93]:

$$\Gamma_t \approx 175\,\mathrm{MeV} \times \left(\frac{M_t}{M_W}\right)^3 \approx 1.8\,\mathrm{GeV} \tag{11.6}$$

The corresponding lifetime is about:

$$\tau_t = \frac{1}{\Gamma_t} \approx 3 \cdot 10^{-25}\mathrm{s} \tag{11.7}$$

Simultaneous semielectronic decays of $W^{\pm}$ bosons ($\mathrm{Br}_{W^{\pm}\rightarrow e\nu_e}$=10.75 % [1]) leads to correlated background. The b quark has moreover a similar probability as the $W^{\pm}$ bosons to fragments and finally decays in a semielectronic channel ($\mathrm{Br}_{b\rightarrow e}$≈10.86 %). Nevertheless the $e^{\pm}$ from $W^{\pm}$ are better isolated as the $e^{\pm}$ from B mesons decay, which are always accompanied by hadrons. As a consequence it is more difficult to reject them with an isolation cut.

11.6 Final estimated background

Before the invariant mass yield with the estimated background contributions is presented, single generated and reconstructed electron p_T spectra are shown.

11.6.1 Single electron spectra

In the left panel of Fig. 11.4, the different generated contributions to the single electron p_T spectra are shown in the total phase space. For $t\bar{t}$ events all electrons are plotted including the ones coming from the underlying event. That explains the enhancement at low p_T. The distributions are normalized to the NLO cross-sections times the appropriate branching ratios. The $e^{\pm}$ from $W^{\pm}$ and Z^0 decays have a similar p_T shape. The $e^{\pm}$ from $W^{\pm}$ are a factor 5 higher ($\sigma_{pp\rightarrow WX\rightarrow e\nu_e X}\approx 5\times(2\times\sigma_{pp\rightarrow Z^0X\rightarrow e^+e^-X})$) and present a peak situated at a slightly lower p_T ($\frac{cM_{W^{\pm}}}{2}\approx 40\,\mathrm{GeV/c}$ compared to $\frac{cM_{Z^0}}{2}\approx 45\,\mathrm{GeV/c}$). The $e^{\pm}$ from $Z^0\rightarrow\tau\rightarrow e$ are shifted to lower p_T values since there is one supplementary decay in the chain. The mass of c and b quarks becomes negligible at high p_T and they are produced with similar rates. Nevertheless the harder beauty fragmentation and the decay of B mesons result in a harder transverse momentum spectrum for the decay electrons. For comparison the p_T $\pi^{\pm}$ distribution from jets is also presented with a scale down factor of 1000. $\pi^{\pm}$, D and B have comparable slopes at high p_T but the electrons from D and B decays are softer due to the three body decay.

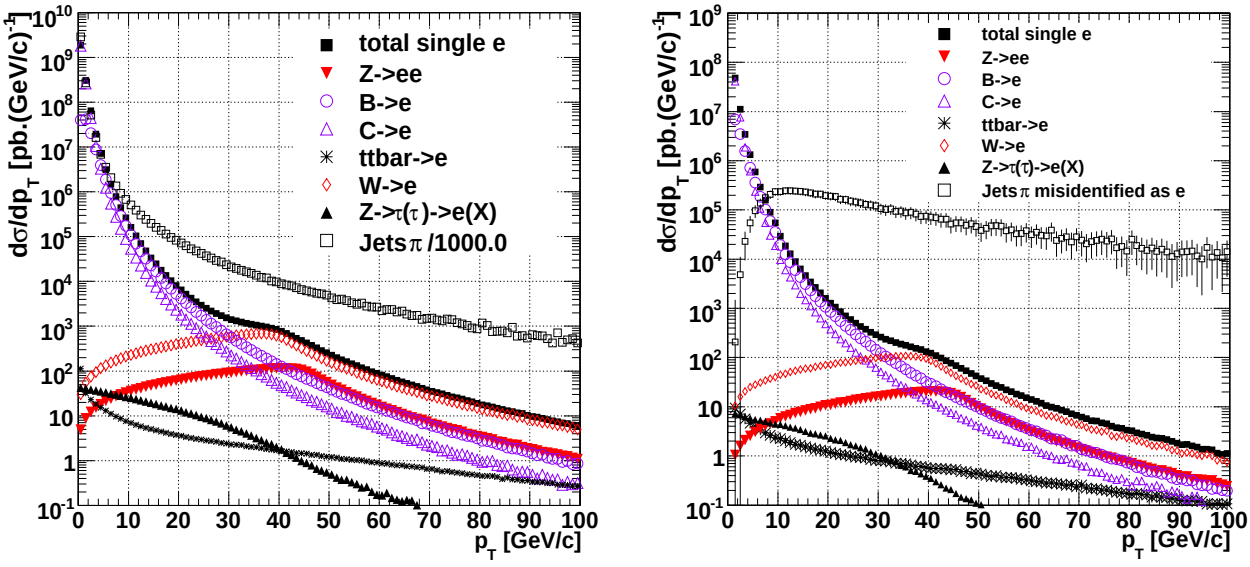

Figure 11.4: Single electron spectra in the total phase space (left) and single reconstructed electron spectra in the central barrel (right) as a function of transverse momentum in pp collisions at $\sqrt{s}$=14 TeV.

In the right panel of Fig. 11.4, the resulting single electron spectra are presented as they are reconstructed in the central barrel ($|\eta|$<0.9). The relative contributions of D and B mesons decays are slightly higher. Moreover one has now to take into account the misidentified $\pi^{\pm}$ from jets. They constitute the main source of reconstructed electrons above 10 GeV/c, even with the combined pion rejection of the TPC and the TRD. At p_T=40 GeV/c, the $\pi^{\pm}$ from jets are 10^4 orders of magnitude higher than the true $e^{\pm}$. With a rejection factor of about 0.10 (see Fig. 9.15), this results to a contribution of misidentified $\pi^{\pm}$ from jets 10^3 higher than true $e^{\pm}$.

11.6.2 Invariant mass yields

Table 11.5 gives the background contributions relative to the signal in the invariant mass range $66\,\mathrm{GeV}/c^2 < M_{e^+e^-} < 116\,\mathrm{GeV}/c^2$ for different cuts. The errors are statistical.

	p_T>10 GeV/c	p_T>25 GeV/c	p_T>10 GeV/c iso cut	p_T>25 GeV/c iso cut
Multi-jets	× (117±42)	×(72±34)	(1.6±8.5)%	(0.5±5.2)%
$t\bar{t}$	(0.2±0.05)%	(0.17±0.05)%	(0.13±0.04)%	(0.10±0.04)%
$W^{\pm} \rightarrow e\nu_e$+jets	(0.1±0.09)%	(0.07±0.08)%	(0.03±0.05)%	(0.02±0.04)%
$b\bar{b} \rightarrow e^+e^- + X$	(0.2±0.04)%	(0.14±0.03)%	<0.01%	<0.01%
$Z^0 \rightarrow \tau\tau \rightarrow (\pi/e)(\pi/e) + X$	(0.01±0.003)%	<0.01%	<0.01%	<0.01%
$c\bar{c} \rightarrow e^+e^- + X$	(0.04±0.01)%	(0.02±0.01)%	<0.005%	<0.005%

Table 11.5: Background contributions relative to the signal for different cuts.

The main contribution comes from misidentified pions from jets. They can be very well rejected with an isolation cut. The rejection factor is of the order of 10^4. The isolation cut suppresses also the correlated background from simultaneous semi-electronic decays of D and $\bar{D}$, or B and $\bar{B}$, mesons. Nevertheless the rejection factor was found to be slightly smaller. Even with a possible enhancement of c and b due to higher order corrections, their contribution to background remains very small. The requirement of isolated reconstructed electrons is not really efficient to reject the contribution from $t\bar{t}$ events. The simultaneous semi-electronic decays of W^+ and W^- bosons emitted in the t and $\bar{t}$ decays leads to a pair of isolated electron-positron. Only $e^{\pm}$ from b decays (after $t \rightarrow Wb$) will be rejected. The situation is slightly better for $W^{\pm} \rightarrow e\nu_e$+jets since misidentified $\pi^{\pm}$ from jets are well rejected. The contributions from $Z^0 \rightarrow \tau^+\tau^- \rightarrow (\pi^{\pm}/e^{\pm})(\pi^{\pm}/e^{\pm}) + X$ is always negligible. The p_T of reconstructed $e^{\pm}$ from $\tau^{\pm}$ decay are much smaller and as a consequence the reconstructed invariant mass lies outside of the mass window for the Z^0. With the help of a p_T cut at 25 GeV/c and the isolation cut, the total background amounts to about (0.7±5.3)% of the signal. However this is dominated by the statistical errors on jets and the uncertainties on the jet cross-section. In conclusion Z^0 is expected to be quasi free of background in its electronic decay channel.

Fig. 11.5 illustrates the results of Table 11.5. In the left panel, the reconstructed Z^0 dielectron invariant mass yield per minimum-bias pp collision is shown. The background yield is also plotted for different cuts. By only requiring a p_T above 10 GeV/c or 25 GeV/c for the electron candidates, the background from jets dominates the dielectron invariant mass yield in the mass range of Z^0. The isolation cut improves dramatically the signal-to-background ratio, that increases from $\approx 10^{-2}$ to ≈ 150. In the right panel of Fig. 11.5, the different contributions to background averaged for M_{inv}=66-116 GeV/c^2 are presented for a p_T cut at 25 GeV/c and the isolation cut together with the signal.

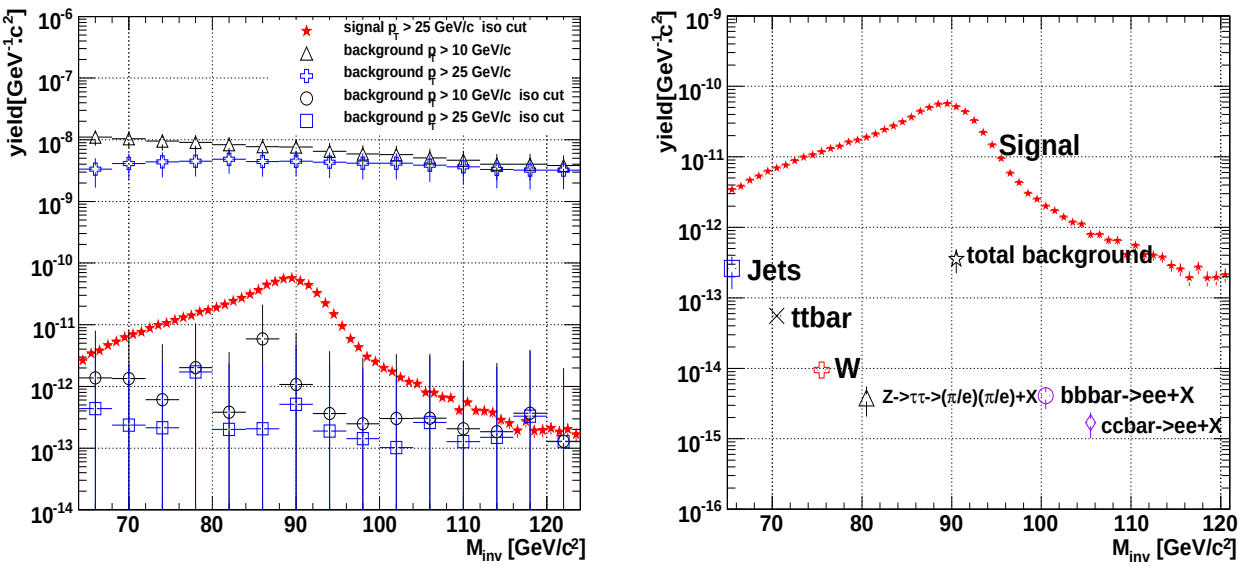

Figure 11.5: Left panel: reconstructed invariant mass yield of electrons from Z^0 decays and from the background sources for different cuts at the single track level. Right panel: different contributions to the background for a p_T cut at 25 GeV/c and with the isolation cut. The contributions have been averaged over the invariant mass range 66 GeV/c^2<M_{inv}<116 GeV/c^2.

11.7 Efficiency of the isolation cut

The isolation cut was applied with the fast simulation program, where no secondary particles are included, since the response of the ACB is directly applied to the generated primary particles and no propagation with Geant 3 through the detector material is performed. This cut is based on the presence of an other reconstructed track with p_T>2 GeV/c in the neighborhood of the $e^{\pm}$ tracks. Secondary particles could eventually contribute to reject the $e^{\pm}$ track. This would improve the rejection factor for the background and decrease the efficiency ϵ_{iso} for the signal. Nevertheless secondary particles are soft particles with low p_T and most of them don't pass the requirement p_T>2 GeV/c. Moreover the other reconstructed track have to be refitted in the ITS, TPC and TRD. This excludes secondary particles produced in the last layers of the ITS and the other detectors.

To check if the effect of secondary particles on the isolation cut is indeed negligible, the same analysis was carried out for a reduced sample of events with the AliRoot framework. By comparing the results with the ones obtained with the fast simulation program, one can quantify the influence of secondary particles or detector effects which may be not well described by the parametrization. The efficiency ϵ_{iso} was estimated with the ratio of electrons and pions passing the isolation cut:

$$\epsilon_{iso} = \frac{(e^{\pm} + \pi^{\pm})_{\text{passing the isolation cut}}}{(e^{\pm} + \pi^{\pm})_{\text{total}}} \tag{11.8}$$

Fig. 11.6 shows the ϵ_{iso} dependence as a function of the $e^{\pm}/\pi^{\pm}$ transverse momentum. The results obtained using the fast simulation program (closed symbols) are very close to those

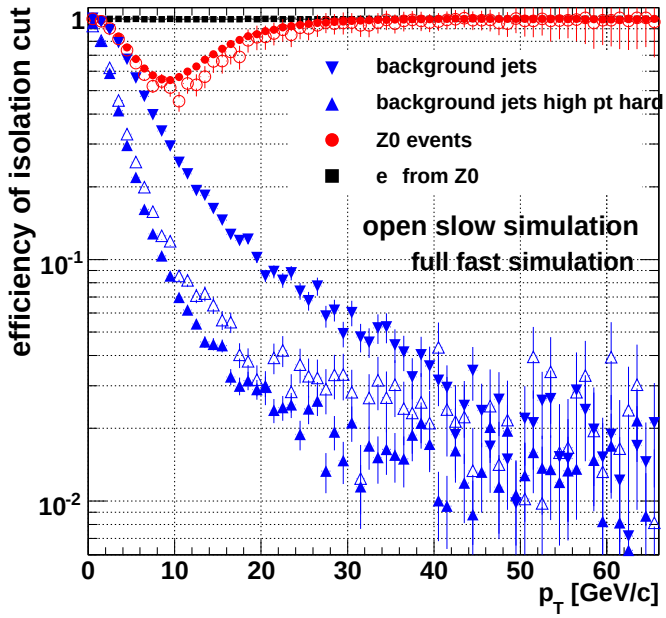

Figure 11.6: Fraction of electrons and pions passing the isolation cut calculated using the full AliRoot framework (open symbols) and the fast simulation (closed symbols) for different event types.

obtained with the calculations done by propagating the primary particles with Geant 3 through the detectors (open symbols). For events containing a $Z^0 \rightarrow e^+e^-$, the ratio for electrons coming from the Z^0 decay alone ($e^{\pm}_{Z^0}$) is also plotted ($e^{\pm}$ *from* Z^0).

$$\epsilon_{iso}^{e^{\pm}_{Z^0}} = \frac{(e^{\pm}_{Z_0})_{\text{passing the isolation cut}}}{(e^{\pm}_{Z^0})_{\text{total}}} \tag{11.9}$$

As expected the electrons emitted in Z^0 decay are isolated and present an efficiency $\epsilon_{iso}^{e^{\pm}_{Z^0}}$ close to 100 %. Pions in the Z^0 events, affected by the isolation cut, reduce the overall efficiency ϵ_{iso} of Z^0 events at low p_T. The rejection factor of pions and electrons from jets increases with p_T and the p_T^{hard} of the interactions. For high p_T^{hard} collision, the isolation cut reject high p_T electrons and pions from jets (p_T=45 GeV/c) by a factor 10^{-2}. This is consistent with the 10^4 rejection factor found in the invariant mass yield of misidentified pions as electrons from jets.

Chapter 12

Trigger strategy and performances in other LHC experiments

The study of rare probes, like the Z^0 with cross-sections in the order of 10 nb, requires dedicated triggers to enhance the events containing the signals. Without trigger, with a yield of about $3{\times}10^{-8}$ per minimum-bias *pp* collisions at 14 TeV and an acceptance of 3 %, only one $Z^0{\rightarrow}e^+e^-$ events for 10^9 *pp* events is reconstructed in the central barrel of ALICE.

12.1 Nominal conditions

The maximal luminosity $\mathcal{L}$ of the accelerator is in the order of $10^{34}\,\mathrm{cm^{-2}s^{-1}}$. This implies a interaction rate $\mathcal{R}$ of 1 GHz.

$$\mathcal{R} = \sigma\mathcal{L} \approx 100\,\mathrm{mb} \times 10^{34}\,\mathrm{cm^{-2}s^{-1}} \approx 10^9\,\mathrm{s^{-1}} \approx 1\,\mathrm{GHz} \tag{12.1}$$

The ALICE detectors, particularly the TPC, can not work properly in these conditions.
The TPC [94] is a huge gas volume with an overall length in the beam direction of 500 cm. The central electrode separates the drift volume in two equal parts 250 cm long with a voltage gradients of 400 V/cm. The resulting electron drift velocity is 2.84 cm/μs. As a consequence, the electrons produced by ionization of the gas along the particle path need a maximal drift time of 88 μs to reach the readout chambers situated at each side of the TPC volume. All charge created in the gas volume is not amplified, otherwise the ions produced in the avalanches during the amplification process would accumulate in the drift volume and cause severe distortions of the drift field. A gating grid is located above the cathode wire grid of the amplification region, designed as the amplification region of the TRD (cathode wire grid, anode wire grid and cathode pad plane). Its role is to let electrons from the drift volume enter the amplification region in the open gate mode and to prevent them from entering in the close gate mode. The typical gate opening time 100 μs is comparable to the maximal drift time. Thus an interaction rate of 1 GHz means 10^5 interactions per 100 μs, 10^5 *pp* collisions at the same time in the TPC. The maximal limit has been estimated to be 100 *pp* collisions [9]. That is why the maximal luminosity, at which the ALICE experiment can run, is about $10^{31}\,\mathrm{cm^{-2}s^{-1}}$. This is achieved

by defocusing the beams. For rare probes, like the Z^0, pile-up of events, will play a role for the scaling of the background. Given the small $Z^0 \rightarrow e^+e^-$ production cross-section, there is no chance that more than one of this type of events are in the 100 collisions. Nevertheless for the background, with production cross-section in the order of 10 % or even more of the total *pp* cross-section, it can happen that more than one collision in the 100 collisions contribute to it. Therefore the capability to distinguish these 100 collisions become crucial.
In the unrealistic case, in which all interactions could be recorded and analyzed, the 8 months of *pp* data taking ($t_{running} = \approx 7 \times 10^6$ s) would provide $t_{running} \times \mathcal{R} = 7 \times 10^{12}$ minimum-bias *pp* events. With one Z^0 reconstructed for 10^9 events, this corresponds to a maximal number of 7000 reconstructed Z^0 per year. In reality, since the events are written at about 500 Hz, only 10^9 events can be recorded per year. One can try to get closer to the ultimate limit of 7000 reconstructed Z^0 per year by writing only events having specific properties. This is the role of a dedicated trigger.
The trigger signals come from a Central Trigger Processor (CTP), that takes decisions at different levels based on the response of the different subdetectors of ALICE. At the Level 0 (L0), the first trigger signal is a minimum-bias *pp* or *PbPb* collision trigger. The delay of the L0 signal is about 900 ns from the interaction up to the arrival at the CTP. This is too long for the TRD, which requires an early *wake-up* signal from the forward detectors (V0, T0) and/or the fast time of light (TOF) detector. This wake up signal is called pretrigger and is given to the TRD 700 ns after the interaction. As a consequence, two more timebins (100 ns each) can be processed by the electronic before L0. A Level 1 (L1) trigger should be delivered 6 μs after the collision to the TPC, whose data will be read in case of positive signal. The 6 μs includes the processing of the signal and trigger decision for each L1 subdetectors like the TRD, and the final decision of the CTP. During this time, the detectors are in a *busy* status and should not receive any L0 signal from the CTP. Two types of Level 2 (L2) trigger are foreseen in the future. One should select the event centrality at a frequency of about 40Hz for *PbPb* collisions and trigger the readout of all ALICE detectors. The other, based on the detection of dimuon in the muon arm, should run at an expected frequency of 1 kHz and trigger only the readout of the muon arm and Silicon Pixel Detector data. At the Level 3 (L3), the data of some detectors are analyzed. This occurs at the High-Level-Trigger (HLT) with a maximal rate of 1 kHz. The events are then finally written. It was first foreseen to open the TPC gating rate at the Level 1. The L1 time decision has to be short compared to the total drift time of the TPC, 88 μs, since the delay in opening the gating grid involves a shortening of some tracks in the TPC at large forward/backward polar angles. In reality for some technical details, it seems now difficult for the TRD to keep the L1 time decision below 6 μs. A delay of about 1.37 μs is for the moment still remaining. Alternate scenarios like opening the gating grid at the Level 0 and closing it with the non occurrence of the TRD trigger are therefore under discussion.

12.2 L1 trigger with the TRD

The TRD trigger allows:

- to find and select tracks with transverse momenta above 3 GeV/c.
- to separate electrons from pions.
- to compute correlation quantities like the invariant mass of track pairs.

Based on this information, the decision to analyze further the event can be taken. The trigger is implemented in the following way:

- In the front-end electronics sitting on the chambers themselves, Local track segment (*tracklet*) are searched independently in parallel processors called Local Tracking Units (LTU). A maximal number of 4 *tracklets* per LTU (16.8 mm in $r\phi \times cm$ in 0.7 cm z) is possible. A low p_T cut at 2.3 GeV/c is implied.
- The data of half chambers are shifted to the Global Tracking Units (GTU, back-end electronics) outside of the magnet by optical fibers. A data transfer of 2 TBit/s is achieved.
- At the GTU, 90 Track Matching Units (TMU), one per TRD stack, search for *tracks* by matching the *tracklets* in the six layers of the stack.
- A final trigger decision is given to the CTP.

Fig. 12.1 shows the time scale on which this is happening. The Fit Calculation and Tracklet Calculation are in the LTUs.

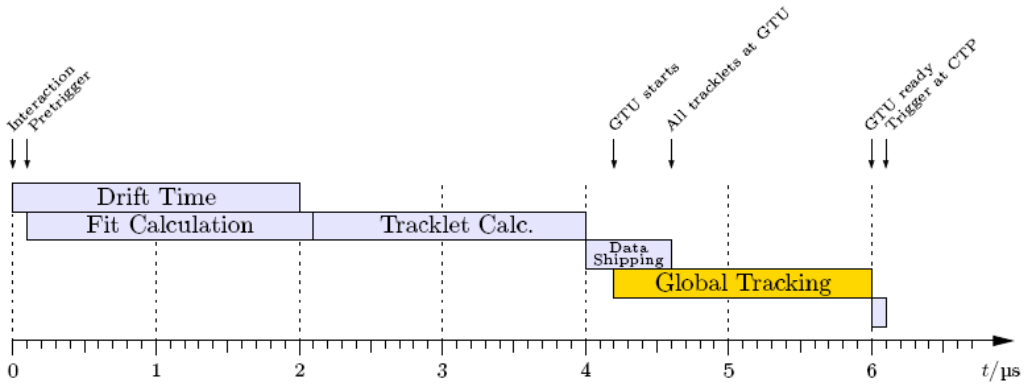

Figure 12.1: Time scale of TRD trigger [95].

12.3 First expectations for a simple L1 trigger

The TRD offers the possibility to have a dedicated L1 trigger based on a low-p_T cut and electron identification. The background-to-signal (B/S) ratio can be estimated with the ratio of charged pions from jets to electrons from Z^0, see Fig. 12.2. Assuming a modest average online pion rejection factor of only 2, the ratio B/S is about 10^6 for a low-p_T cut of 10 GeV/c. The ratio B/S is dramatically improved to 2.5×10^5 if a p_T cut of 20 GeV/c could be employed,

however, the selectivity of the TRD L1 trigger for such a higher value of p_T remains to be demonstrated. A further reduction of B/S can be achieved in the High-Level Trigger. For the present estimates we use B/S=10^6 achievable with the conservative TRD L1 trigger.

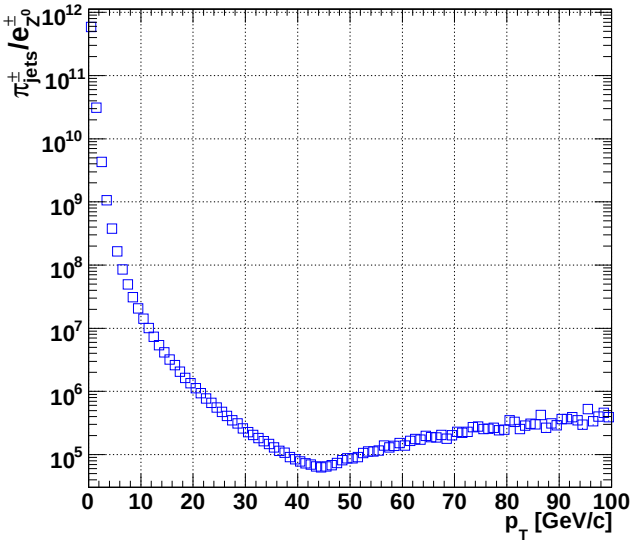

Figure 12.2: Ratio of $\pi^{\pm}$ from jets to $e^{\pm}$ from decay of Z^0 as a function of transverse momentum. No $e^{\pm}/\pi^{\pm}$ identification is employed.

Assuming that 10 % of the total number of events acquired in pp collisions during one year are with this L1 trigger (10^8 events), 100=$10^8/(B/S)$ Z^0s will be reconstructed per year. Taking into account that we could reconstruct one $Z^0 \rightarrow e^+e^-$ in 10^9 minimum-bias pp collisions, a minimal limit of 10^{11} interactions have to take placed during one year pp data taking (7×10^6 s). The required interaction rate to make this sample available is 14 kHz, corresponding to a luminosity of $2\times10^{29}\,s^{-1}cm^{-2}$.

12.4 Other decay channel and LHC experiments

12.5 $Z^0 \rightarrow \mu^+\mu^-$ in the ALICE muon spectrometer

ALICE is equipped with a muon spectrometer [96], that covers the η-range -4<η<-2.5. It consists of 3 absorbers, a muon magnet, a trigger system and a tracking system. The lay-out of the muon spectrometer is presented in Fig. 12.3.

The role of the absorbers is to absorb the primary hadrons produced in the collision. Only muons can penetrate the big amount of material placed in front of the spectrometer and be tracked in the muon spectrometer tracking chambers. The momentum of the $\mu^{\pm}$ is reconstructed in the tracking chambers (stations 1-5) inside a magnetic field (0.7 T) directed in the horizontal plane perpendicular to the beam direction. The muon spectrometer triggers on high p_T $\mu^{\pm}$

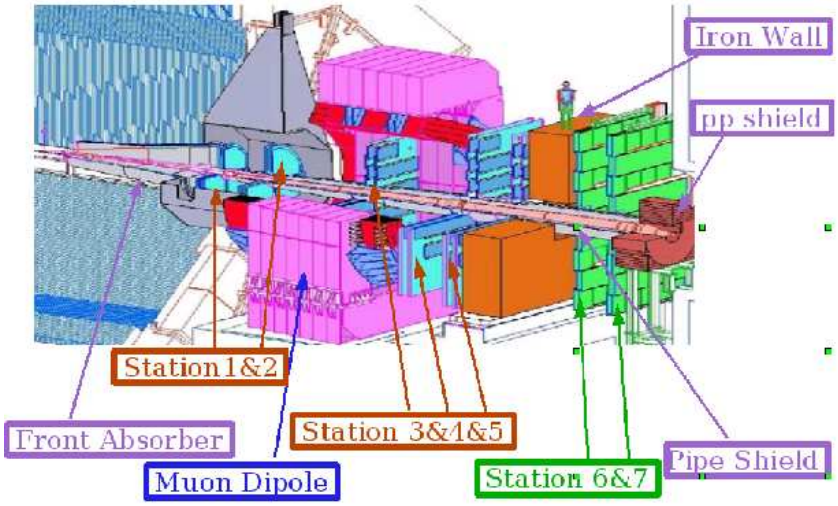

Figure 12.3: Muon Spectrometer in ALICE.

(p_T>1 GeV/c) with the stations 6-7.
$Z^0 \rightarrow \mu^+\mu^-$ events can be reconstructed in the muon spectrometer. The geometrical acceptance A_{geo} was found to be about 4.4 % [97]. This is the fraction of $Z^0 \rightarrow \mu^+\mu^-$ events, in which both of $\mu^\pm$ are in the muon spectrometer acceptance. The tracking efficiency, ϵ_{tr} was estimated to be in the order of 97 %, which leads to a total acceptance of $A_{geo} \times {\epsilon_{tr}}^2 \approx 4\,\%$. Not trigger efficiency study was done yet. For 100 % trigger efficiency and an integrated luminosity of 70 pb^{-1}, about 130,000 $Z^0 \rightarrow \mu^+\mu^-$ are produced in the total phase space and 5300 are reconstructed in the ALICE muon spectrometer.

12.6 Other LHC experiments

The ATLAS [98] and CMS [99] experiments at the LHC have a complete different general trigger strategy than ALICE. Since they have been designed to discovery the Higgs-boson, they have to be sensitive to production cross-sections in the order of 100 fb. To achieve this challenging goal, they plan to run at a *low* luminosity of $\mathcal{L} = 10^{33}\,\mathrm{cm}^{-2}\mathrm{s}^{-1}$ in the first year(s) and reach finally the maximal luminosity of $\mathcal{L} = 10^{34}\,\mathrm{cm}^{-2}\mathrm{s}^{-1}$ in the following years. No detector can follow the corresponding interaction rates, but since they are only interested in rare probes, they don't care so much about the pile-up of events, as soon as the background is under control. The lay-out of the ATLAS and CMS detectors is principally based on:

- an Inner Tracking System inside a high magnetic field (2 T for ATLAS and 4 T for CMS) to track charged particles and reconstruct the primary vertex and distance of closest approach to the primary vertex.
- a most hermetic electromagnetic and hadronic calorimeters system as possible to identify γ, $e^\pm$ and jets with energy from 10 GeV to 1 TeV and determine missing transverse energy.
- muon chambers after (and in) absorbers inside a magnetic field (≈3.9-4 T for ATLAS and

2 T for CMS) to look at muonic decays of particles.

Even if the ATLAS experiment is equipped with a Transition Radiation Tracker in its Inner Tracking System, it is used only for intermediate p_T $e^{\pm}$ identification. High p_T $e^{\pm}$ are identified with calorimeters. ATLAS and CMS benefit from a very high luminosity and a large η-range covered by their detectors.

Experiment	electrons	muons
ALICE	$\|\eta\|<0.9$ $p_T>1$ GeV/c	$-4<\eta<-2.5$ $p_T>1$ GeV/c
ATLAS	$\|\eta\|<2.5$ $p_T>5$ GeV/c	$-4<\eta<2.4$ $p_T>3$ GeV/c
CMS	$\|\eta\|<3$ $p_T>5$-10 GeV/c	$-4<\eta<2.4$ $p_T>3.5$ GeV/c

Table 12.1: η and p_T range covered by the different LHC experiments for the electrons and muons.

Table 12.1 summarizes the η and p_T acceptances for $e^{\pm}$ and $\mu^{\pm}$. Definitively the ALICE experiment can not compete with the ATLAS and CMS experiments concerning the Z^0. The goal of the ALICE experiment is also not a precise measurement of the Z^0 production cross-section, but more to use Z^0 as a *candle* for our understanding of the detectors at high p_T. For an integrated luminosity of 50 pb^{-1}, the ATLAS experiment expect to reconstruct about 30,000 $Z^0 \rightarrow \mu^+\mu^-$ events with a background below 1 % [100, 101]. At a luminosity of $\mathcal{L}= 10^{33}$ cm^{-2}s^{-1}, this correspond to 5×10^4 s running time, about 14 hours running.

Part III

Measurement of $c\bar{c}$ and $b\bar{b}$ cross-sections through semi-electronic decays of heavy-flavored hadrons in pp collisions

Chapter 13

Measurement of $c\bar{c}$ and $b\bar{b}$ cross-sections in ALICE

13.1 Physics Motivations

In pp collisions, heavy quark production allows to test pQCD calculations at high p_T because of the large virtualities that characterize the process. The total cross-section is computed as the convolution of the Parton Distribution Functions and the partonic cross-section. Since $c\bar{c}$ and $b\bar{b}$ are mainly produced by gluon fusion, the measurement will probe the gluon PDF at low Bjorken scale x ($x_{c\bar{c}}$≈2×10^{-4} and $x_{b\bar{b}}$≈6×10^{-4} at mid-rapidity for $\sqrt{s}$=14 TeV).

In $PbPb$ collisions, the c and b cross-sections are crucial ingredients for models predicting the J/Ψ production in QGP. The initial and final state effects on the production rates are studied via the comparison with pp collisions at the same $\sqrt{s}$. The cold matter effects, like shadowing, can be separated from the hot matter effects due to the high density medium created during the collision, by analyzing pPb collisions. No pp runs at $\sqrt{s}$=5.5 TeV are foreseen. Nevertheless given the large intrinsic virtualities of the heavy quark production, the extrapolation from 14 TeV to 5.5 TeV has small theoretical errors. Using the Glauber model, the nuclear modification factor R_{AA} is defined as the ratio of measured yield in $PbPb$ collisions to the one in pp collisions scaled with the mean number of inelastic nucleon-nucleon collisions $\langle N_{coll}\rangle$:

$$R_{AA} = \frac{1}{\langle N_{coll}\rangle}\frac{d^2N_{AA}/dp_Tdy}{d^2N_{pp}/dp_Tdy} \tag{13.1}$$

In absence of any medium effect, R_{AA} is unity. Deviations from unity allow to study the heavy quark energy loss. The last one is expected to be smaller than for light quarks at small momenta due to the dead-cone effect [102]. Surprisingly similar high p_T suppressions were observed for light-flavored hadrons and single electrons from heavy quarks at the Relativistic Heavy Ion Collider in $AuAu$ collisions at $\sqrt{s}$=200 GeV. The interpretation of the results is still under discussion and more precise measurements at LHC will help understanding the process.
The measurement of $c\bar{c}$ and $b\bar{b}$ cross-sections in $PbPb$ collisions provides also a reference for the production of quarkonia. The cross-sections are larger than the one of the Drell-Yan process

and vector boson Z^0 production, and the heavy quarks are produced by the same $gg \rightarrow q_{hv} \bar{q_{hv}}$ process as the quarkonia. Moreover, the knowledge of the B meson production is important in order to estimate the contribution of secondary J/Ψ from $B \rightarrow J/\Psi + X$ decays to the total J/Ψ yield.

13.2 Previous measurements

Up to the energies of the Intersecting Storage Rings at CERN ($\sqrt{s}$=63 GeV), the $c\bar{c}$ production is reasonably reproduced by NLO pQCD calculations in pp and pA collisions with binary nucleon-nucleon collision scaling [103]. At the Relativistic Heavy Ion Collider in pp collisions at $\sqrt{s}$=200 GeV, the STAR $c\bar{c}$ cross-section is a factor two higher than the PHENIX results [104, 105, 106]. Both measurements are larger than pQCD calculations but PHENIX $c\bar{c}$ cross-section is compatible with pQCD within errors. The charm and beauty production was also studied at the Tevatron in $p\bar{p}$ collisions at $\sqrt{s}$=1.96 TeV. While the theory slightly underpredicts the $c\bar{c}$ cross-section, the beauty production is fairly well reproduced [107].
In heavy-ion collisions, the PHENIX and STAR experiments found a suppression of the $e^{\pm}$ coming from c and b quarks [108, 106, 109], similar to that of light-flavored hadrons. This raises interest since it contradicts expectations.

13.3 Computed cross-sections at the LHC

At LHC energies, the $c\bar{c}$ and $b\bar{b}$ production was estimated at NLO with the HVQMNR code for pp collisions [85]. Fig. 13.1 shows the production cross-sections as a function of $\sqrt{s}$.

The values are summarized in Table 13.1 for the two c.m.s energies, at which the LHC will be operated in the next years.

$\sqrt{s}$ [TeV]	$\sigma_{pp}^{c\bar{c}}$ [mb]	total yield
14	11.2	0.16
10	9	0.13
	$\sigma_{pp}^{b\bar{b}}$ [mb]	
14	0.51	0.0072
10	0.32	0.005

Table 13.1: Heavy quark production calculated at NLO for LHC energies in pp collisions.

The cross-sections in $PbPb$ collisions were computed for two centrality ranges (0-5 % and 0-10 %) using the NLO pQCD cross-sections in pp collisions at the same $\sqrt{s}$ and the Glauber model. The modification of the PDFs inside the Pb nucleus leads to smaller cross-sections with

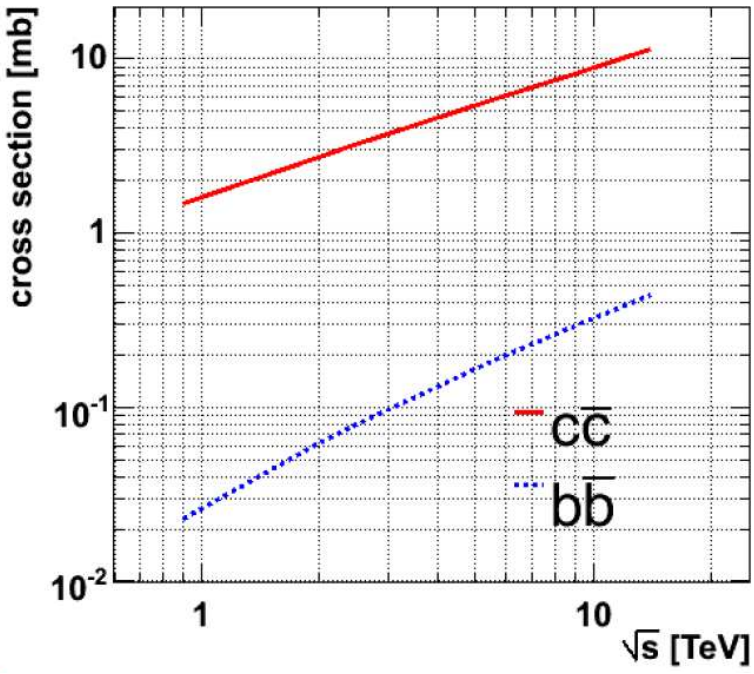

Figure 13.1: Heavy quarks production as a function of $\sqrt{s}$ in pp collisions estimated at NLO with the HVQMNR code [110].

respect to the simple geometrical scaling. The shadowing effect is quantified by the ratio C_{shad} of the cross-sections calculated with and without modification of the PDFs. The results are given in Table 13.2.

	Charm	Beauty
$\sigma_{NN}^{q_{hv}q_{\bar{hv}}}$ [mb]	6.64	0.21
C_{shad}	0.65	0.84
$\sigma_{PbPb}^{q_{hv}q_{\bar{hv}}}$ [b] $5\,\%\sigma^{inel}$	45.0	1.79
$10\,\%\sigma^{inel}$	81.0	3.38
$N_{PbPb}^{q_{hv}q_{\bar{hv}}}$ $5\,\%\sigma^{inel}$	115	4.56
$10\,\%\sigma^{inel}$	102	4.06

Table 13.2: Heavy quark production in $PbPb$ collisions at 5.5 TeV computed with the NLO pQCD cross-sections and the Glauber model. A shadowing factor C_{shad} estimated with the EKS98 parametrization has also been taken into account [68].

13.4 How to measure $c\bar{c}$ and $b\bar{b}$ cross-sections in ALICE?

The c and b quarks hadronize in open-charm and open-beauty hadrons, principally mesons. Since the formation time of mesons ($\approx$1 fm/c) is one order of magnitude larger than the formation time of heavy quarks ($\approx$0.1 fm/c for c and 0.02 fm/c for b), the heavy-flavored hadron production can be estimated in the framework of collinear factorization. The expected relative

abundances of open-charm and open-beauty hadrons are given in Table 13.3.

$c\bar{c}$	D^0,$\bar{D}^0$	$D^\pm$	$D_s^\pm$	$\Lambda_c^\pm$
relative abundance [%]	≈61	≈19	≈12	≈8
$b\bar{b}$	B^0,$\bar{B}^0$	$B^\pm$	$B_s^\pm$	Λ_b^0,$\bar{\Lambda}_b^0$
relative abundance [%]	≈40	≈40	≈6	≈4

Table 13.3: Relative abundances of open-charm and open-beauty hadrons [68].

What is seen in the ALICE detector, are the charged particles from heavy-flavored hadron decays. The relevant decay channels are summarized for the charm hadrons in Table 13.4.

	M [MeV]	$c\tau$ [μm]	decay channels
D^0,$\bar{D}^0$	1864.5	≈123	e+X (≈6.5 %) μ+X (≈6.7 %) $K\pi$(3.8 %) $K\pi\pi$(7.72 %)
$D^\pm$	1869.3	≈312	e+X(≈17.2 %) μ+X(1≈7.2 %) $K\pi\pi$(9.51 %)
$D_s^\pm$	1968.2	≈150	e+X(≈8 %) μ+X(≈8 %) $KK\pi$(5.2 %)
$\Lambda_c^\pm$	2286	≈60	$pK\pi$(≈5 %)

Table 13.4: Decay channels of D mesons and Λ_c used for the measurement of the $c\bar{c}$ cross-section in ALICE ($c\rightarrow e$+X(9.6 %)).

Two types of measurements are foreseen:

- a direct reconstruction of D and B mesons through their hadronic decays. The p, K and π are charged particles, that can be identified with the TOF detector. By mean of the innermost layers of the ITS, track doublets or triplets pointing to a common secondary vertex are selected and their invariant mass is computed. Displaced secondary vertices are the signature of such decays. A very good resolution on the impact parameter projection in the bending plane is required. This depends on the material budget of the beam pipe and first layers of the ITS and on the alignment of the detectors. An impact parameter resolution of about 60 μm is expected.

  A similar reconstruction method is used for the selection of B mesons through the decay channel $B\rightarrow J/\Psi+X$(≈1 %). The displaced dielectronic decay of J/Ψ ($J/\Psi\rightarrow l^+l^-$(≈5.94 %)) is in this case the signature. The lifetime of the B mesons is summarized in Table 13.5.

	$B^0/\bar{B}^0$	B^+/B^-	B_s^+/B_s^-
$c\tau$ [μm]	458.7	491.1	439.0

Table 13.5: Lifetime of the B mesons.

- an indirect estimate of the $c\bar{c}$ and $b\bar{b}$ cross-sections through the semi-leptonic decays of D and B mesons. The large branching ratios, $c\rightarrow l+$X(9.6 %), $b\rightarrow l+$X(10.86 %) and $b\rightarrow(D\rightarrow l+X)+$X($\approx$11 %), are an advantage compared to the direct measurements ($c\rightarrow(D^0\rightarrow K\pi)+X$ (4.6 %=2$\times$61 %$\times$3.8 %)). The final single lepton yields are given in Table 13.6 for pp collisions at 14 and 10 TeV.

$\sqrt{s}$ [TeV]	$l^{\pm}$ from	total yield
14	$c\bar{c}$	$\approx$0.03
	$b\bar{b}$	$\approx$0.003
10	$c\bar{c}$	$\approx$0.025
	$b\bar{b}$	$\approx$0.002

Table 13.6: Total yield of single electrons or muons coming from c or b in pp collisions.

Nevertheless there are other sources of single electrons or muons, which have to be understood and subtracted from the inclusive spectra, to isolate the signal. In case of muon, the single muon background comes principally from $\pi^{\pm}$ and $K^{\pm}$ decays, which have large lifetime, $c\tau\approx$7.8 m and $c\tau\approx$3.7 m, respectively. The muonic channels allow to extend the pseudo-rapidity range, over which the $c\bar{c}$ and $b\bar{b}$ cross-sections are reconstructed in ALICE, since the muon spectrometer covers the range -4<η<-2.5.

In this thesis we will focus on the measurement of the $c\bar{c}$ and $b\bar{b}$ cross-sections through the semi electronic decay of charm and beauty hadrons.

Chapter 14

Acceptance and Particle Identification

14.1 Acceptance

The $c\bar{c}$ and $b\bar{b}$ production was simulated with PYTHIA and the CTEQ 5L PDF [46]. PYTHIA is a Leading Order generator suited for the computation of pair creation processes (mainly $gg \rightarrow q_{hv}\bar{q_{hv}}$ but also $q\bar{q} \rightarrow q_{hv}\bar{q_{hv}}$). Nevertheless the NLO processes, flavor excitations ($qq_{hv} \rightarrow qq_{hv}$) and gluon splitting ($g \rightarrow q_{hv}\bar{q_{hv}}$), can not be neglected. Therefore they were also included, requiring the choice of a low p_T^{hard} cut-off [68]. The simulation was performed in p_T^{hard} bins. To better match the p_T distribution of c and b quarks obtained at NLO with the HVQMNR program [85], the weight of each p_T^{hard} bin was tuned. The c and b quarks then hadronize with the default Lund String fragmentation model in PYTHIA and the charm and beauty hadrons are let decay according to their branching ratios. The spectra are normalized to the NLO cross-sections.

The number of simulated $c\bar{c}$ and $b\bar{b}$ events correspond to 4,629,100 minimum-bias pp collisions at 10 TeV. The residual misalignment and calibration were taken into account by using the residual database at the simulation step and the ideal one at the reconstruction step with AliRoot v4-13-Rev-05 [49]. Unfortunately some overlapping in the ITS geometry were present in this version of the software. Since the simulation was performed before the accident in the sector 34 of the LHC, the detector setup is the one expected for the end of 2008, if any pp collisions would have taken place. The ITS, TPC and TOF were already complete, while four TRD supermodules were installed covering the azimuthal angle $0° \leq \phi \leq 20°$, $160° \leq \phi \leq 200°$ and $340° \leq \phi \leq 360°$. The Monte Carlo events were produced over the rapidity range $-12 \leq y \leq 12$ with the nominal 0.5 T magnetic field. Fig. 14.1 shows the two dimensional $\eta \times p_T$ distributions of $e^{\pm}$ from D and B meson decays. The η distribution gets narrower at high p_T. As a consequence, the geometrical acceptance in the central barrel ($|\eta| < 0.9$) improves with p_T.

The TRD is the main detector for the $e^{\pm}$ identification at high momenta ($p_T > 1$ GeV/c). Unfortunately the 18 supermodules will not be present for the first pp collisions but only a fraction of them. Between 6 and 8 supermodules should be installed in April 2009. In the simulation, 4 were foreseen for the end of 2008. By requiring that the track is also reconstructed in the TRD, the acceptance decreases by about 78 % compared to the full azimuthal coverage of the TPC

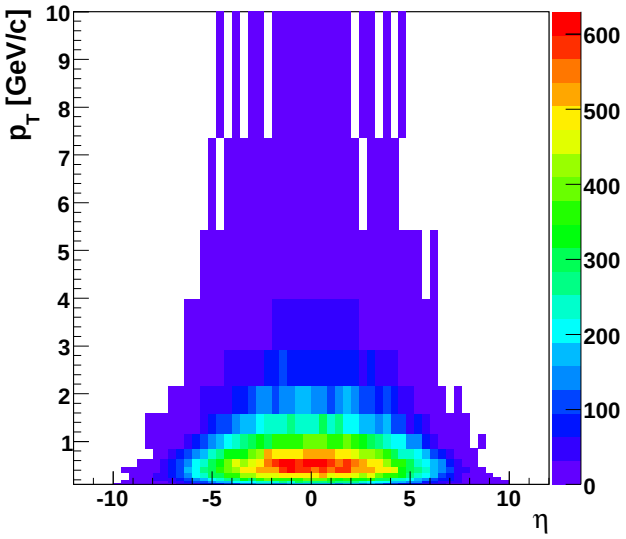

Figure 14.1: Two dimensional $\eta \times p_T$ distributions of $e^{\pm}$ from D and B mesons decays at $\sqrt{s}$=10 TeV.

($\Delta\phi$=360°). In general, while the PID improves with the use of the TRD and TOF detectors, the fraction of the signal passing the cuts decreases. The different cuts studied are defined in the following:

- TPC alone. To stay in a region where the tracking efficiency is uniform, only tracks with $|\eta|$<0.9 are considered. Moreover the tracks have to have at least 50 attached clusters in the TPC, with a maximum χ^2 per cluster of 3.5. The track should be refitted in the TPC during the reconstruction backwards from the outermost detector to the ITS. The kink daughters are rejected. This is the signature of charged particles (for example charged kaons) that decay into one or two neutral daughters (which are not detected) and one charged daughter which is observed in the TPC. The track of the charged parent appears to have a discontinuity at the point of the parent decay. Two tracks are then reconstructed, one before the kink and one after, flagged as *kink daughter*.

- TPC and ITS with a hit in the first pixel layer. The same quality cuts are required in the TPC. The main role of the ITS is to allow to cut on the impact parameter of the track and reduce the fraction of secondary electrons produced by gamma conversion in the ITS layers. Therefore it is interesting to consider tracks with clusters in the ITS, particularly in its first layer, a silicon-pixel detector. A cluster in this layer is required and the refit includes the ITS.

- ITS (first pixel), TPC and TOF. In addition to the previous cuts, one requires a PID signal in the TOF. The TOF helps to separate $e^{\pm}$ from (p,$\bar{p}$) and $K^{\pm}$ at low momenta (below 1 GeV/c).

- ITS (first pixel), TPC and TRD with a TRD PID quality above 5. Only the TRD can

improve the purity of the reconstructed $e^{\pm}$ sample above 1 GeV/c by rejecting the very numerous $\pi^{\pm}$. To assure a good TRD PID, the number of layers used to calculate the TRD PID signal, given by the TRD PID quality, has to be at least 5.

- ITS (first pixel), TPC, TRD (TRD PID quality at least 5) and TOF. The best purity of the reconstructed $e^{\pm}$ sample over a large momentum range above 1 GeV/c is achieved by requiring a good PID signal in the TRD and the TOF detector, together with the information of the TPC.

The left panel of Fig 14.2 shows the p_T spectra of $e^{\pm}$ from D and B meson decays as they were simulated, in the geometrical acceptance of the central barrel ($|\eta|$<0.9) and with the track quality cuts mentioned above. The spectra were scaled to 10^8 minimum-bias pp events. Thanks to the large cross-sections and branching ratios, a p_T spectrum extending up to 6-6.5 GeV/c can be reached with 10^8 events even with only four TRD supermodules. The fraction of $e^{\pm}$ from D and B meson decays passing the different cuts (with respect to the generated ones) is presented in the right panel of Fig 14.2.

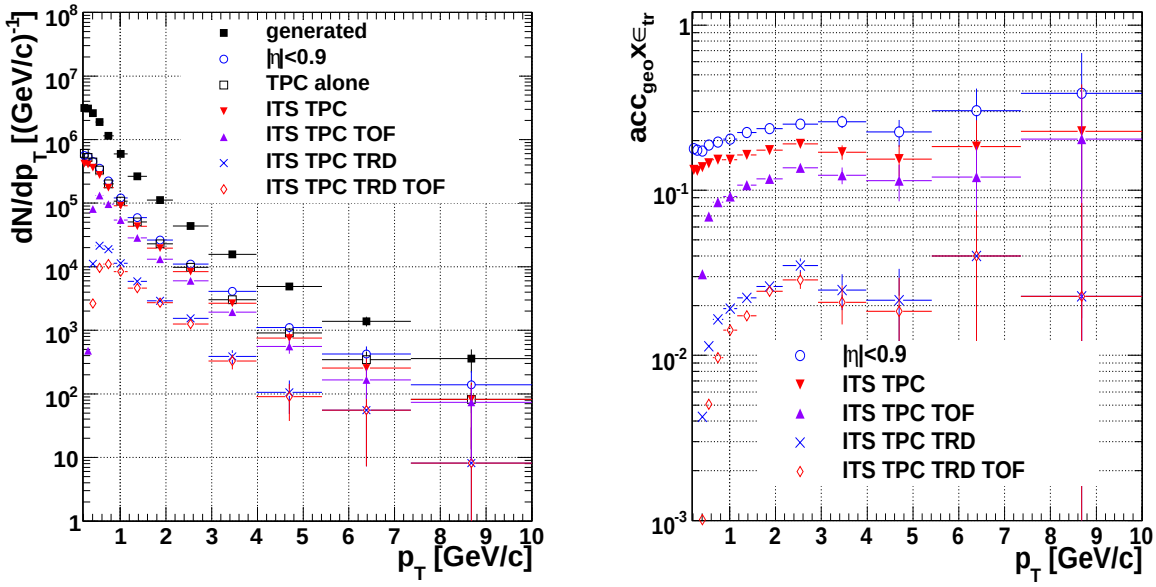

Figure 14.2: Generated and reconstructed (left panel) and ratios of the reconstructed to generated (right panel) $e^{\pm}$ from D and B meson decays for different track quality cuts, as a function of p_T. The spectra are scaled to 10^8 minimum-bias pp collisions at $\sqrt{s}$=10 TeV.

As expected from Fig. 14.1, the product of the geometrical acceptance and the tracking efficiency, $acc_{\rm geo}\times\epsilon_{tr}$, increases with p_T. The central barrel acceptance ($|\eta|$<0.9) is of the order of 30 % at high p_T, while the ITS(first pixel)-TPC requirement reduces $acc_{\rm geo}\times\epsilon_{tr}$ to about 20 %. The minimum p_T needed to reach the TOF at the radial distance of r_{TOF}≈3.70-3.99 m is given by:

$$p_T\,[\mathrm{GeV/c}] = 0.3 \times q \times B\,[\mathrm{T}] \times (r_{TOF}/2)[\mathrm{m}] \approx 300\,\mathrm{MeV/c} \qquad (14.1)$$

Multiple scattering reduces also the matching efficiency between the track in the ITS, TPC and eventually TRD, and the signal let in the TOF at low momenta. This effect is particularly important when a TRD supermodule is installed before the TOF supermodule, since the material budget of the TRD is about 25 % of radiation length X_0. Therefore a non-negligible fraction of the tracks passing the ITS(first pixel)-TPC cut below 1 GeV/c don't have a TOF PID signal. The fraction decreases with p_T to reach about 20 % at high p_T. The TOF is particularly helpful from 0.6 GeV/c to 1 GeV/c for the Particle Identification. In this range the overall efficiency is still acceptable. Due to the partial ϕ coverage of the four TRD supermodules, the factor $acc_{\rm geo}\times\epsilon_{tr}$ should be $\frac{4}{18}\approx$22 % compared to the tracks passing the ITS(first pixel)-TPC cut. Since there are some gaps between each TRD supermodule in ϕ and between each TRD stack in η, the acceptance is about 18 % at high p_T. The matching efficiency between the TRD and the TOF is given by the ratio of the tracks passing the ITS(first pixel)-TPC-TRD and the ITS(first pixel)-TPC-TRD-TOF cut. It is about 85 % at high p_T and decreases at low p_T due to multiple scattering.

14.2 Particle Identification

Bayesian approach for combined PID The PID strategy in ALICE software is based on Bayesian approach [111]. For each reconstructed track, the probabilities $w(i)$ to be of type i are computed. The 5 types of particle considered, that reach the detectors, are $e^{\pm}$, $\mu^{\pm}$, $\pi^{\pm}$, $K^{\pm}$ and $(p,\bar{p})$. The sign of the electric charge and the momentum of the particle are given by the curvature of the track in the magnetic field. The variables $w(i)$ are calculated from the so-called detector response probabilities, $P(i)$. The detectors use different information to identify particles, such as the arrival time t for the TOF or the deposited energy dE/dx in the detector for the TPC, the ITS and the TRD. The detector response probabilities correspond to the conditional probability that a particle of type i and momentum equal to the one of the reconstructed track is characterized by a given signal (t or dE/dx) in the detector ($P(i)$=$P(t|i)$ or $P(dE/dx|i)$). For one detector, $w(i)$ is deduced from $P(i)$ using the definition of the conditional probability and Bayes's theorem:

$$w(i) = P(i|dE/dx) = \frac{P(dE/dx|i)\times C(i)}{P(dE/dx)} = \frac{P(dE/dx|i)\times C(i)}{\sum_{j=1}^{j=5} P(dE/dx|j)\times C(j)} = \frac{P(i)\times C(i)}{\sum_{j=1}^{j=5} P(j)\times C(j)} \tag{14.2}$$

where $C(j)$ are the so-called prior probabilities, which describe the relative concentrations of particle species. A reasonable hypothesis for the unknown charged particle is the index i for which $w(i)$ is the largest of the five values. Eq. 14.2 can be generalized for several detectors. Since the measurements of the ITS, TPC, TRD and TOF are independent, the overall detector response probability $P_{tot}(i)$ is the product of the single detector response probabilities:

$$P_{tot}(i) = P_{ITS}(i)\times P_{TPC}(i)\times P_{TRD}(i)\times P_{TOF}(i) \tag{14.3}$$

For each detector, the detector response can be obtained from its PID calibration. Thus the prior probabilities $C(i)$ are the only unknown quantity. They depend on the data selection and

the studied final states. The first single electron spectrum will be obtained from minimum-bias pp events. Therefore we decided to use the prior probabilities $C(i)$ determined by the study of identified charged particle p_T spectra with the TPC alone (in minimum-bias pp events also). The PID using only the TPC relies on a 2σ cut to the distance of the expected mean dE/dx value ($\Delta dE/dx$), or a fit of the $\Delta dE/dx$ distributions in $p_T \times \eta$ bins with a multiple Gauss function [112].

TPC PID alone Fig. 14.3 shows the mean dE/dx for different particle species in the TPC as obtained from simulated pp collisions at 14 TeV.

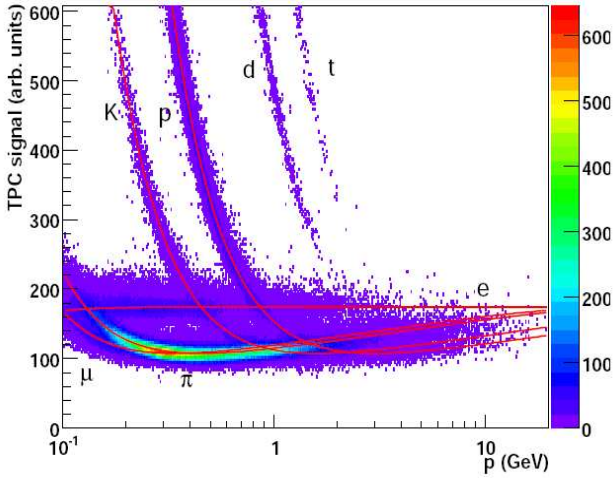

Figure 14.3: The expected energy loss signal for different particle species. The lines are the result of a fit with a parametrized Bethe-Bloch formula for 50,000 simulated pp collisions [113].

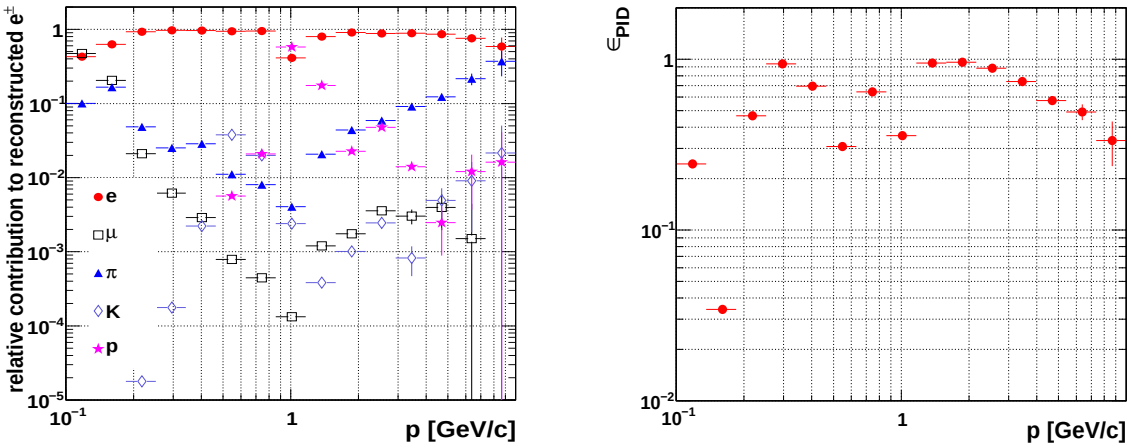

Figure 14.4: Contamination of the reconstructed electron sample (left panel) and PID efficiency (right panel) as a function of momentum for a PID with the TPC alone.

Due to the small electron mass, $e^{\pm}$ of 100 MeV/c momentum are already in the Fermi plateau of the Bethe Bloch formula. At low momenta, the dE/dx bands of the $K^{\pm}$ and the (p,$\bar{p}$) cross at about 500 MeV/c and 800 MeV/c respectively the $e^{\pm}$ band. At high momenta, the $\pi^{\pm}$ are in the relativistic rise and the distance between $e^{\pm}$ and $\pi^{\pm}$ bands decrease. Therefore the $e^{\pm}$ can be separated from the other particles in the momentum ranges [200 MeV/c,400 MeV/c], [600 MeV/c,700 MeV/c] and from 1 GeV/c to about 4-5 GeV/c.
The resulting contamination of the reconstructed electron sample is presented in the left panel of Fig. 14.4. The crossing of the $K^{\pm}$ and (p,$\bar{p}$) dE/dx bands can be seen, as well as the increasing contamination in $\pi^{\pm}$ with the momentum. In the right panel, the PID efficiency is plotted. The condition that the maximum probability $w(i)$ is larger than 0.5 has been required.

TOF PID With the TOF detector, the interval between the arrival time of the particle at the TOF and the time of the collision is measured. Knowing the momentum p and length l of the track reconstructed from the central barrel detectors, the mass of the particle is computed as:

$$M^2 = p^2(\beta^2 - 1) = p^2(c^2t^2/l^2 - 1) \tag{14.4}$$

Fig. 14.5 shows the mass as a function of the momentum for different particle species. The $e^{\pm}$ are well separated from the $K^{\pm}$ and (p,$\bar{p}$) in the momentum range, where their dE/dx bands cross below 1 GeV/c each other in the TPC. At high momenta, the time resolution (≈50 ps) is not sufficient anymore to separate properly the different species.

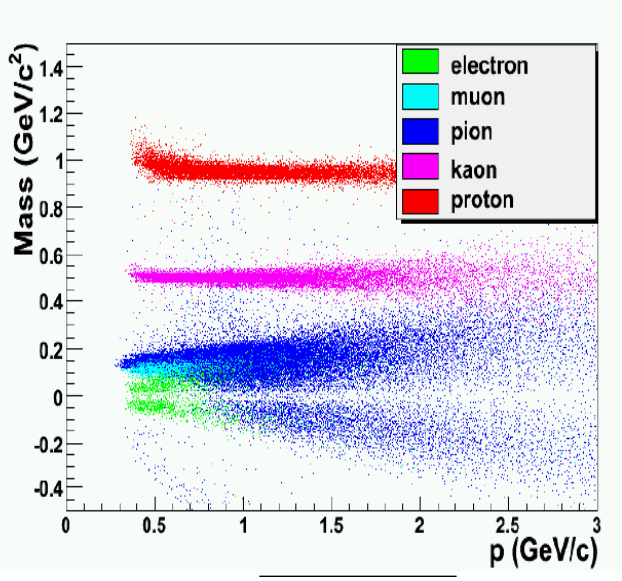

Figure 14.5: The calculated mass of different particle species from the TOF signal and tracking variables as a function of the momentum of the particle [114].

The contamination of the selected electron sample with the combined ITS, TPC and TOF PID is plotted in the left panel of Fig. 14.6. The $K^{\pm}$ and (p,$\bar{p}$) contamination at low p is suppressed compared to the case with the TPC PID alone. Nevertheless the ITS and TOF can not help

to separate the $e^{\pm}$ from $\pi^{\pm}$ at high momenta.

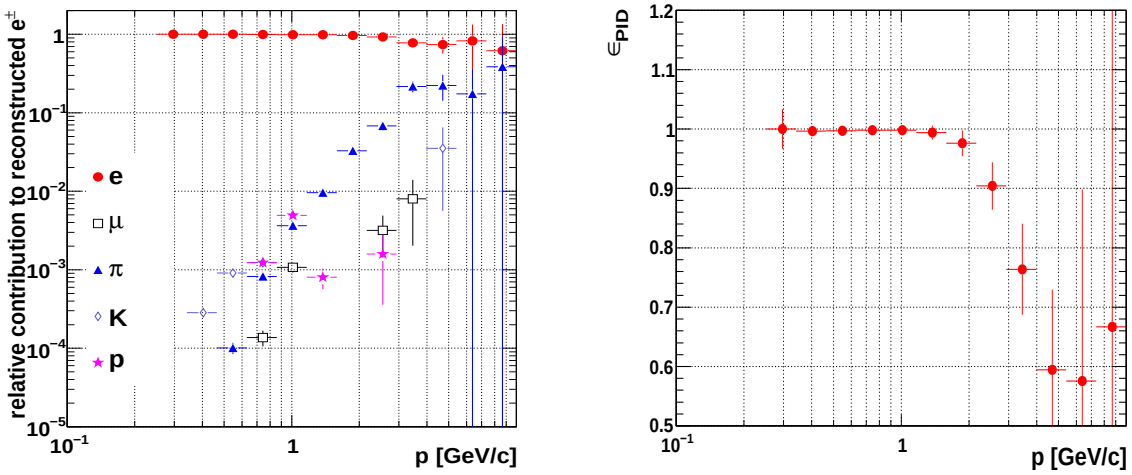

Figure 14.6: Contamination of the reconstructed electron sample (left panel) and PID efficiency (right panel) as a function of momentum for a PID with the ITS, TPC and TOF detectors.

The PID efficiency is shown as a function of momentum in the right panel of Fig. 14.6. This corresponds to the fraction of correctly identified $e^{\pm}$, which have a PID signal in the TOF (ITS TPC TOF cut presented in the previous paragraph). The ITS-TPC-TOF acceptance and tracking efficiency is shown for $e^{\pm}$ and $K^{\pm}$ as a function of momentum in Fig. 14.7. The efficiency is smaller for $K^{\pm}$ than for $e^{\pm}$ because the $K^{\pm}$ decay with $c\tau$=3.713 m and some of them have already decayed before reaching the TOF situated at a radial distance of 3.7 m.

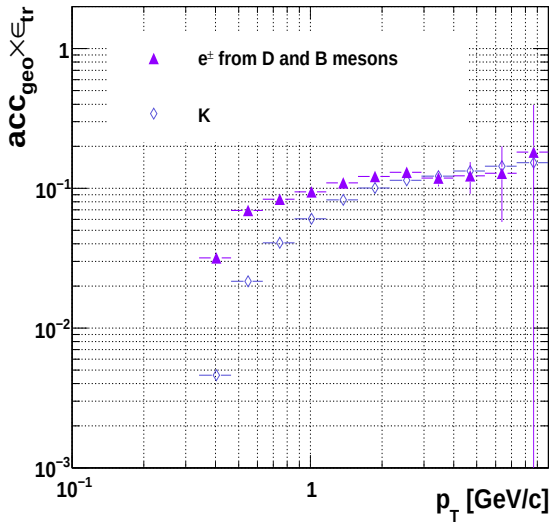

Figure 14.7: Acceptance and tracking efficiency in the ITS, TPC and TOF for electrons from charm and beauty hadrons and for kaons.

TRD PID The $e^{\pm}$ can be best separated from pions for momenta higher than 1 GeV/c.

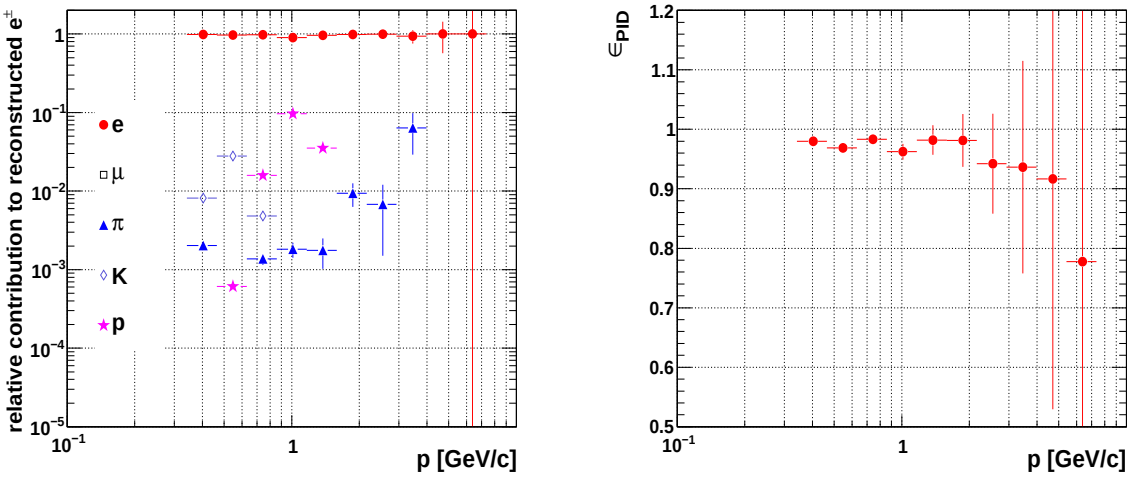

Figure 14.8: Contamination of the reconstructed electron sample (left panel) and PID efficiency (right panel) as a function of momentum for a PID with the ITS, TPC and TRD detectors.

In the left panel of Fig. 14.8, the contamination of the reconstructed electron sample is shown for a PID with the ITS, TPC and TRD. The PID method used for the TRD is the 2D likelihood based on the amplitude of the deposited energy in two slices of the gas volume. The impurity of the reconstructed electron still increases with the momentum of the particle but stays below 10 %. A factor 2 in rejection can be gained with the neural network method. The PID efficiency is plotted in the right panel of Fig. 14.8.
The best results are obtained by combining the TRD and TOF PID for low and high momenta in addition to the ITS-TPC PID. The contamination and efficiency are shown in Fig. 14.9.

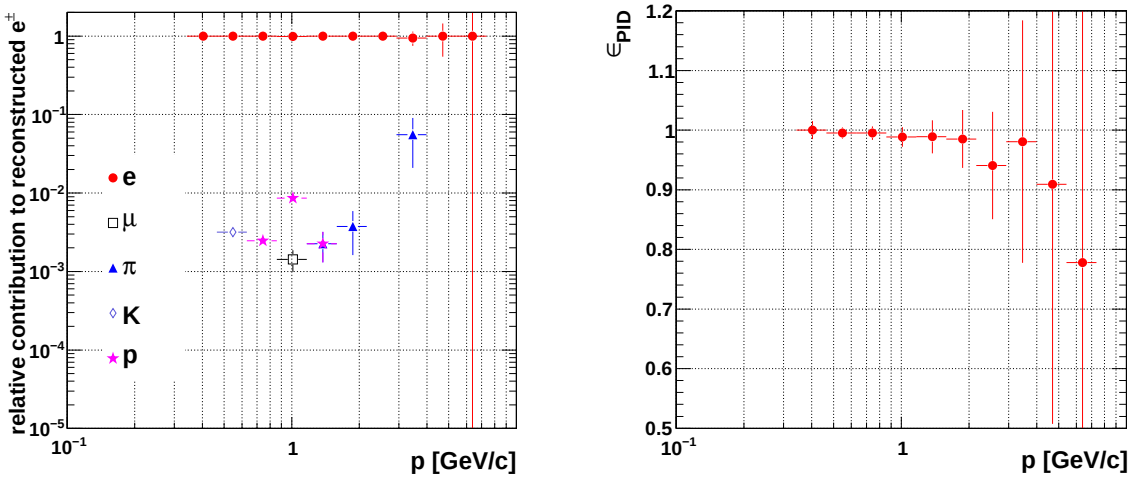

Figure 14.9: Contamination of the reconstructed electron sample (left panel) and PID efficiency (right panel) as a function of momentum for a PID with the ITS, TPC, TRD and TOF detectors.

Chapter 15

Background study

15.1 Sources of background

The $e^{\pm}$ from charm and beauty hadrons are few among hadrons, which can be misidentified as $e^{\pm}$, and $e^{\pm}$ from other sources. The different sources of background true $e^{\pm}$ are:

- so called photonic electrons by the PHENIX collaboration, even if there are not all coming from γ conversion:

	M [MeV]	decay channels
π^0	134.98	$2\gamma(98.8\,\%)$, $e^+e^-\gamma(1.198\,\%)$
η	547.51	$2\gamma(39.38\,\%)$,$e^+e^-\gamma(0.6\,\%)$
$\eta^{'}$	957.78	$\pi^+\pi^-e^+e^-(<0.6\,\%)$,$e^+e^-\gamma(<0.09\,\%)$
ρ^0	775.5	$e^+e^-(0.00470\,\%)$
ω	782.65	$\pi^0\gamma(0.0890\,\%)$,$e^+e^-\pi^0(0.077\,\%)$,$e^+e^-(0.00718\,\%)$
ϕ	1019.5	$\pi^0e^+e^-(0.0297\,\%)$,$e^+e^-\eta(0.0115\,\%)$

Table 15.1: Decay channels of scalar and vector mesons.

  - Dalitz decays of light neutral mesons. The most important contribution comes from the π^0 Dalitz decay $\pi^0\rightarrow\gamma e^+e^-$ (1.198 %). The decay channels of scalar and vector mesons are summarized in Table 15.1.
  - conversion of photons in material. The main photon source at low p_T comes from the π^0 decay $\pi^0\rightarrow\gamma\gamma$ (98.8 %). At high p_T the contribution of direct photons becomes dominant.
  - direct radiation. Besides the conversion of direct photons in material, virtual photons, $\gamma^*\rightarrow e^+e^-$, are also a source of $e^{\pm}$.

- non photonic sources:

  - weak kaon decays $K^{\pm}\rightarrow\pi^0e^{\pm}\nu_e$ (4.98 % with $c\tau$=3.7 m).

– dielectron decays of vector mesons ρ, ω and ϕ.

Two different analysis approaches are possible. Contrary to the heavy flavor decays, most of the background $e^{\pm}$ come from very short lived particles. Thus, while the tracks of $e^{\pm}$ from B and D mesons don't point to the primary vertex, the background tracks are coming from the interaction point. Therefore the distance of closest approach to the primary vertex (impact parameter) of the reconstructed electron track can be used to reject the background (even γ conversion $e^{\pm}$, which point also to the primary vertex at a sufficient high p_T) and enrich the beauty contribution ($c\tau{\approx}450\,\mu$m for B mesons) [68] [115]. Due to the smaller lifetime of the D mesons and lower p_T of the decay $e^{\pm}$, it becomes more difficult to separate the charm contribution from the background by a minimum impact parameter cut. In pp collisions the resolution on the primary vertex is critically important. Since the mean number of charged particles is not as large as in $PbPb$ collisions, the primary vertex can not be directly reconstructed in about 20 % of the minimum-bias pp collisions. The impact parameter resolution depends also on the misalignment of the ITS. For electrons, Bremsstrahlung, for which the track parameters are not corrected during the Kalman tracking procedure, can moreover deteriorate the impact parameter resolution.
The second approach consists in subtracting the sources of background with a cocktail. The cocktail is built from the measured p_T spectra of the background sources (π^0, direct photons $\cdots$). It has the advantage to keep the contribution of $e^{\pm}$ from c decays in the analysis and allows an indirect reconstruction of the $c\bar{c}$+$b\bar{b}$ cross-section. Nevertheless the dominant contribution of the photonic sources at low p_T requires a very good understanding of the detector material budget. The PHENIX experiment used this method at high p_T, where the signal-to-background ratio improves. They completed their analysis at low p_T with the mean of a converter method. The photonic background was directly measured by placing extra material with a well-known radiation thickness between the beam pipe and the first tracking chambers. The two methods were found to be consistent in the overlapping p_T range [104].
Here we discuss this second approach.

15.2 Monte Carlo simulation of the background

A total amount of $4.6{\cdot}10^6$ minimum-bias pp collisions at $\sqrt{s}$=10 TeV were simulated and reconstructed with the AliRoot release v4-13-Rev-05 at GSI. It was decided by the ALICE Physics Board to use PYTHIA 6.2 with the CTEQ5L PDFs to generate minimum-bias events for physics analysis. The whole mixture is composed of:

- PYTHIA minimum-bias pp collisions including diffractive events (MSEL=0). The heavy quark production is switched off in these events, which are partly enriched with Ω and J/Ψ.

- events containing at least a $c\bar{c}$ or a $b\bar{b}$ pair. The PYTHIA parameters are the same as what we used in this thesis for the background simulation of the Z^0. The LO and NLO

processes are simulated with a tuned minimum p_T^{hard} cut-off to avoid divergences [68]. The heavy flavored quarks are produced in four p_T^{hard} bins with proper relative abundances. To better match the NLO calculations at low p_T (p_T of the c quark $< 20\,\mathrm{GeV/c}$), more weights were put on the low p_T^{hard} bins compared to results from the PYTHIA computations for the $c\bar{c}$ production. All decay channels are considered.

The left panel of Fig. 15.1 shows the inclusive electron p_T spectrum as selected using Monte-Carlo information reconstructed in the ITS and TPC for pp collisions at 10 TeV. No acceptance corrections were performed. The results were scaled to 10^8 minimum-bias events. The different contributions to the spectrum are also plotted. At high p_T, the signal ($e^{\pm}$ from D and B meson decays) becomes dominant, while at low p_T, $e^{\pm}$ from π^0 Dalitz decays and γ conversions are the main source of single electrons. The p_T spectrum of $e^{\pm}$ from beauty crosses the one of $e^{\pm}$ from charm between 2 and 3 GeV/c.

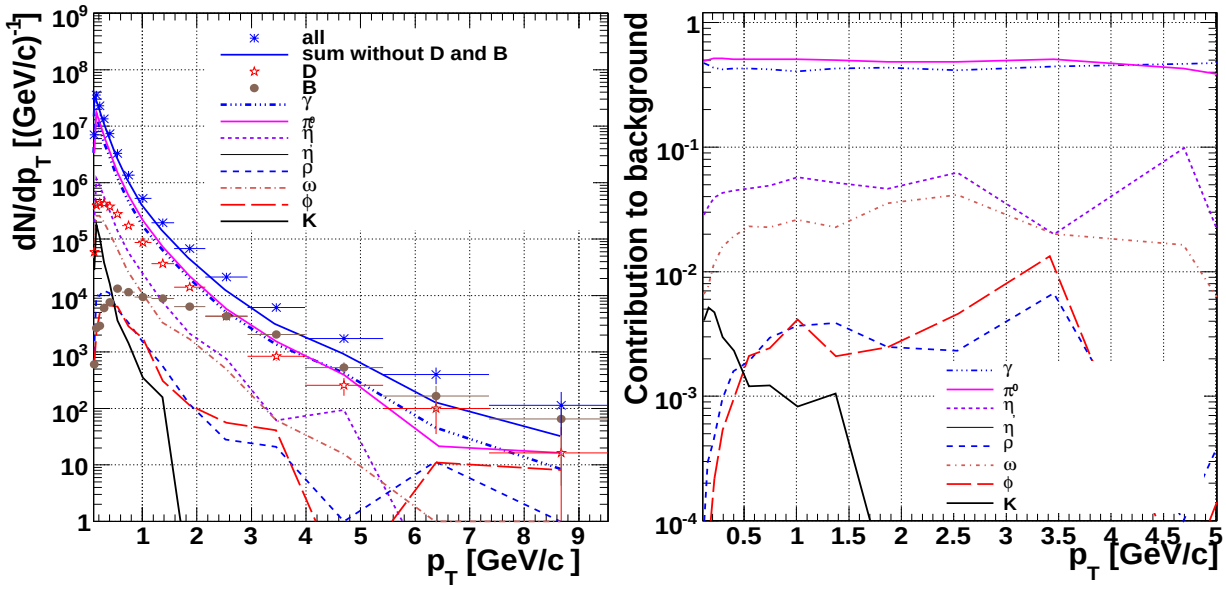

Figure 15.1: Left panel: simulated reconstructed true electron p_T spectra in the ITS, TPC and TRD corresponding to 10^8 minimum-bias pp collisions at 10 TeV.

In the right panel of Fig. 15.1, the relative contributions of all electron sources to the background are plotted. The main contribution comes from $e^{\pm}$ from π^0 Dalitz decays and from γ conversions. The material crossed by the particles is similar as in the PHENIX detector [116, 104]. The ratio of $e^{\pm}$ from π^0 Dalitz decays to $e^{\pm}$ from γ conversion was found to be about 0.73, independent on p_T, by GEANT simulation in PHENIX. The π^0 Dalitz decay contribution was calculated with a hadron decay generator using a parametrization of measured π^0 and $\pi^{\pm}$ spectra as input. Using the $\pi^0 \rightarrow \gamma\gamma$ (98.8 %) decay channel, the diphoton invariant mass allows to identify π^0. In ALICE, the γ can be detected indirectly in the TPC by γ conversion in the ITS layers ($\gamma \rightarrow e^+e^-$) [117] or it can be directly identified in the Photon Spectrometer (PHOS)

($\Delta\phi$=100 ° for the complete PHOS, $\Delta\eta$=0.24) [118]. Since the first tracking chamber of the PHENIX experiment is situated about 2 m away from the interaction point, the contribution of $K^{\pm}$ decays is more important in their case. The electronic decay channels of the $\eta^{'}$ were not included in the simulation of minimum-bias events for ALICE. It was decided to take the upper limit for the branching ratios of the $\eta^{'}\rightarrow\pi^{+}\pi^{-}e^{+}e^{-}$ (0.6 %) and $\eta^{'}\rightarrow\gamma e^{+}e^{-}$ (0.09 %) decay channels [1]. The direct γ production is also not included in the simulations for ALICE. The PHENIX collaboration used their measurement of direct γ to evaluate this contribution which plays a role at high p_T. The direct photons will be in the next step included in the simulated minimum-bias pp collisions using PYTHIA (with MSEL=10). The photons produced are so-called prompt photons coming from hard-parton collisions (in comparison to thermal γ at low p_T in heavy ion collisions). The basic processes, Compton scattering ($q\bar{q}\rightarrow g\gamma$ and $qg\rightarrow q\gamma$ with an additional smaller contribution from $gg\rightarrow g\gamma$), annihilation ($gg\rightarrow\gamma\gamma$ and $q\bar{q}\rightarrow\gamma\gamma$) and Bremsstrahlung of incoming or outgoing quarks are included. The Bremsstrahlung contribution is simulated in PYTHIA with its parton shower algorithm. Usually the ratio γ_{prompt}/π^{0} is used for the normalization and comparison between measurements and calculations [68]. Therefore it was checked that the PYTHIA ratio γ_{prompt}/π^{0} is in agreement with the NLO QCD predictions.

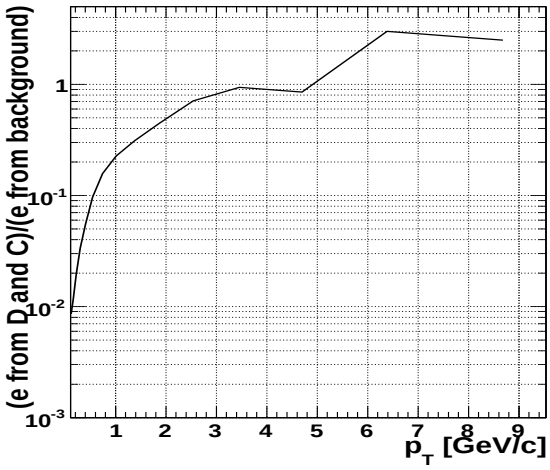

Figure 15.2: Ratio of electrons from heavy-flavor decays to electrons from background sources as a function of p_T in simulated pp collisions at 10 TeV.

Fig. 15.2 shows the estimated ratio of $e^{\pm}$ from charm and beauty hadron decays to $e^{\pm}$ from the background sources for pp collisions at 14 TeV. The signal-to-background ratio becomes higher than 1.0 at around 3.5 GeV/c.

Conclusion

The measurement of the p_T spectrum of $e^{\pm}$ from charm and beauty hadrons can be done up to about 6 GeV/c with 10^8 minimum-bias pp events at 10 TeV. The background subtraction with a cocktail requires nevertheless a very good understanding of the ITS material budget for the contribution from γ conversions and the measurement of the π^0 p_T spectrum. The b cross-section measurement based on a impact parameter cut requires a good alignment of the detectors and the knowledge of the impact parameter distributions of the electron background sources. Further work is needed for a realistic electron identification strategy.

Appendix A

Role of the Shuttle

The Shuttle framework is shown schematically in Fig. A.1.

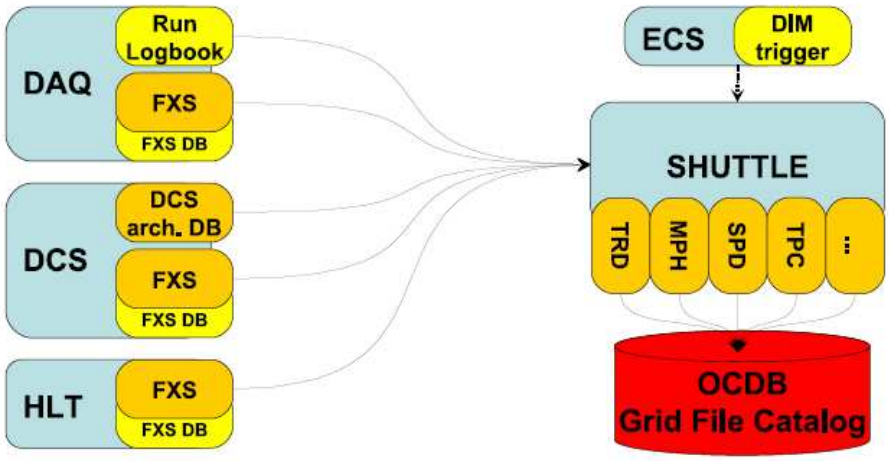

Figure A.1: Schema of the Shuttle framework [119].

The main role of the Shuttle is to make available offline the information read or produced online during the run. These data can be still processed or analyzed before. Thus the task of the Shuttle can be decomposed in the following way:

- **retrieve data produced by the online systems (DAQ, DCS, HLT)**. For this purpose, the shuttle has access to the DCS, DAQ, and HLT File Exchange Servers (FXS). At the end of the run, online procedures, like the calibration on DAQ and HLT, export on the online system FXS files containing information about the detector. The FXS are used as a temporary storage for data, which has to be available offline.
  In addition, certain condition parameters (e.g. temperatures, voltages, currents...) are monitored and archived continuously in the DCS archive database by the DCS system. A service called AMANDA was developed to copy the data from the archive database and pass it to the Shuttle.
  Finally the Shuttle reads also the run logbook to identify the run with its run number,

the time when it has started and ended and its run type (PEDESTAL, STANDALONE, PHYSICS). Depending on the run type, different files are expected to be on the FXS.

- **process the data**. From the FXS, the Shuttle retrieves reference data, which allow to determine the calibration constants. Fits are performed at the shuttle and appropriate calibration objects are produced for each variable.
  The information from the condition data from the DCS archive database or from the DCS FXS need also to be converted to ROOT format.

- **store the data in the Grid Offline Conditions Data Base (OCDB) or the Grid reference Data Base** in case of reference data. The new set of calibration objects are valid for all the following runs until they are updated, whereas the reference data are per definition attached only to the current run. Any ALICE member having a Grid certificate can look at the data in the Grid under the official base folders:

$$/alice/data/\langle year\rangle/\langle LHCPeriod\rangle/OCDB/$$

$$/alice/data/\langle year\rangle/\langle LHCPeriod\rangle/Reference/$$

The operations are done in a particular chronological order. At the end of each run, the ECS informs the online systems DCS, DAQ and HLT that the data-taking has stopped. The information is passed to the DA or other procedure, which is executed, the results being stored on the corresponding FXS. Onces all the procedures have finished on a given online system, a *ready* signal is sent back to the ECS. The end-of-run signal (EOR) is given by the ECS to the Shuttle only when all online systems are ready. The Shuttle executes then the mentioned tasks per detector beginning with the query of the data stored in the DCS archive. The code corresponding to the retrieving of the data from the FXS, the processing of the data and storing in the OCDB or reference database is contained in the so called detector **preprocessor**. The detector preprocessors are executed subsequently even if they could be run in parallel since they are totally independent. There are in total 20 preprocessors, one per detector (18), one to retrieve HLT specific parameters and another for data not specific to a particular detector but to the whole experiment (LHC state, LHC period, LHC luminosity, $\cdots$, trigger clusters and corresponding trigger masks), called Global Run Parameters (GRP) preprocessor.

Appendix B

Kinematic Variables

In this chapter, c is taken equal to unity. It is convenient in the description of ultra-relativistic heavy-ion collisions to use kinematic variables, which have simple properties under a change of the frame of reference, particularly under a Lorentz transformation. In this appendix, they will be presented. The invariant mass of an electron pair will be also calculated.

rapidity and pseudo-rapidity

The four-momentum of a particle is noted p^{μ}, with E its energy and $\mathbf{p}$ its three momentum vector.

$$p^{\mu} = (E, \mathbf{p}) \tag{B.1}$$

$\mathbf{p}$ can be divided into a longitudinal component,p_z, and a transverse component, $\mathbf{p_T}$. $\mathbf{p_T}$ is invariant under Lorentz transformations and can be used to characterize the kinematic of the particle. p_Z, on the contrary, has no good Lorentz properties. Thus the longitudinal movement is better defined by the rapidity y:

$$y = \frac{1}{2} \ln \left(\frac{E + p_z}{E - p_z} \right) \tag{B.2}$$

y is additive under Lorentz transformations. If one considers a frame $F^{'}$ moving along the z direction at a velocity β in a frame F, the rapidity $y^{'}$ in $F^{'}$ is related to the rapidity y in F by:

$$y^{'} = y - y_{\beta} \tag{B.3}$$

$$y_{\beta} = \frac{1}{2} \ln \left(\frac{1 + \beta}{1 - \beta} \right) \tag{B.4}$$

For a fixed target experiment, the rapidity distribution of charged particles is shifted by a constant y_{β} in the labor system compared to the distribution in the center-of-mass frame. The mid-rapidity is defined as the region in the center-of-mass frame, where y=0. For a colliding experiment like Alice, this corresponds to a polar angle θ equal to 90°. The initial rapidities of the colliding beams in the labor system can be calculated using the following equations:

$$p_z = M_T \sinh(y) \quad y = \sinh^{-1} \left(\frac{p_z}{M_T} \right) \tag{B.5}$$

M_T is the transverse mass.

$$M_T = \sqrt{M^2 + \mathbf{p_T}^2} \tag{B.6}$$

The incident particles of the beams have a negligible p_T and M_T is equal to the rest mass M. Table B.1 gives the beam rapidity for pp and $PbPb$ collisions.

$\sqrt{s_{NN}}$ [TeV]	colliding system	y_{beam}
14	pp	$\approx\pm 9.6$
10	pp	$\approx\pm 9.3$
5.5	$PbPb$	$\approx\pm 8.7$

Table B.1: Initial rapidity of the beam.

The determination of y is complicated since it requires to know the energy E and the longitudinal momentum p_z of the particle. Thus it is more convenient to use the pseudo-rapidity η.

$$\eta = \frac{1}{2} \ln \left(\frac{|\mathbf{p}| + p_z}{|\mathbf{p}| - p_z} \right) \tag{B.7}$$

In Alice,

$$\eta = -\ln \left(\tan \left(\theta/2 \right) \right) \tag{B.8}$$

For mass-less or ultra-relativistic particles the rapidity y is identical to the pseudo-rapidity η.

Invariant mass

The invariant mass, M_{inv}, of a particle with four-momentum p^μ is invariant under Lorentz transformations.

$$M_{inv}^2 = p^\mu p_\mu = E^2 - \mathbf{p} \cdot \mathbf{p} \tag{B.9}$$

The same equation can be used to calculate the rest mass of a particle which decayed into several others, whose momenta have been measured. For the case of two particles (momenta p_1^μ and p_2^μ):

$$M_{inv}^2 = (p_1^\mu + p_2^\mu)^2 = p_1^\mu p_{\mu 1} + p_2^\mu p_{\mu 2} + 2 p_1^\mu p_{\mu 2} \tag{B.10}$$

$$M_{inv}^2 = m_1^2 + m_2^2 + 2 p_1^\mu p_{\mu 2} \tag{B.11}$$

The equation can be simplified in the case of $e^\pm$, since their mass $M_{e^\pm}$=0.5 MeV is negligible compared to their energy.

$$M_{inv}^2 = 2 \left(E_1 E_2 - \mathbf{p_1} \cdot \mathbf{p_2} \right) = 2 \left(E_1 E_2 - p_{z1} p_{z2} - \mathbf{p_{T1}} \cdot \mathbf{p_{T2}} \right) \tag{B.12}$$

With:

$$E_{e^\pm} \approx |\mathbf{p_{e^\pm}}| = p_{Te^\pm} \cosh(\eta_{e^\pm}) \tag{B.13}$$

$$p_{ze^\pm} = p_{Te^\pm} \sinh(\eta_{e^\pm}) \tag{B.14}$$

From Eq. B.12. B.13 and . B.14, one deduces:

$$M_{inv}^2 = 2\left(p_{T1}p_{T2}[\cosh\left(\eta_1 - \eta_2\right) - \cos\left(\phi_1 - \phi_2\right)]\right) \tag{B.15}$$

Eq. B.15 is used to compute the invariant mass of an electron-positron pair inside an event. To estimate the relative error on m_{inv} due to the momentum resolution of the two $e^{\pm}$, it is interesting to write:

$$m_{inv}^2 = 2|\mathbf{p_1}||\mathbf{p_2}|\left(1 - cos\left(\mathbf{p_1}\cdot\mathbf{p_2}\right)\right) \tag{B.16}$$

For a parent particle produced with a small momentum (the labor frame is then quasi the rest frame of the particle), the electron and positron are quasi back-to-back and $(1 - cos\left(\mathbf{p_1}\cdot\mathbf{p_2}\right))\approx 2$. The $e^{\pm}$ momenta are about half of the mass of the parent particle. Assuming the measurements of the electron and positron are independent, one finds:

$$\frac{\Delta M_{inv}}{M_{inv}} = \sqrt{2} \times \frac{\Delta p_{e^{\pm}}}{p_{e^{\pm}}} \tag{B.17}$$

The mass resolution is $\sqrt{2}$ of the $e^{\pm}$ momentum resolution.

Appendix C

Nuclear shadowing

C.1 Definition of the x Bjorken variable

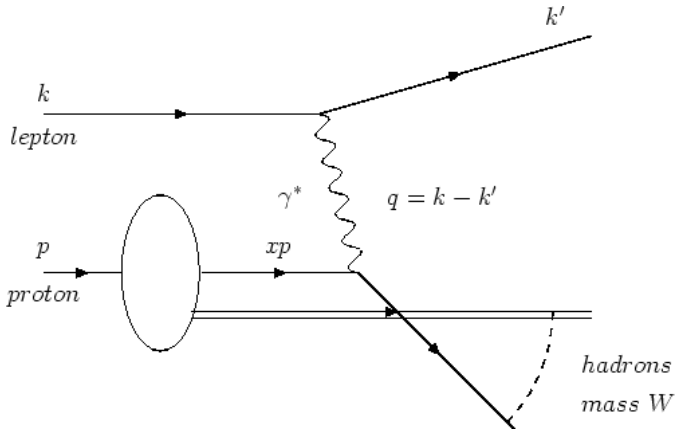

Figure C.1: Graphical representation of an electron-proton collision in the Deep Inelastic Scattering Ansatz

In this appendix c is taken equal to unity and the four momentum p^μ is written p. The Bjorken variable, x, can be introduced with the kinematic variables of electron-nucleon or electron-nucleus Deep Inelastic Scatterings (DIS). Fig.C.1 schematizes an electron-proton inelastic scattering. The four momenta squared, q^2, of the virtual photon exchanged between the electron and the proton is negative. Q^2 is commonly used, Q^2=-q^2. The Bjorken variable x is defined as

$$x = \frac{Q^2}{2(p \cdot q)} \tag{C.1}$$

where p is the 4-momentum of the incoming proton of mass M, p=(M,0,0,0) in the labor system. p·q is Lorentz-invariant and the computation in the labor frame gives:

$$x = \frac{Q^2}{2M\nu} \tag{C.2}$$

where ν is the energy transferred from the electron to the proton.

$$Q^2 = 2M\nu - W^2 + M^2 \tag{C.3}$$

W^2 is the mass of the hadronic final state. In elastic scattering, W=M and as a consequence x=1. In inelastic scattering, W>M and 0<x<1.
In the Parton-Model, first introduced in 1978 by Feynman, the electron-nucleon DIS is interpreted as an elastic scattering between the electron and a constituent, so-called parton, of the nucleon. In the infinite momentum frame of the nucleon, the transverse momenta of the partons and their masses can be neglected and x is the longitudinal momentum fraction of the nucleon carried by the parton. An other interpretation of x in the labor-system comes from the fact that the scattering between the electron and the parton is elastic. Then similarly to Eq. C.3 when W=M, Q^2=2mν, where m is the effective mass of the parton. As a consequence, x corresponds to the effective mass fraction of the parton.

$$x = \frac{Q^2}{2M\nu} = \frac{Q^2}{2m\nu} \cdot \frac{m}{M} = \frac{m}{M} \tag{C.4}$$

In a electron-nucleus DIS, x (=x_A) is the momentum fraction of the nucleus, A, carried by the parton. Nevertheless one is used to consider x_N, the momentum fraction of the nucleon, N, carried by the parton. On average,

$$x_A = \frac{Q^2}{2(p_A \cdot q)} = \frac{Q^2}{2A(p_N \cdot q)} = \frac{x_N}{A} \tag{C.5}$$

That is why, in a nucleus the variable x_N goes a priori up to A. Most of the time, the tail above 1 is neglected, like, for example, in the parametrization of the nuclear modifications of the Parton Distribution Functions.

C.2 Parton distribution function (PDF)

The parton distribution functions (PDF's), $f_i^a(x,\mathrm{Q}^2)$, gives the probability to find a parton i with a fraction x of the beam energy when the beam particle a is probed by a hard scattering at virtuality scale Q^2. The momentum-weighted combination is normalized in the following way:

$$\sum_i \int_0^1 dx\, x \times f_i^a(x, Q^2) \equiv 1 \tag{C.6}$$

The proton parton distributions are related to nonpertubative aspect of QCD and are therefore parametrized. The Q^2-dependence is perturbatively calculable by the DGLAP equations, found independently in 1972 by Gribov-Lipatov and in 1977 by Altarelli-Parisi and Dokshitzer [120, 121, 122]. Lepton-nucleus Deep Inelastic Scattering data, Drell-Yan cross-section in proton-nucleus collisions and hard scattering data are used to estimated the PDF's at given x and Q^2. A global fit is performed to choose the best set of parameters that can reproduce the data together. To reduce the number of parameters, some assumptions have to be done, particularly for low x or parton types, like gluons, not well constrained by the data. The neutron parton distributions are obtained by isospin conjugation:

$$f_u^n = f_d^p, \quad f_d^n = f_u^p \tag{C.7}$$

There are a lot of PDF's available that correspond to different sets of experimental data and different extrapolations. We used the CTEQ5L PDF's[46] which are leading order extrapolated PDF's. Fig. C.2 shows the MRST HO proton parton distribution functions[123] evaluated at $Q^2=M^2_{Z^0}$. The valence distributions are larger than the corresponding sea quark distributions at

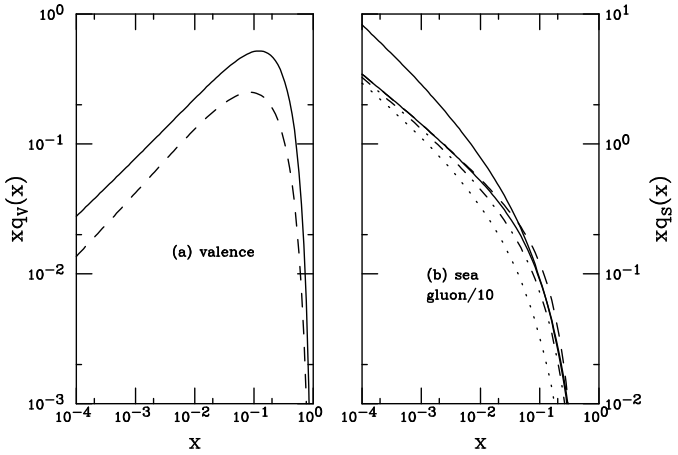

Figure C.2: The MRST HO parton distribution functions at $Q^2=M^2_{Z^0}$. The up (solid line) and down (dashed line) valence distributions are given in (a) while the up (lower solid line), down (dashed line), strange (dot-dashed line), and charm (dotted line) sea quark distributions are shown in (b), along with the gluon distribution (upper solid line), reduced by a factor of 10 for comparison [67].

$x \geq 0.1$ and extend to higher x values but the sea distributions plays a important role at $x \approx 10^{-4}$ where they are a factor 100 larger than the valence distributions. The gluon distribution is shown at 1/10 of its magnitude.

The Z^0 is mainly produced by $q\bar{q}$ annihilation. Due to isospin conjugation,

$$\frac{d^2\sigma^{Z^0}_{pp}}{dp_T dy} = \frac{d^2\sigma^{Z^0}_{nn}}{dp_T dy} \tag{C.8}$$

Moreover $f^n_{\bar{u}} \approx f^n_{\bar{d}}$ and $f^p_{\bar{u}} \approx f^p_{\bar{d}}$. As a consequence,

$$\frac{d^2\sigma^{Z^0}_{pn}}{dp_T dy} \approx \frac{d^2\sigma^{Z^0}_{pp}}{dp_T dy} \tag{C.9}$$

Without taking into account the modification of the PDF's for nucleons inside a nucleus, $PbPb$ collisions can be simulated as a combination of weighted pp, nn, pn and np collisions, according to

$$\frac{d^2\sigma^{Z^0}_{NN}}{dp_T dy} = \frac{Z^2}{A^2} \times \frac{d^2\sigma^{Z^0}_{pp}}{dp_T dy} + \frac{(A-Z)^2}{A^2} \times \frac{d^2\sigma^{Z^0}_{nn}}{dp_T dy} + \frac{Z \cdot (A-Z)}{A^2} \times \frac{d^2\sigma^{Z^0}_{pn}}{dp_T dy} + \frac{d^2\sigma^{Z^0}_{np}}{dp_T dy} \tag{C.10}$$

where $\frac{d^2\sigma^{Z^0}_{NN}}{dp_T dy}$ represents Z^0 differential cross-section per nucleon-nucleon collision in $PbPb$ reactions, and A and Z are the mass number and the atomic number of Pb nuclei. Nevertheless it can be simplified by taking in a good approximation

$$\frac{d^2\sigma^{Z^0}_{NN}}{dp_T dy} = \frac{d^2\sigma^{Z^0}_{pp}}{dp_T dy} \tag{C.11}$$

C.3 x probed by the Z^0 boson

The x range probed by the production of the Z^0 boson in $(A_1,Z_1)\cdot(A_2,Z_2)$ collisions can be estimated by taking the leading-order kinematic. The cross-section is dominated by the leading-order process $q\bar{q}\rightarrow Z^0$. By neglecting the intrinsic transverse momentum of the parton in the nucleon, the four-momenta of the incoming quark and anti-quark are

$$p_1 = \frac{\sqrt{s_{pp}}}{2}\frac{Z_1}{A_1}(x_1,0,0,x_1) \quad p_2 = \frac{\sqrt{s_{pp}}}{2}\frac{Z_2}{A_2}(x_2,0,0,-x_2) \tag{C.12}$$

x_1 and x_2 are the longitudinal momentum fraction of the nucleon carried by the quark and the antiquark. $\sqrt{s_{pp}}$ is the c.m.s. energy for pp collisions. $\sqrt{s_{NN}}$ is the c.m.s. energy per nucleon pair. For symmetric colliding system (A_1=A_2=A, Z_1=Z_2=Z)

$$\sqrt{s_{NN}} = \frac{Z}{A}\sqrt{s_{pp}} \tag{C.13}$$

For production at threshold the squared invariant mass of the two partons equals to the mass of the Z^0 boson:

$$M^2_{z^0} = (p_1+p_2)^2 = x_1x_2s_{NN} = x_1\frac{Z_1}{A_1}x_2\frac{Z_2}{A_2}s_{pp} \tag{C.14}$$

$$p_{Z^0} = p_1 + p_2 \tag{C.15}$$

The rapidity of the produced Z^0 is defined as:

$$y_{Z^0} = \frac{1}{2}\ln(\frac{E+p_z}{E-p_z}) = \frac{1}{2}\ln(\frac{x_1}{x_2}\frac{Z_1A_2}{Z_2A_1}) \tag{C.16}$$

From the two relations.C.14 and C.16, x_1 and x_2 can be derived.

$$x_1 = \frac{M_{Z^0}}{\sqrt{s_{pp}}}\cdot\frac{A_1}{Z_1}\cdot e^{y_{Z^0}} \quad x_2 = \frac{M_{Z^0}}{\sqrt{s_{pp}}}\cdot\frac{A_2}{Z_2}\cdot e^{-y_{Z^0}} \tag{C.17}$$

$$x_1 = \frac{M_{Z^0}}{\sqrt{s_{NN}}}\cdot e^{y_{Z^0}} \quad x_2 = \frac{M_{Z^0}}{\sqrt{s_{NN}}}\cdot e^{-y_{Z^0}} \tag{C.18}$$

At central rapidities $x_1{\approx}x_2$. The values obtained using Eq. C.18 are given in Table C.1 for pp and $PbPb$ collisions. As a reference, they are also reported for $c\bar{c}$ and $b\bar{b}$ produced at threshold ($M_{c\bar{c}}$=$2M_c{\approx}2.4\,\mathrm{GeV}$, $M_{b\bar{b}}$=$2M_b{\approx}9\,\mathrm{GeV}$) by the leading-order process $gg\rightarrow q_{hv}\bar{q_{hv}}$.

System	$PbPb$ 5.5 TeV	pp 14 TeV
$c\bar{c}$	$x{\approx}4{\times}10^{-4}$	$x{\approx}2{\times}10^{-4}$
$b\bar{b}$	$x{\approx}2{\times}10^{-3}$	$x{\approx}6{\times}10^{-4}$
Z^0	$x{\approx}1.66{\times}10^{-2}$	$x{\approx}6.5{\times}10^{-3}$

Table C.1: x-range probed at mid-rapidity and $p_T\rightarrow 0$ by the charm, bottom and Z^0 productions for $PbPb$ and pp collisions.

Z^0 production probed the quark and antiquark PDF's at a relative high x range and high energy scale $Q^2(=M^2_{z^0})$, whereas $c\bar{c}$ and $b\bar{b}$ production probed the gluon PDF at smaller x range and smaller energy scale $Q^2(=M^2_{q_{hv}q_{\bar{hv}}})$. The knowledge of the gluon PDF is very limited, since at leading-order it is only constrained sightly by the Q^2 dependence of the structure function F_2, given by the DGLAP equation and measured in lepton-nucleus deep inelastic scattering (DIS), and by inclusive hadron production data at RHIC. In the small-x region $x<10^{-2}$, the modification of the gluon PDF's is typically given by by momentum conservation and the knowledge of the modifications for the other parton types. On the contrary the quark and antiquark PDF's are better know, since they are directly constrained by F_2 in DIS and the Drell-Yan cross-sections in proton-nucleus collisions. This explains the fact that the theoretical errors of $c\bar{c}$ and $b\bar{b}$ inclusive cross-sections are big compared to the one of Z^0 production. Nevertheless at low x ($x<0.01$), the valence quarks are principally determined by baryon number conservation and the sea quarks have to be extrapolated assuming a smooth behavior. As a consequence, the error band is bigger at the LHC than at the Tevatron for Z^0 production. The x range probed is namely smaller.

C.4 Shadowing effects

The nPDF's of the bound nucleons inside a nucleus A, $f^A_{q_i}$, are different from the PDF's of the free nucleon, $f^N_{q_i}$, due to non-perturbative effects. As for the PDF's in a free nucleon itself, the modifications of the parton distribution functions in the nucleus are parametrized. More precisely the ratio $S^{q_i}=\frac{f^A_{q_i}}{f^N_{q_i}}$ is parametrized since it was shown that it doesn't depend on the PDF's in the free nucleon used to determine it. Updated PDF's in the free nucleon can be used to recalculate the nPDF's in the nucleus with the same S^{q_i} parametrized functions.

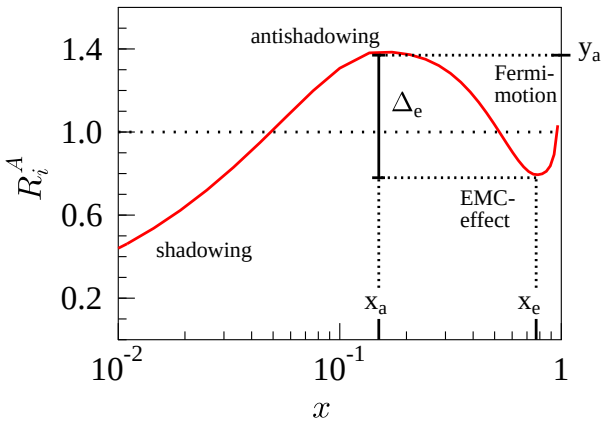

Figure C.3: Example of a nuclear modification functions $S^{q_i}=R^A_i=\frac{f^A_{q_i}}{f^N_{q_i}}$ as a function of the Bjorken variable x for a given energy scale Q^2 and nucleus A [124].

The function $S^{q_i}(A,x,Q^2)$ depends on the number of nucleons in the nucleus A, the Bjorken

variable x and the energy scale Q^2. A priori it depends also on the transversal position of the parton q_i in the nucleus. It implies that it should be impact parameter dependent but we concentrate here on impact-parameter integrated results. The typical shape of the S^{q_i} functions as a function of x is presented in Fig. C.3 for a given energy scale Q^2 and nucleus A. The PDF's are shifted toward higher x values. At small x, where the Z^0, $c\bar{c}$ and $b\bar{b}$ productions probe the nPDF's at the LHC energies (see Table C.1), the shadowing effect plays a role for any Q^2 and parton types. Therefore the cross-sections in $PbPb$ collisions are expected to be smaller than the ones, calculated with the simple geometrical Glauber model from nucleon-nucleon collisions. Moreover since the x range probed by the $c\bar{c}$ and $b\bar{b}$ production is smaller than for the Z^0, this will affect them more deeply. However there is a difference in the Q^2 and production mechanisms, predominantly $q\overline{q}$ with $Q^2{=}M_{Z^0}$ for Z^0 and gg with $Q^2{=}M_{q_{hv}q_{\bar{hv}}}$ for quarkomium.

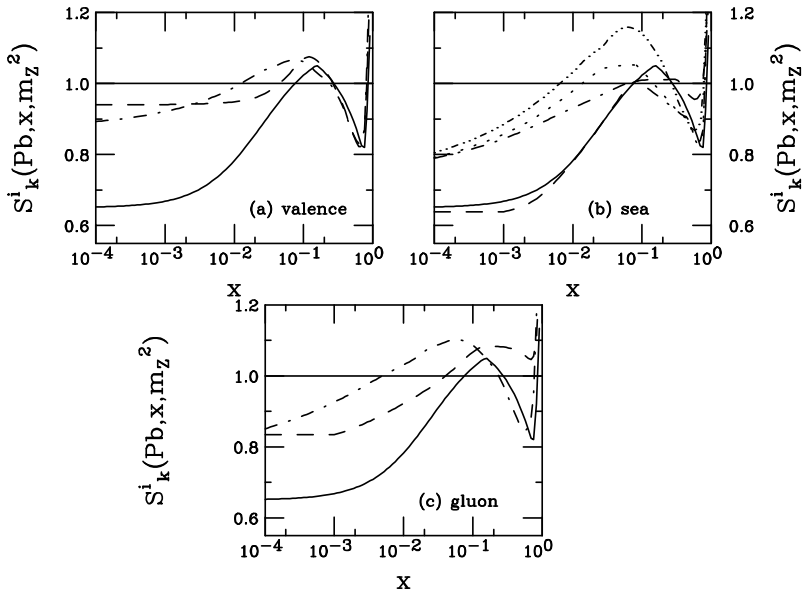

Figure C.4: Valence shadowing is shown in (a) for the S_1 (solid line), S_2 (dashed line) and S_3 (dot-dashed line) parametrizations (see text). Sea quark shadowing is shown in (b) for S_1^s (solid line), S_2^s (dashed line), $S_3^{\overline{u}}{=}S_3^{\overline{d}}$ (dot-dashed line), $S_3^{\overline{s}}$ (dotted line), and $S_3^{\overline{c}}$ (dot-dot-dot-dashed line). Gluon shadowing is shown in (c) for S_1^g (solid line), S_2^g (dashed line), and S_3^g (dot-dashed line).

Z^0 production in $PbPb$ collisions at 5.5 TeV allows to probe S^{q_i} at $A{=}208$, in a x range given by Table C.1 and $Q^2{=}M_{Z^0}$. Different parametrizations have been studied in ref. [67]. The most serious difficulty in the global fit is the lack of experimental data sets, which would more directly constrain the nuclear gluons distributions in particular. To obtain a converging well-constrained fit, S^{q_i} can not be determined for each type of parton, q_i. Fig. C.4 shows three homogeneous shadowing parametrizations used in calculations for Pb at $Q^2{=}M_z^2$. In the parametrization S_1, one assumes that all the parton modifications are equivalent and includes no Q^2 evolution. In S_2, the case of valence quarks, sea quarks and gluons are distinguished and a Q^2 evolution is included from $4{<}Q^2{<}100\,\mathrm{GeV}^2$. The parametrization S_3

is based on the GRV LO [125] parton densities with $S_3^{u_v}=S_3^{d_v}$, $S_3^{\bar{u}}=S_3^{\bar{d}}$. The ratios are evolved over $2.25<Q^2<10^4\,\mathrm{GeV}^2$. Both S_2 and S_3 are evolved using the DGLAP equations [120]. Unfortunately the Q^2 evolution of S_2 stops below the vector boson mass. Thus the S_3 results are the most reliable.

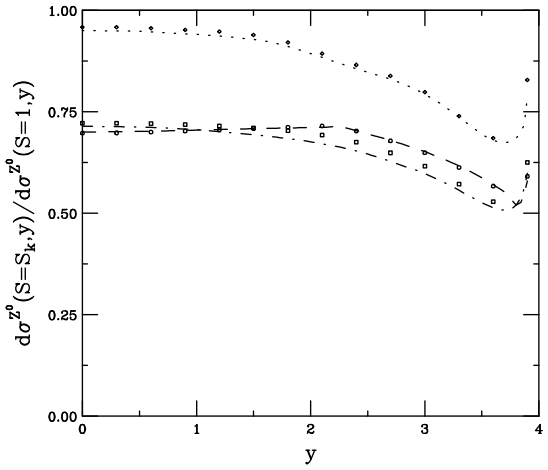

Figure C.5: The shadowing results at LO and NLO are compared. The NLO results are given in the dashed, S_1, dot-dashed, S_2, and dotted, S_3, lined. The LO shadowing ratios for S_1, circles, S_2, squares, and S_3, diamonds, are also shown.

Fig. C.5 shows the ratio of Z^0 production in $PbPb$ collisions ($\sqrt{s_{NN}}$=5.5 TeV) with and without shadowing as a function of the rapidity at both LO and NLO. The results are independent of the order of the calculation. For the pseudo-rapidity range in which we are interested in, the shadowing factor C_{shad} is between 0.7 and 0.95. Given the most realistic assumptions and appropriate Q^2 used for S_3, 0.95 should be considered as the final estimation. For comparison, with the EKS98 parametrizations the expected C_{shad} for charm and bottom productions is 0.65 and 0.84 respectively [68]. At higher x the shadowing effect is expected to be negligible or even to be over 1 (anti-shadowing) for any of the different parametrizations in general. As a conclusion, the Z^0 vector boson should be less affected by shadowing effects.

Bibliography

[1] W.-M. Yao et al. *J. Phys.*, G 33:1, 2006.

[2] D. Gross. Nobel Lecture: The discovery of asymptotic freedom and the emergence of QCD. *Rev. Mod. Phys.*, 77:837, 2005.

[3] D. Politzer. Nobel Lecture: The dilemma of attribution. *Rev. Mod. Phys.*, 77:851, 2005.

[4] F. Wilczek. Nobel Lecture: Asymptotic freedom: From paradox to paradigm. *Rev. Mod. Phys.*, 77:857, 2005.

[5] P.Braun-Munzinger A.Andronic. Ultrarelativistic nucleus-nucleus collisions and the quark-gluon plasma. arXiv:hep-ph/0402291v1, 2004.

[6] J. Wambach P.Braun-Munzinger. The Phase Diagram of Strongly-Interacting Matter. arXiv:hep-ph/0801.4256v1, submitted to Rev. Mod. Phys., 2008.

[7] J. D. Bjorken. Highly relativistic nucleus-nucleus collisions: the central rapidity region. *Phys. Rev.*, D 27:140, 1983.

[8] R. LEY PS Division. CERN 02.09.96 revised and updated by A. Del Russo, HIT Div, in collaboration with H. Desforges and D. Manglanki, CERN, 23.05.01.

[9] Alice Collaboration. Alice Physics Performance Report Volume I. *Nucl. Part. Phys.*, 30:1517, 2004.

[10] D. Miskowiec. Private communication, 2008.

[11] A. Andronic et al. for the ALICE TRD Collaboration. Electron identification performance with ALICE TRD prototypes. *Nucl. Instr. Meth.*, A 522:40, 2004.

[12] ALICE TRD Collaboration. ALICE TRD Technical Design Report. CERN/LHCC 2001-021, 2001.

[13] F. Sauli. Principles of operation of multiwire proportional and drift chambers. CERN Report 77-09, 1977.

[14] L. Rolandi W. Blum. *Particle Detection with Drift Chambers*. Springer verlag, Berlin, Heidelberg, New York, ISBN 3-540-56425-X, 1993.

[15] R.Veenhof. GARFIELD. *Nucl. Instr. and Meth.*, A 419:726, 1998.

[16] S. F. Biagi. Monte Carlo simulation of electron drift and diffusion in counting gases under the influence of electric and magnetic fields. *Nucl. Instr. and Meth.*, A 421:234, 1999.

[17] E.Mathieson. Cathode charge distributions in multiwire chambers: 4 Empirical formula for small anode-cathode separation. *Nucl. Instr. and Meth.*, A 270:602, 1988.

[18] C. Lippmann for the ALICE TRD Collaboration. Position reconstruction in drift chambers operated with Xe,CO2(15%). *Nucl. Instr. Meth.*, A 540:140, 2005.

[19] S. Altinpinar. Entwicklung und Aufbau von Testverfahren fuer die ALICE TRD Auslesekammern, diploma thesis, University of Darmstadt (Germany), 2006.

[20] B. Vulpescu for the TRD collaboration. TRD Software Meeting 30/06. http://www-alice.gsi.de/trd/meetings/sim/sim.html, 2005.

[21] M. Fasel. Stand-alone tracking in the ALICE TRD, diploma thesis, University of Darmstadt (Germany), 2007.

[22] B. Bathen. Aufbau eines Triggers fuer Tests der ALICE-TRD-Supermodule mit kosmischer strahlung, diploma thesis, University of Muenster (Germany), 2007.

[23] E. Sicking. Private Communications, 2008.

[24] P. Vande Vyvre and ALICE DAQ Team. ALICE DAQ and ECS User's guide. ALICE Internal Note/DAQ ALICE-INT-2005-015, 2005.

[25] S.R. Bablok and al. High Level Trigger Online Calibration framework in ALICE. *Journal of Physics: Conference Series*, 119:022007, 2008.

[26] ETM professional control firma. Process visualization and steering system. http://www.infocenter.pvss.com/.

[27] B. Doenigus. Assembly and tests of the first supermodule of the ALICE Transition Radiation Detector, diploma thesis, University of Darmstadt (Germany), 2007.

[28] G. Arnison et al. for the UA1 Collaboration. Experimental observation of isolated large transverse energy electrons with associated missing energy at $\sqrt{s}$=540 GeV. *Phys. Lett.*, B 122:103, 1983.

[29] P. Bagnaia et al. for the UA2 Collaboration. Observation of single isolated electrons of high transverse momentum in events with missing transverse energy at the CERN $\bar{p}p$ collider. *Phys. Lett.*, B 122:476, 1983.

[30] G. Arnison et al. for the UA1 Collaboration. Experimental observation of lepton pairs of invariant mass arount 95 GeV/c^2 at the CERN SPS collider. *Phys. Lett.*, B 126:398, 1983.

[31] P. Bagnaia et al. for the UA2 Collaboration. Evidence for $z^0 \rightarrow e^+e^-$ at the CERN $\bar{p}p$ collider. *Phys. Lett.*, B 129:130, 1983.

[32] S.Drell and T.M. Yan. Massive Lepton-Pair Production in Hadron-Hadron Collisions at High Energies. *Phys. Rev. Lett*, 25:316, 1970.

[33] G. Altarelli et al. Vector Boson production at colliders: A theoretical reappraisal. *Nucl. Phys.*, B 246:12, 1984.

[34] G. Altarelli et al. *Z. Phys.*, C 27:617, 1985.

[35] S. Geer and W.J. Stirling. Jet activity associated with w and z^0 production. *Phys. Lett.*, B 152:373, 1985.

[36] S.L. Glashow. Partial symmetries of weak interactions. *Nucl. Phys.*, 22:579, 1961.

[37] S. Weinberg. A Model of Leptons. *Phys. Rev. Lett.*, 19:1264, 1967.

[38] A. Salam. Proc. 8th Nobel Symp.

[39] Review of Particle Physics, author = R.M. Barnett et al., journal = Phys. Rev., year = 1996, volume =D 54, pages = 1.

[40] A.D. Martin et al. Estimating the effect of NNLO contributions on global parton analyses. *Eur. Phys. J.C.*, 18:117, 2000.

[41] J.I. Kapusta and S.M.H. Wong. Modification of Z boson properties in the quark-gluon plasma. *Phys. Rev.*, D 62:037301, 2000.

[42] A.D. Martin et al. Parton Distributions and the LHC: W and Z Production. *Eur.Phys. J.C.*, 14:133, 2000.

[43] A. M. Copper-Sarkar A. Tricoli and C. Gwenlan. Uncertainties on W and Z production at LHC. arXiv:hep-ex/0509002, 2005.

[44] A. M. Copper-Sarkar. Low-x physics and W and Z production at LHC. arXiv:hep-ex/0512228, 2005.

[45] Torbjorn Sjostrand et al. PYTHIA 6.3 physics and manual. arXiv:hep-ph/0308153, 2003.

[46] CTEQ Collaboration: H.L. Lai et al. arXiv:hep-ph/9903282.

[47] Britta Tiller for the D0 Collaboration. DPG Berlin 04/03/2005. For the Parton Distributions Function CTEQ5L (MSTP(51)=7) we use the parameter PARP(91)=1.3 GeV (D=1 GeV) and PARP(64)=0.1 (D=1).

[48] R. Brun et al. ROOT An Object Oriented Framework For Large Scale Data Analysis. http://root.cern.ch/.

[49] AliRoot, An Object-Oriented Data Analysis Framework. http://aliweb.cern.ch/offline.

[50] GEANT 3. http://wwwasd.web.cern.ch/wwwasd/geant/.

[51] C. Albajar et al. for the UA1 Collaboration. Intermediate vector boson cross sections at the CERN super proton synchroton collider and the number of neutrino types. *Phys. Lett.*, B 198:271, 1987.

[52] J. Alitti et al. for the UA2 Collaboration. A measurement of the w and z production cross sections and a determination of γ_W at the CERN $\bar{p}p$ collider. *Phys. Lett.*, B 276:365, 1992.

[53] B. Abbott et al. for the D0 Collaboration. Extraction of the with of the w boson from measurements of $\sigma(p\bar{p}\rightarrow w+x)\times b(w\rightarrow ev)$ and $\sigma(p\bar{p}\rightarrow z+x)\times b(z\rightarrow ee)$ and their ratio. *Phys. Rev.*, D 61:072001, 2000.

[54] T. Affolder et al. for the CDF Collaboration. Transverse Momentum and Total Cross Section of e^+e^- Pairs in the z-Boson Region from $p\bar{p}$ Collisions at $\sqrt{s}$=1.8 TeV. *Phys. Rev. Lett.*, 84:845, 2000.

[55] T. Affolder et al. for the CDF Collaboration. Measurement of $d\sigma/dy$ for high mass Drell-Yan e^+e^- pairs from $p\bar{p}$ collisions at $\sqrt{s}$=1.8 TeV. *Phys. Rev.*, D 63:011101, 2001.

[56] A. Abulencia et al. for the CDF Collaboration. Measurements of inclusive W and Z cross sections in $\bar{p}p$ collisions at $\sqrt{s}$=1.96 TeV. *Nucl. Part. Phys.*, 34:2457, 2007.

[57] B. Abbott et al. for the D0 Collaboration. Measurement of the inclusive differential cross section for z bosons as a function of transverse momentum in $\bar{p}p$ collisions at $\sqrt{s}$=1.8 TeV. *Phys. Rev.*, D 61:032004, 2000.

[58] D0 Collaboration. Note 4403. 2004.

[59] V.M. Abazov for the D0 Collaboration. Measurement of the Shape of the Boson-Transverse Momentum Distributions in $p\bar{p}\rightarrow z/\gamma^*\rightarrow e^+e^-+x$ Events Produced at $\sqrt{s}$=1.96 TeV. *Phys. Rev. Lett.*, 100:102002, 2008.

[60] V.M. Abazov et al. for the D0 Collaboration. Measurement of the ratio of differential cross sections for w and z boson production as a function of transverse momentum in $\bar{p}p$ collisions at $\sqrt{s}$=1.8 TeV. *Phys. Lett.*, B 517:299, 2001.

[61] CDF Collaboration F. Abe et al. Measurement of $\sigma b(w\rightarrow ev)$ and $\sigma b(z^0\rightarrow e^+e^-)$ in $p\bar{p}$ collisions at $\sqrt{s}$=1800 GeV. *Phys. Rev.*, D 44:29, 1991.

[62] CDF Collaboration F. Abe et al. Measurement of $\sigma b(w\rightarrow ev)$ and $\sigma b(z^0\rightarrow e^+e^-)$ in $p\bar{p}$ collisions at $\sqrt{s}$=1.8 TeV. *Phys. Rev. Lett.*, 76:3070, 1996.

[63] R. J. Glauber and G. Matthiae. High-energy scattering of protons by nuclei. *Nucl. Phys.*, B 21:135, 1970.

[64] R. Arnaldi. Phd thesis, University of Torino (Italy), 2000.

[65] D. Miskowiec. http://www-linux.gsi.de/ misko/overlap/.

[66] H. de Vries C.W. de Jager and C. de Vries. Nuclear Charge-and Magnetization-Density-Distribution Parameters from Elastic Electron Scattering. *Atomic Data and Nuclear Data Tables*, 14:479, 1974.

[67] R. Vogt. Shadowing effects on vector boson production. *Phys. Rev.*, C 64:044901, 2001.

[68] ALICE Collaboration. Alice Physics Performance Report volume II. *J. Phys.*, G 32:1753, 2006.

[69] Torbjorm Sjostrand et al. A Brief Introduction to PYTHIA 8.1. CERN-LCGAPP-2007-04,arXiv:0710.3820.

[70] M. Gyulassy and X. N. Wang. HIJING. http://www-nsdth.lbl.gov/ xnwang/hijing/.

[71] et al. S. Agostinelli. GEANT 4. *Nucl. Instr. and Meth.*, A 506:250, 2003.

[72] J. Ranft A. Fasso, A. Ferrari and P. Sala. FLUKA. http://www.fluka.org/.

[73] J. F. Grosse-Oetringhaus. Determination of the Physics Performance of ALICE Central Barrel using a Distributied GRID Computing Environment, diploma thesis, University of Muenster (Germany), 2005.

[74] R. Bailhache. Energieverlust und Elektron/Pion-Identifikation im ALICE TRD, diploma thesis, University of Darmstadt (Germany), 2000.

[75] A. Andronic et al. Electron identification performance with ALICE TRD prototypes. *Nucl. Instr. and Meth.*, A 522:40, 2004.

[76] ALICE TRD Collaboration. First beam test with a real size, six layer, series production detector stack for the ALICE TRD. *GSI Scientific Report*, page 355, 2004.

[77] A. Wilk et al. Electron/pion identification with ALICE TRD prototypes using a neural network algorithm. *Nucl. Instr. Meth.*, A 552:364, 2005.

[78] C. Lippmann R. Bailhache. New test beam results with prototypes of the ALICE TRD. *Nucl. Instr. Meth.*, A 563:310, 2006.

[79] Alexander Kalweit. Private communications.

[80] M.L. Mangano P. Nason G. Ridolfi M. Cacciari, S. Frixione. *JHEP*, 068:0404, 2004.

[81] CDF and D0 Collaboration. http://arxiv.org/abs/0804.1159v1.

[82] M.L. Mangano P. Nason R. Bonciani, S. Catani. NLL resummation of the heavy-quark hadroproduction cross-section. *Nucl. Phys.*, B 529:424, 1998.

[83] CDF Collaboration T. Affolder et al. Charged jet evolution and the underlying event in proton-antiproton collisions at 1.8 TeV. *Phys. Rev.*, D 65:092002, 2002.

[84] R. Craig Group for the CDF Collaboration Rick Field. arXiv:hep-ph/0510198v1, 2005.

[85] P. Nason M. Mangano and G. Ridolfi. Heavy-quark correlations in hadron collisions at next-to-leading order. *Nucl. Phys.*, B 373:295, 1992.

[86] Y. Kubota et al. for the CLEO Collaboration. The CLEO ii detector. *Nucl. Inst. and Meth.*, A 320:66, 1992.

[87] A. Abashian et al. for the BELLE collaboration. The Belle detector. *Nucl. Inst. and Meth.*, A 479:117, 2002.

[88] M. Ridel et al. for the ALEPH collaboration. Performance of the ALEPH detector at LEP. *Nucl. Inst. and Meth.*, A 360:481, 1995.

[89] P. Aarnio et al. for the DELPHI collaboration. The DELPHI detector at LEP. *Nucl. Inst. and Meth.*, A 303:233, 1991.

[90] K.Ahmet et al. for the OPAL collaboration. The OPAL detector at LEP. *Nucl. Inst. and Meth.*, A 305:275, 1991.

[91] R. Barate et al. for the ALEPH collaboration. Study of Charm Production in Z Decays. *Eur. Phys. J. C*, 16:597, 2000.

[92] C. Buttar A. Moraes and I. Dawson. Prediction for minimum bias and the underlying event at LHC energies. *Eur. Phys. J. C*, 50:435, 2007.

[93] J. H. Kuehn. arXiv:hep-ph/9707321, 1997.

[94] TPC Collaboration. ALICE TPC Technical Design Report. CERN/LHCC 2000-001, 2000.

[95] J. de Cuveland. Entwicklung der globalen Spurrekonstruktionseinheit für den ALICE-übergangsstrahlungsdetektor am LHC (CERN), diploma thesis, University of Heildelberg (Germany), 2003.

[96] ALICE Muon Collaboration. ALICE Muon Spectrometer Technical Design Report. CERN/LHCC 1999-022, 1999.

[97] Z. Conesa Del Valle. Performance du spectrometre a muons d'ALICE. Production et mesure des bosons faibles dans des collisions d'ions lourds aupres du LHC, phd thesis, University of Nantes (France), 2007.

[98] ATLAS Collaboration. ATLAS Physics Technical Design Report. CERN/LHCC 1999-014, 1999.

[99] CMS Collaboration. CMS Physics Technical Design Report. CERN/LHCC 2006-001, 2006.

[100] M. Schott. Study of the z Boson Production at the ATLAS Experiment with First Data, phd thesis, University of Munich (Germany), 2007.

[101] M. Schott. *Journal Of Physics: Conference Series*, 110:042024, 2008.

[102] Y.L. Dokshitzer and D.E. Kharzeev. Heavy-quark colorimetry of QCD matter. *Phys. Lett.*, B 519:199, 2001.

[103] R.Vogt. The A Dependence of Open Charm and Bottom Production. *Int. J. Mod. Phys.*, E 12:211, 2003.

[104] A. Adare et al for the PHENIX Collaboration. Measurement of high-p_T single electrons from heavy-flavor decays in p+p collisions at 200 GeV. *Phys. Rev. Lett.*, 97:252002, 2006.

[105] Y. Morino for the PHENIX Collaboration. Measurement of charm and bottom production in p+p collisions at $\sqrt{s}$ = 200 GeV at RHIC-PHENIX. arXiv:hep-ex/08053871, 2008.

[106] J. Bielcik for the STAR Collaboration. Centrality dependence of heavy flavor production from single electron measurement. *Nucl. Phys.*, A 774:697, 2006.

[107] D. Acosta et al for the CDF Collaboration. Measurement of Prompt Charm Meson Production Cross Sections in $p\bar{p}$ Collisions at $\sqrt{s}$=1.96 TeV. *Phys. Rev. Lett.*, 91:241804, 2003.

[108] S.S. Adler et al for the PHENIX Collaboration. Nuclear Modification of Single Electron Spectra and Implications for Heavy Quark Energy Loss in Au + Au collisions at 200 GeV. *Phys. Rev. Lett.*, 96:032301, 2006.

[109] S. Baumgart for the STAR Collaboration. Measurement of the Open Charm Cross-Section in 200 GeV Heavy-Ion Collisions at STAR. arXiv:hep-ex/0805.4228v1, 2008.

[110] A. Dainese. Heavy flavour cross sections at 10 TeV (PWG3 Meeting 02/06). http://indico.cern.ch/conferenceDisplay.py?confId=24896, 2008.

[111] Ding Tian. The Application of Bayesian Technique for Particle Identification. arXiv:physics/0602170v1, 2006.

[112] A. Kalweit. Identified charged particle spectra (presentation at the ALICE Week PWG2 Meeting). http://indico.cern.ch/conferenceDisplay.py?confId=24911, 2008.

[113] A. Kalweit. Energy Loss Calibration of the ALICE Time Projection Chamber, diploma thesis, University of Darmstadt (Germany), 2007.

[114] Y. Wang. Study on d^{*+} reconstruction in pp (presentation at the pgw3 meeting 15/09). http://indico.cern.ch/conferenceDisplay.py?confId=24900, 2008.

[115] M. Lunardon A. Dainese F. Antinori, C. Bombonati. Study of the ALICE performance for the measurement of beauty production in pp collisions at $\sqrt{s}$=14 tev via displaced electrons. ALICE-INT-2006-015, 2006.

[116] A. Adare et al for the PHENIX Collaboration. Single Electrons from Heavy Flavor Decays in pp Collisions at $\sqrt{s}$=200 *gev*. *Phys. Rev. Lett.*, 96:032001, 2006.

[117] A. Marin. Progress report on conversion electrons measurement (presentation at the pwg4 meeting 28/10). http://indico.cern.ch/conferenceDisplay.py?confId=24943, 2008.

[118] Y. Kharlov. Progress report on π^0 working group (presentation at the pgw4 meeting 28/10). http://indico.cern.ch/conferenceDisplay.py?confId=24943, 2008.

[119] J.F. Grosse-Oetringhaus A. Colla. The Shuttle Framework - A system for automatic readout and processing of conditions data. ALICE Internal Note/Computing ALICE-INT-2008-011, 2008.

[120] V.N. Gribov and L.N. Lipatov. e^+e^- pair annihilation and deep inelastic ep scattering in perturbation theory. *Sov. J. Nucl. Phys.*, 15:438, 1972.

[121] G.Parisi G. Altarelli. Asymptotic freedom in parton language. *Nucl. Phys.*, B 126:298, 1977.

[122] Yu.L. Dokshitzer. *Sov. Phys. JETP*, 46:641, 1977.

[123] W.J. Stirling A.D. Martin, R.G. Roberts and R.S. Thorne for the MRST Collaboration. Parton distributions incorporating QED contributions. *Eur. Phys. J.C*, 39:155, 2005.

[124] Hannu Paukkumen Kari J. Eskola and Carlos A. Salgado. arXiv:hep-ph/0802.0139v1.

[125] E. Reya M.Gluck and A. Vogt. *Z. Phys. C*, 53:127, 1992.

Acknowledgements

I would like to thank the people, who help me during this work and without whom it would not have been possible to realise it.
First I am deeply grateful towards Prof. Peter Braun-Munzinger, who gave me the unique opportunity to join his research groups and work inside the ALICE collaboration. I profited very much from his enthusiasm for physics leading to interesting discussions in our group about our work or in other fields of physics. We had also the chance to be informed about the last news in ALICE and more generally at the LHC am CERN.
I would like to express my gratitude to my supervisor Dr. Anton Andronic for his advice and patience. He had always very interesting suggestions to solve problems.
I am deeply indebted to Prof. Johanna Stachel and Prof. Christoph Blum for many stimulating discussions about the TRD and the calibration software. Special mention also deserve Dr. Marian Ivanov, from whom I learnt a lot about the TPC calibration and as consequence the TRD calibration, Dr. Silvia Masciocchi for her help in the single electron study and Dr. Alexandru Bercuci, who was never at loss for a new idea to improve the TRD reconstruction algorithm. Many thanks to Markus Fasel for his collaboration during the calibration of the TRD and to Alexander Kalweit for the helpful discussions on the TPC PID.
I would like to thank the ALICE Heavy Flavours Working Group (PWG3) and in particular F. Antinori, G. Martinez-Garcia, Z. Conesa del Valle, H.T. Ding, and A. Dainese for fruitful discussions about the Z^0 study. I am grateful to H.T. Ding for help with the MNR code. Chuncheng Xu is gratefully acknowledged for his helpful discussion on the isolation cut.
I also want to express my thanks to my colleagues with whom I had such pleasant discussions at the coffee-break, in particular Dr. Chilo Garabatos, present at the beginning of my time at GSI, Dr. Oliver Busch, who was during a long time my office mate, Dr. Dariusz Miskowiec for the beautiful organisation of some group excursions, Dr. Matus Kalisky, Dr. Georgios Tsiledakis, Juan Castillo and Sedat Altinpinar.
I finally express my thankfulness to my parents for their encouragement and support during all this time.

Curriculum Vitae

Name:	Bailhache, Raphaëlle
Born the:	19.01.1982 in Nantes (France)
Nationality:	French
Address:	Obere Mühlstraße 56 A
	64289 Darmstadt
	Germany
E-mail address:	r.bailhache@gsi.de

Education:

04/07	Virtual Institute of Strongly Interacting Matter (VI-SIM) 2006
	prize for the master thesis
10/06 - present	Integration of the Helmholtz Research School
	for PhD students (Frankfurt-Darmstadt)
	Quark Matter Studies
10/03 - 08/05	Technical University Darmstadt, Physics department
	Physics diploma with honours
	Energy loss and e/π identification with the ALICE TRD
09/01 - 07/03	Ecole Centrale Paris (ECP)
	Engineer diploma (2006)
09/99 - 07/01	Lycee Clemenceau, Nantes
	Classes preparatoires MPSI, MP* (Math-Physik)
12/01	Prize in Physics from the Lycee Jules Verne, Nantes
07/99	Lycee Jules Verne, Nantes
	Baccalaureat with honours

Work Experience:

09/05-12/08	preparation for PhD
	GSI, Darmstadt
10/04-08/05	preparation for physics diploma
	GSI, Darmstadt
07/02-08/02	1 month work in solid state physics
	Technical University Vienna, Physics department

Publications:

Z Boson Measurement with the ALICE central barrel in pp collisions at 14 TeV
R. Bailhache, A. Andronic and P. Braun-Munzinger for the ALICE Collaboration
To be published in Indian Journal of Physics
arXiv:0808.0453

New testbeam results with prototypes of the ALICE TRD
R. Bailhache and C. Lippmann for the ALICE TRD Collaboration
Nucl. Instr. and Meth. A 563 (2006) 310-313

Calibration of the ALICE TRD
GSI Annual Report 2006

Z Boson simulations with the central barrel detectors of ALICE
GSI Annual Report 2005

Talks and Posters:

Measurements of single electrons from charm and beauty with the central barrel of ALICE
Poster at 417^{th} WE-Heraeus-Seminar in Bad Honnef (Germany) 07/08

Z reconstruction in the electronic channel with the central barrel
Talk at the ALICE Physics Week in Prague 27/02/08

Z boson measurement with the ALICE central barrel
Poster at Quark Matter 2008 in Jaipur 02/08

TRD Calibration
Talk at the DPG Tagungen in Darmstadt 11/03/08

Z Boson simulations with the central barrel detectors of ALICE
Poster at the DPG Tagungen in München 03/06

New test beam results with prototypes of ALICE TRD
Talk at the TRDs for the 3^{rd} Millenium, 09/05, Brindisi, Italy

Erklärung

Hiermit erkläre ich an Eides statt, daß ich die vorliegende Dissertation selbständig verfasst, keine anderen als die angegebenen Hilfsmittel benutzt und noch keinen Promotionsversuch unternommen habe.

Darmstadt, den 11. November 2008,

gez. Raphaëlle Bailhache